



Leibniz-Institut
für Festkörper- und
Werkstoffforschung
Dresden

Annual Report 2017

Contents

3 Review of 2017

7 Facts & Figures

Highlights from Research Areas

Research Area 1: **Functional Quantum Materials**

- 9 Evidence for a magnetic field induced nematic liquid in the spin chain LiCuSbO_4
- 13 Correlation induced electron-hole asymmetry in quasi-2D iridates
- 17 Large, three-dimensional and faceted LaFeAsO crystals
- 20 Nanotubular spin-waves conduits
- 23 Generic coexistence of Fermi arcs and Dirac cones on the surface of time-reversal invariant Weyl semimetals
- 27 Evidence for a field-induced quantum spin liquid in $\alpha\text{-RuCl}_3$
- 31 Magnetic characterization in the TEM: Skyrmions and electron vortex beams

Research Area 2: **Function through Size**

- 35 Sperm-tetrapod micromotor for targeted drug delivery
- 39 Metastable phase formation in undercooled Fe-Co melts under terrestrial and microgravity conditions

Research Area 3: **Quantum Effects at the Nanoscale**

- 43 Magnetism in iron nanoislands tuned by epitaxial growth and magneto-ionic reactions
- 47 Addressable and color-tunable piezophotonic light-emitting stripes
- 51 A quantum material that emits pairs of entangled photons on demand
- 55 Single-electron lanthanide-lanthanide bonds inside the fullerene cage: en route to unusual electronic and magnetic properties
- 59 Theoretical prediction of a giant anisotropic magnetoresistance in carbon nanoscrolls
- 63 Chemical gating of a weak topological insulator: $\text{Bi}_{14}\text{Rh}_3\text{I}_9$

Research Area 4: **Towards Products**

- 67 Surface Acoustic Waves: concepts, materials and applications
- 71 Materials for biomedical applications
- 75 Ultra-high-strength tool steels prepared by selective laser melting and casting – a comparative study

Appendix

- 79 Publications
- 108 Patents
- 110 Graduation of young researchers
- 112 Calls and awards
- 113 Scientific conferences and colloquia
- 114 Guests and scholarships
- 117 Guest stays of IFW members at other institutes
- 119 Board of Trustees, Scientific Advisory Board



Review of 2017

This Annual Report addresses our cooperation partners worldwide, friends and all those who are interested in the Institute's progress. It presents a cross section of our scientific activities in the past year, highlighting exemplary some results in the main part and giving a systematic overview of the institute's output on the back pages. The very first pages of the Annual Report are used for a short flashback to the institutes development in 2017 beyond scientific results.

The year 2017 began with the celebration of a jubilee at the Leibniz Institute for Solid State and Materials Research Dresden: It have been 25 years since the IFW Dresden has been founded on January 1, 1992. We took this opportunity to thank all our partners and friends for their support and cooperation during an official ceremony on February 6, 2017 in the Congress Center Leipzig where we celebrated the event together with the other Saxon Leibniz Institutes. Together we looked back to a very successful development and presented our recent achievement to our prominent guests, among them the Saxon Minister for Science and the Fine Art Eva-Maria Stange and the president of the Leibniz Association Matthias Kleiner. On the IFW exhibition stand, our four ERC grantees presented their projects which reflected nicely the scope of IFW research. Later on, on February 27, 2017, we had the IFW's annual reception, where we celebrated a birthday party with all the members IFW staff.

In terms of scientific work, 2017 was again a very productive and successful year for IFW. As in previous years, our scientific output has been on a high level, both qualitatively and quantitatively, which has been also confirmed by the annual evaluation of the IFW's Scientific Advisory Board. The range of materials that we investigate is broad but well-defined. It contains Quantum Materials, a highly topical class of materials in condensed matter physics, as well as Functional Materials, representing an important part of modern materials engineering. In addition, in the last years, Nanoscale Materials became a strong focus of present-day materials science and a crucial material class for cutting-edge developments in electrical engineering. These three classes, Quantum Materials,



Functional Materials and Nanoscale Materials, provide the three materials-oriented pillars of our scientific work. While being distinctly multidisciplinary, there is a clear common thread to all our activities: all researchers at the IFW Dresden investigate yet unexplored properties of novel materials with the aim to establish new functionalities and applications.

The IFW's Research Program has been adjusted during the program meeting with all responsible scientists of IFW in April 2017. The structuring into the four research areas

- Research Area 1: Functional quantum materials
- Research Area 2: Function through size
- Research Area 3: Quantum effects at the nanoscale
- Research Area 4: Towards products

has been proven to be suitable, providing continuity on the level of research areas and flexibility on the level of research topics.

In September 2017 the German Research Foundation announced the successful draft proposals which are invited to submit a full cluster application in the German wide Excellence Strategy. We are very proud that the Technische Universität Dresden has been successful with six cluster proposals and enters the next round for the Clusters of Excellence. We are especially happy that the IFW participates in three of these proposals for Clusters of Excellence, namely:

- cfaed: Center for Advancing Electronics Dresden
- DCM: Dresden Center for Materiomics
- t.qmat: Complexity and Topology in Quantum Matter

Together with our colleagues at the TU Dresden and the other Dresden research institutes we are currently working very hard to prepare the full proposals. In the case of approval these new clusters will have strong impact on the IFW's strategy as the respective fields will be essentially strengthened.



2017 was again a yielding year with respect to prizes and honours awarded to members of the IFW. The most prestigious of the prizes won by IFW members is the Gottfried-Wilhelm-Leibniz-Prize 2018 of the German Research Foundation, which will be awarded to Prof. Dr. Oliver G. Schmidt in spring 2018. Furthermore, two outstanding PhD thesis of IFW junior scientist have been acknowledged with prizes: The Wilhelm-Ostwald-Society awarded its Young Investigator Prize 2017 to Daniil Karnaushenko, and Julia Körner achieved the Measurement Technology Award of council of university teachers of metrology.

The training of students and young scientists remains a very important concern of our work. PhD and diploma students are involved in nearly all scientific projects and in the resulting publications. Altogether, 26 PhD theses have been successfully completed in 2017, three of them with the best grade possible – summa cum laude. Traditionally, the IFW acknowledges these outstanding achievements of young scientist by awarding the Tschirnhaus-Medal.

As a Leibniz Institute, the IFW is financed by the federal government and the German federal states in equal parts. However, a considerable extension of capability is the amount of third-party project funding which is also an important index of quality. The level of third-party funding in 2017 amounts to 8.5 Mio. Euro. Most of this project funding was acquired in a highly competitive mode from the DFG and the European Commission. In particular, the high number of four running ERC groups and the substantial participation in two Collaborative Research Centres (SFB's) prove the competitiveness of IFW. Among the large number of other third-party funded projects are two DFG Priority Programs that are coordinated by scientists from the IFW, as well as six DFG Priority Programs and two DFG Research Groups where scientists from the IFW participate.



Essentially publicly funded, it is our mission to make our research results public. In 2017, IFW scientists have published about 450 articles in scientific journals and conference proceedings. 169 invited talks were presented by IFW scientists at conferences, workshops, seminars and other occasions around the world. In 2017, we were granted 18 patents, and applications for 12 more patents have been made. Apart from these scientific communications the IFW continued its large efforts to make scientific work accessible for the general public and to inspire young people to study science or engineering. The most prominent event in this respect is the Dresden Long Night of Sciences which takes place once a year before the summer vacancies. In 2017, again, the IFW offered an ample program which attracted about 3500 visitors. The highlight was an experimental show on low temperature physics presented by two IFW scientists in the roles of Heike Kamerlingh Onnes and Carl von Linde. A closer look to our research was offered to about 100 participants of the “Junior Doctor” action and the German wide Girls’ Day. Besides these big events we organize almost weekly lab-tours for various visitor groups, from school classes through official representatives to guests from foreign organization.

So we are looking back to a successful year 2017 in the Institute’s development. We are quite aware that this is due to the sustainable network of colleagues and partners in universities, research institutes and industry, both, on the regional and the international scale. We thank all of them for their constructive cooperation and are looking forward to taking up future challenges together. Special tribute is paid to the members of the Scientific Advisory Board and of the Board of Trustees as well as the funding organizations that continuously support and foster the positive development of the IFW.



Facts & Figures

Organization

The Leibniz Institute for Solid State and Material Research Dresden (IFW) is one of currently 93 institutes of the Leibniz Association in Germany. It is a legally independent association, headed by the Scientific Director, Prof. Dr. Burkard Hillebrands, and the Administrative Director, Dr. Doreen Kirmse.

The scientific body of the IFW Dresden is structured into five institutes, the directors of which are simultaneously full professors at Dresden, respectively Chemnitz Universities of Technology:

- IFW Institute for Solid State Research, Prof. Dr. Bernd Büchner
- IFW Institute for Metallic Materials, Prof. Dr. Kornelius Nielsch
- IFW Institute for Complex Materials, Dr. Thomas Gemming (temporarily)
- IFW Institute for Integrative Nanosciences, Prof. Dr. Oliver G. Schmidt
- IFW Institute for Theoretical Solid State Physics, Prof. Dr. Jeroen van den Brink

Further divisions are the Research Technology Division and the Administrative Division.

Financing

The institutional funding of IFW is supplied by the Federal government and by the German states (Länder). In 2017, this funding was EUR 32,245,000 in total.

In addition, the IFW receives project funding from external sources of about 8.5 million Euro. Thereof, about 3.4 million Euro came from German Research Foundation (DFG), 2.4 million Euro from European Union programs, 1.1 million Euro from Federal Government projects, 0.6 million Euro from industry and 1.0 million Euro from other donors including the Free State of Saxony.



Personnel

On 31 December 2017, 479 staff members were employed at the IFW, including 88 doctorate students as well as 16 apprentices in seven different vocational trainings and two business students of a vocational academy. Additionally 53 fellowship holders worked at IFW, among them 20 doctorate students.

Gender equality, as well as work life balance, are defined goals of the IFW Dresden. In 2017, the percentage of women in scientific positions was 22,4% and the percentage of women in scientific leading positions was 19,4%. The IFW is regularly audited for the certificate “audit berufundfamilie” – a strategic management tool for a better compatibility of family and career.

Number of publications and patents

In terms of publications, the qualitative and quantitative level remains high at the IFW. In 2017, IFW scientists have published 444 refereed journal articles, a considerable number of them in high impact journals. Furthermore, IFW members held 169 invited talks at conferences and colloquia.

By 31 December 2017, the IFW holds 117 patents in Germany and 94 international patents.

Research Area 1

Evidence for a magnetic field induced nematic liquid in the spin chain LiCuSbO_4

H.-J. Grafe, S. Nishimoto, M. Iakovleva, E. Vavilova¹, L. Spillecke, A. Alfonsov, M.-I. Sturza, S. Wurmehl, H. Nojiri², H. Rosner³, J. Richter⁴, U. Rößler, S.-L. Drechsler, V. Kataev, B. Büchner

Abstract: We report combined experimental and theoretical evidence of a magnetic field-induced nematic liquid arising above a field of ~ 13 T in the edge-sharing chain cuprate LiCuSbO_4 [1]. Our interpretation is based on the observation of a field induced spin-gap in the measurements of the ^7Li NMR spin relaxation rate T_1^{-1} as well as contrasting field-dependent power-law behavior of T_1^{-1} vs. T , and is further supported by static magnetization and ESR data. An underlying theoretical microscopic approach favoring a nematic scenario is based essentially on the nearest neighbor xyz exchange anisotropy within a model for frustrated spin-1/2 chains and is investigated by the DMRG technique. The employed exchange parameters are justified qualitatively by electronic structure calculations for LiCuSbO_4 .

Low dimensional spin systems

Electronic correlations in solids give rise to novel ground states of matter such as spin liquid states in low dimensional quantum magnets [2,3]. Here, long-range magnetic order is suppressed down to $T = 0$ due to quantum fluctuations [4]. Though individual spins remain non-ordered in the spin liquid, higher rank magnetic multipoles can order under favorable conditions [5]. Such a multipolar order does not break time-reversal symmetry and is often referred to as a “hidden order” since it is difficult to detect it. However, the spin rotational symmetry is broken in this hidden phase which is therefore also called a spin-nematic state, in analogy with the nematic order in liquid crystals, where the translational order is absent but rotational symmetry is broken. The ground state of a Heisenberg spin-1/2 chain with nearest neighbor antiferromagnetic (AFM) interaction J_1 is described by the gapless Tomonaga-Luttinger spin liquid [5]. Including next-nearest neighbor interaction J_2 can cause spin frustration and may yield different phases depending on the frustration ratio $\alpha = |J_2/J_1|$, irrespective of the sign of J_1 [6-8]. Theoretical works [8-11] on such frustrated $J_1(\text{FM})$ - $J_2(\text{AFM})$ chain models have predicted field-induced multipolar states near the saturation field H_{sat} above which all spins are aligned by an external magnetic field H at $T = 0$. These states form a spin liquid of multiple p -bound states of magnons corresponding to nematic, triatic, quartic multipolar phases ($p = 2, 3, 4, \dots$). In contrast, at lower fields H -dependent incommensurate spin density wave phases (SDW_p) can appear in such systems [12]. Recently, the synthesis of LiCuSbO_4 , a novel, strongly frustrated $J_1(\text{FM})$ - $J_2(\text{AFM})$ spin chain compound (Fig. 1) has been reported [13]. It exhibits short-range incommensurate spin correlations below $T \sim 9$ K but does not show long-range magnetic order at $H = 0$ down to $T \sim 0.1$ K. A sizeable exchange anisotropy was estimated, and magnetization approaches saturation near 16 T only [13], making LiCuSbO_4 an ideal candidate to search for field induced SDW_p or multipolar orders.

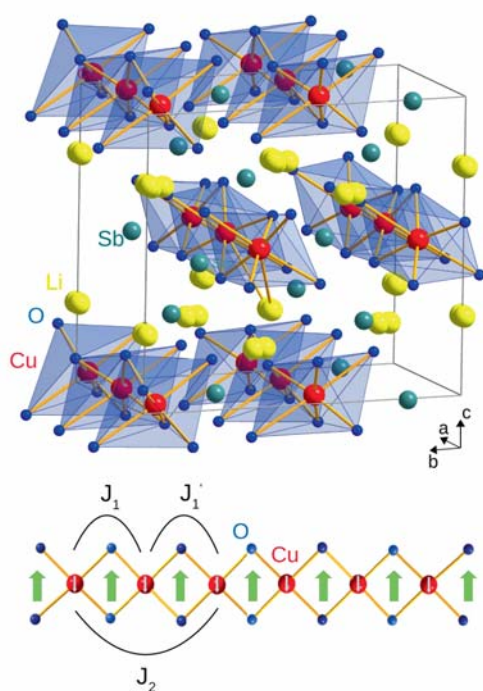


Fig. 1: Crystal structure of LiCuSbO_4 . The lower panel shows a spin chain running along the a direction with the main interactions J_1 , J_1' , and J_2 between the Cu spins (small arrows). The big arrows indicate the DM vector, see text.

Results in LiCuSbO₄ and Discussion

In magnetic materials, the nuclear spin lattice relaxation rate, T_1^{-1} , is caused by the transverse (i.e. \perp to the nuclear spin quantization axis) components of the fluctuating field exerted on the nuclei by the electron spin system. In addition, in certain cases such as the dipolar hyperfine coupling of the ^7Li nucleus to the Cu electronic spins in LiCuSbO₄, also longitudinal fluctuations (i.e. \parallel to the nuclear spin quantization axis) can contribute to T_1^{-1} . This is a fortunate circumstance in LiCuSbO₄ since the parallel fluctuations are those which can evidence nematic spin fluctuations when the transverse fluctuations are gapped.

In weakly coupled AFM Heisenberg chains above the Néel ordering temperature T_N , T_1^{-1} increases with decreasing T and/or increasing magnetic field H and tends to diverge by approaching T_N . This is mainly due to the growth of transverse spin fluctuations whereas parallel spin fluctuations decay smoothly [14,15]. In LiCuSbO₄, however, T_1^{-1} shows a contrasting behavior with respect to temperature and magnetic field (see Fig. 2 b,c,d,e). At relatively small fields (3-12 T) the low-temperature region is determined by a sharp increase of $T_1^{-1}(T)$ (Fig. 2 b,c), pointing to the vicinity of a magnetically ordered state at a lower T . Especially at $H = 9$ T the increase is substantially more pronounced than at lower fields such as for 3 T indicating an increase of the ordering temperature of this magnetic phase. Such a behavior is not expected for an ordinary AFM Néel state where T_N is usually suppressed by an external magnetic field. In fact, the field region around 9 T is also identified by the low-temperature anomaly in the magnetic specific heat [13]. It is conjectured to be a signature of an unusual field-induced SDW_p phase in LiCuSbO₄. Above a critical field $H_{c1} = 13$ T, T_1^{-1} changes from the upturn

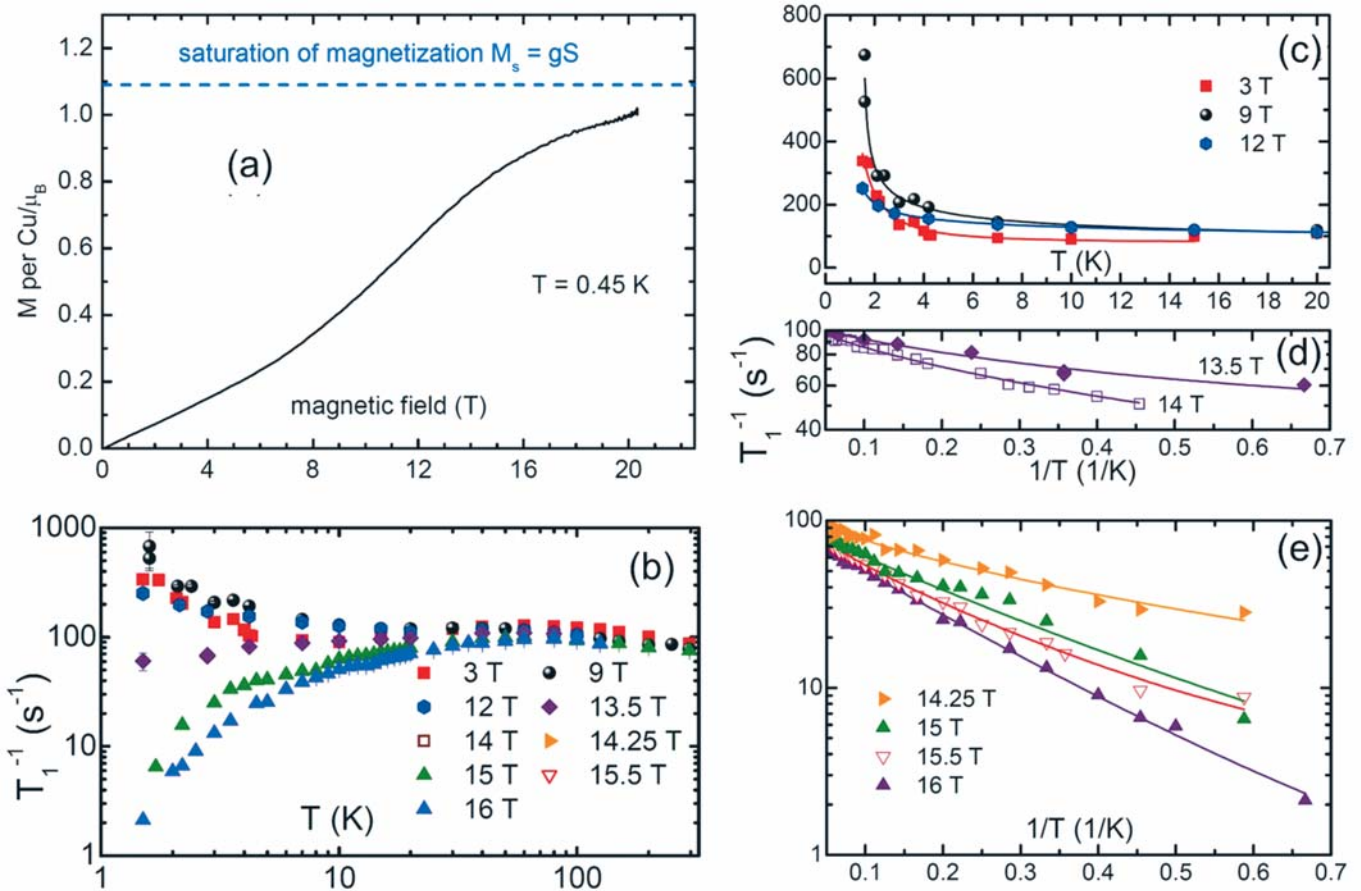


Fig. 2: (a) Field dependence of the magnetization at $T = 0.45$ K. (b) Temperature dependence of the ^7Li nuclear spin lattice relaxation rate at different magnetic fields. (c) The $T_1^{-1}(T)$ dependence at $T < 20$ K for 3 T, 9 T and 12 T. (d,e) T_1^{-1} vs. inverse temperature T_1^{-1} at $T < 20$ K for fields > 13 T. Solid lines in (c–e) are model curves (see text).

behavior to a suppression at low T , suggesting the opening of a gap Δ in the spin excitations. We can extract Δ and a power-law exponent β from a fit of the experimental data to $T_1^{-1}(T) = C_1(H) \exp(-\Delta/T) + C_2(H) (T-T_c)^\beta$, which takes into account theoretical predictions [14,15]. This equation implies the contrasting gapped and critical power-law contributions to T_1^{-1} with $\Delta > 0$ and $\beta < 1$. By crossing $H_{c1} = 13$ T the growth of T_1^{-1} turns into a decay corresponding to the sign change of the exponent β . Concomitantly, the weight C_1 of the gapped term increases on expense of the decreasing weight C_2 of the power-law term. At the same time Δ increases non-linearly, and a finite power law contribution with positive β , in contrast to $\beta < 0$ for $H < H_{c1}$, is required to achieve the best fit of T_1^{-1} . All of these characteristics are consistent with a field induced SDW_p with $p=2$ around an intermediate field of ~ 9 T, and a spin-nematic state above H_{c1} . In the gapped regime the longitudinal correlations are decaying with lowering T which corresponds to the sign change of the power-law exponent β [14,15]. The gapped excitation spectrum is a distinct feature of the spin-nematic state of the weakly coupled 1D-chains with only a weak soft mode in the longitudinal channel [12]. Furthermore, with the help of ESR measurements and theoretical considerations, by the field dependence of the gap, and by the fact that the magnetization does not saturate above 13 T (Fig. 2a), we could exclude that the gap in T_1^{-1} arises from full polarization of the spins or from staggered antisymmetric Dzyaloshinskii-Moriya interactions. Instead, the gap is indeed a signature of a spin-nematic state, where the transverse spin fluctuations are expected to be gapped, and the longitudinal correlations follow the power law $\sim T^\beta$.

Beyond the experimental work, we have performed extensive theoretical calculations. Relativistic density functional (DFT and DFT+U) electronic structure calculations have been performed with the aim to understand (i) the amount of interchain couplings and (ii) the magnitude of the intra-chain couplings. With respect to (i) we have analyzed the dispersion of bands and found pronounced 1D van Hove singularities near the Fermi level. Thus, we have confirmed the nearly 1D behavior of LiCuSbO₄. Regarding (ii), we arrive at a sizable splitting of the two NN exchange integrals: $J_1 = -160$ K and $J_1' = -90$ K (Fig. 1), whereas $J_2 \approx 37.6$ K, only. Thus, we are left with a dominant FM total NN coupling and an unrenormalized mean frustration parameter $\alpha = J_2 / [(J_1 + J_1')/2] \approx 0.3$, close to the quantum critical $\alpha = 0.25$.

Density matrix renormalization group calculations (DMRG) were done to analyse a novel anisotropy mechanism based on the low-symmetric NN exchange anisotropy, which in addition to the J_1 - J_2 frustration, stabilizes a nematic phase in a moderate high-field region. In addition, a weak homogeneous and staggered NN DM coupling was found not to destroy the nematicity. We introduced a 1D frustrated Heisenberg model with a xyz exchange anisotropy and a magnetic field H along the z axis, and calculated the magnetization curve using DMRG. By fitting the experimental curve in Fig. 2a, we have found a possible parameter set of the J_x , J_y , and J_z couplings, and a nematic state is established by the xyz exchange anisotropy in the calculations. To check this possibility, we have calculated the nematic correlation function as an indicator of magnon pairing. Our single chain Hamiltonian with the involved specific exchange anisotropy describes a 1D system with a distinctive nematically ordered ground state at $T = 0$ and at high enough magnetic fields in contrast with simple AFM Heisenberg chains. With increasing finite T this distinct order is more and more suppressed. The field range with the enhanced nematic correlations agrees well with that region where the spin gap has been experimentally observed, namely, in between $H = 13$ – 16 T. A similar nematicity scenario has been proposed in our recent work devoted to linarite [16], but there yet not fully confirmed experimentally. Furthermore, we have also studied the effect of additional uniform or staggered DM couplings allowed by the crystallographic symmetry as mentioned above. As a result we found that the nematic state is hardly affected by a weak DM coupling. The effect of a staggered DM interaction is even weaker than that of a uniform one.

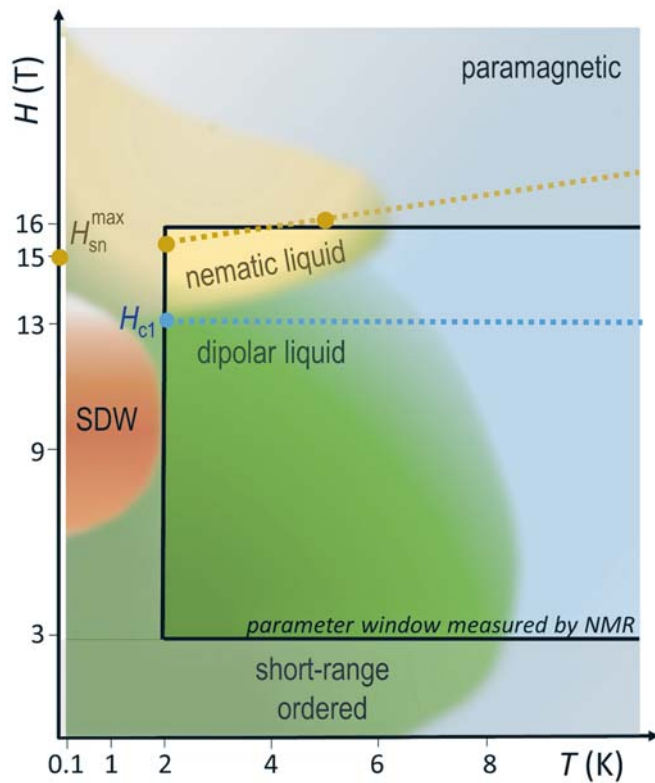


Fig. 3: Schematic phase diagram of LiCuSbO₄, in part reproduced from Dutton et al. [13]. The red area presents an anomalous field induced SDW_p phase, whereas the yellow area depicts a stability region of the nematic state. The region measured by NMR is marked by the black rectangle. The blue dashed line denotes the critical field H_{c1} . The brown closed circles labelled H_{sn}^{max} connected with the dashed line depict the field of the maximum of the spin-nematic correlation function as found in the DMRG analysis.

Conclusion

We have identified experimentally and theoretically a field induced SDW₂ phase, which is followed by a spin-nematic state above a critical field H_{c1} . These phases and the parameter window measured by NMR are visualized in the schematic phase diagram of LiCuSbO₄ in Fig. 3. Certainly, there must be also a second “upper” critical field H_{c2} framing the stability region of the strong nematic state in LiCuSbO₄. This calls for further experimental studies of LiCuSbO₄ at higher fields and also at lower temperatures.

- [1] H.-J. Grafe, et al. Scientific Reports 7, 6720 (2017)
- [2] E. Fradkin, et al. Annu. Rev. Condens. Matter Phys. 1, 153 (2010).
- [3] S. Sachdev, et al. Nature Physics 4, 173 (2008).
- [4] L. Balents, et al. Nature 464, 199 (2010).
- [5] K. Penc, et al. Springer Series in Solid-State Sciences 164, 331 (2011).
- [6] C. K. Majumdar, et al. I. J. Math. Phys. 10, 1388 (1969).
- [7] F. Haldane, et al. Phys. Rev. B 25, 4925(R) (1982).
- [8] A. Chubukov, Phys. Rev. B 44, 4693 (1991).
- [9] L. Kecke, et al. Phys. Rev. B 76, 060407 (2007).
- [10] R. Kuzian, et al. Phys. Rev. B 75, 024401 (2007).
- [11] T. Vekua, et al. Phys. Rev. B 76, 174420 (2007).
- [12] O. Starykh, et al. Phys. Rev. B 89, 104407 (2014).
- [13] S. Dutton, et al. Phys. Rev. Lett. 108, 187206 (2012).
- [14] M. Sato, et al. Phys. Rev. B. 79, 060406(R) (2009).
- [15] M. Sato, et al. Phys. Rev. B. 83, 064405 (2011).
- [16] B. Willenberg, et al. Phys. Rev. Lett. 116, 047202 (2016).

Funding: Deutsche Forschungsgemeinschaft, grants SFB 1143, KA 1694/8-1, GR 3330/4-1, Emmy Noether Programme projects WU595/3-1, and WU595/3-2, project RFBR 14-02-01194. ICC-IMR.

Cooperation: ¹Zavoisky Physical-Technical Institute of the Russian Academy of Sciences, 420029, Kazan, Russia; ²Institute of Materials Research, Tohoku University, 980-8577, Sendai, Japan; ³Max-Planck-Institute for Chemical Physics of Solids, Dresden, Germany; ⁴Universität Magdeburg, Institut für Theoretische Physik, Magdeburg, Germany

Correlation induced electron-hole asymmetry in quasi-2D iridates

E. M. Pärshcke, K. Wohlfeld¹, K. Foyevtsova², J. van den Brink

Abstract: The iridate Sr_2IrO_4 closely resembles the cuprate La_2CuO_4 from a magnetic and crystallographic point of view. When doped with charge carriers, the insulating, antiferromagnetic cuprate La_2CuO_4 becomes a superconductor with a relatively high transition temperature. This raises the question how far Sr_2IrO_4 is away from superconductivity upon doping. The first step towards understanding this issue is provided by a study of the motion of a *single* charge carrier that is introduced to the compound.

Our theoretical study shows that an electron added to Sr_2IrO_4 forms a spin- polaron, similar to the cuprates. But the situation of a removed electron - an added hole - is far more intricate. In this case complex many-body configurations of singlet and triplet character form. This effect is due to the presence of strong spin-orbit coupling in iridium ions in combination with electronic correlation effects. As a consequence the calculated photoemission spectrum of Sr_2IrO_4 (left panel) is very different from its inverse photoemission spectrum (right panel). We conclude that, unlike in the case of the cuprates, the electronic structure of electron and hole doped iridates are fundamentally different.

Motivated by similarities between Sr_2IrO_4 and La_2CuO_4 , we ask the question whether the quasi-2D iridates can also become superconducting upon charge doping. On the experimental side, very recently signatures of Fermi arcs and the pseudogap physics were found in the electron- and hole-doped iridates [4, 3] on top of the *d*-wave gap in the electron-doped iridate. On the theoretical side, one needs to study a doped multiorbital two-dimensional Hubbard model supplemented by the non-negligible spin-orbit coupling, which is a very difficult task. Fortunately, there exists one nontrivial limit of the two-dimensional doped Hubbard-like problems, whose solution can be obtained in a relatively exact manner. It is the so-called single-hole problem which relates to the motion of a single charge (hole or doublon) added to the AF and insulating ground state of the undoped two-dimensional Hubbard-like model [5]. In the case of the cuprates, this problem has been intensively studied both on the theoretical as well as the experimental side and its solution (the formation of the spin polaron, i.e. strong coupling of the propagating hole to the magnons) is considered a first step in understanding the motion of doped charge [5]. Here we calculate the spectral function of the correlated strong coupling model describing the motion of a single charge doped into the AF and insulating ground state of the quasi-2D iridate. The main result is that we find a fundamental difference between the motion of a single electron or hole added to the undoped iridate.

In particular, introducing a single electron into the quasi-2D iridates, as experimentally realised in an inverse photoemission (IPES) experiment, leads to the creation of a single $5d^6$ doublon in the bulk, leaving the nominal $5d^5$ configuration on all other iridium sites. Since the t_{2g} shell is for the $5d^6$ configuration completely filled, the only eigenstate of the appropriate ionic Hamiltonian is the one carrying $J = 0$ total angular momentum. Therefore, just as in the cuprates, the $5d^6$ doublon formed in IPES has no internal degrees of freedom, i.e. $|d\rangle \equiv |J = 0\rangle$, see Fig. 1.

On the contrary, the hopping of a hole to the nearest neighbor site does not necessarily lead to the coupling to the magnetic excitations from $j = 1/2$ AF. In [12] we derive the microscopic model for a single hole introduced into the iridate forming $5d^4$ configuration, which resembles the case encountered in the photoemission (PES) experiment. Ommiting the details, we point out that due to the strong Hund's coupling the lowest eigenstate of the appropriate ionic Hamiltonian for four t_{2g} electrons has the

a) $d^4 \longleftrightarrow d^5 \longleftrightarrow d^6$

$$\begin{array}{ccc}
 S=1 \left. \begin{array}{l} L=1 \end{array} \right\} J=\overset{\textcircled{0}}{\frac{1}{2}} & s=\frac{1}{2} \left. \begin{array}{l} l=1 \end{array} \right\} j=\overset{\textcircled{\frac{1}{2}}}{\frac{3}{2}} & S=0 \left. \begin{array}{l} L=0 \end{array} \right\} J=\overset{\textcircled{0}}{0}
 \end{array}$$

b) $d^4: S = \frac{1}{\sqrt{3}} (\uparrow \times \uparrow + \downarrow \times \downarrow) - \frac{1}{\sqrt{6}} (\uparrow \times \downarrow + \downarrow \times \uparrow)$

$$T_1 = \frac{1}{\sqrt{2}} (\uparrow \times \uparrow - \downarrow \times \downarrow) + \frac{1}{2} (\downarrow \times \uparrow - \uparrow \times \downarrow)$$

$$T_0 = \frac{1}{\sqrt{2}} (\uparrow \times \downarrow - \downarrow \times \uparrow)$$

$$T_{-1} = -\frac{1}{\sqrt{2}} (\downarrow \times \downarrow) + \frac{1}{2} (\uparrow \times \downarrow - \downarrow \times \uparrow)$$

c) $d^5: j_{\frac{1}{2}} = -\frac{1}{\sqrt{3}} \uparrow + \frac{\sqrt{2}}{\sqrt{3}} \downarrow; \quad j_{-\frac{1}{2}} = \frac{1}{\sqrt{3}} \downarrow - \frac{\sqrt{2}}{\sqrt{3}} \uparrow$

d) $d^6: J=0 = \text{beige sphere}$

Fig. 1: Low energy eigenstates of iridium ions (a) Quantum numbers characterising certain electronic configuration, where j , l , and s (J , L , and S) stands for single-particle (multi-particle) total, orbital, and spin angular momentum. The red circles indicate the states that are explicitly taken into account in our effective low-energy theory. (b) Eigenstates for the $5d^4$ configuration (relevant for the $5d^4$ hole case) of the appropriate ionic Hamiltonian of iridium ion. (c) Same as (b) but for the $5d^5$ configuration (as relevant for the quasi-2D iridate ground state). (d) Same as (b) but for the $5d^6$ configuration (relevant for $5d^6$ doublon case). Blue, red and beige cartoon orbitals indicate the one-particle states with the effective angular momentum $l = 1$ and $l^z = 1$, $l^z = -1$ and $l^z = 0$ respectively. Round beige cartoon orbital indicates full shell with $L = 0$. Up (down) black arrows indicate $s^z = 1/2$ ($s^z = -1/2$) of spin $s = 1/2$ states. No arrow on an orbital indicates $S = 0$ state.

total (effective) orbital momentum $L = 1$ and the total spin momentum $S = 1$. Moreover, in the strong spin-orbit coupled regime the eigenstates of such an ionic Hamiltonian are the lowest lying $J = 0$ singlet S , and the higher lying $J = 1$ triplets $T\sigma$ ($\sigma = -1, 0, 1$, split by energy λ from the singlet state) and $J = 2$ quintets. Thus, one obtains that, unlike e.g. in the cuprates, the $5d^4$ hole formed in PES is effectively left with four internal degrees of freedom, i.e. $|\mathbf{h}\rangle \equiv \{|S\rangle, |T_1\rangle, |T_0\rangle, |T_{-1}\rangle\}$, see Fig. 1.

Once the hybridization between the iridium ions is turned on, the hopping of the $5d^4$ hole between iridium sites i and j is possible, which, similarly to the IPES case, may or may not couple to magnons. However, there is one crucial difference w.r.t. IPES: the $5d^4$ hole can carry finite angular momentum and thus the $5d^4$ doublon may move between the nearest neighbor sites without coupling to magnons.

Using SCBA [5] we calculate the relevant Green functions for the single electron ($5d^6$ doublon) and the single hole ($5d^4$ hole) doped into the AF ground state of the quasi-2D iridate.

We first discuss the calculated angle-resolved IPES spectral function shown in Fig. 2(b). One can see that the first addition state has a quasiparticle character, though its dispersion is relatively small: there is a rather shallow minimum at $(\pi/2, \pi/2)$ and a maximum at the Γ point. Moreover, a large part of the spectral weight is transferred from the quasiparticle to the higher lying ladder spectrum, due to the rather small ratio of the spin exchange constants and the electronic hopping [5]. Altogether, these are all well-known signatures of the spin-polaron physics: the mobile defect in an AF is

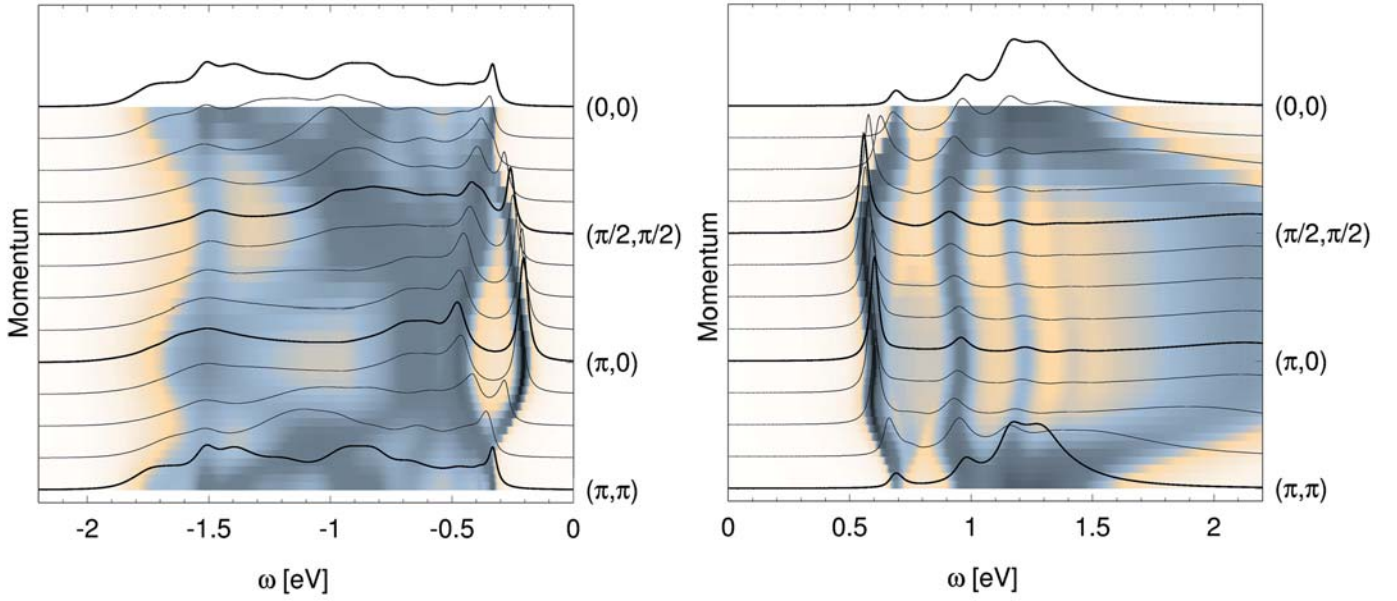


Fig. 2: Theoretical spectral functions of iridates (a) Photoemission (PES) and **(b)** inverse photoemission (IPES) spectral function of the low-energy (polaronic) models developed for the quasi-2D iridates and solved using the self-consistent Born approximation

strongly coupled to magnons (leading to the ladder spectrum) and can move coherently as a quasiparticle only on the scale of the spin exchange J_1 [5]. Thus, it is not striking that the calculated IPES spectrum of the iridates is similar to the PES spectrum of the $t-J$ model with a negative next nearest neighbor hopping – the model case of the hole-doped cuprates. This agrees with a more general conjecture, previously reported in the literature: the correspondence between the physics of the hole-doped cuprates and the electron-doped iridates [14].

Due to the internal spin and orbital angular momentum degrees of freedom of the $5d^4$ states, the angle-resolved PES spectrum of the iridates (Fig. 2a) is very different. In good agreement with experiment [1, 9, 7], the first removal state shows a quasiparticle character with a relatively small dispersion and a minimum is at the $(\pi, 0)$ point (so that we obtain an indirect gap for the quasi-2D iridates). Also the plateau around $(\pi/2, \pi/2)$ and the shallow minimum of the dispersion at the Γ point are reproduced, where the latter is related to a strong back-bending of higher energy $J = 1$ triplets [12]. On a qualitative level this quasiparticle dispersion resembles the situation found in the PES spectrum of the $t-J$ model with a positive next nearest neighbor hopping, which should model the electron-doped cuprates (or IPES on the undoped). However, the higher energy part of the PES spectrum of the iridates is quite distinct not only w.r.t. the IPES but also the PES spectrum of the $t-J$ model with the positive next nearest neighbor hopping. Thus, the spin-polaron physics, as we know it from the cuprate studies [5], is modified in this case and we find only very partial agreement with the paradigm stating that the electron-doped cuprates and the hole-doped iridates show similar physics [14].

This difference follows from the interplay between the free and polaronic hoppings of the introduced hole which is typically highly nontrivial. The free hopping of the $5d^4$ hole is possible here for both the $J = 0$ singlet and $J = 1$ triplets which leads to the onset of several bands. Moreover, the $J = 1$ triplets can freely hop not only to the next nearest neighbors but also to the nearest neighbors. For the polaronic hopping, the appearance of several polaronic channels, originating in the free J -bands being dressed by the $j=1/2$ magnons, contributes to the strong quantitative differences w.r.t. the $5d^6$ doublon case or the cuprates.

- [1] B. J. Kim et al., *Phys. Rev. Lett.* 101, 076402 (2008).
- [2] J. Kim et al., *Phys. Rev. Lett.* 108, 177003 (2012).
- [3] Y. Cao et al., *Nature Communications* 7, 11367 (2016).
- [4] Y. K. Kim et al., *Science* 345, 187 (2014).
- [5] G. Martinez and P. Horsch, *Phys. Rev. B* 44, 317 (1991).
- [6] Q. Wang et al., *Phys. Rev. B* 87, 245109 (2013).
- [7] A. de la Torre et al., *Phys. Rev. Lett.* 115, 176402 (2015).
- [8] Y. Liu et al., *Scientific Reports* 5, 13036 (2015).
- [9] Y. Nie et al., *Phys. Rev. Lett.* 114, 016401 (2015).
- [10] V. Brouet et al., *Phys. Rev. B* 92, 081117 (2015).
- [11] A. Yamasaki et al., *Phys. Rev. B* 94, 115103 (2016).
- [12] E. P. ¨arschke et al., *Nat. Commun.* 8, (2017).
- [13] J. Kim et al., *Nat. Commun.* 5, 4453 (2014).
- [14] F. Wanq and T. Senthil, *Phys. Rev. Lett.* 106, 136402 (2011).

Funding: Narodowe Centrum Nauki (NCN, National Science Center) under Project No. 2012/04/A/ST3/00331 and Project No. 2016/22/E/ST3/00560; Deutsche Forschungsgemeinschaft via SFB 1143

Cooperation: ¹Institute of Theoretical Physics, University of Warsaw;

²University of British Columbia, Vancouver

Large, three-dimensional and faceted LaFeAsO crystals

R. Kappenberger, S. Aswartham, F. Scaravaggi, C. G. F. Blum, M. I. Sturza, P. Lepucki, F. Caglieris, X. Hong, C. Hess, H.-J. Grafe, A. U. B. Wolter, S. Wurmehl, B. Büchner

Abstract: Even after nine years of intense research on iron-based superconductors, large and well faceted single crystals with considerable *c* axis growth of the 1111 family are still a challenge to be grown. The lack of crystals is hindering their investigation as posing limits to methods yielding results in *k*-space (e.g., ARPES, STM, ...) and any *c*-axis dependent measurements.

In 2017, we were able to apply a sophisticated route based on the not-so-well-known method of solid state single crystal growth (SSCG) to yield large LaFeAsO single crystals with a considerable crystal growth along the *c*-axis [1].

State-of-the-art

Soon after the discovery of iron-based superconductors single crystals were successfully grown in the 11, 122 and 111 families [2-4], the method of choice being self-flux growth. In the 1111 family, single crystals are hard to be obtained via flux growth [5,6], although crystals could be successfully synthesized using high pressure high temperature synthesis [7]. However, this method yields rather small crystals and also does not lead to a reasonable growth along the *c* direction either. This hurdle has, so far, limited the detailed investigation of the 1111 family of pnictide superconductors rendering them the least studied family among all iron-based superconductors. In this work, we have the SSCG growth method to yield large LaFeAsO single crystals with a considerable crystal growth along the *c* axis.

Solid state single crystal growth (SSCG)

Solid state single crystal growth (SSCG) is a rather uncommon crystal growth technique. SSCG has been used to synthesize ceramic materials such as BaTiO₃ [8] as well as metallic materials [9]. This method utilizes the phenomenon of abnormal grain growth (AGG) to grow single crystals from a polycrystalline matrix. While many systems exhibit AGG, its origin and mechanism is not fully explained so far [10]. Facetted growth and the presence of a secondary phase have been empirically reported to aid SSCG as well as deliberately chosen additives [11]. Several mechanisms have been discussed, for example grain boundary roughening [12] or the aid of a liquid phase [13].

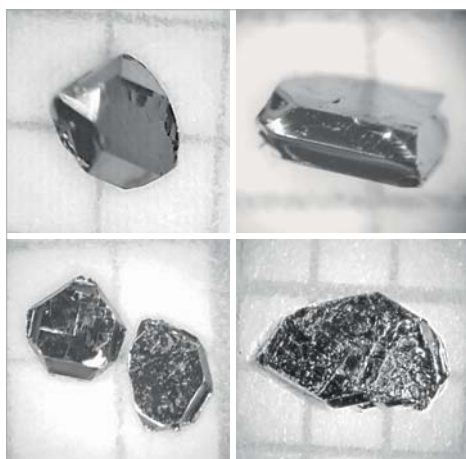


Fig. 1: As-grown LaFeAsO single crystals with pronounced facets and a thickness of up to 0.4 mm. One square on the paper is 1 mm x 1 mm [1].

In our solid state crystal growth experiments, we used polycrystalline pellets and Na-As powder. Both materials were eventually prepared before the growth and layered into an alumina crucible. The molar ratio of LaFeAsO to Na-As used was 1:4, which corresponds to a ratio in volume of about 1:1. The alumina crucible was welded into an Nb crucible using approximately 1 bar of argon pressure. For protection from air, the Nb crucible was enclosed in quartz glass. Subsequently, the material was heated to 1080 °C and annealed for 200 h. After the reaction, the pellets were removed from the crucible and placed into a 1:1 mixture of ethanol and distilled water to remove the water-soluble Na-As. For removing remaining flux on the crystal surface, the crystals were placed in an ultrasonic bath using acetone as a solvent. Single crystals sized up to 2 x 3 x 0.4 mm³ were obtained. Representative crystals with pronounced facets are shown in Fig. 1. Crystal growth occurred mainly on the outer surface of the pellets, whereas the crystal size is considerably smaller in the inside of the pellets.

Solid state single crystal growth occurs when the growth of grains with a specific orientation is preferred, therefore producing abnormally fast growing grains which consume the neighbouring grains, leading to a bimodal size distribution [12]. A scheme of the

process is shown in Fig. 2. In the present case, a liquid phase is introduced to facilitate SSCG in the form of Na-As. Na-As is actually a phase mix consisting of several phases. The mixture is melting at 550°C as seen in our DTA measurement (not shown) and starts penetrating the pores of the polycrystalline LaFeAsO matrix. At the maximum synthesis temperature of 1080°C the mobility of the atoms in the polycrystal is high enough to start the SSCG process. The fact that Na-As diffuses into the pores of the polycrystals is evident by looking at the LaFeAsO pellets after the crystal growth - the pellets retain their shape, but on contact with water Na-As starts dissolving, thereby releasing the insoluble grown crystals from the pellet.

We explored several parameters to verify the SSCG scenario and to optimize growth conditions:

- Time:** The time spent at the maximum temperature is directly correlated to the sample size and the growth along c -axis. A first experiment where the sample was held at 1080°C for only 48 h yielded crystals with a thickness of only about $50\text{ }\mu\text{m}$ without well-formed facets. This observation demonstrates that the growth is not a growth from a solution, where the crystals grow upon cooling and, hence, upon exceeding the solubility product, but in solid matter, where the diffusion process scales with time.
- Liquid phase:** FeAs and LaAs were also tested as liquid phases to avoid incorporation of foreign atoms, but FeAs did not diffuse into the polycrystalline matrix and the melting point of LaAs is considerably higher than 1080°C .
- Temperature:** Unfortunately, high synthesis temperatures where LaAs could be used as the liquid phase are limited by another effect - high temperatures lead to interface roughening, thereby preventing the formation of faceted grains which are known to be crucial for abnormal grain growth [14]. An experiment with Na-As as a liquid phase with 1110°C as the maximum temperature yielded considerably smaller crystals.
- Mixing:** Ground polycrystalline LaFeAsO powder which is thoroughly mixed with Na-As leads to strongly decreased crystal size, as expected if growth is via SSCG method.

Powder and single crystal X-ray diffraction were performed on the crystals to confirm the tetragonal crystal structure $P4/nmm$ (No. 129) of LaFeAsO at room temperature. Laue diffraction was performed to check for single crystallinity (to exclude twinning and intergrowth of crystals) and to identify the facets. Fig. 3 shows a schematic drawing of the crystal morphology and measured Laue diffraction patterns for the $\{001\}$ and $\{101\}$ facets.

Properties of LaOFeAs crystals

The magnetic susceptibility data of LaFeAsO obtained at an external fields of $\mu_0 H = 1\text{ T}$ is shown in Fig. 4. Both the magnetic and the structural transition can be assigned to anomalies shown in Fig. 4. The left inset shows the derivative of the curve, highlighting the two transitions which can be determined to be at $T_N = 127\text{ K}$ (emergence of the spin-density wave) and $T_S = 145\text{ K}$ (structural transition from $P4/nmm$ to $Cmmm$). The clearly visible splitting of the two transitions in the susceptibility measurements has not been clearly observed before in polycrystalline samples. Above the phase transitions the susceptibility increases linearly, a behavior which has often been observed in the ironpnictides [14] and which so far is unexplained as it cannot be described with models referring to purely localised or purely itinerant charge carriers.

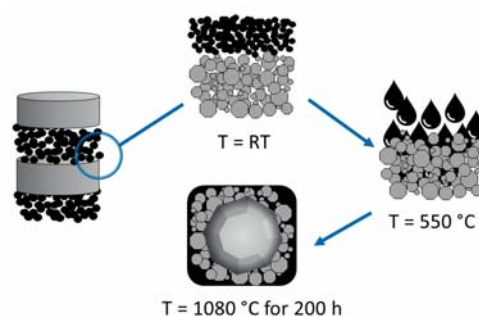


Fig. 2: Schematic drawing of the SSCG process. A liquid phase is added to a polycrystalline matrix with a unimodal size distribution. After annealing, a bimodal size distribution has developed, including large faceted crystals [1].

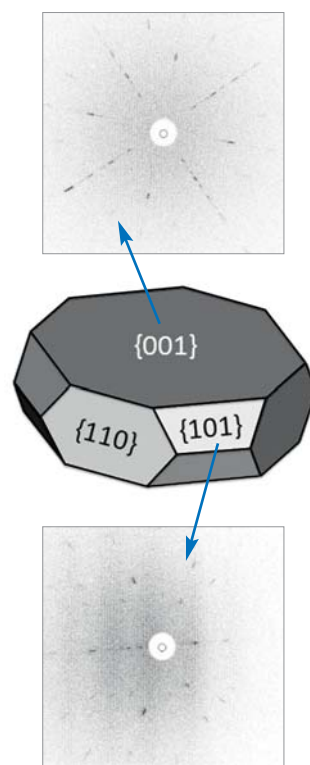


Fig. 3: Schematic drawing of a crystal indicating the facets featuring corresponding Laue patterns which were used to identify the facets [1].

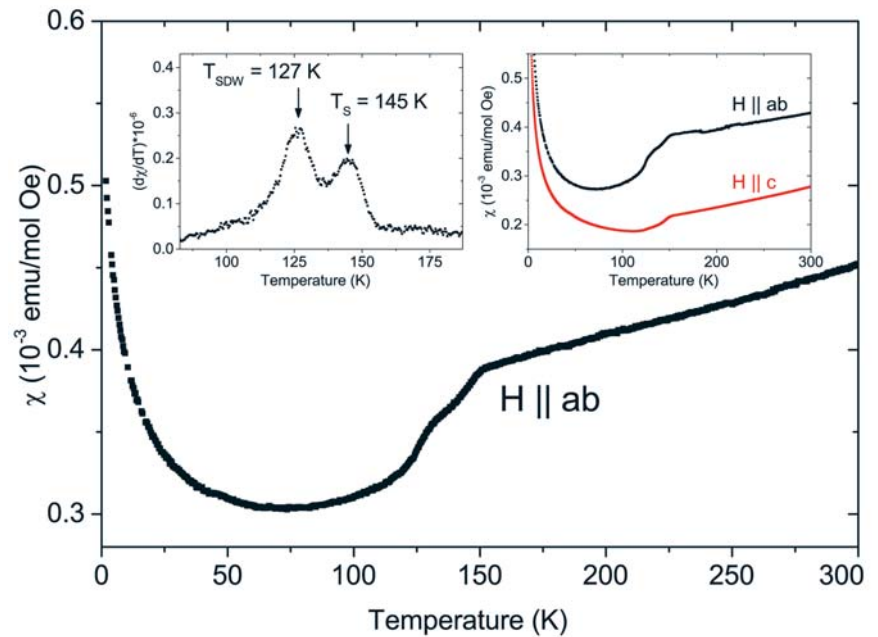


Fig. 4: Magnetic susceptibility measurement on a LaFeAsO single crystal parallel to *ab* with $\mu_0 H = 1$ T. The left inset shows the first derivative of the measurement, highlighting the structural and magnetic transitions. The inset on the right shows the susceptibility with the field aligned parallel to the *ab* plane and parallel to the *c* axis.

Outlook

We will continue to extend the materials basis in the 1111 family to other members. Our large, three-dimensional and faceted crystals set the stage for investigations that were until now limited due to the lack of suitable crystals. We will use the crystals to further explore nematic fluctuations and polarons aiming towards a deeper understanding of the physics of Fe-based superconductors.

- [1] R. Kappenberger et al., J. Cryst. Growth, 483, 9 (2018).
- [2] I. Morozov, et al., Crystal Growth & Design 10, 4428 (2010).
- [3] N. Ni, et al., Phys. Rev. B 78, 014507 (2008).
- [4] A. S. Sefat, et al., Phys. Rev. Lett. 101, 117004 (2008).
- [5] J.-Q. Yan, et al., Appl. Phys. Lett. 95, 222504 (2009).
- [6] A. Jesche et al., Phys. Rev. B 86, 134511 (2012).
- [7] N. D. Zhigadlo, et al., Phys. Rev. B 86, 214509 (2012).
- [8] B.-K. Lee, et al., Acta Materialia 48, 1575 (2000).
- [9] S.-M. Na and A. Flatau, AIP Advances 7, 056406 (2017).
- [10] S.-J. L. Kang, et al., J. Amer. Ceram. Soc. 98, 347 (2015).
- [11] S.-J. L. Kang, Butterworth-Heinemann, (2005).
- [12] E. A. Holm and S. M. Foiles, Science 328, 1138 (2010).
- [13] D. F. K. Hennings, et al., J. Amer. Ceram. Soc. 70, 23 (1987).
- [14] R. Klingeler et al., Phys. Rev. B 81, 024506 (2010).

Funding: DFG Priority Programme SPP1458: BU887/15-1, STU 695/1-1;
DFG Research Training Group 1621; DFG Emmy Noether Programme WU595/3-3

Nanotubular spin-waves conduits

J. A. Otálora, A. Kákay, ¹J. Lindner, ¹H. Schultheiss, ¹K. Geishendorf, A. Thomas, K. Nielsch

Abstract: Substantial efforts for understanding and controlling mechanisms governing the spin-wave's (SW) behavior in a wide variety of ferromagnetic architectures are taking place. This is because of its potential for boosting spintronics devices towards applications with unprecedented technological advantages. In this context, a novel layout is proposed and it would significantly foster the endeavor: magnetic nanotubes. Its outstanding non-reciprocal SWs properties might be the key for their success. These features are maximum at the ground state and are present not only in the SWs dispersion, but also manifest via non-reciprocal SWs absorption. This leads to a difference in the decay length of counter-propagating magnons along the tube length and the azimuthal direction [1,2]. Its magnons are plane-waves and its non-reciprocities can be controlled with an application of weak DC magnetic fields around the tube's large axis. Our findings suggest the magnetic nanotubes as a novel layout for efficient, flexible and reconfigurable magnonic applications.

Curvature-induced non-reciprocal effects

New routes to modify the characteristics of materials with ferromagnetic order are to bend thin film membranes. Bending the membrane can lead to internal strains and to a break of local inversion symmetry [3], resulting, for example, in an unambiguous distinction between the outer and inner surfaces in case of curved geometries such as nanotubes. The internal energies are also affected, especially when the curvature radius reaches intrinsic length scales. In strongly curved systems [4], off-diagonal elements of the exchange interaction are not negligible, leading to chiral ordering. Moreover, the fields are also influenced by the break of the inversion symmetry. Due to the modified energies, the magnetic ordering and the magnetization dynamics differ from those known for thin-films [5-7]. Therefore the curvature can be seen as an extra degree of freedom for controlling the characteristics of ferromagnetic materials.

In Magnonics, spin waves (SWs) or magnons are proposed to transport and process information analog to, for instance, the charge currents in electronics. Engineering magnon properties to control the SW excitation and propagation is therefore a crucial task and, under this goal, the membrane curvature can be used to extend the toolbox of operations for controlling SWs, which is required in applications such as communication and logic devices [1,2,8]. Geometries like Möbius rings, helices, grooves stripes, and nanotubes can be accounted as few sets of layouts wherein the system curvature has an impact on the SW dynamics. Such topologies are being investigated in our group, with magnetic nanotubes as our main focus.

Our theoretical predictions suggest magnetic nanotubes as layouts with outstanding SWs properties, which might boost spintronics devices towards applications with unprecedented lower power consumption, reconfigurable functionality, faster operative rates and further miniaturization. The tunable non-reciprocal SW features induced by the nanotubular curvature [1,2,8] is the key. The SWs dispersion relation and absorption is asymmetric regarding the sign of the propagation vector. This means that counter-propagating magnons have different wave vectors and different extinction lengths for a given frequency. This can be exploited, for instance, to avoid the formation of standing spin wave resonances. Therefore, it provides conditions for uni-directional propagation of SWs packages that is fundamental to enhance the efficiency of SWs-based logic devices [9]. Figure 1(a) sketches a Permalloy (Ni-Fe) nanotube in a circular magnetic state wherein the SWs are excited by an rf-field applied at the center of the tube.

Fig. 1: (a) Circular magnetic configuration is excited with a monochromatic RF field in order to create spin waves traveling in opposite directions. The wave vectors of the left and right propagating SWs differ, although they have the same frequency. (b) Distribution of counter-propagating radial magnon-mode amplitude excited at 4.7 GHz and their (c) orientation of magnon vector field along the nanotube perimeter for modes $n = 0, \pm 1, \pm 2$. λ_L and λ_R denotes the wavelength of magnons propagating to the left (L) and right (R), respectively. The Permalloy nanotube radius is 80 nm with a thickness of 10 nm.

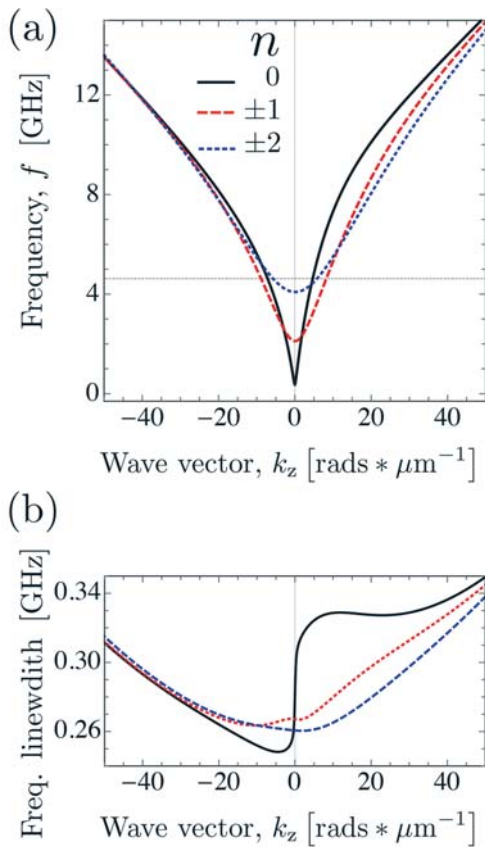
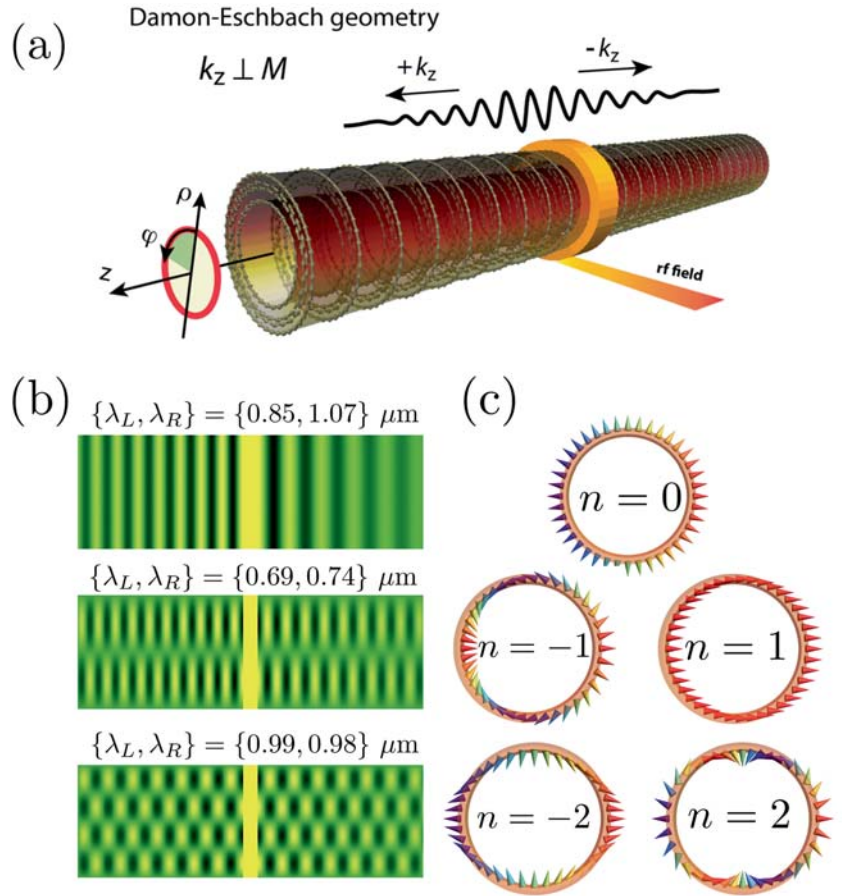


Fig. 2: (a) Dispersion relation of magnons traveling along the large nanotube axis with wave-vector k_z . Modes of different order are labeled with $n = 0, \pm 1, \pm 2$. (b) Frequency linewidth of the first three-magnon modes. The Permalloy nanotube radius is 80 nm with a thickness of 10 nm.



Quasi-monochromatic magnons of different orders ($n = 0, \pm 1, \pm 2$) excited at 4.7 GHz are shown in Fig. 1(b, c). The radial component of the excited magnon modes is represented by the color code in Fig. 1(b). Note that the wavelength and transport length of counter-propagating magnons differ. Figure 1(c) shows the magnon field distribution along the nanotube perimeter. The case of non-reciprocal SW dispersion and intrinsic linewidth are presented in Fig. 2(a) and (b), respectively. Aspects like the optimization of the curvature-induced non-reciprocity as a function of the system size and magnetic ground state are currently under research in our group. It means to control the magnons mode profile and the tuning of non-reciprocity via weak DC external magnetic fields.

We believe that three dimensional curvilinear magnetic membranes, in particular nanotubes, can be exploited as a novel layouts for non-reciprocal conduits, for magnons transport along curved paths, and as one-dimensional magnonic crystals.

Synthesis and characterization of nanotubular magnonic devices

Based on the experimental techniques available in our facilities and in our partner's laboratories for synthesis and magnetic characterization, our research is focused to one type of curved multilayered nanoconduits: core-shell magnetic nanotubes (CSMNs), which consist in elongated cylindrically-shaped shells disposed in a concentric configuration [11], as illustrated in Fig. 3.

Processes for synthesis are performed by the combination of atomic layer deposition (ALD) and electrodeposition techniques, leading to the availability of CSMNs with inner metal wire (Pd, Cu, Au) and outer Insulator Magnetic shell ($\gamma\text{-Fe}_2\text{O}_4$), with diameters ranging between 100 nm and 1 micron diameter, 1 micron and 20 microns length and 1 nm and 50 nm shell thickness.

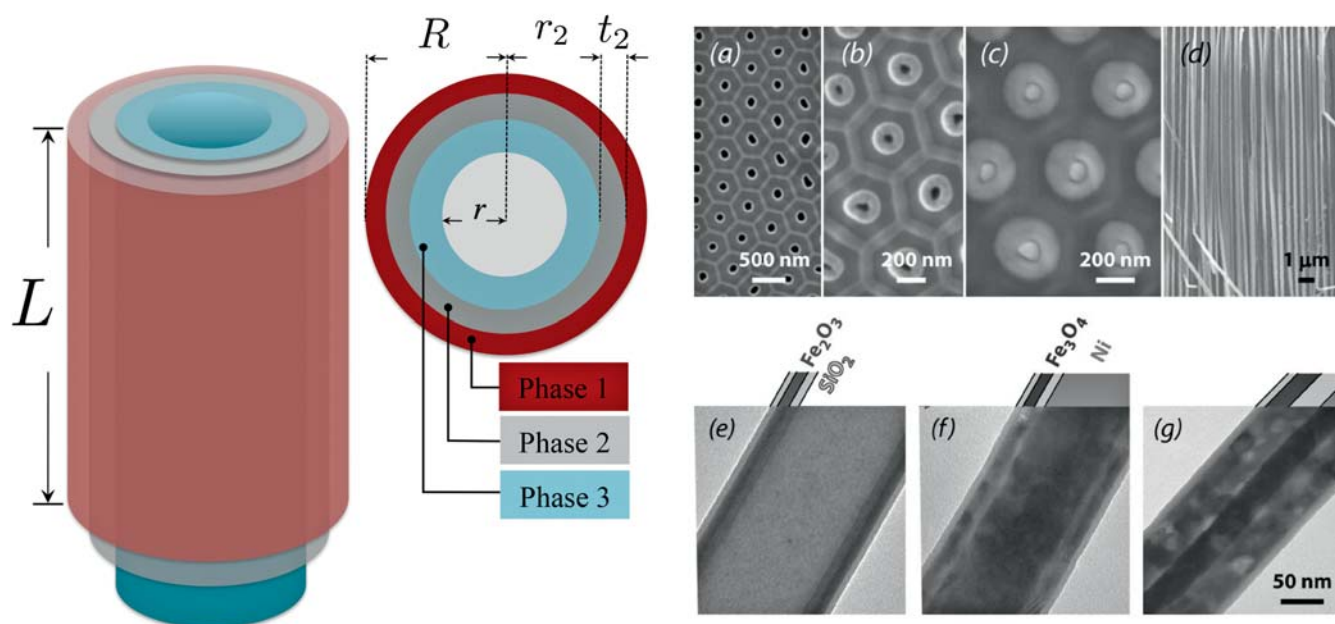


Fig. 3: Illustration of a core-shell magnetic nanotube (Left) made of three concentric shells and its synthesis by combination of ALD and electrodeposition in alumina templates (Right) [11]

Our laboratory accounts with multiple ALD set ups for conformal coating of different templates, which can either be arranged of freestanding metal nanowires or nanoporous anodic aluminum oxide (AAO). In the first case, the insulating magnetic shell is directly deposited on the cylindrical metal nanowires using ALD. In the latter, case the AAO is first coated with the insulating magnetic shell and then filled with a metal using electrodeposition. In a last step, this technique requires to etch away the AAO leading to an array of CSMNs.

Both approaches exploit the outstanding ability of ALD to coat high aspect ratio templates in a uniform manner. The synthesis of magnetic materials via ALD often requires special modifications of the standard deposition setups. Our laboratory can meet those requirements with a number of different reactors. The growth of $\gamma\text{-Fe}_3\text{O}_4$ using ferrocene as precursor, for example, requires ozone as oxidizer, which can be supplied with an external ozone generator. ALD thin films of FeO_x have already been successfully deposited in our lab. The next steps are to optimize the film composition and the magnetic properties with suitable deposition parameters and heat treatments. This optimized process can then be used to synthesis CSMNs with $\gamma\text{-Fe}_3\text{O}_4$ as insulating magnetic shell.

- [1] J. A. Otálora et al., Phys. Rev. Lett. 117 (2016) 227203.
- [2] J. A. Otálora et al., Phys. Rev. B. 95 (2017) 184415.
- [3] R. Hertel, Spin. 3 (2013) 03.
- [4] D. D. Sheka et al., Phys. Rev. B. 92 (2015) 054417.
- [5] R. Streubel et al., J. Phys D: Appl. Phys 49 (2016) 363001.
- [6] M. Yang et al., Appl. Phys. Lett. 99, (2011) 122505.
- [7] J. A. Otálora et al., Appl. Phys. Lett. 100 (2012) 072407.
- [8] R. Arias, et al., Phys. Rev. B. 66.14 (2002) 149903
- [9] A. V. Chumak et al., Nat. Phys. 11 (2015) 453.
- [11] Y. T. Chong et al., Adv. Mat. 22 (2010) 2435.

Cooperation: ¹Helmholtz-Zentrum Dresden-Rossendorf (HZDR), Institute of Ion Beam Physics and Materials Research, Dresden

Generic Coexistence of Fermi Arcs and Dirac Cones on the Surface of Time-Reversal Invariant Weyl Semimetals

A. Lau, K. Koepernik, J. van den Brink, C. Ortix

Abstract: The hallmark of Weyl semimetals is the existence of open constant-energy contours on their surface – the so-called Fermi arcs – connecting Weyl points. In this work, we show that for time-reversal symmetric realizations of Weyl semimetals these Fermi arcs in many cases coexist with closed Fermi pockets originating from surface Dirac cones pinned to time-reversal invariant momenta. The existence of Fermi pockets is required for certain Fermi-arc connectivities due to additional restrictions imposed by the six \mathbb{Z}_2 topological invariants characterizing a generic time-reversal invariant Weyl semimetal. We show that a change of the Fermi-arc connectivity generally leads to a different topology of the surface Fermi surface, and identify the half-Heusler compound LaPtBi under in-plane compressive strain as a material that realizes this surface Lifshitz transition. We also discuss universal features of this coexistence in quasi-particle interference spectra.

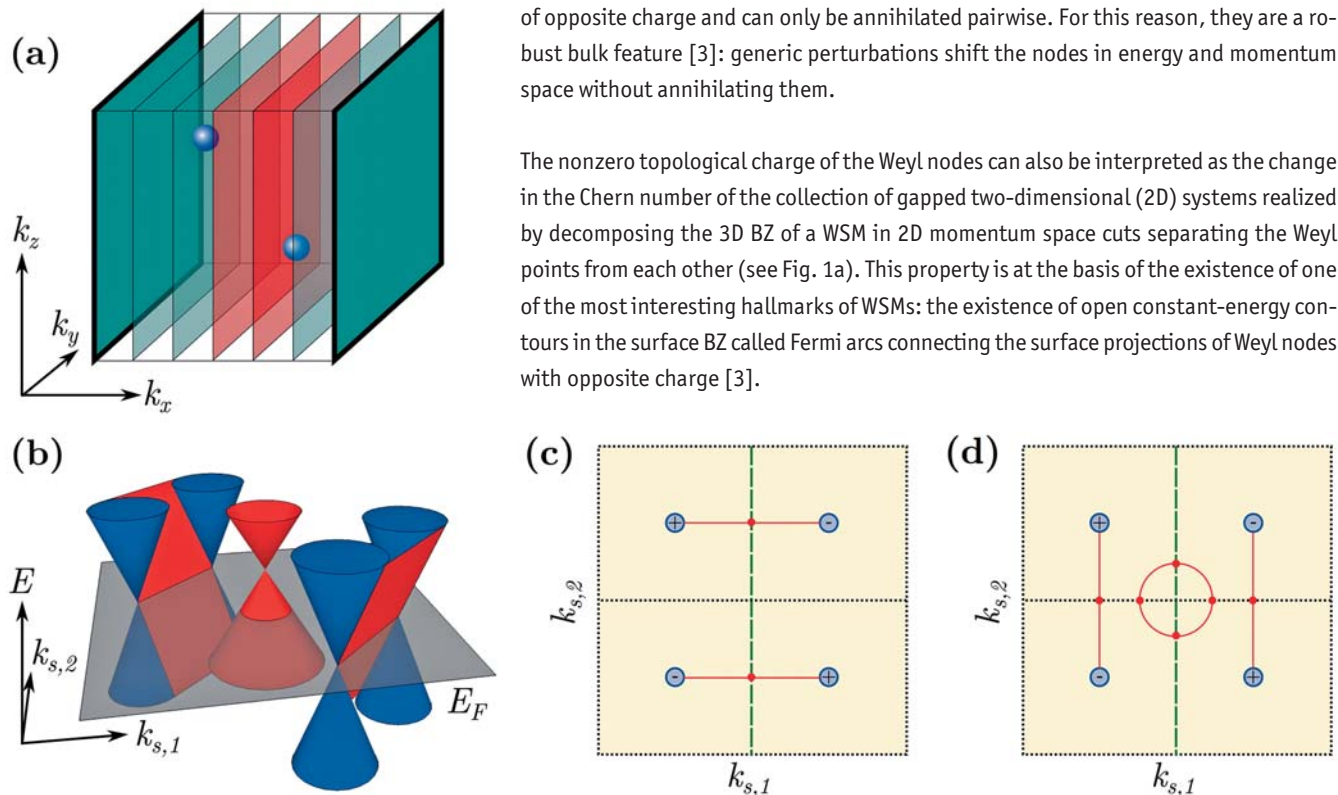
Weyl Semimetals

Sparked by the discovery of the quantum Hall effect and its theoretical explanation, the study of topological phases of matter has been one of the driving forces in modern condensed matter physics [1,2]. In recent years, the family of topological materials has been extended by topological semimetals [3]. A milestone was the experimental discovery of Weyl semimetals (WSMs) [4-6]. WSMs are three-dimensional (3D) gapless materials whose bulk energy bands cross linearly at isolated points, the so-called Weyl nodes, in the Brillouin zone (BZ) [3].

A Weyl node represents a monopole of the Berry flux in momentum space. Consequently, an integral of the Berry flux over a closed surface enclosing the Weyl node results in a nonzero integer value, which defines the topological charge of the node. Since the total topological charge of the whole BZ must vanish, Weyl nodes always appear in pairs of opposite charge and can only be annihilated pairwise. For this reason, they are a robust bulk feature [3]: generic perturbations shift the nodes in energy and momentum space without annihilating them.

The nonzero topological charge of the Weyl nodes can also be interpreted as the change in the Chern number of the collection of gapped two-dimensional (2D) systems realized by decomposing the 3D BZ of a WSM in 2D momentum space cuts separating the Weyl points from each other (see Fig. 1a). This property is at the basis of the existence of one of the most interesting hallmarks of WSMs: the existence of open constant-energy contours in the surface BZ called Fermi arcs connecting the surface projections of Weyl nodes with opposite charge [3].

Fig. 1: (a) The BZ of a WSM as a collection of 2D insulators with zero (green) or nonzero (red) Chern numbers. Weyl nodes (blue spheres) separate planes with different Chern numbers. The bold frames indicate the TRI 2D insulators characterized by a \mathbb{Z}_2 invariant. (b) Typical low-energy surface spectrum of a TRI WSM with an additional surface Dirac cone: surface states are shown in red, whereas the surface projections of the 3D bulk Weyl cones are highlighted in blue. (c)-(d) Fermi arc connectivities in the surface BZ of a TRI WSM with four Weyl points indicated by their topological charge \pm . The surface projections of the TRI planes are highlighted by dotted black ($v = 0$) or dashed green ($v = 1$) lines.



\mathbb{Z}_2 Invariants in TRI Weyl Semimetals

Time-reversal invariant (TRI) realizations of WSMs are special because they can be additionally characterized by six \mathbb{Z}_2 invariants associated with the TRI planes of the BZ [7]. The Chern number of the effective 2D insulators realized by the TRI planes will be zero, but the time-reversal polarizations still allow to characterize the effective 2D systems in terms of a \mathbb{Z}_2 topological invariant ν [8].

For a generic surface of a WSM, by bulk-boundary correspondence the ν_i determine whether an even ($\nu_i = 0$) or odd ($\nu_i = 1$) number of Kramers pairs of surface states cross the Fermi level along the surface projection of the i -th TRI plane. This imposes restrictions on the structure of the surface Fermi surface but still does not uniquely determine it. Figs. 1(c) and (d) sketch two allowed but qualitatively very different surface Fermi surfaces of a TRI WSM with corresponding \mathbb{Z}_2 invariants. A surface Fermi surface consisting of only two open arcs, connecting Weyl points as depicted in Fig. 1c, is entirely allowed. However, different pairs of Weyl points of opposite charge can be connected only if an additional Fermi pocket, enclosing a TRI point, is created (see Fig. 1d). The latter situation is a unique signature of Fermi arcs coexisting with a surface Dirac cone (see Fig. 1b), which is an exclusive feature of TRI WSMs [7]. This surface Dirac cone is protected for a given connectivity of the Fermi arcs. We emphasize that while this transition does not change the \mathbb{Z}_2 invariants of the TRI WSM, the change of the Fermi surface topology does imply a Lifshitz transition on the surface of the material.

Phenomenological QPI Patterns

Having established the coexistence of Fermi arcs and Dirac cones in TRI WSMs, we proceed to analyze their fingerprints in quasiparticle interference (QPI) patterns, which can be observed in scanning tunnelling spectroscopy experiments. QPI spectra can be approximated in terms of the joint density of states (JDOS) [9,10]. To understand the characteristic features arising in QPI spectra, we have therefore performed a phenomenological analysis of the JDOS. As a result, we identify two kidney-shaped features, corresponding to scattering events between the Fermi arcs and the Fermi pocket, as the universal QPI feature of the coexistence [7].

Tight-Binding Model

Next, we study a generic tight-binding model for a TRI WSM to investigate on a microscopic basis the coexistence of surface Dirac cones and Fermi arcs [7,10]. For this purpose, we start from a particular WSM phase and vary a tuning parameter β . The results are presented in Fig. 2. With the chosen parameters, the model features four bulk Weyl points with topological charge ± 1 . For the topological invariants of the TRI planes we find that $\nu_{k_z=\pi} = 1$ while the remaining five \mathbb{Z}_2 invariants are all zero. At the (010) surface we therefore expect an odd number of Kramers pairs at $k_z = \pi$ and an even number at $k_z = 0$ and $k_x = 0, \pi$.

For large values of β we find that Fermi arcs connect two Weyl nodes in the left half-plane and two Weyl nodes in the right half-plane (see Fig. 2a). In Fig. 2b we show the calculated JDOS of the system. By decreasing the parameter β , a Lifshitz transition takes place (see Fig. 2c) and the connectivity of the Fermi arcs changes (see Fig. 2e): surface Fermi arcs connect now two Weyl nodes in the upper half-plane and two Weyl nodes in the lower half-plane. In addition, we find an elliptical Fermi pocket of surface states corresponding to a surface Dirac cone around the Z point of the surface BZ. The Fermi pocket is required for this particular connectivity of Weyl nodes to satisfy the number of surface states imposed by the invariants ν_i which have not changed during the transition. In agreement with our general considerations, the corresponding JDOS exhibits the kidney-shaped features indicative of scattering between the Fermi arcs and the Fermi pocket (see Fig. 2f).

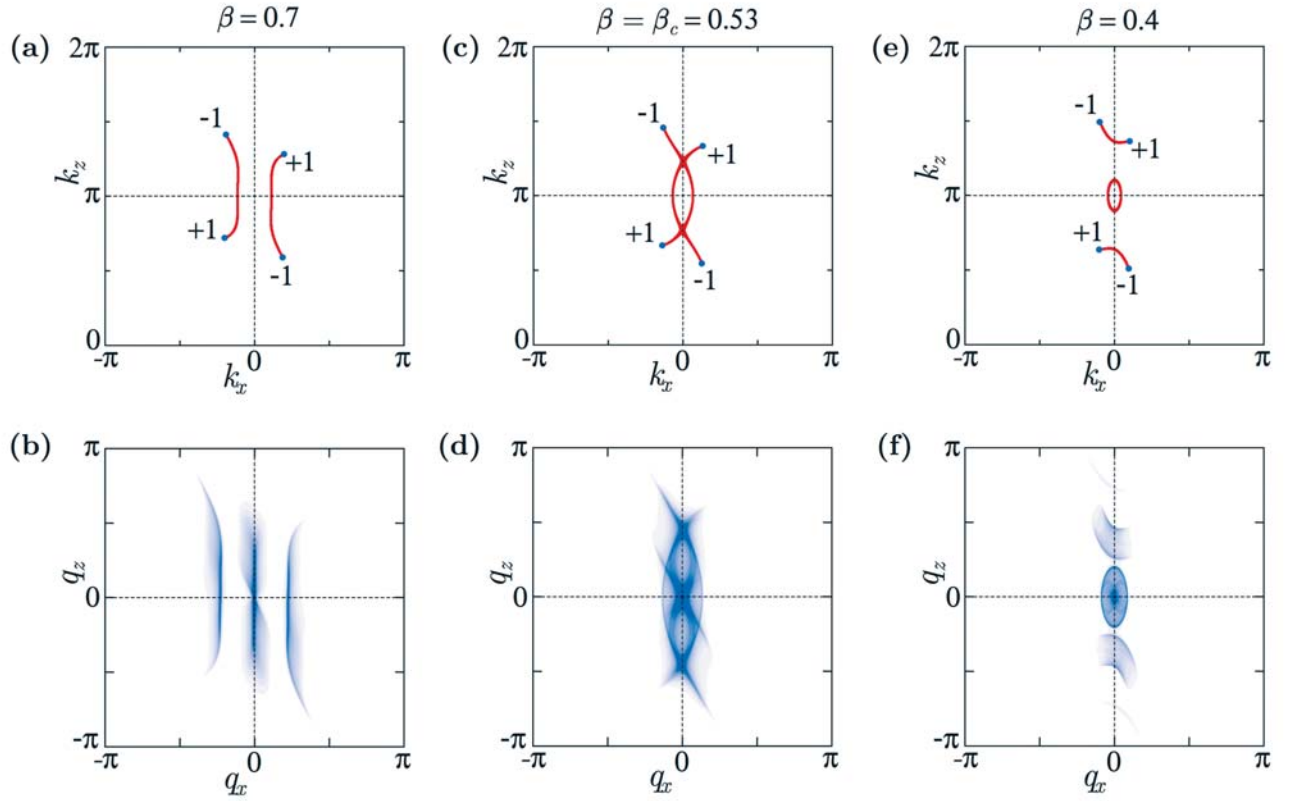
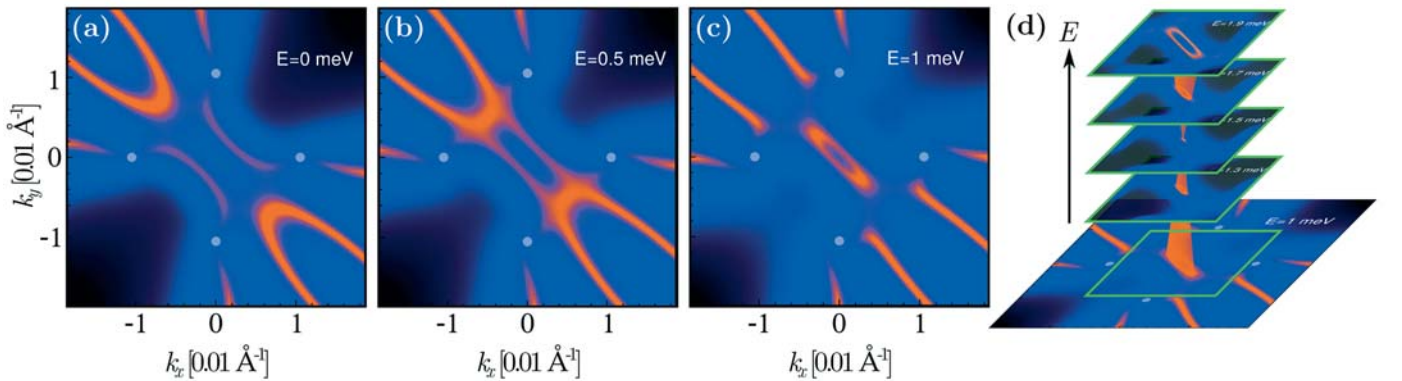


Fig. 2: Fermi surfaces and JDOS for (010) surfaces in the tight-binding model: the first column shows the Fermi surfaces for different values of the tuning parameter β . The bulk Weyl nodes are highlighted in blue and their topological charge is indicated. Surface states are highlighted in red. The second column shows the corresponding JDOS spectra. In (f), the kidney-shaped features indicative of the coexistence of Fermi arcs and Dirac cones are clearly visible in the JDOS.

Fig. 3: Surface Fermi surfaces of LaPtBi with (001) termination: shown is the surface spectral weight. The positions of the four Weyl-point projections are marked by grey dots. The panels display the transition between different Fermi-arc connectivities by varying the Fermi level. The connectivity shown in (c) requires the presence of an additional Fermi pocket around the origin. (d) A further increase of the Fermi level reveals that the Fermi pocket indeed originates from a Dirac cone around Γ .



LaPtBi under Strain

We next show the coexistence of Dirac cones and Fermi arcs in the half-Heusler compound LaPtBi. Theoretical ab-initio studies suggest that LaPtBi realizes a WSM phase with eight Weyl nodes under a broad range of in-plane biaxial compressive strain [11]. We confirm this by performing DFT calculations employing the Full Potential Local Orbital method [12]. We find eight Weyl points of charge ± 1 located at the $k_x = 0$ and $k_y = 0$ planes of the bulk BZ.

For the study of surface states, we investigate a semi-infinite slab with a (001) surface corresponding to a termination along one of the LaBi planes. In the (001) surface BZ, the Weyl points are projected pairwise on four different surface momenta thereby giving the projected Weyl points an effective topological charge of ± 2 . Hence, there must be two outgoing Fermi arcs for each Weyl-point projection. Moreover, we find that the projections of the TRI planes $k_x = k_y$ and $k_x = -k_y$ feature an odd number of surface Kramers pairs (see Fig. 3). This implies non-trivial \mathbb{Z}_2 invariants which we confirm by explicit calculations [7]. This gives rise to restrictions on the Fermi surface topology (see Fig. 3).

In Figure 3a, the Fermi level coincides with the Weyl-point energies. In this case, the Fermi arcs connect in a way that does not require an additional Fermi pocket. By raising the Fermi level, which can be accomplished for instance by doping, a Lifshitz transition takes place (compare Fig. 3b to Fig. 2c). Finally, the connectivity of the Weyl nodes switches which leads to the emergence of an additional Fermi pocket around the projected Γ point, as shown in Fig. 3c. This Fermi pocket is indeed associated with a surface Dirac cone (see Fig. 3d) as one can infer from surface Fermi surfaces at larger E_F . This establishes LaPtBi under strain as a potential candidate material for the coexistence of Fermi arcs and Dirac cones [7].

- [1] M. Z. Hasan et al., *Rev. Mod. Phys.* 82 (2010) 3045.
- [2] X.-L. Qi et al., *Rev. Mod. Phys.* 83 (2011) 1057.
- [3] N. P. Armitage et al., *arXiv:1705.01111* (2017).
- [4] S.-M. Huang et al., *Nat. Commun.* 6 (2015) 7373.
- [5] B. Q. Lv et al., *Phys. Rev. X* 5 (2015) 031013.
- [6] S.-Y. Xu et al., *Science* 349 (2015) 613.
- [7] A. Lau et al., *Phys. Rev. Lett.* 119 (2017) 076801.
- [8] L. Fu et al., *Phys. Rev. B* 74 (2017) 195312.
- [9] P. G. Derry et al., *Phys. Rev. B* 92 (2015) 035126.
- [10] S. Kourtis et al., *Phys. Rev. B* 93 (2016) 041109.
- [11] J. Ruan et al., *Nat. Commun.* 7 (2016) 11136.
- [12] K. Koepernik et al., *Phys. Rev. B* 59 (1999) 1743.

Funding: FET programme: FET-Open grant number 618083 (CNTQC); DFG: Grant No. OR 404/1-1 and SFB 1143; NWO: VIDI grant (Project 680-47-543)

Evidence for a Field-Induced Quantum Spin Liquid in α -RuCl₃

S.-H. Baek, A. U. B. Wolter, S. Nishimoto, J. van den Brink, B. Büchner

Abstract: The Kitaev model on a honeycomb lattice has attracted much attention due to its exact solubility and its quantum spin liquid (QSL) ground state, which would be relevant for quantum computing. We report a combined ³⁵Cl nuclear magnetic resonance and specific heat study in the honeycomb lattice α -RuCl₃, a material that has been suggested to potentially realize a Kitaev quantum spin liquid ground state. Our results provide direct evidence that α -RuCl₃ exhibits a magnetic-field-induced QSL. For fields larger than ~ 10 T, a spin gap opens up, while resonance lines remain sharp, evidencing that spins are quantum disordered and locally fluctuating. The spin gap increases linearly with an increasing magnetic field, reaching ~ 50 K at 15 T.

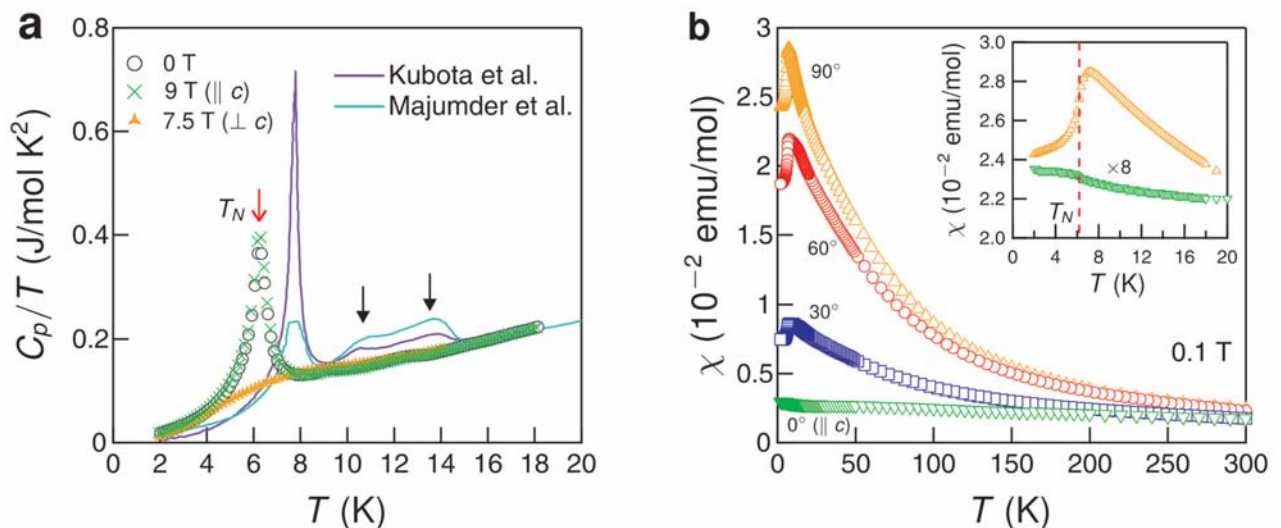
State-of-the-art

When the interactions between magnetic spins are strongly frustrated, quantum fluctuations can cause spins to remain disordered even at very low temperatures [1]. The quantum spin liquid (QSL) state that ensues is conceptually very interesting – for instance, new fractionalized excitations appear that are very different from the ordinary spin-wave excitations in ordered magnets [2-5]. A QSL appears in the so-called Kitaev honeycomb model [6,7], which has motivated the search for its experimental realization and its topological QSL phases. Within the last 3 years the quest is mainly centered on α -RuCl₃, which is actually believed to be the prime material to-date to harbor physics related to the Kitaev model.

α -RuCl₃ is a Mott insulator with a 2D layered structure of edge-sharing RuCl₆ octahedra arranged in a honeycomb lattice. The spin and orbital moments on the ruthenium sites are strongly coupled by the spin-orbit interaction leading to the formation of isospins $J_{\text{eff}} = 1/2$. While α -RuCl₃ displays magnetic long-range order at low temperature of the so-called zigzag type due to additional non-Kitaev terms in the Hamiltonian, it has been proposed to still be proximate to the Kitaev spin liquid based on e.g. its small magnetic ordering temperature $T_N \sim 7$ K and spin excitation spectrum [8-13].

In α -RuCl₃ a very peculiar strongly anisotropic magnetism has been reported [8-10] based on measurements of the uniform magnetic susceptibility χ and the specific heat C_p/T . From the data it is clear that the antiferromagnetic (AFM) state observed at low temperature (T) is hardly affected by external fields along the c direction whereas the signatures of the long-range magnetic order disappear for moderate fields (H) of about 8 T applied along the ab plane. This pronounced anisotropy of the magnetism is also found in our crystals (see Fig. 1a and b). Note that whereas earlier studies [8-10] reported

Fig. 1: (a) Low- T specific heat C_p/T at zero and chosen magnetic fields. The data at zero field taken from Refs. [8,9] are compared. (b) Temperature dependence of the uniform magnetic susceptibility χ at $\mu_0 H = 0.1$ T obtained for the four different field orientations with respect to the c axis. The inset enlarges the low- T region. [14]



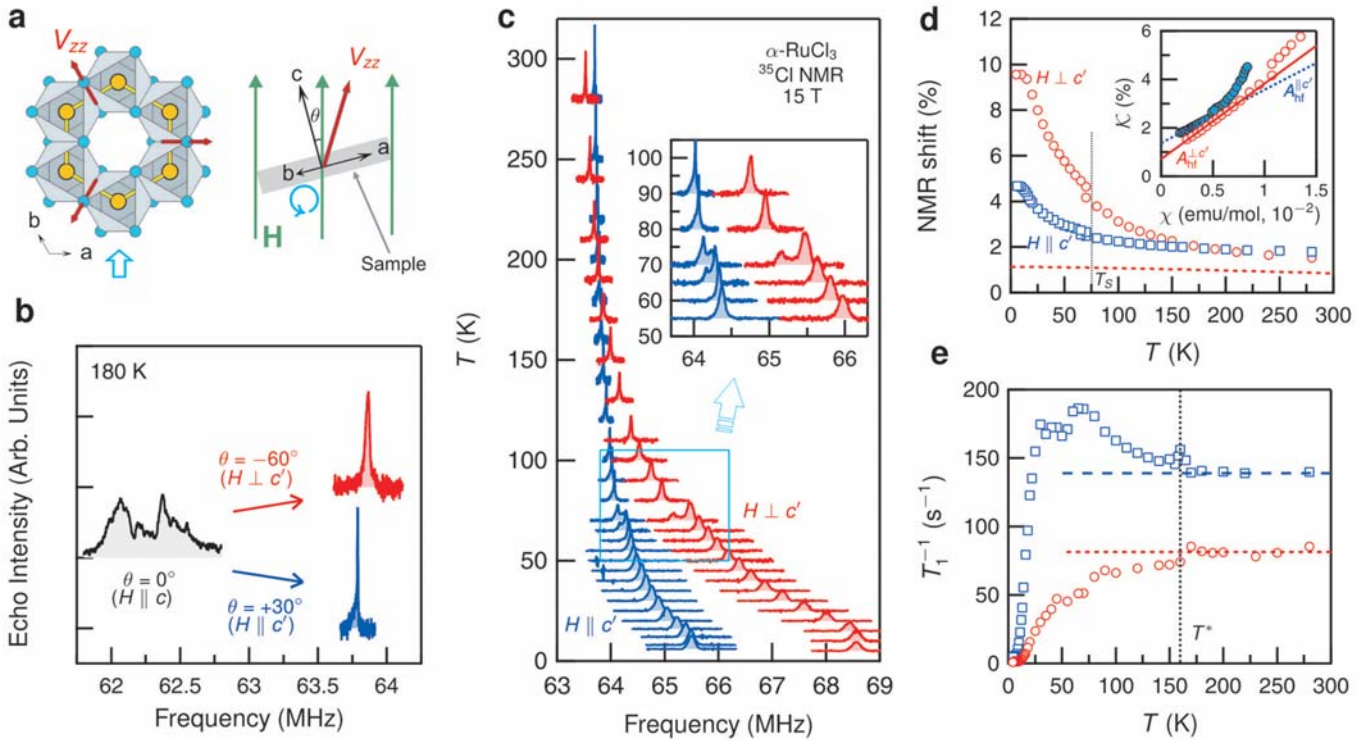
either two magnetic transitions at $T_{N1} \sim 8$ K and $T_{N2} \sim 14$ K or a single transition at $T_N \sim 13$ K, our measurements show, essentially, a single transition occurring at a considerably lower temperature, $T_{N1} \sim 6.2$ K. This evidences that our sample is of high quality with a (nearly) uniform stacking pattern [12].

NMR spectra

Since the ^{35}Cl nuclei (nuclear spin $I = 3/2$) possess a large quadrupole moment, the NMR spectra are strongly affected by the electric field gradient (EFG). In $\alpha\text{-RuCl}_3$, the principal axis of the largest eigenvalue of the EFG tensor V_{zz} at ^{35}Cl is expected to point along the shared edges of the RuCl_6 octahedra, which are tilted $\sim 35^\circ$ away from the c axis as illustrated in Fig. 2a. As a result, there exist three inequivalent ^{35}Cl sites, yielding a very complex and broad ^{35}Cl spectrum in a magnetic field, as shown in Fig. 2b. Taking advantage of the fact that the influence of the quadrupole interaction is very sensitive to the angle between the direction of V_{zz} and H , it is possible to separate one ^{35}Cl spectrum from the other two spectra by applying H along one of the three local directions of V_{zz} at ^{35}Cl (see Fig. 2b). Therefore, in the following we will present our NMR results with respect to the $V_{zz} = c'$ axis.

The T dependence of the ^{35}Cl NMR spectrum at 15 T is presented in Fig. 2c. Clearly, there is no signature of long-range magnetic order, which would cause a large broadening or splitting of the ^{35}Cl line. Another feature is the appearance of a new NMR peak that replaces the original one below ~ 75 K. This is due to a first-order structural phase transition [9,10]. Figure 2d presents the T dependence of the resonance frequency ν in terms of the NMR shift $K = (\nu - \nu_0)/\nu_0$ where ν_0 is the unshifted Larmor frequency. K is composed, mainly, of the three terms: $K = A_{\text{hf}}\chi_{\text{spin}} + K_{\text{chem}} + K_{\text{quad}}$, where A_{hf} is the hyperfine (hf) coupling constant, χ_{spin} the local spin susceptibility, K_{chem} the T independent chemical shift, and K_{quad} the second order quadrupole shift. The strong upturn of K observed at low T is attributed to χ_{spin} , which is consistent with the macroscopic susceptibility (see Fig. 1b).

Fig. 2: (a) The principal axis of the EFG V_{zz} at the ^{35}Cl nuclei is along the shared edges of the RuCl_6 octahedra, resulting in three inequivalent ^{35}Cl sites in field. (b) When $H \parallel c$ ($\theta = 0$), the ^{35}Cl spectrum is extremely complex and broad. As H is either parallel or perpendicular to the direction of V_{zz} , very narrow ^{35}Cl NMR lines were obtained. (c) ^{35}Cl NMR spectrum measured at $\mu_0 H = 15$ T as a function of T with cooling for two different field orientations. The first-order character of the structural transition is evidenced by the gradual transfer of the ^{35}Cl spectral weight below $T_S \sim 75$ K, as clearly shown in the inset. (d) NMR shift K as a function of T . The strong anisotropy of K increases rapidly with decreasing T , approaching a saturated value below ~ 10 K. The dotted line is the estimated T dependence of K_{quad} . The inset shows the K vs χ plot, which yields the hyperfine coupling constants, $A_{\text{hf}}^{\perp c'} = 17.4$ kG/ μ_B and $A_{\text{hf}}^{\parallel c'} = 12.3$ kG/ μ_B . (e) Spin-lattice relaxation rate T_1^{-1} vs. T . Whereas T_1^{-1} is nearly T -independent above $T^* \approx 160$ K, it increases (decreases) for $H \parallel c'$ ($H \perp c'$) below T^* , implying the development of in-plane spin correlations. [14]



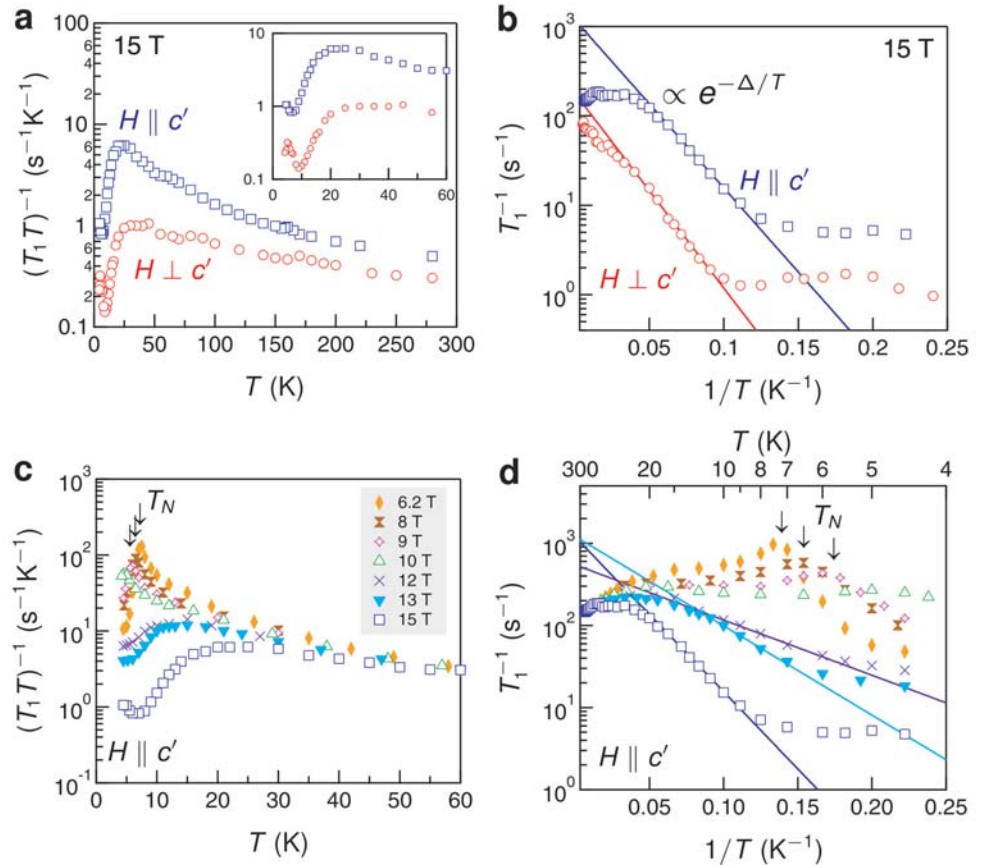
Spin-lattice relaxation rate

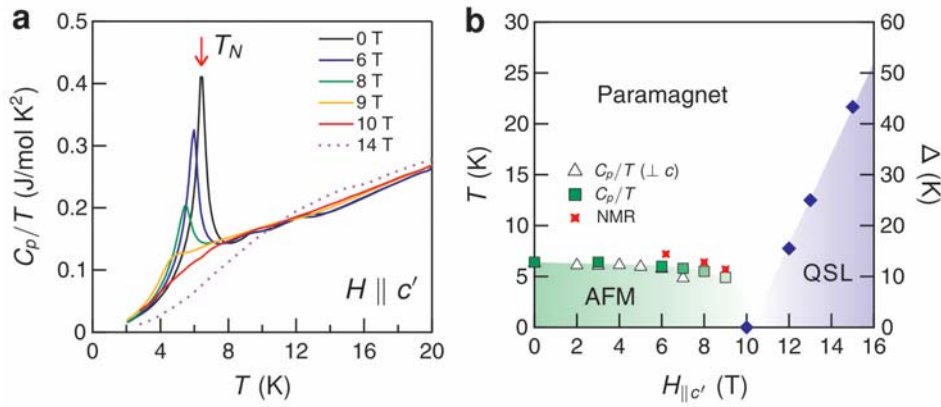
Figure 2e shows the T dependence of the spin-lattice relaxation rate T_1^{-1} at $\mu_0 H = 15$ T. At high $T > T^* \sim 160$ K, T_1^{-1} follows roughly the behavior expected for simple paramagnets. The different absolute values of T_1^{-1} for the two orientations of H are ascribed to the anisotropic hf couplings (see Fig. 2d). As T is lowered below T^* , T_1^{-1} increases for $H \parallel c'$ but it decreases for $H \perp c'$. Since the spin-lattice relaxation process is induced by the transverse components of spin fluctuations (SFs) with respect to the nuclear quantization axis, it is clear that T_1^{-1} for $H \parallel c'$ experiences stronger in-plane and weaker out-of-plane SFs than for $H \perp c'$. Hence, the increase of the T_1^{-1} anisotropy with lowering T is an indication of the development of strong in-plane SFs below T^* .

At low temperatures, roughly below 50 K, T_1^{-1} starts to decrease. For the study of spin dynamics at low T , it is convenient to consider the quantity $(T_1 T)^{-1}$, which is proportional to the q -average of the imaginary part of the dynamical susceptibility. As shown in Fig. 3a, a broad maximum of $(T_1 T)^{-1}$ occurs near 30 K, being followed by a rapid drop towards low T in an identical manner for both field orientations. The rapid decrease of $(T_1 T)^{-1}$ implies a pronounced depletion of spectral weight in the spin excitation spectrum. The semilog plot of T_1^{-1} against $1/T$ drawn in Fig. 3b unambiguously reveals a spin gap behavior, $T_1^{-1} \sim \exp(-\Delta/T)$, with the gap $\Delta \sim 44$ and 50 K for $H \parallel c'$ and $\perp c'$, respectively.

In order to study the H dependence of Δ , we measured $(T_1 T)^{-1}$ as a function of $H \parallel c'$ at low T . The results are shown in Fig. 3c and 3d. A spin gap is only seen for $\mu_0 H > 10$ T and Δ increases linearly with increasing H . At $\mu_0 H = 10$ T our data show a Curie-like upturn of the SFs, i.e., $(T_1 T)^{-1}$ diverges for low T . Upon further lowering H below 10 T, a sharp peak in $(T_1 T)^{-1}$ signals static magnetic order below T_N which decreases with increasing H . Below T_N , the ^{35}Cl spectrum progressively spreads out with decreasing T , indicating the incommensurate character of AFM order [8]. Thus, our data for $(T_1 T)^{-1}$ clearly show a qualitative change of the behavior as a function of H : the peak due to static order occurring at low field is replaced by a spin gap for $\mu_0 H > 10$ T. At the border the spin dynamics

Fig. 3: (a) $(T_1 T)^{-1}$ as a function of T measured at 15 T. At low T , $(T_1 T)^{-1}$ reaches a maximum at ~ 30 K for both field directions which is followed by a rapid drop upon further cooling. Inset enlarges the low T region. (b) Semilog plot of T_1^{-1} vs. $1/T$ unravels a spin gap behaviour $T_1^{-1} \sim \exp(-\Delta/T)$. The deviation from the gap behavior takes place below ~ 10 K, probably indicating a small amount of magnetic defects in the crystal. (c) Strong field dependence of $(T_1 T)^{-1}$ at low T as a function of $H \parallel c'$. Below 10 T, the AFM ordered phase was clearly detected by sharp peaks of $(T_1 T)^{-1}$. (d) The spin gap Δ is rapidly filled up with decreasing $H \parallel c'$, vanishing completely at 10 T. [14]





suggest quantum criticality, i.e. a divergence of $(T_1 T)^{-1}$ for $T=0$. To back our NMR findings, we measured C_p/T for $H || c'$ (Fig. 4a). The anomaly associated with AFM order is rapidly suppressed toward 10 T, which perfectly agrees with the T_1^{-1} results. Further, we confirmed that at 14 T C_p/T is significantly suppressed at low T , evidencing the opening of a spin gap for $\mu_0 H > 10$ T.

An explanation of the observed spin gap in terms of static magnetic order can be ruled out. For example, the ^{35}Cl spectra measured at $\mu_0 H = 15$ T do not show any signature of magnetic order down to 4.2 K (see Fig. 2c). Moreover, it is difficult to attribute the extracted large spin gap to some kind of anisotropy gap occurring in the spin wave spectrum in magnetically ordered systems. Not only the measured large gap size, but also the rather isotropic gap behavior, contradicts any interpretation in terms of anisotropy gaps. The findings are also incompatible with the gap being due to a saturating ferromagnetic polarization of spins. The magnetization near 10 T is far less than the saturated value, particularly for $H || c'$ [15]. This clear-cut conclusion from the bare experimental findings is further supported by a theoretical analysis, where a forced-ferromagnetic state of $\alpha\text{-RuCl}_3$ appears at a critical field of $\mu_0 H_c = 23.2$ T [14].

T - H phase diagram

Our findings are summarized in the T - H phase diagram, see Fig. 4b. The data indicate a field-induced crossover from a magnetically ordered state at low fields to a disordered state showing gapped spin excitations in large fields. Moreover, as evident from Fig. 4b, the field dependence of $T_1^{-1}(T)$ reveals that Δ increases linearly with H above 10 T. Our data suggest that when the magnetic field and gap become large enough, it can overcome the energy scale related to the residual non-Kitaev interactions so that a QSL emerges.

Fig. 4: (a) The dependence of C_p/T for $H || c'$. With increasing H , AFM order is suppressed and completely disappears at 10 T; at 14 T a gap appears to be present. **(b)** The T - H phase diagram obtained by NMR and specific heat measurements. T_N obtained by specific heat for $H \perp c$ is compared. In the QSL region the field dependence of the spin-gap Δ is shown (right axis). [14]

- [1] L. Balents, *Nature* 464, 199 (2010).
- [2] Y. Shimizu et al., *Phys. Rev. Lett.* 91, 107001 (2003).
- [3] M. Yamashita et al., *Science* 328, 1246 (2010).
- [4] T.-H. Han et al., *Nature* 492, 406 (2012).
- [5] M. Fu et al., *Science* 350, 655 (2015).
- [6] A. Kitaev, *Ann. Phys.* 321, 2 (2006).
- [7] J. K. Pachos, *Introduction to Topological Quantum Computation*, Cambridge University Press, Cambridge, UK, 2012.
- [8] M. Majumder et al., *Phys. Rev. B* 91, 180401 (2015).
- [9] Y. Kubota et al., *Phys. Rev. B* 91, 094422 (2015).
- [10] J. Sears et al., *Phys. Rev. B* 91, 144420 (2015).
- [11] L. J. Sandilands et al., *Phys. Rev. B* 93, 075144 (2016).
- [12] A. Banerjee et al., *Nat. Mater.* 15, 733 (2016).
- [13] R. Yadav et al., *Sci. Rep.* 6, 37925 (2016).
- [14] S.-H. Baek et al., *Phys. Rev. Lett.* 119, 037201 (2017).
- [15] R. D. Johnson et al., *Phys. Rev. B* 92, 235119 (2015).

Funding: DFG Research Grant BA 4927/1-3, DFG Collaborative Research Center SFB 1143
Cooperation: Department of Physics, Chung-Ang University, Seoul, Republic of Korea

Magnetic characterization in the TEM: Skyrmions and electron vortex beams

S.Schneider, D. Pohl, D. Wolf, A. Lubk, B. Büchner, K. Nielsch, B. Rellinghaus

Abstract: Topological spin solitons and in particular skyrmions possess spin textures that provide for local variations of the magnetization at nanoscopic length scales. To exploit their unique transport and topological properties for, e.g., memory applications a detailed understanding of the interplay between skyrmionic structures, confined geometries (in thin films or at interfaces), lattice defects or inhomogeneities is indispensable. We aim at determining the details of skyrmionic spin textures in 3D and with nanometer and sub-nanometer resolution by combining, augmenting and developing transmission electron microscopy (TEM) based techniques such as Lorentz microscopy, electron holography and electron energy-loss magnetic chiral dichroism (EMCD) including recently developed vortex beam microscopy.

Skyrmions in thin films

Skyrmions [3] are topologically non-trivial vortex-like spin textures, anticipated for application in spintronic technologies, referred to as skyrmionics, in next generation magnetic data processing and storage due to their facile manipulation by spin-polarized currents of very low magnitude [4, 5]. In chiral-lattice ferromagnets without spatial inversion symmetry, such as the B20 compound $\text{Fe}_{0.95}\text{Co}_{0.05}\text{Ge}$ (see Fig. 1a) investigated in this work, skyrmions arise from the interplay between the Dzyaloshinskii-Moriya interaction [6, 7] and ferromagnetic exchange mechanisms [8]. Indeed, these and similar competing interactions, such as surface dipolar interaction, may lead to a whole zoo of non-trivial spin textures, including helical, cycloidal and various skyrmionic phases (antiskyrmions [9], Néel skyrmions [10]).

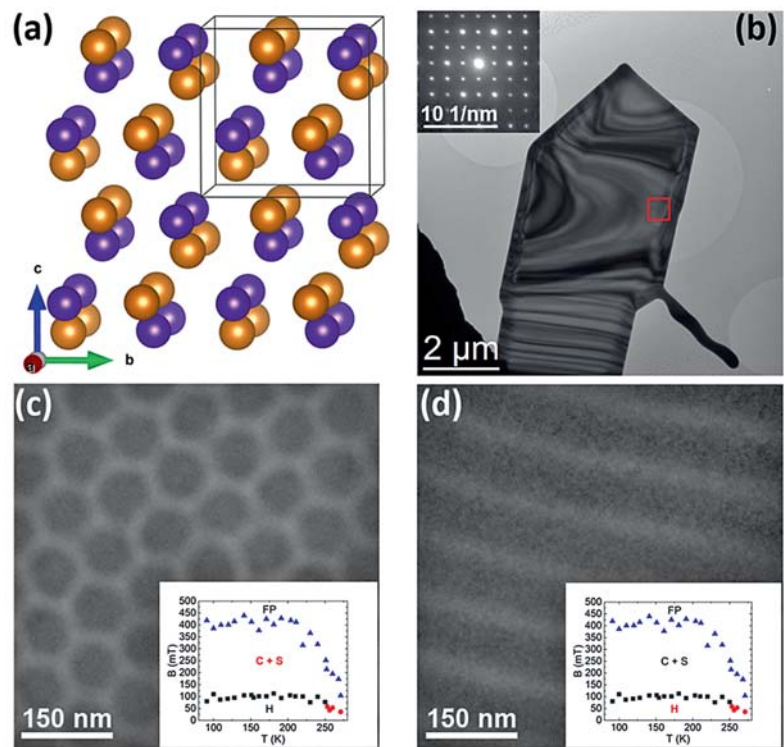


Fig. 1: (a) Structure of $\text{Fe}_{0.95}\text{Co}_{0.05}\text{Ge}$ in the cubic B20 phase. Fe and Co atoms are shown in violet and Ge in brown. (b) TEM image of a $\text{Fe}_{0.95}\text{Co}_{0.05}\text{Ge}$ nanoplate in [001] with the diffraction pattern in the inset. (c) Skyrmion lattice and (d) helical phase as observed within the marked area in panel (a). The insets show the experimentally determined magnetic phase diagrams with the corresponding phases marked in red. H, C, S, and FP denote the helical, cycloidal, skyrmion and so-called “field polarized ferromagnetic” phases, respectively.

Unfortunately, little is known about the three-dimensional shape of skyrmions [11, 12], although considerable similarities to smectic liquid crystals may be established [13, 14]. Experimental studies on the 3D spin texture in skyrmions have not been reported to date. Here, we fill that gap by combining the concept of the transport of intensity equation (TIE) [15], focal series in-line electron holography (EH), and off-axis EH [16] to quantitatively reconstruct the projected magnetic field pertaining to both the helical and the skyrmion lattice phase in single crystal nanoparticles of the isotropic chiral magnet $\text{Fe}_{0.95}\text{Co}_{0.05}\text{Ge}$.

All applied methods have the drawback, that cycloidal modulations (and hence also Néel skyrmions) are invisible in these techniques, if they are aligned perpendicular to the beam, either because the z -component of the rotation vanishes directly or because the stray fields above and below the thin film sample cancel the lateral fields within the sample in projection.

The skyrmion phase in the $\text{Fe}_{0.95}\text{Co}_{0.05}\text{Ge}$ particles was investigated using a double corrected FEI Titan³ 80–300 microscope operated in imaging corrected Lorentz mode (conventional objective lens turned off) at an acceleration voltage of 300 kV. All measurements were performed at a sample temperature of 90 K and an applied field of 43 mT in out-of-plane direction (see Fig. 1d). A focal series of Lorentz TEM (L-TEM) images of a single isolated nanoplate oriented along [001] zone axis (see Fig. 1b) was recorded. Reconstruction of the electron wave's phase and thereby the magnetic induction was obtained with the help of a modified Gerchberg-Saxton type algorithm. To supplement the focal series reconstructions from large field of views, smaller areas of the identical nanoplate were investigated by off-axis EH [16]. A direct tomographic investigation of the 3D structure of the skyrmionic lattice is currently experimentally unfeasible, because this would require an externally applied out-of-plane magnetic field to be tilted with the sample. In the current experimental setup, the skyrmions align along the magnetic field of the objective lens which has a fixed orientation along the optical axis.

Thus, indirect experimental evidence for the 3D structure of the skyrmionic lattice may be currently only inferred from a quantitative analysis of the projected magnetic induction in the sample conducted with the help of in-line and off-axis electron holography. Fig. 2a depicts a L-TEM micrograph in underfocus showing the hexagonal skyrmion lattice as dark contrast. The image is one out of 21 of the focal series used for in-line holography reconstruction of the object exit wave in amplitude and phase. Figs. 2b,c

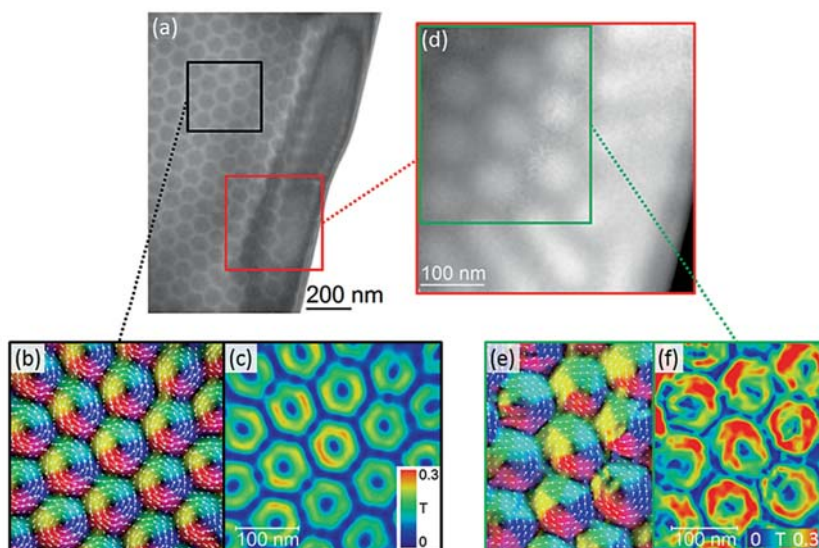


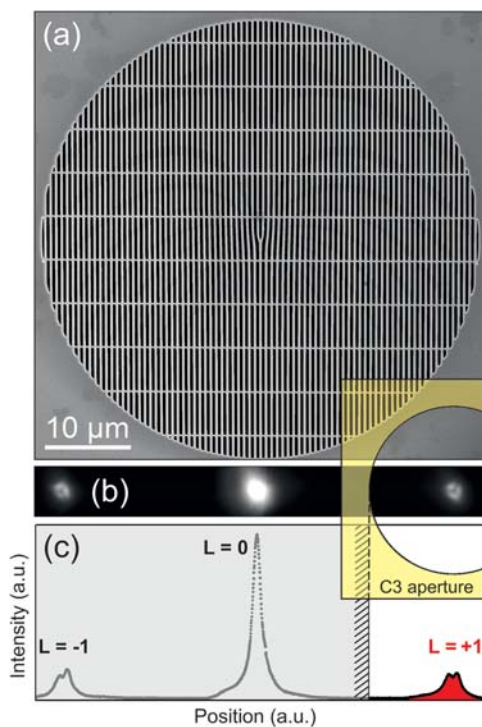
Fig. 2: (a) L-TEM image in under-focus showing the skyrmions as dark contrast. (d) Phase image of the position indicated by the red square in (a). (b,e) Mapping of the direction of the in-plane magnetic flux by combining a vector plot (white arrows) and a false color image. (c,f) False colour mapping of the magnitude of the in-plane magnetic flux.

show magnetic induction maps $\vec{B}_\perp(x, y)$ in cylindrical coordinate representation visualizing the spin texture of the skyrmions by $\vec{B}_\phi(x, y)$ (Fig. 2b) and their donut-shaped magnitude by $\vec{B}_r(x, y)$ (Fig. 2c). Likewise, we observed magnetic induction maps (Figs. 2e,f) from a phase image reconstructed by off-axis EH (Fig. 2d) on the same $\text{Fe}_{0.95}\text{Co}_{0.05}\text{Ge}$ nanoplate. Comparing the results of the two holographic methods, we measure a slightly higher magnetic induction $\vec{B}_r(x, y)$ with a slightly higher spatial resolution in the case of off-axis holography. However, we consistently observe a reduction of the B-fields ($\vec{B}_{\max} = (0.2 \dots 0.3)T$) with respect to the z-invariant case ($\vec{B}_{\max} = 0.48T$) obtained from magnetostatic simulations. Therefore, we propose two models for the 3D structure of skyrmions. One possible explanation for the reduced in-plane magnetic flux is a spiraling skyrmion through the thickness of the film, rather than z-invariant tube like skyrmions. Alternatively, magnetic dead layers at the surfaces or even more complex spin configurations may account for the experimentally determined magnetic field reduction.

Our recent experimental results corroborate the importance of the knowledge of the exact 3D structure for the skyrmion lattice in thin films. In order to overcome the pertaining experimental challenges, in-situ magnetic vector field application devices and auxiliary magnetic signals such as EMCD and electron vortex microscopy [17–20] need to be applied.

Electron Vortex microscopy

Recently discovered electron vortex beams (EVBs), which carry quantized orbital angular momenta (OAM) L , promise to also reveal magnetic signals similar to electron energy-loss magnetic chiral dichroism (EMCD) [21], which complementary to L-TEM and EH, provides direct access to the out-of-plane component of the magnetization. Since electron beams can be easily focused down to sub-nanometer diameters, this novel technique provides the possibility to quantitatively determine local magnetic properties with unrivalled lateral resolution. In order to generate the spiralling wave front of an electron vortex beam with an azimuthally growing phase shift of up to 2π and a phase singularity in its axial centre, specially designed apertures are needed [22, 23]. Dichroic signals on the L_2 and L_3 edge are expected to be of the order of 5% [24, 25].



The generation of EVBs is achieved by the implementation of a dislocation-type aperture into the condenser lens system. The setup allows for scanning TEM investigations (STEM) with vortex beams, whose OAM is selected by means of an additional discriminator aperture. New FIB cutting strategies facilitate the production of 50 μm wide and 300 nm thick high quality vortex apertures (see Fig. 3a). However, in the case of a fork-type aperture, the EVB are dispersed in the x-y plane resulting in a mixed probe that interacts with the magnetic sample.

We have recently devised an escape route to this problem by blocking any partial beams that carry other but the desired OAM prior to the interaction of the beam with the magnetic sample [19]. This is achieved by using a fork-type aperture in combination with a special condenser aperture to select a single partial beam with the chosen OAM (see Fig. 3b). This approach allows to generate atom-sized EVB with angstrom-sized

Fig. 3: (a) Scanning electron microscope image of a 50 μm dislocation aperture (placed at the C2 aperture level in the TEM). The horizontal ligaments are used as reinforcement of the 200 nm wide Pt bars. (b), Image of the electron probe at the sample. The position of the selected probe ($L = +1$) with respect to the discriminator aperture at the C3 aperture level is illustrated by the overlaid yellow schematic. (c), Intensity profile across the probe (in arbitrary units). The signature donut shape of the outer vortices with $|L| = 1$ is reflected by a dip in the intensity distribution.

probes and a well-defined OAM by which atomic resolution HR-STEM is achieved (see Fig. 4). Even the fingerprint of the Bessel wave function of the vortex beam that interacts with the sample can be seen in the HRSTEM images from an intensity drop in the centre of the atomic column images.

In addition, this novel technique is capable of atomic resolution EELS measurements, which is the prerequisite for atomic resolution EMCD measurements. The quality of the HR-STEM images and EELS-based elemental maps, which both provide atomic resolution, promise to open the door for future quantitative measurements of magnetic properties with ultimate spatial resolution and their local correlation with structural features at the very same position within the identical sample.

- [1] A. Leonov et al., *Physical Review Letters* 117, 087202 (2016).
- [2] F. N. Rybakov et al., *New Journal of Physics* 18, 045002 (2016).
- [3] A. N. Bogdanov and A. Hubert, *Journal of Magnetism and Magnetic Materials* 138, 255 (1994).
- [4] N. Nagaosa and Y. Tokura, *Nature Nanotechnology* 8, 899 (2013).
- [5] N. Kanazawa et al., „Noncentrosymmetric Magnets Hosting Magnetic Skyrmions“ (2017).
- [6] I. Dzyaloshinsky, *Journal of Physics and Chemistry of Solids* 4, 241 (1958).
- [7] T. Moriya, *Physical Review* 120, 91 (1960).
- [8] W. Heisenberg, *Zeitschrift für Physik* 38, 411 (1926).
- [9] A. K. Nayak et al., *Nature* 548, 561 (2017).
- [10] I. Kézsmárki et al., *Nature Materials* 14, 1116 (2015).
- [11] F. N. Rybakov et al., *Physical Review B - Condensed Matter and Materials Physics* 87, 094424 (2013).
- [12] H. S. Park et al., *Nature Nanotechnology* 9, 337 (2014).
- [13] G. A. Hinshaw et al., *Physical Review Letters* 60, 1864 (1988).
- [14] M. Glogarová et al., *Molecular Crystals and Liquid Crystals Science and Technology* 301, 325 (1997).
- [15] A. Lubk et al., *Physical Review Letters* 111, 173902 (2013).
- [16] H. Lichte et al., *Ultramicroscopy* 134, 126 (2013).
- [17] P. Schattschneider et al., *Nature* 441, 486 (2006).
- [18] S. Schneider et al., *Ultramicroscopy* 171, 186 (2016).
- [19] D. Pohl et al., *Scientific Reports* 7, 934 (2017).
- [20] A. Edström et al., *Physical Review Letters* 116, 127203 (2016).
- [21] J. Verbeeck et al., *Nature* 467, 301 (2010).
- [22] J. Verbeeck et al., *Ultramicroscopy* 113, 83 (2012).
- [23] D. Pohl et al., *Ultramicroscopy* 150, 16 (2015).
- [24] P. Schattschneider et al., *Ultramicroscopy* 136, 81 (2014).
- [25] J. Ruzs and S. Bhowmick, *Phys. Rev. Lett.* 111, 105504 (2013).

Funding: NSF grant ECCS-1609585, DGE-1256259, ERC grant agreement No 715620

Cooperation: Prof. Dr. Song Jin – University of Wisconsin-Madison, Madison, WI, USA; Dr. Marcus Schmidt – Max Planck Institute for Chemical Physics of Solids, Dresden, Germany; Dr. Peter Tiemeijer and Dr. Sorin Lazar, Thermo Fisher Scientific, Eindhoven, Netherlands; Dr. Xiaoyan Zhong, Tsinghua University, Beijing, China; Dr. Jan Ruzs, Paul Zeiger and Jakob Spiegelberg, Uppsala University, Uppsala, Sweden

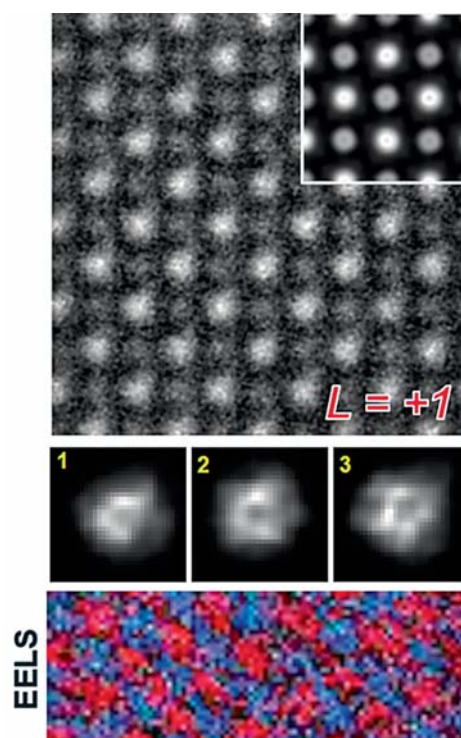


Fig. 4: (a) Scanning transmission electron microscopy and spectroscopy performance using single vortex beams ($L = +1$) on SrTiO_3 . Lower panel show false-color elemental maps of Ti (red) and Sr (blue) as obtained from EELS at the Ti-L and Sr-M edges. The inset shows the result of an ADF simulation for a sample thickness of 20 nm and a source size broadening of the $L = +1$ beam of 30 pm. Single Sr atomic columns are enlarged to show the intensity drop in the center of the column.

Research Area 2

Sperm-Tetrapod Micromotor for Targeted Drug Delivery

H. Xu, M. Medina-Sánchez, V. Magdanz, L. Schwarz, F. Hebenstreit, O. G. Schmidt

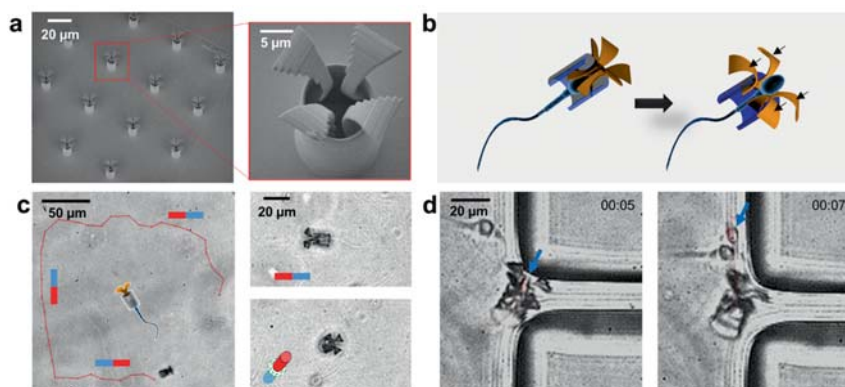
Abstract: Bio-hybrid micromotors have been well developed for various bio-applications as they combine the advantages of their biological and the synthetic parts. An example of them are the sperm-hybrid micromotors, where the sperms are used as propulsion force while the synthetic component is used for their guidance towards the area of interest by using external magnetic fields. Here we present a new type of sperm-hybrid micromotor and its prospective application in targeted drug delivery. The single sperm serves as an active drug carrier and driving force, while a laser-printed microstructure, coated with iron, is used to guide and release the sperm in the *in vitro* cultured cancer spheroid by using an external magnet and a structurally imposed mechanical actuation, respectively. The tubular structure (also called “tetrapod”) features four arms which release the drug-loaded sperm cell *in situ* when they bend upon pushing against a tumor spheroid, resulting in the drug delivery, which occurs when the sperm squeezes through the tumor spheroid and fuses with the cancer cell membrane.

Guidance and sperm release

Arrays of polymeric tetrapods were fabricated by 3D laser lithography. The arms protrude from one opening of the microtube in a curved manner. The dimensions of the structure were optimized according to the dimensions of the sperm, allowing a single sperm to be blocked in (Fig. 1a). The fabricated tetrapods were coated with 10 nm Fe and 2 nm Ti by e-beam metal evaporation for magnetic guidance. When an approaching sperm cell reaches the microstructure, it gets mechanically trapped inside the cavity of the tubular part and starts to push the tetrapod forward (Fig. 1b). The tubular body of the tetrapod is only $2\ \mu\text{m}$ longer than the sperm head, thus the sperm tail can still beat freely outside the tube to provide powerful propulsion as it was previously demonstrated by our group. Compared to free sperms, the average swimming velocity of the sperm-hybrid micromotors is nonetheless decreased by 43 % from $73 \pm 16\ \mu\text{m/s}$ to $41 \pm 10\ \mu\text{m/s}$ (for 15 samples of sperm-hybrid micromotors). The asymmetrically distributed metal coating makes it possible to guide the tetrapod microstructure or the sperm-hybrid micromotor and even manipulate several of them simultaneously. Figure 1c illustrates a rectangular track of a guided sperm-hybrid micromotor. The hybrid motor was easily steered by changing the direction of the external magnet.

PDMS microfluidic channels were fabricated as a platform for the investigation of the sperm release mechanism. Once the rotation stopped, the sperm cell escaped when the tetrapod arms were bent and enlarged the opening (Fig. 1d). Tetrapods were pushed back by around $3\ \mu\text{m}$ after the sperms escaped. The reason for this recoils is the existence of an elastic force that makes the tetrapod arms recover their original shape once the

Fig. 1: (a) SEM images of an array of printed tetrapod microstructures. (b) Schematic illustrating the mechanical release mechanism. (c) Track (red line) of a sperm-hybrid motor under magnetic guidance in the horizontal and vertical planes, respectively. (d) Image sequence of a sperm release process when the arms hit the corner of a PDMS wall. Blue arrows point at the sperm head. Time lapse in min:s.



pushing sperm is gone. Even though there is a substantial diversity in bovine sperm dimensions, swimming behaviors and fabricated tetrapods within a sample, more than 2/3 (15 out of 22) of the coupled motors were shown to successfully release sperm cells. It was reported that the sperm can generate a more powerful force when the head is pushing against an obstacle. In our simulation, the applied force was given according to the maximum pushing force (450 pN) [1] of a sperm in low-viscosity fluid ($2.29 \cdot 10^{-3}$ Pa·s). It was reported that the sperm force can be up to 20 times higher when the sperm is hyperactivated and swims in the viscoelastic fluid of the female reproductive system [2]. Thus, this mechanical trigger system can be expected to perform efficiently under physiological conditions.

Drug loading in sperm

Our previous research demonstrated the capture and guidance/transport of sperm cell towards in vivo fertilization, using tubular [3] and helical [4] microstructures, respectively. Here, the potential of sperm as a drug carrier was investigated. Doxorubicin hydrochloride (DOX-HCl, commercial anti-cancer drug) was employed as a model drug to evaluate the encapsulation performance of sperm cells. DOX-HCl-loaded sperms were obtained by simple co-incubation of DOX-HCl and live sperms. After purification by centrifugation, the incubated sperm sample was redispersed in sperm medium. The fluorescence image shows that majority of the sperm cells were loaded with DOX-HCl (self-fluorescent at 470 nm excitation wavelength), demonstrating an efficiency of 98% with a count of 3502 sperm cells (Fig. 2a). Drug loading efficiency was evaluated by calculating the loading ratio. The drug loading amount was determined by the difference between the initial amount of DOX-HCl before incubation and the residual amount in the supernatant after co-incubation, which were both quantified by their respective fluorescence signals. Figure 2b depicts the drug loading profiles related to DOX-HCl concentration. In the solution with a concentration of 3×10^6 sperms per mL, the loading amount of DOX-HCl increased approximatively linearly with the concentration of DOX-HCl ranging from 10 to 200 $\mu\text{g/mL}$. Hence, the loading ratio remains at around 15% for all concentrations, indicating an average encapsulation of up to 15 pg of DOX-HCl per single sperm cell.

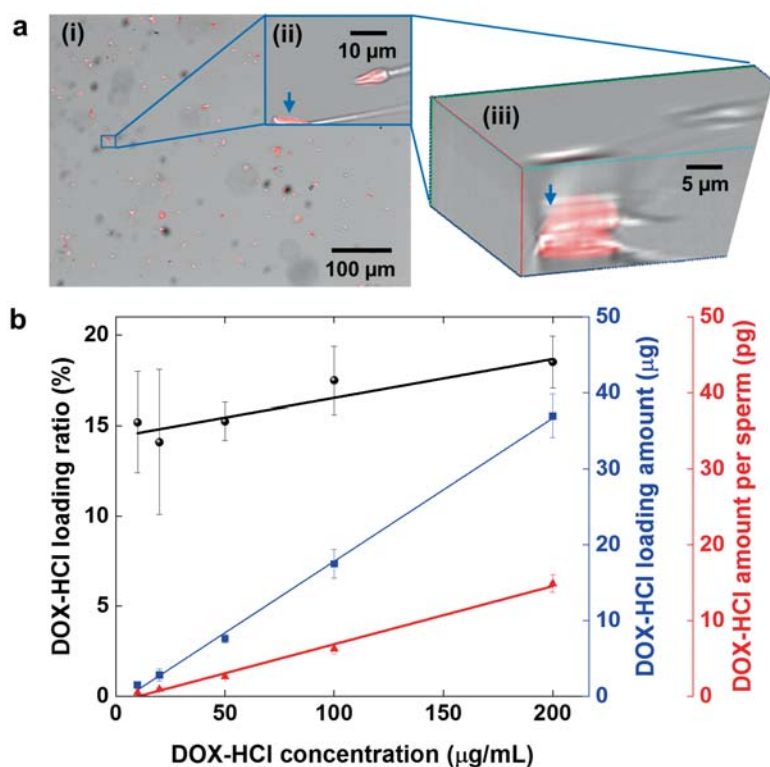
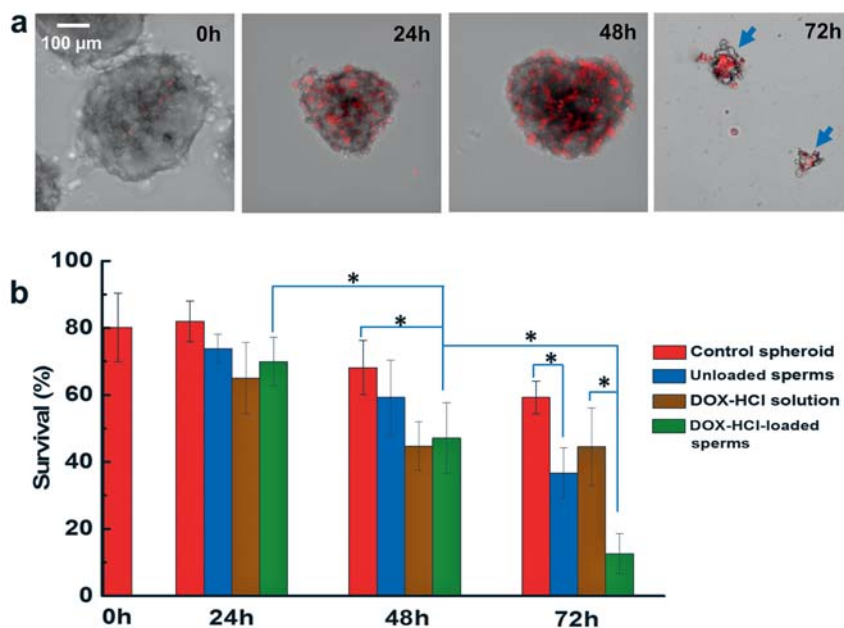


Fig. 2: (a) Fluorescence and brightfield overlay images of DOX-HCl-loaded sperms in (i) 10X and (ii) 40X, (iii) 3D reconstruction of 36 z-stack images with stack separation distance of $0.3 \mu\text{m}$. (b) Plots of the drug loading results versus DOX-HCl concentrations in the loading solution (error bars represent the standard deviation of 4 replicates). The drug loading ratio is obtained by the ratio of the encapsulated DOX-HCl into the sperms by the original amount of DOX-HCl in solution. The drug loading amount is the encapsulated amount of DOX-HCl in $500 \mu\text{l}$ sperm solution at a concentration of 3×10^6 sperms/mL. The drug loading efficiency was evaluated by calculating the loading ratio, *i.e.* the ratio of the amount of drug loaded into sperms to the initial drug amount in solution.

Drug delivery to tumour spheroid

HeLa spheroids were cultured as three dimensional *in vitro* model of cervix cancer. After 24 hours co-incubation of drug-loaded sperms with spheroids, sperms were found not only in the solution, but also in the spheroids as shown in the overlaid z-stack images. This proves the tissue penetration capability of sperms. Cell-killing efficacy was investigated by using SYBR Green LIVE/DEAD kit [5]. Spheroids without any sperms or drugs, with only unloaded sperms and with only DOX-HCl solution were cultured as control experiments. Fig. 3a illustrates the drug transport into a spheroid during 72 h when it was treated with DOX-HCl-loaded sperms. Red fluorescence shows the average intensity of 36 overlaid z-stack images and indicates the presence of DOX-HCl. Gradually, DOX-HCl was found in the center of the spheroid over time. After 72 h, the size of all spheroids decreased owing to drug-induced cell apoptosis. In addition, broken clusters and ruptured cells were observed in the medium. After 72 h, the percentage of dead cells after treatment with DOX-HCl-loaded sperms was significantly higher than in the control samples. Quantitative results of cell counting are shown in Fig. 3b. In the first 24 h of culture, there was no significant change in all groups, while after 48 h, DOX-HCl-loaded sperms showed a cell-killing effect comparable to the DOX-HCl solution treatment with the same amount of DOX-HCl ($1.5 \mu\text{g}$) in the same sample volume ($100 \mu\text{L}$). Unloaded sperms showed a negative effect on HeLa spheroids as well, as the percentage of live cells was only 37%, attributed to the spheroid disintegration induced by the sperm beating and hyaluronidases reaction (from sperm membrane) with the extracellular matrix.

Fig. 3: Cell-killing effect of DOX-HCl-loaded sperms on HeLa spheroids. **(a)** Overlaid z-stack images of HeLa spheroids under treatment by DOX-HCl-loaded sperms. Red color shows the fluorescence of DOX-HCl under an excitation light with a wavelength of 470 nm. Blue arrows point at ruptured spheroids. **(b)** Histogram of the percentage of live cells relative to the total amount of cells at different time points. ($n = 4$, cell count = 10^4 for each sample, $*p < 0.01$, ANOVA analysis).



In order to improve drug availability and to avoid undesired drug accumulation and sperm fusion with healthy cells, a precise transport of drug-loaded sperm cells is required. As performed in a microfluidic channel (Fig. 4a), the experiment showed that coupled sperms swam into the cell cluster after being released, and then the sperm head connected to the cells in the cluster due to membrane adhesion. In another experiment, the hybrid micromotor was guided for around 2 cm through the constriction channel and released sperm in a tumor spheroid. The sperm cell was released into the spheroid when the tetrapod arms hit the outer boundary of the tumor spheroid, and then continued swimming into the spheroid until it was trapped inside. As shown in Fig. 4b, fluorescence intensity at the sperm position decreased while the fluorescent area within the spheroid increased, indicating that DOX-HCl was released from the sperm cell and distributed within the spheroid. SEM images (Fig. 4c) demonstrates the fusion between sperm and HeLa cell. Anterior part of the sperm head was fused with the targeted HeLa cell while

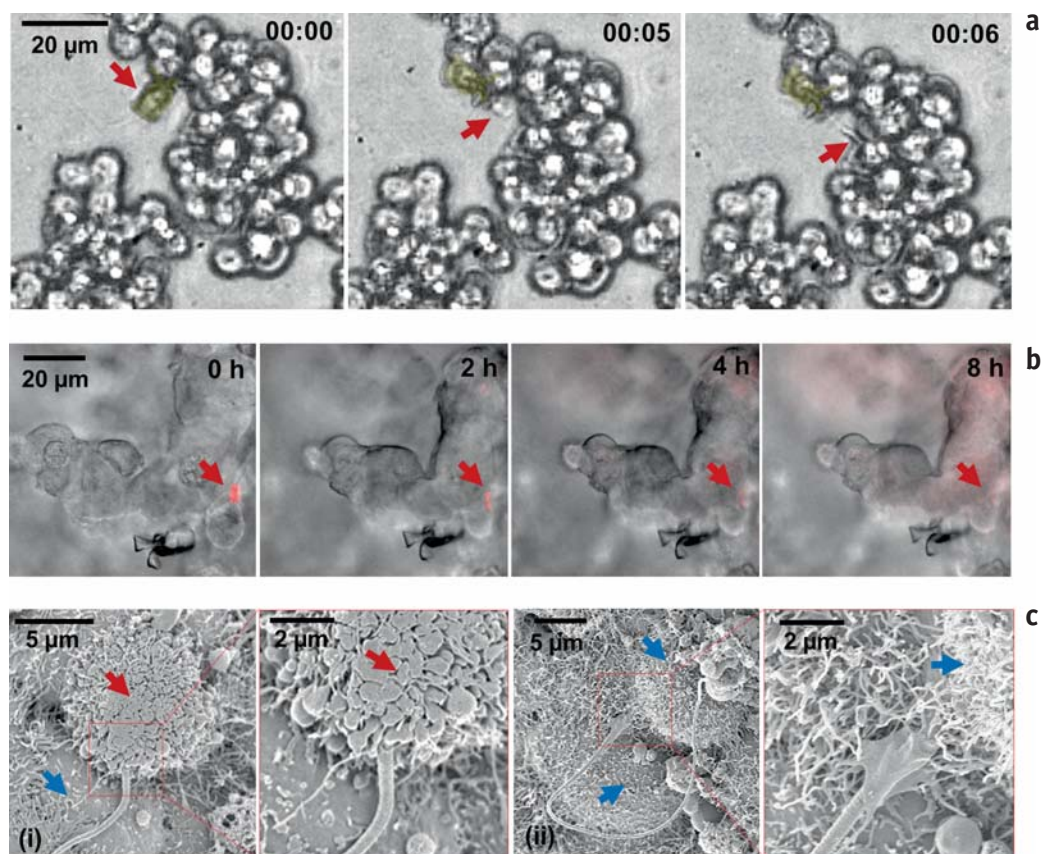


Fig. 4: (a) Image sequence of the sperm release process when the arms hit HeLa cells. Time lapse in min:s. Red arrows point at the sperm head. (b) DOX-HCl distribution in a HeLa spheroid with overlaid z-stack images of the fluorescence channel (20 images with a stack separation distance of 2 μm). Red arrows point at the sperm head. (c) SEM images showing the sperm-HeLa cell fusion. (i) Cell fusion with the DOX-HCl-loaded sperm; (ii) Cell fusion with an unloaded sperm. Red arrows point at a cell in apoptosis and the blue arrows point at live cells.

the midpiece and the flagellum remained outside. Blebs and vesicles were observed on the HeLa cell that was fused with a DOX-HCl-loaded sperm, indicating its death by apoptosis (Fig. 4d, i). Cells fused with unloaded sperms did not show such blebs (Fig. 4d, ii) and thus were presumably still alive, just as unfused cells. Taking advantage of this cell fusion ability of sperm cells, our sperm-hybrid system yields a practical potential to enhance the drug uptake and availability by transporting it from cell to cell (sperm to HeLa cell) without dilution into the extracellular medium.

In summary, a novel drug delivery system based on sperm-hybrid micromotors has been developed. This system exhibits impressive advantages such as, efficient drug entrapment, precise guidance and enhanced drug-uptake by membrane fusion. Although there are still some challenges to overcome before this system can be applied in *in vivo* environments, such as imaging and biodegradability,⁶ sperm-hybrid systems can be envisioned to be applied in *in situ* diagnosis and treatment in the near future.

- [1] Ishijima et al., *Reproduction* 142 (2011) 409.
- [2] Ishimoto et al., *J. R. Soc. Interface*. 13 (2016) 20160633.
- [3] Magdanz et al., *Adv. Mater.* 25 (2013) 6581.
- [4] Medina-Sánchez, *Nano Lett.* 16 (2015) 555.
- [5] Grimes et al., *J. R. Soc. Interface* 11 (2014) 20131124.
- [6] Medina-Sánchez et al., *Nature* 545 (2017) 406.

Funding: SPP Program “Microswimmer”

Metastable phase formation in undercooled Fe-Co melts under terrestrial and microgravity conditions

O. Shuleshova, I. Kaban, W. Löser, S. Ziller, U. Reinhold, D. Lindackers

Abstract: Solidification of deeply undercooled metallic liquids with help of the electro-magnetic levitation technique has been studied at the IFW Dresden since more than 20 years. Currently, in the frame of the ELIPS programme of the European Space Agency, our institute participates in the international EML microgravity experiments comprising parabolic flight campaigns and experiments on board of the International Space Station. Aiming to answer a fundamental question about the influence of the melt convection on solidification process, several industrially relevant materials, such as Fe-Co soft-magnetic alloys, Fe-Ni-Cr stainless steels, and light-weight Ti-Al-based alloys, are studied.

Non-equilibrium solidification on ground

Non-equilibrium solidification of high-performance Fe-Co-based magnetic alloys remains a matter of intensive fundamental research. It is known [1] that above the critical undercooling in a wide composition range these alloys solidify in a metastable phase with the *bcc* structure (δ -ferrite), which subsequently transforms into a stable γ -phase with the *fcc* structure (austenite), Fig. 1. The solidification pathway which involves transient metastable phase formation alters the microstructure and resulting material properties, thus making it crucial to understand the peculiarities of this process. The time between the two nucleation events (transformation delay) strongly depends on the alloy composition as the thermodynamic driving force, defined by the difference between the liquidus temperatures of stable and metastable phases, increases with increasing Co content. Besides, the delay time shows a strong dependence on the level of undercooling and on the melt convection, varying from microseconds at turbulent convective conditions to milliseconds in absence of the melt flow. Under terrestrial conditions, these two extreme cases are realised using different types of levitation techniques such as electromagnetic and electrostatic levitation, EML and ESL respectively [2]. In the EML, liquid metallic sample, held by Lorentz force within a high-frequency induction coil, experiences a strong electromagnetic stirring. On contrast, in the ESL, electrically charged drop, positioned by Coulomb force in a static electric field and heated by a laser, is in almost stagnant state. In both techniques, nucleation and growth of crystal phases are commonly studied by observation of the sample surface with a high-speed video camera, as demonstrated for the $\text{Fe}_{60}\text{Co}_{40}$ alloy in Fig. 2. Due to the release of the latent heat, the rapidly growing solid phase (δ -ferrite) is clearly distinguishable from the undercooled melt, and the secondary, γ -phase (austenite) – from the primary phase. Obviously, the main drawback of the video observations is that the crystalline phases and their sequence cannot be identified directly.

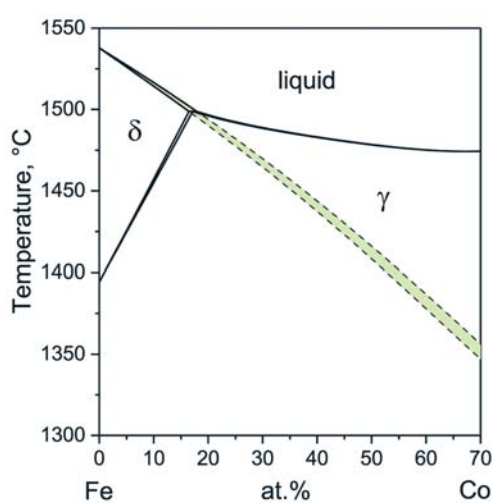


Fig. 1: High-temperature part of the binary Fe-Co phase diagram with metastable extensions of the solidus and liquidus lines of the δ -*bcc* phase (dashed lines) into a stable γ -*fcc* range [1]. Below the metastable extension of the δ -ferrite liquidus line the nucleation of both phases (δ -ferrite and austenite) becomes thermodynamically possible.

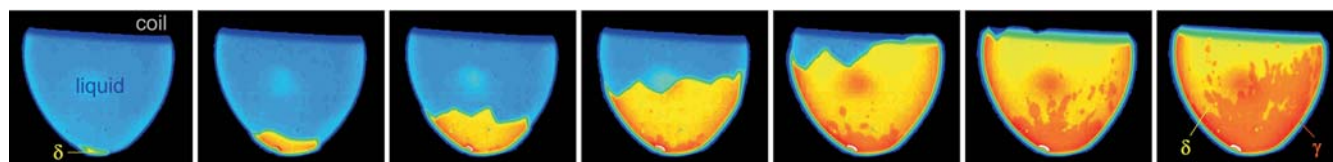


Fig. 2: Heat evolution on the sample surface during solidification of the $\text{Fe}_{60}\text{Co}_{40}$ alloy undercooled to 250 K in ground-based EML (false colour). The primary δ -ferrite (yellow) sweeps across the sample surface with the velocity of about 30 m/s. After a few μs , γ -phase (austenite, orange) nucleates and takes over the whole sample. Images are taken at 30 000 fps (corresponds to approx. 33 μs between each frame).

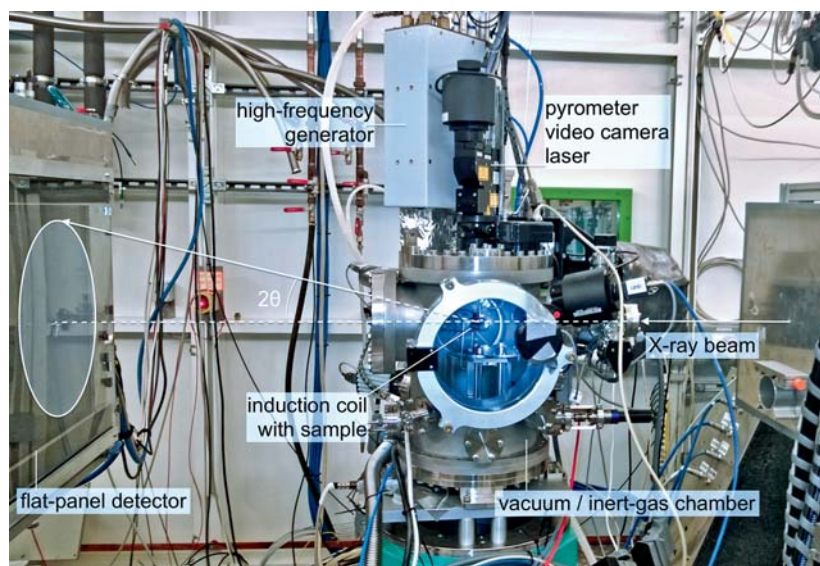


Fig. 3: Mobile electromagnetic levitation facility developed and constructed at the IFW Dresden for solidification and structural studies of undercooled melts: the EML chamber with equipment, X-ray beam layout, and flat-panel detector at the beamline P07 at the PETRA III synchrotron storage ring at DESY Hamburg.

Time-resolved X-ray diffraction on levitated samples

Recently, the metastable formation of the δ -ferrite and its transformation to the stable austenite in the Fe-Co and Fe-Ni-Cr alloys [3] has been studied *in situ* by time-resolved diffraction of synchrotron X-rays conducted at the PETRA III storage ring at the German Electron Synchrotron (DESY) in Hamburg. The samples of about 1 gram mass were processed in a mobile EML facility, specifically developed for solidification and structural investigations through joint efforts of the Research Technology Division and our group (Fig. 3). The vacuum chamber of the IFW-EML enables sample processing either at a high vacuum or in a high-purity inert gas atmosphere. In case of the Fe-Co and Fe-Ni-Cr alloys, the chamber was evacuated to about 10^{-6} mbar and backfilled to about 250 mbar with high-purity He (6N). The positioning and heating of a sample is realized with a water-cooled copper coil powered by a generator operating at a frequency of 230–300 kHz. The cooling is achieved by directing the inert gas streams, the same as the chamber atmosphere, onto the sample surface. The sample temperature is measured with a single colour pyrometer operating at acquisition rate of 100 Hz.

The structure of electromagnetically levitated samples was measured in transmission geometry with monochromatic radiation of 121.3 keV and a beam size of $0.5 \times 0.5 \text{ mm}^2$. The scattered intensity was acquired using a flat-panel Perkin Elmer 1621 X-ray detector providing sufficient counting statistics at the acquisition rate up to 15 Hz. The detector was mounted perpendicular to the direct beam at 0.8 m sample-to-detector distance. The total scattering intensity as a function of the diffraction vector Q was obtained by azimuthal integration of the two-dimensional XRD patterns. Due to a high time-resolution of the PE 1621 detector, formation of the metastable phase in Fe-Co and Fe-Ni-Cr alloys has been for the first time captured *in situ* by XRD. An example of the high-energy XRD data measured during melting and solidification of the $\text{Fe}_{80}\text{Co}_{20}$ alloy, as well as the corresponding thermogram, are shown in Fig. 4.

Microgravity experiments with TEMPUS facility on parabolic flights

To explore the effects of the intermediate levels of induced convection, the undercooling and solidification experiments have been carried out using EML technique under reduced gravity conditions during joint DLR and ESA parabolic flight campaigns operated

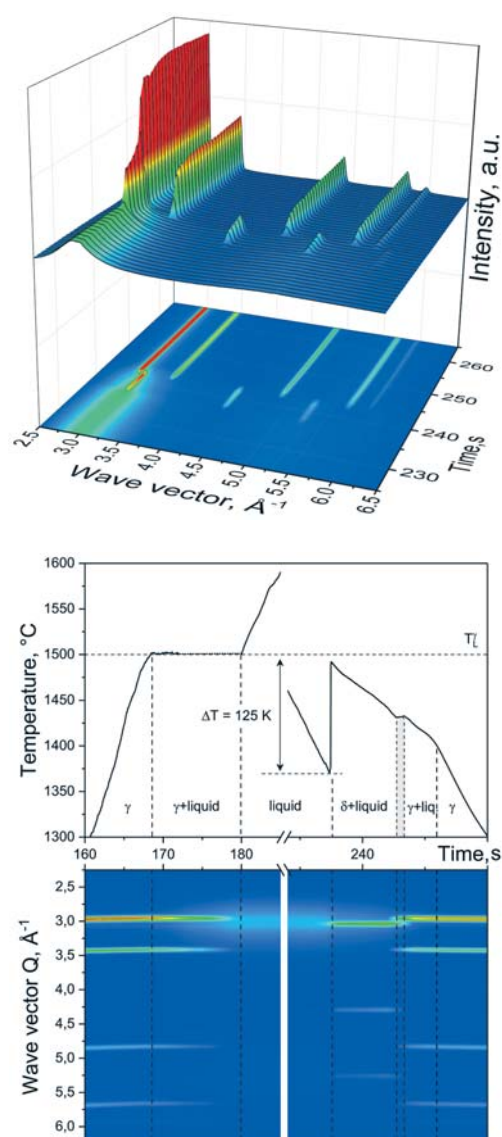


Fig. 4: Synchrotron XRD patterns measured during melting, undercooling and solidification of the $\text{Fe}_{80}\text{Co}_{20}$ alloy: **top panel** – 3D view; **bottom panel** – XRD data synchronised in time with the temperature profile. The primary, metastable δ -bcc phase forms upon solidification from the undercooled melt, and then completely transforms into a stable γ -fcc phase.

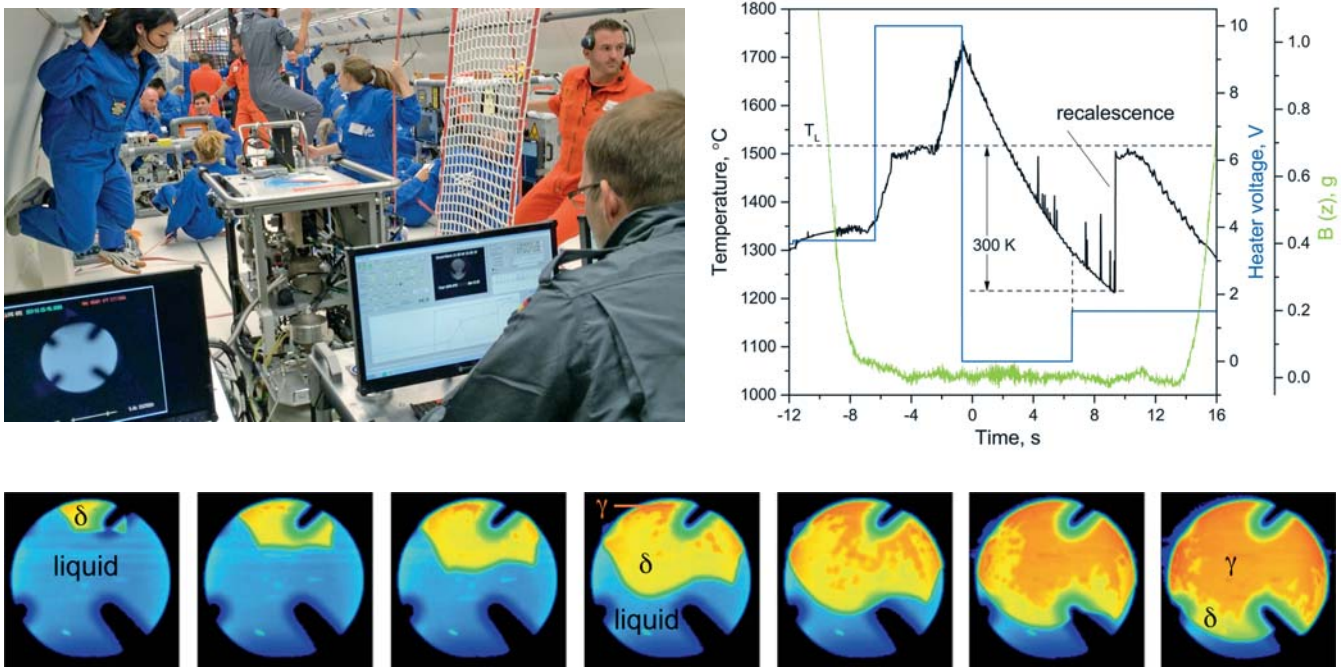


Fig. 5: Top left panel: undercooling experiments with the Fe₅₀Co₅₀ alloy in TEMPUS facility on a parabolic flight; top right panel – temperature profile (black line) acquired during the first parabola along with the values of the heater voltage (blue line) and the μg -level (green line); bottom panel – high-speed imaging of the solidification; rapid recalence event discloses formation of the metastable δ -bcc phase (the time between each frame is 25 μs).

by Novespace SA in Bordeaux, France [4]. During a flight, the Airbus A310 ZERO-G aircraft performs a nose-up manoeuvre with a steep climb for about 20 seconds followed by reducing the engine thrust almost to zero. This injects the aircraft into parabolic free fall for about 22 seconds. Afterwards, the aircraft accelerates again and comes to a steady horizontal flight. These manoeuvres are usually repeated 30 times per flight day. The Airbus A310 ZERO-G is equipped with scientific instruments for different experiments under microgravity conditions, among which one of the largest is the TEMPUS facility (Fig. 5 top left panel); from German “Tiegelfreies elektromagnetisches Positionieren unter Schwerelosigkeit”, meaning containerless electromagnetic positioning under zero gravity [5]. The main difference of the TEMPUS from the ground-based EML is decoupling of the sample positioning and heating, realized by two separate coils inserted into each other. The power supplied to the positioning coil is considerably smaller than that required to levitate a sample in a ground-based EML, which allows minimizing the induced convection in the melt during parabolic flights.

To enhance the accuracy of the solidification studies, the TEMPUS facility has been equipped with a high-speed video camera recently. The extensive experimental program conducted in 2016 and 2017 campaigns included investigations of the Fe-Co alloys. The Fe₅₀Co₅₀ composition has shown excellent performance reproducing the undercooling in two ranges: 85 ± 10 K and 300 ± 10 K (Fig. 5). The solidification experiments have been done at different levels of the residual heater voltage. This provided different stirring conditions in the melt, ranging from laminar to turbulent regime according to the magneto-hydrodynamic (MHD) calculations [7]. However, the detected time between the nucleation of δ -ferrite and austenite has shown a marginal deviation from that measured by EML at 1 g for a given undercooling. This rather unexpected finding suggests that, in contrast to the MHD calculations, the laminar regime has not been completely reached for the Fe-Co system in the parabolic flight experiments. The limiting factor here is the minimal power required for stable positioning of the sample during parabolic flight.

Upcoming microgravity experiments with MSL-EML facility on board of the ISS

In 2014 a new microgravity platform for levitation experiments has become available at the European space laboratory Columbus on board of the International Space Station (ISS). The Material Science Laboratory Electromagnetic Levitator (MSL-EML) is a multi-user facility, developed in a long-term cooperation between the European Space Agency (ESA) and the German Aerospace Centre (DLR) [7]. Maintaining the main features of the TEMPUS facility – decoupling of the sample positioning and heating – the MSL-EML does not impose the time limitations on the experiment duration. More importantly, the monotonous operation under μg allows to further reduce the positioning power so that truly laminar flow conditions within the Fe-based samples can be reached [3]. The on-orbit experiments with defined levels of melt convection for the $\text{Fe}_{60}\text{Co}_{40}$ alloy, delivered and integrated to the MSL-EML in 2017, are planned for April 2018.

- [1] T.G. Woodcock et al., *Calphad* 31 (2007) 256.
- [2] D. M. Herlach and D. M. Matson (eds.), *Solidification of Containerless Undercooled Melts*, Wiley-VCH Verl., Weinheim, Germany, 2012.
- [3] D. M. Matson et al., *JOM* 69 (2017) 1311.
- [4] <http://www.novespace.fr/en/home.html>
- [5] http://www.dlr.de/mp/desktopdefault.aspx/tabid-3106/4785_read-6942
- [6] J. Lee et al., *Metall. Mater. Trans. B* 46 (2014) 199.
- [7] <http://www.dglr.de/publikationen/2015/370222.pdf>

Funding: DLR Space Administration: project PARMAG, contract no. 50WM1546
ESA project MAGNEPHAS, contract no. 4200014980

Cooperation: Institute of Materials Physics in Space, German Aerospace Center, Cologne, Germany; Photon Science group, DESY, Hamburg, Germany; Tufts University, Medford, USA; Ingenieurbüro Dr. Sellger, Ratingen, Germany; VDM Metals, Altena, Germany

Research Area 3

Magnetism in iron nanoislands tuned by epitaxial growth and magneto-ionic reactions

K. Leistner, M. Yang¹, J. Zehner, K. Duschek, S. Oswald, A. Petr, C. Damm, K. L. Kavanagh¹, K. Nielsch

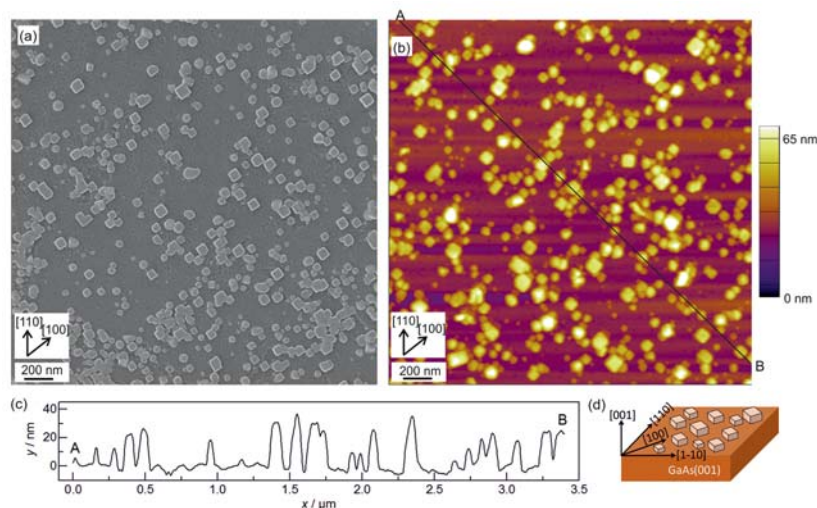
Abstract: The control of interfacial properties offers genuine routes to tailor magnetism at the nanoscale. Epitaxial growth on suitable substrates is one approach to define the shape and orientation of nanobjects. We achieved individual cuboid iron nanoparticles by taking advantage of epitaxial growth during electrodeposition on GaAs. The interplay between metal nuclei growth and hydrogen evolution is found to be decisive for the epitaxial interface formation. While in this case, electrochemistry at the interface is exploited to irreversibly define the shape, structure and magnetism of the iron nanoparticles, reversible manipulation of solid/liquid electrolyte interfaces can be achieved by magneto-ionic reactions. We, for the first time, utilized iron/iron oxide nanoislands as magneto-ionic starting material. Voltage-controlled ON/OFF switching of magnetism is achieved in this case, which presents a highly promising path for the development of tunable and energy-efficient magnetic nanodevices.

Epitaxial iron nanocuboid assemblies

Iron/iron oxide nanoparticles are of great technological interest because they possess distinct electronic, catalytic and magnetic properties while at the same time they are abundant and non-toxic. Conventional synthesis routes for iron/iron oxide nanoparticles are often hampered by the toxicity of precursors, complicated reaction pathways and/or the need for high temperatures and reaction gas pressures. Electrodeposition is a room-temperature synthesis method that provides a competitive technological alternative to gas phase and vacuum techniques.

We investigated the electrodeposition of iron nanoparticles on GaAs(001) to achieve epitaxial growth. The use of an electrolyte with low iron ion concentration (0.01 mol/l FeSO_4) and a short deposition time (10 s) resulted in the formation and growth of individual Fe nuclei. For electrochemical conditions with dominating hydrogen evolution, the deposited nanoparticles exhibit a faceted shape, crystallographic alignment and notable magnetic in-plane anisotropy. The beneficial role of the hydrogen evolution on the epitaxy is found to be related to the effect of hydrogen adsorption during the Fe/GaAs interface formation [1]. In consequence, we applied a compliance voltage during immersion of the substrate to boost the hydrogen evolution at the very start of the deposition. This lead to the formation of epitaxial nanocuboids that are aligned throughout the substrate [2]. The resulting surface morphology is shown in Fig. 1. The

Fig. 1: Morphological analysis of iron nanoparticles electrodeposited on GaAs(001). (a) Surface secondary electron image by helium ion microscopy, (b) Atomic force microscopy image, (c) Atomic force microscopy height profile along the line AB as indicated in (b), and (d) schematic view of the orientation relationship between the iron nanoparticles and the GaAs(001) substrate.



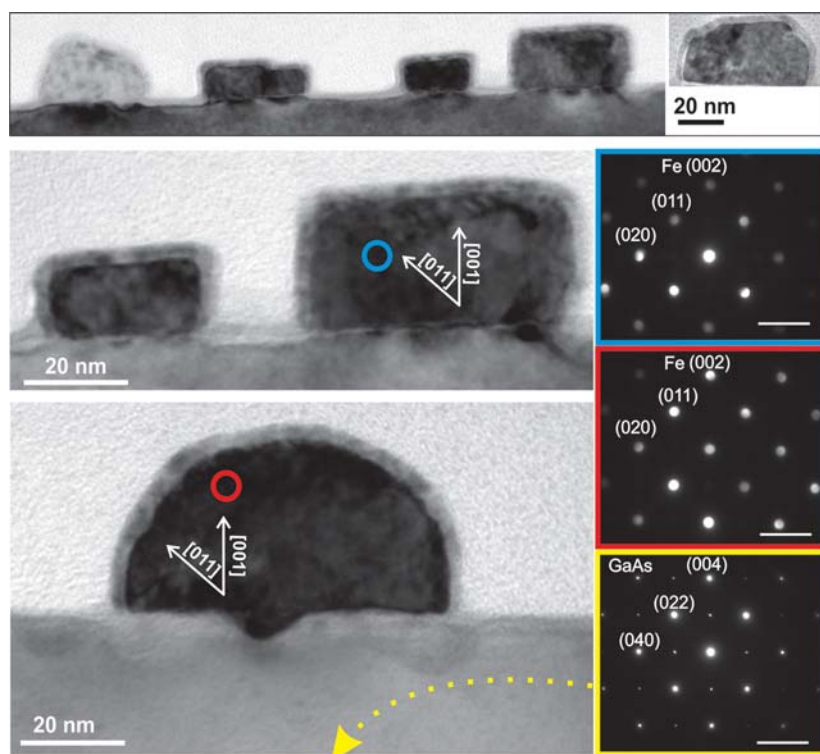


Fig. 2: Cross-sectional bright field transmission electron microscopy images of typical iron nanoparticles on GaAs(001) with nanodirection patterns from the indicated regions and a selected area diffraction pattern of the substrate. The scale bars in the diffraction patterns are 5 nm^{-1} . The diffraction patterns of the nanoparticle core give lattice plane distances of 0.205 nm for the (011) planes and 0.145 nm for the (002) planes, agreeing with those of bcc iron (0.205 nm and 0.143 nm, respectively).

iron nanocuboids exhibit side lengths between 30 and 80 nm and heights of up to 30 nm. The shape and alignment of these nanoparticles, with respect to the GaAs substrate orientation, agrees with epitaxial cube on cube growth of body centered cubic (bcc) Fe(001) on GaAs(001) with predominantly $\{100\}$ facets. The presence of an epitaxial crystalline bcc iron core is confirmed by cross-sectional analytical TEM investigations (Fig. 2) for all shapes. This finding is notable, since it reveals that the round- and square-based nanoparticles only differ in shape, but not in structure and crystallographic alignment. The nanoislands are covered by a 2–3 nm crystalline Fe_3O_4 shell, which preserves the iron core in ambient conditions. The ferromagnetic resonance spectra in Fig. 3 show the high-frequency magnetic response of the electrodeposited nanoparticles. A clear shift to a higher resonance field is observed for magnetization along the [110] axis in comparison to the [100] axis. Thus, the [100] axis is magnetically easier than the [110] axis, which is as expected from the cubic magnetocrystalline anisotropy of bcc iron.

The achieved electrochemical epitaxial growth of iron nanoparticles presents a novel and competitive fabrication route for stable iron nanoparticles attached to a substrate. This is especially favorable for catalytic and electronic applications requiring a conductive substrate. The aligned nanoparticles achieved in the present study also offer unprecedented routes for the fundamental study of the magnetic and electronic properties of individual nanoobjects. They will be helpful for the experimental validation of simulations describing arrays of nanoparticles with a single orientation and the study of magnetic spin structures evolving at reduced dimensions for specific shapes.

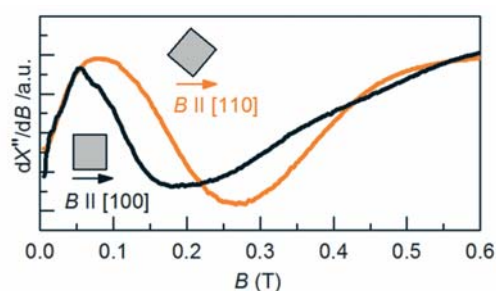


Fig. 3: In-plane ferromagnetic resonance spectra for iron nanoparticles electrodeposited on GaAs (001) for the magnetic field B applied along the [110] and [100] directions.

Magneto-ionic ON/OFF switching of iron nanoislands

The great prospects for low-power magnetoelectronic devices have triggered significant research activities in the field of voltage-control of magnetism. Magneto-ionic effects have recently been proposed to achieve voltage-programmable magnetic materials [3,4]. The magneto-ionic effect relies on voltage-triggered charge transfer reactions in solid or liquid electrolyte-gated architectures. For instance, a repeatable electrochemical transformation between metal and oxide can be exploited to manipulate magnetic metals at room temperature and via the application of only a few volts. This makes the magneto-ionic approach very competitive to many other magnetoelectric mechanisms such as multiferroics and magnetic semiconductors.

All previous studies related to magneto-ionic effects in metal films utilized physical methods such as sputtering or molecular beam epitaxy for film preparation. We show that ultrathin iron nanostructures suitable for magneto-ionic effects can be efficiently prepared by electrodeposition in ambient conditions. Iron is electrodeposited on a Au/Cr/SiO₂/Si substrate. The 3D growth mode leads to a nanogranular morphology when the deposition is stopped prior to coalescence. Upon removal from the electrodeposition setup natural oxidation sets in and iron/iron oxide nanoislands are present as starting material.

To achieve voltage-control of magnetism in these electrodeposited nanoislands, an aqueous electrolyte containing 1 mol/l KOH was chosen that was already proven to be suitable for magneto-ionic effects in sputter-deposited continuous FeO_x/Fe films [5]. The magneto-ionic reactions are directly linked to the electrochemical processes at the solid/liquid interface [6]. The cyclic voltammogram in Fig. 4 shows that the electrochemical reduction to metallic iron, the subsequent oxidation to iron oxyhydroxide, and the formation of the passive layer is achieved for the nanoislands.

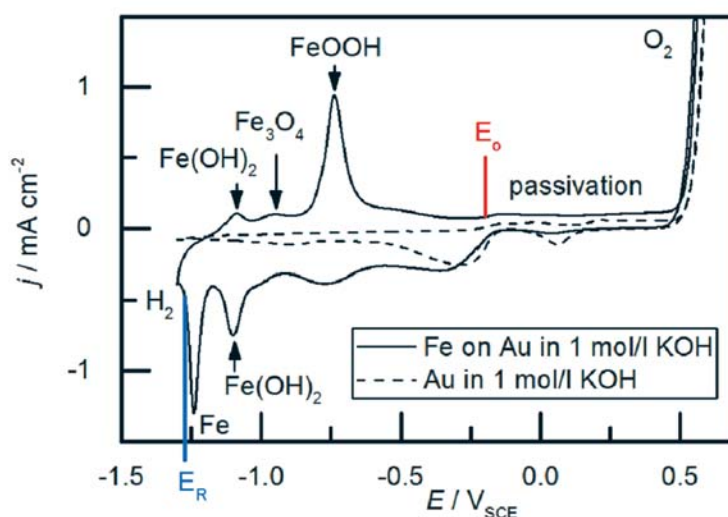


Fig. 4: Cyclic voltammogram of electrodeposited iron nanoislands on Au polarized in 1 mol/l KOH. The cathodic and anodic current peaks show the electrochemically induced phase transformations. The potentials suitable for reversible oxidation and reduction between a passive layer composed of iron oxides and metallic iron are indicated.

The nanostructures were then repeatedly polarized in the electrolyte at suitable reduction and oxidation potentials, E_{red} and E_{ox} , respectively. The magneto-ionic changes were probed by in situ anomalous Hall Effect (AHE) measurements. The AHE curves obtained during application of E_{red} and E_{ox} are displayed in Fig. 5. A strong dependence of the maximum AHE resistance, which scales with the saturation magnetization, on the applied

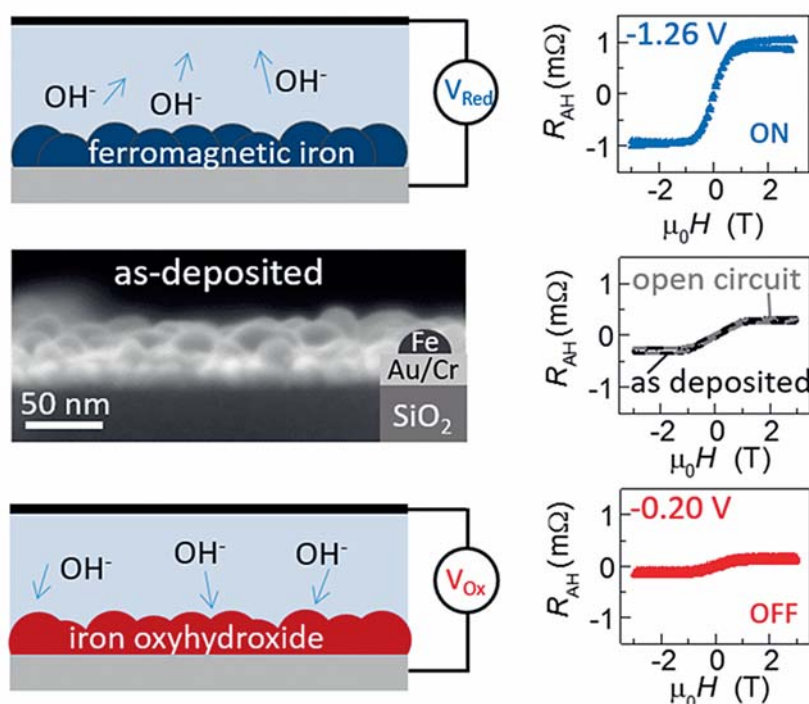


Fig. 5: Magneto-ionic ON/OFF switching of magnetism in electrodeposited iron nanoislands (scanning electron microscopy cross-sectional image in the middle) as probed by in situ Anomalous Hall Effect measurements (on the right). It is based on the voltage-triggered and reversible transformation between the weakly or non-magnetic oxide state and the ferromagnetic iron metal (sketched on the left side bottom and top, respectively) that can be achieved in the liquid-electrolyte-gated architecture.

potential is evident. The switching between E_{red} and E_{ox} leads to a repeatable reduction to the ferromagnetic metal iron and oxidation to a non-ferromagnetic oxide phase with significantly lower magnetization. Almost complete ON/OFF switching is achieved. The effect is larger than in continuous sputtered films of similar nominal thickness [5], which can be seen as a direct result of the higher interface/volume ratio of the nanoisland structures. Thus, for the first time, the crucial impact of the morphology on the magneto-ionic effects could be elucidated. The electrochemical synthesis of magneto-ionic starting material is especially favorable because tunable magnetic material can also be deposited in channel walls and recesses. This may become important when applying magneto-ionically active layers, e.g., in magnet-based nanofluidic devices.

The presented magneto-ionically active electrodeposited nanostructures demonstrate an all-electrochemical approach for voltage-control of magnetism that does not require vacuum technologies. This opens up an important energy-saving pathway that may bridge the gap between tunable electromagnets involving Joule heating and non-tunable permanent magnets. On the base of magneto-ionic manipulation, unprecedented low-power yet tunable magnet-based nanoscale devices come within reach.

- [1] K. Leistner et al., J. Electrochem. Soc. 165 (2018) H3076.
- [2] K. Leistner et al., Nanoscale 9 (2017) 5315.
- [3] K. Leistner et al., Phys. Rev. B 87 (2013) 224411.
- [4] U. Bauer et al., Nat. Mater. 14 (2015) 174.
- [5] K. Duschek et al., APL Mater. 4 (2016) 032301.
- [6] K. Duschek et al., Electrochem. Comm. 72 (2016) 153.

Funding: This work is partially supported by the DFG (project no. LE2558/1-1), NSERC, 4D Labs, and the excellence program initiative of the IFW Dresden.

Cooperation: ¹Department of Physics, Simon Fraser University, Burnaby, Canada; Institute of Physics, University Kassel; Helmholtz-Zentrum Dresden-Rossendorf; Shanghai Institute of Microsystem and Information Technology, Shanghai, China

Addressable and Color-Tunable Piezophotonic Light-Emitting Stripes

Y. Chen, Y. Zhang, D. Karnaushenko, L. Chen¹, J. Hao¹, F. Ding, O. G. Schmidt

Abstract: As an emerging solid-state lighting (SSL) technology, piezophotonic light-emitting devices have great potential for future micro- and nanoscale systems due to the added functionality provided by the electromechanical transduction coupled with the ability of light emission [1]. The piezophotonic effect is a two-way coupling effect between piezoelectricity and photoexcitation properties, where the strain-induced piezoelectric potential modulates the band structure within piezoelectric phosphors, and thus tunes/controls the relevant optical process [2]. The realization of light emission stimulated by the piezophotonic effect is to initiate the mechanoluminescence (ML) process replacing p-n junction based light-emitting diodes (LEDs) for general lighting purposes. ML emission triggered by mechanical sources offers an enticing range of possibilities.

Piezophotonic device fabrication

The most common and controllable piezophotonic luminescence devices are composed of ML phosphor coated on the top of piezoelectric actuators. Relaxor ferroelectric single-crystal $\text{Pb}(\text{Mg}_{1/3}\text{Nb}_{2/3})\text{O}_3\text{-PbTiO}_3$ (PMN-PT) has superior piezoelectric coefficients ($d_{33} > 1500$ pm/V) and electromechanical coupling factors ($k_{33} > 90\%$) along the [001] crystallographic direction [3].

Piezophotonic light-emitting sources based on PMN-PT bulk are severely restricted by many challenges, such as a high voltage burden (up to hundreds of volts), low integration density and micro-manufacturing difficulties. Also, it is difficult to integrate many piezoelectric elements with different patterns together on a single chip.

In this work, a patterned single-crystal PMN-PT thin film of $7\text{ }\mu\text{m}$ thickness is obtained as the active layer. Zinc sulfides doped with Mn, Cu and Al ions (ZnS:Mn and ZnS:Cu,Al) were selected as the phosphors due to their intense and durable ML characteristics[4]. The utilization of piezoelectric thin films strongly reduces the voltage burden, and allows us to take advantage of mature micro-manufacturing techniques.

Figure 1a schematically illustrates the device fabrication process. The (001)-oriented single-crystal PMN-PT was bonded on Si. Then it was mechanically grinded down to tens of microns. We further etched the PMN-PT film down to $7\text{ }\mu\text{m}$ thickness with RIE. Afterwards photolithography and gold sputtering were used to define the array of top

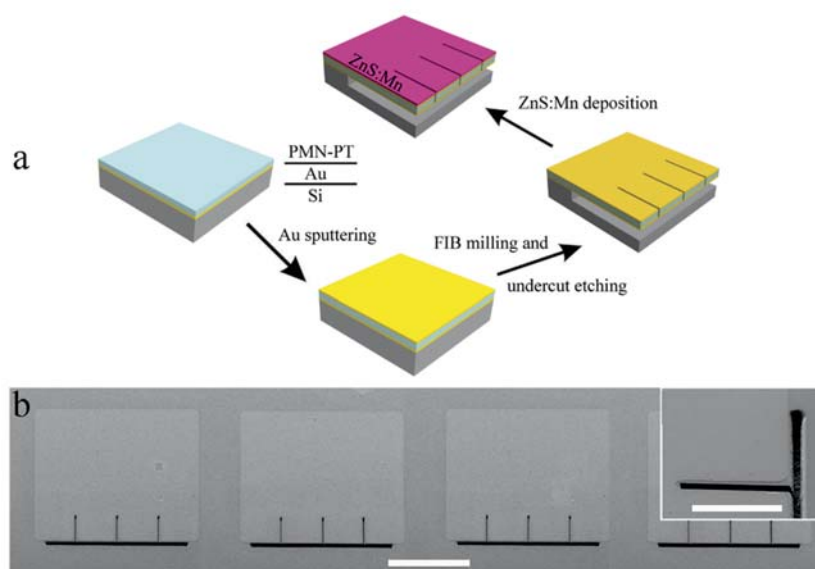


Fig. 1: (a) Schematic illustration of the device fabrication process. (b) SEM image of an array of patterned single-crystal PMN-PT actuators. Scale bar, $50\text{ }\mu\text{m}$. The inset shows the details of the trenches in the PMN-PT thin film. Scale bar, $20\text{ }\mu\text{m}$.

contacts. We used focused ion beam (FIB) to etch the trenches into the single crystal PMN-PT thin film around the top contacts. Figure 1b shows the scanning electron microscopy (SEM) image of an array of the etched PMN-PT actuators on Si. Each element has a footprint of $120\mu\text{m} \times 100\mu\text{m}$. The inset of Fig. 1b shows the details of the trenches in the film. The trenches are deep enough to penetrate into the silicon substrate, facilitating subsequent undercut etching. The wet chemical undercut etching was used to release the single-crystal PMN-PT thin film from the substrate. As shown in SEM image, no cracks on the PMN-PT were found after the processing. The distinctive cantilever geometry of the single-crystal PMN-PT thin film is likely to be important to reduce the clamping strain and improve the piezoelectric response. ZnS:Mn thin films were afterwards deposited onto the PMN-PT actuators.

Piezoluminescence characterization

Figure 2 shows the piezoluminescence intensity as a function of the frequency and magnitude of the applied voltage. The luminescence intensity increases linearly when increasing the frequency from 25 to 150 Hz as shown in Fig. 2a and 2b. The luminescence intensity is also enhanced by an increase of the applied voltage from 8 to 24 Vpp (Fig. 2c). Photographs of tunable light emissions from the ZnS:Mn stripe is demonstrated in Fig. 2e. The piezophotonic device reaches a luminous efficacy of 1.2 lm/W at 24 Vpp and 150 Hz. The brightness increased linearly with the increasing frequency as shown in Fig. 2e. The luminance values were found to be 20.8 cd/m^2 , 41.5 cd/m^2 , and 64.2 cd/m^2 , at the frequencies of 50 Hz, 100 Hz, and 150 Hz, respectively, while the applied voltage kept at 24 Vpp.

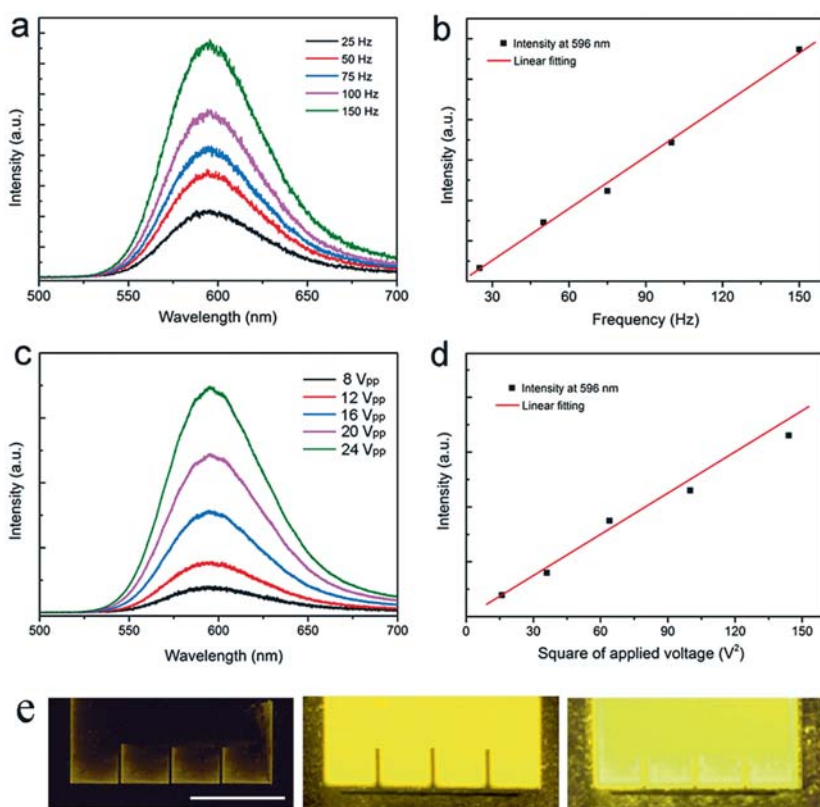


Fig. 2: (a) Luminescence spectra at different frequencies under fixed voltage 20 Vpp. (b) Peak intensity at 596 nm versus applied frequency. (c) Luminescence spectra under different voltage amplitudes at 150 Hz. (d) Peak intensity at 596 nm versus square of amplitude. (e) Light-emitting images of ZnS:Mn stripes operating with 24 Vpp, and at varying frequencies of 50, 100, and 150 Hz (left to right, respectively). Scale bar indicates $50\mu\text{m}$.

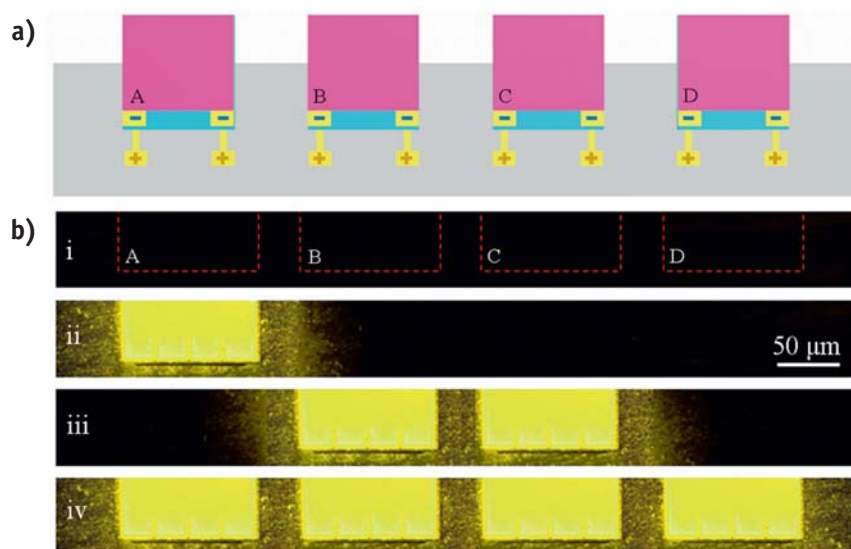


Fig. 3: (a) Schematic illustration of the prototype device. Four individual light-emitting units are addressed: A, B, C, and D, from left to right, respectively. Each unit incorporates ZnS:Mn layer (purple), PMN-PT thin film actuator (blue), and top and bottom Au electrodes (yellow). The whole device is integrated on Si (gray). (b) Demonstration of four representative addressable light emission states. Switch-off of all units (i); Trigger unit A solely (ii); Turn on units B and C simultaneously (iii); Turn on all units (iv).

The ability to individually control the chip-integrated piezophotonic components is highly desirable. Incorporating such components onto a Si platform should be appealing for developing on-chip piezophotonic devices. The integration of such devices on PMN-PT bulk has been challenging because of the large footprint of individual light-emitting elements, high voltage burden, and high production costs. Here, we demonstrate a prototype piezophotonic device to circumvent these challenges. Figure 3a shows the sketch of such a device. Four light-emitting units are encoded from A to D, which can be electrically triggered independently. Each unit can produce local deformation not influenced by others. Figure 3b demonstrates the addressable characteristics of the device. When all the external voltage is switched off, there is no light-emission observed from all the four units (situation i). To individually address each unit, we first trigger unit A with 24 Vpp at 150 Hz and bright light can be observed in unit A only (situation ii). In situation iii, we switch off unit A, and excite units B and C. As shown in Fig. 3b, only units B and C glow. Situation iv shows that four elements are triggered simultaneously. The addressability shown here promises more flexibility for many intriguing applications, especially when used as light sources or displays with each unit as active pixel.

Piezoluminescence color manipulation

The ability to manipulate the color of the piezophotonic luminescence is highly desirable. By regulating the mixing ratio of two or more ML materials can realize color tuning. However, it is essentially an irreversible and ex-situ method. Previous research reported that the ML spectrum of ZnS:Cu,Al shifted to short wavelength as the strain rate was increased [5] due to the increasing recombination of the electrons in the conduction band (or shallow donor level) and holes in the valence band (or the e state of Cu) [6]. The normal mechanical stretching-releasing system can only provide the strain rate up to several hundred Hertz. Thus shifts of only several nanometers were observed. Here, our electrical-triggered PMN-PT based device can be stimulated up to megahertz, which is suitable for realizing color manipulation of ML from ZnS:Cu,Al contained phosphor layers. Figure 4a shows the spectral shape of ZnS:Cu,Al under the frequencies increased from 50 Hz to 100 kHz, the applied voltage was kept at 20 Vpp. The spectra are normalized to the peak of ZnS:Cu,Al at 522 nm for intuitively showing the changes. With the strain rate increased,

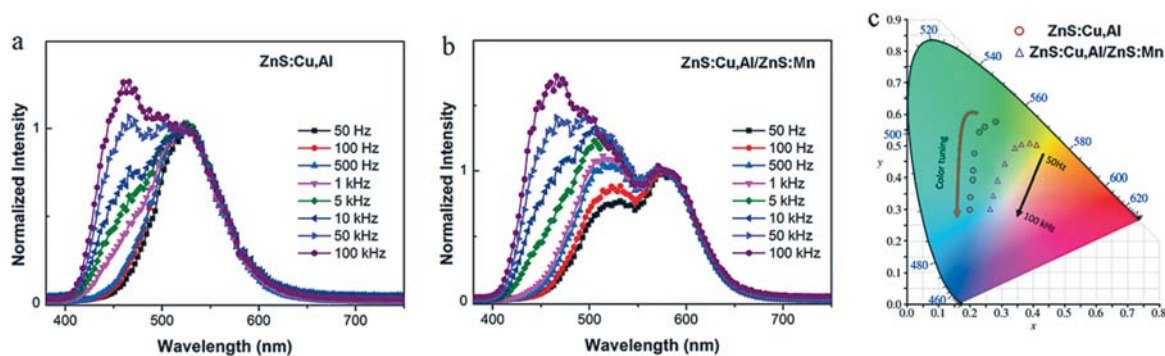


Fig. 4: The normalized piezophotonic luminescence spectra under the selective frequency conditions (a) ZnS:Cu,Al film and (b) ZnS:Cu,Al/ZnS:Mn bilayer film. (c) The CIE coordinates showing the color tuning with the frequency increasing.

the light emission of ZnS:Cu,Al around 460 nm enhances and gradually dominates the emission. The calculated Commission Internationale de L'Eclairage (CIE) coordinates clearly suggest the shift from (0.27, 0.57) at 50 Hz to (0.20, 0.30) at 100 kHz (Fig. 4c). In order to obtain a more colorful patterned device, a bilayer film composed of ZnS:Cu,Al and ZnS:Mn was deposited on the PMN-PT. Fig. 4b shows the normalized spectra of ZnS:Cu,Al/ZnS:Mn bilayer. The calculated spectra is normalized by the peak wavelength of the ZnS:Mn. Results have shown that the spectral shape of ZnS:Mn is unchanged with increasing frequency, which is consistent with previous reports. While, the intensity of ZnS:Cu,Al clearly increases. The calculated CIE coordinates shift from (0.39, 0.50) to (0.26, 0.31) with the frequency increasing from 50 Hz to 100 kHz for the ZnS:Cu,Al/ZnS:Mn bilayer emission. As a result, a color-tunable light emission from orange to blue-green is obtained. These results imply that continuous and reversible controllable color manipulation can be achieved through real-time regulating the strain actuating rate.

- [1] F. Xue et al., *Adv. Mater.* 28, (2016) 3391.
- [2] X. Wang et al., *Adv. Mater.* 27, (2015) 2324.
- [3] Y. Chen et al., *Nano Energy* 31 (2017) 239.
- [4] S. Jeong et al., *Adv. Mater.* 25, (2013) 6194.
- [5] W. Shin et al., *ACS Applied Materials & Interfaces* 8 (2016) 1098.
- [6] S. Jeong et al., *Appl. Phys. Lett.* 102 (2013) 051110.

Funding: DFG Research Fellowships: DI 2013/2-1; BMBF: Q.Com-H(16KIS0106)

Cooperation: ¹Department of Applied Physics, The Hong Kong Polytechnic University

A quantum material that emits pairs of entangled photons on demand

R. Keil, M. Zopf, Y. Chen, B. Höfer, F. Ding, O. G. Schmidt

Abstract: Polarization-entangled photons play an essential role in many quantum communication concepts. Semiconductor quantum dots are among the leading candidates for the deterministic generation of entangled photons, offering pure single photon emission with high internal quantum efficiency. However, most investigated quantum dot species suffer from low yield, low degree of entanglement and poor wavelength control.

We show that with a new generation of GaAs/AlGaAs quantum dots grown by local droplet etching, a large solid-state emitter ensemble of highly entangled photon pairs can be obtained - without any post-growth tuning. Under resonant two-photon excitation, all measured dots emit single pairs of entangled photons with ultra-high purity, high degree of entanglement and ultra-narrow wavelength distribution at rubidium transitions. Therefore, this material system is an attractive candidate for the realization of a solid-state quantum repeater - among many other key enabling quantum photonic elements.

Solid-state ensemble of highly entangled photon sources at rubidium atomic transitions

Single pairs of entangled photons are a key element in quantum information technology. They enable secure quantum communication [1], robust qubit transfer [2] and can distribute entanglement between separate computation nodes, rendering even a “quantum internet” possible [3].

However, deterministic sources of highly entangled photon pairs remain a challenge. So far, photons generated from spontaneous parametric down conversion [4] have been used to demonstrate various entanglement-based concepts, but this process is characterized by Poissonian statistics, i.e. a tradeoff has to be made between source brightness and multi-photon emission probability, fundamentally limiting their applicability in complex quantum protocols.

Semiconductor quantum dots (QDs) are among the leading candidates to overcome these restraints. The cascaded decay of the biexciton (XX) via the intermediate exciton states (X) generates single, polarization-entangled photon pairs $|\psi^+\rangle = \frac{1}{\sqrt{2}} (|HH\rangle + |VV\rangle)$, where H and V denote horizontal and vertical linear polarization. However, anisotropies in strain, composition and shape can reduce the QD symmetry, resulting in two non-degenerate X states split by the fine structure splitting (FSS). The resulting two-photon state has the form $|\psi\rangle = \frac{1}{\sqrt{2}} (|HH\rangle + e^{iT_1 S/\hbar} |VV\rangle)$, where T_1 is the radiative lifetime of the exciton and S the FSS. To obtain a high degree of entanglement, the experimental strategies are to reduce the FSS S and/or the exciton lifetime T_1 .

Despite various investigated material systems and architectures [5-8], most QD species suffer from extremely low yield, low degree of entanglement and poor wavelength control, blocking the way towards scalable applications.

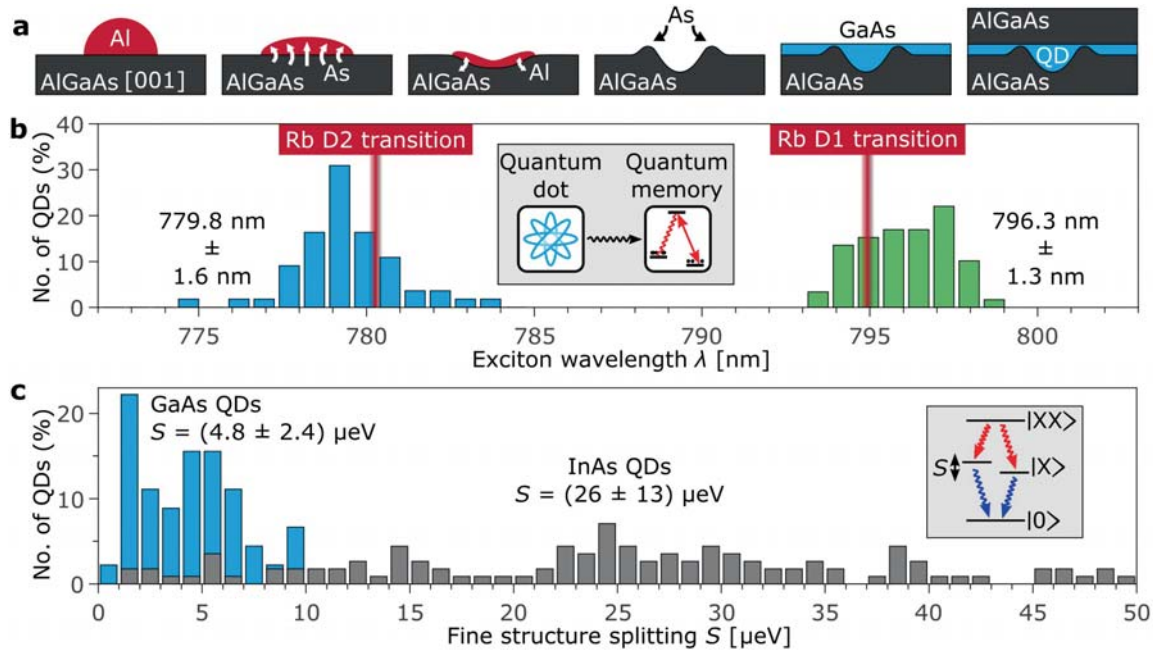
In this work, we show that a large ensemble of as-grown polarization-entangled photon emitters can be obtained, using an emerging family of GaAs/AlGaAs QDs grown by local droplet etching [9]. These QDs exhibit very small FSS and short radiative lifetimes. Under pulsed resonant two-photon excitation all measured QDs emit single pairs of entangled photons with ultra-high purity and high degree of entanglement (fidelity F up to 0.91). These QDs offer a deterministic wavelength control and ultra-narrow wavelength distribution, specifically tailored to match the optical transitions of rubidium. Thereby, we envision a hybrid quantum repeater that incorporates QD-generated entangled photon qubits interfaced with a rubidium-based quantum memory.

Sample growth

The QDs in this work are fabricated by solid-source molecular beam epitaxy. Fig. 1a shows a sketch of the processes involved in the QD formation. Al is deposited on AlGaAs, forming liquid droplets. Driven by concentration gradients, dissolution of As and diffusion of Al induce the formation of nanoholes with high in-plane symmetry, which crystallize under As atmosphere and are then filled with GaAs and overgrown by AlGaAs to obtain QDs with three-dimensional carrier confinement.

The QD emission wavelength depends on the GaAs infilling amount. Envisioning a hybrid interface between QD and an atom based quantum memory several samples with varying GaAs amount have been grown, targeting the D1 and D2 transition of rubidium at a wavelength of 794.9 and 780.2 nm. Fig. 1b shows the exciton wavelength distribution for two samples with 2 nm (blue) and 2.75 nm (green) GaAs. Statistics on over 50 QDs show an unprecedented control on the central emission wavelength and distribution with mean values of 779.8 ± 1.6 nm and 796.3 ± 1.3 nm.

The symmetric shape in combination with negligible composition intermixing and a strain-free interface between GaAs and AlGaAs suggest low FSS values. Fig. 1c shows the statistical distribution of the FSS for the GaAs/AlGaAs QD sample studied in this work (blue) and a typical InAs/GaAs QD sample (grey) for 45 and 114 measured dots. The GaAs QDs feature an average FSS of only 4.8 ± 2.4 eV that is among the best values reported for any QD species and is a prerequisite for highly polarization-entangled photon emission.



Resonant excitation of the biexciton

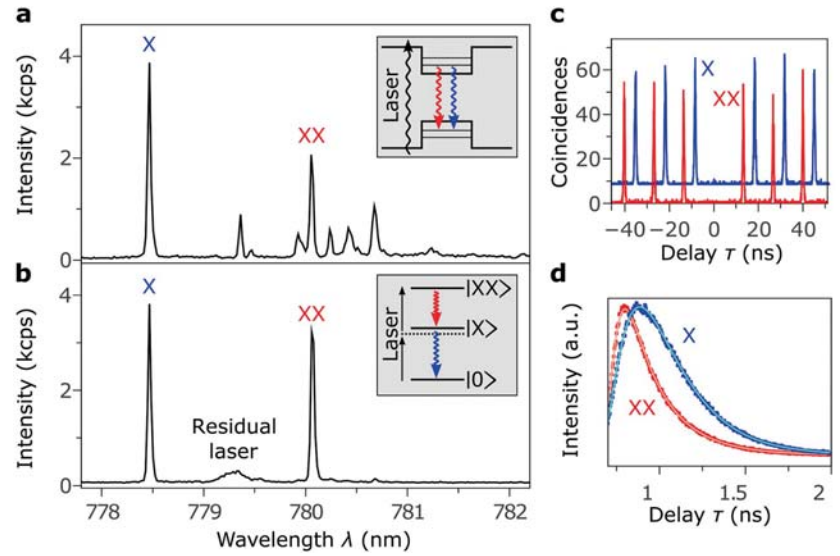
A QD emitting close to the Rb D2 transition (~ 780.2 nm) is optically excited by a laser pumping the surrounding higher-bandgap AlGaAs. The resulting spectrum (Fig. 2a) shows the exciton (X) at $\lambda = 778.5$ nm and the biexciton (XX) transition at $\lambda = 780.1$ nm among other excitonic states.

In order to drive the XX transition coherently, the two-photon resonance of the XX state is addressed by a pulsed laser. The laser background can be effectively suppressed using notch filters, resulting in a very pure spectrum (Fig. 2b).

To verify pure single-photon emissions from XX and X, we perform an autocorrelation measurement using a Hanbury Brown and Twiss setup. The autocorrelation function $g^2(\tau)$ plotted over the photon arrival delay τ shows a clear absence of coincidences at zero delay and proves the high purity single-photon emission (Fig. 2c).

Fig. 1: Growth of highly homogeneous GaAs/AlGaAs quantum dots. **(a)** Schematic of involved processes during the quantum dot (QD) formation. **(b)** Exciton emission wavelength distribution for two different samples tailored for coupling to atomic transitions of rubidium. Inset: sketch of envisioned interface between QD and an atomic quantum memory. **(c)** Occurrence of the exciton fine structure splitting S , comparing the GaAs/AlGaAs QDs (blue) with InAs/GaAs QDs (grey). Inset: scheme of the biexciton decay.

Fig. 2: Resonant excitation of the biexciton state in GaAs/AlGaAs quantum dots. **(a)** QD emission spectrum for above-band excitation, showing dominant exciton (X) and biexciton (XX) emission. **(b)** Resonant excitation of the XX state using a two-photon excitation scheme. The residual laser is suppressed by using notch filters. **(c)** Intensity-auto-correlation measurement of the XX and X transition confirming very pure single-photon emission. **(d)** Measurement of the fluorescence lifetime T_1 for the XX and X state. The solid lines are theoretical fits. Short radiative lifetimes of $T_{1,XX} = 112$ ps and $T_{1,X} = 134$ ps are determined.



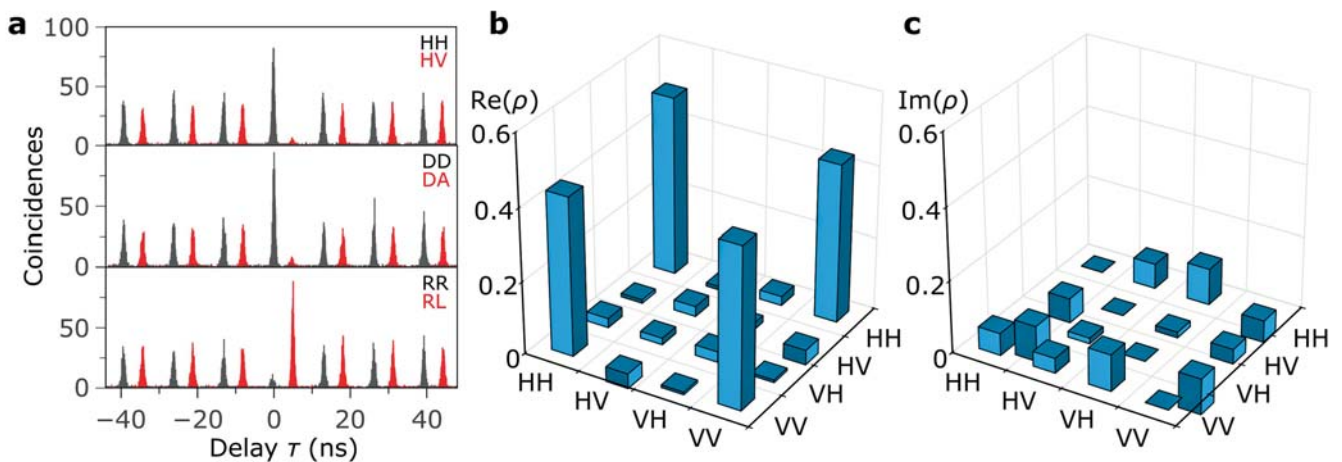
Next, we measure the luminescence lifetime T_1 by recording the intensity correlation between the laser pulse and the arrival time of the photons (Fig. 2d). The extracted lifetimes $T_{1,XX} = 112$ ps and $T_{1,X} = 134$ ps are among the lowest values recorded for as-grown QDs. The lifetime-limited linewidth of the X emission is therefore $\Delta E = 4.9 \mu\text{eV}$, close to the average FSS in our sample.

Evaluating the degree of entanglement

To determine the degree of entanglement, a QD with a FSS of $S = 2.3 \mu\text{eV}$ is chosen, representing a large portion ($\sim 22\%$) of QDs in the sample. The emitted photons are sent onto a beam splitter with polarization analyzers in each output arm. The X and XX photons are spectrally separated and sent to single-photon detectors and the second-order cross-correlation function $g_{XX,X}^2$ for any polarization configuration can be obtained. Fig. 3a shows $g_{XX,X}^2$ for three bases of co-polarized and cross-polarized photons: rectilinear (HV), diagonal (DA) and circular (RL). As expected for an ideal entangled state $|\psi^+\rangle = \frac{1}{\sqrt{2}}(|L_{XX}R_X\rangle + |R_{XX}L_X\rangle)$, a strong bunching (antibunching) at $\tau = 0$ is observed for co-polarization (cross-polarization) in the rectilinear and orthogonal base, whereas this behaviour is reversed for the circular base.

Next, the density matrix ρ of the two-photon state is reconstructed from cross-correlation measurements for 16 different base configurations. The matrix is shown in Fig. 3, split into real (Fig. 3b) and imaginary part (Fig. 3c). It is characterized by outer-diagonal, real-part matrix elements close to 0.5, while all other elements are close to zero. This is in agreement with the expected entangled state and a fidelity to $|\psi^+\rangle$ of $F = 0.91$ is obtained, which surpasses any other reported QD system.

Fig. 3: Degree of entanglement from a quantum dot with finite fine structure splitting. **(a)** Cross-correlation measurements between the XX and X emission on a QD with a FSS of $S = 2.3 \mu\text{eV}$ for co- and cross-polarized photons in the rectilinear (HV), diagonal (DA) and circular (RL) polarization bases. For better visibility an offset in the delay time is added in the cross-polarized case. **(b,c)** Real **(b)** and imaginary **(c)** part of the two-photon density matrix. The fidelity extracted from this matrix is $F = 0.91$.



Furthermore, six additional QDs were selected, representing the full range of observed FSS. Fig. 4 shows the values of F plotted as a function of the FSS (black circles), overlaid on the FSS distribution in the sample (grey histogram). The data from Zhang et al. [10] are shown as reference for typical InAs/GaAs QDs (orange).

All measured dots exhibit fidelities $F > 0.5$ leading to the conclusion that almost 100% of the QDs in the sample generate polarization-entangled photons, which is a milestone for solid-state entangled photon sources.

Fig. 4 also shows the theoretically expected fidelity versus the FSS for the range of observed X lifetimes [11]. The significantly higher fidelities compared with that of InAs/GaAs QDs even for vanishing FSS are expected to originate from the weak electron–nuclear spin hyperfine interactions in this type of QDs.

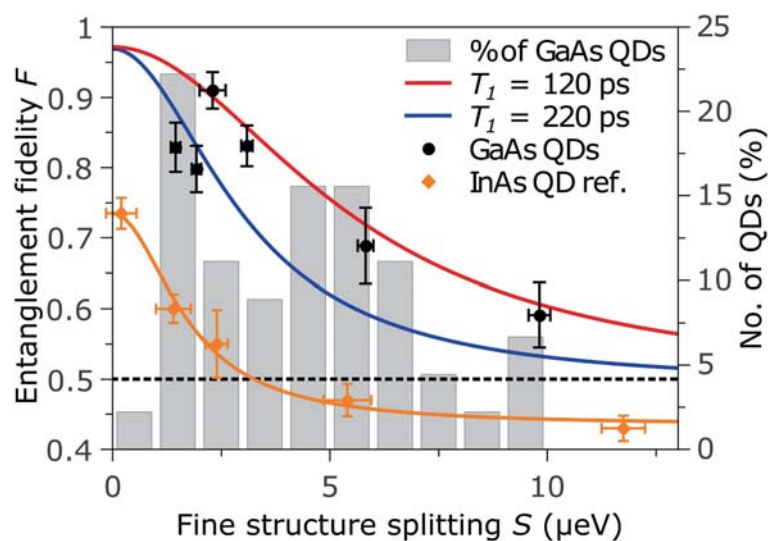


Fig. 4: Entanglement fidelity of quantum dots with different fine structure splitting. The entanglement fidelity and the occurrence of QDs are plotted over the FSS S . All measured GaAs/AlGaAs QDs from the sample (black circles) emit entangled photons with a fidelity above the classical limit (dashed line). For comparison, fidelity values of InAs/GaAs QDs taken from ref. 10 are plotted in orange. Using a theoretical model, the fidelity $F(T_1, S)$ is plotted for two radiative lifetimes $T_1 = 120$ ps (red) and $T_1 = 220$ ps (blue), representing the range of all measured values for T_1 in the sample.

Discussion

In summary, we demonstrated a new type of solid-state polarization-entangled photon source based on an emerging family of GaAs/AlGaAs QDs. These QDs can be grown with unprecedented wavelength control, ultra-small FSS and short radiative lifetime, enabling entanglement fidelities up to $F = 0.91$, which are among the highest values reported for QD-based sources. Remarkably, the whole set of measurements draws an unambiguous conclusion that we have obtained a large ensemble of entangled photon emitters on a single wafer, with almost 100% of QDs in the sample having fidelities > 0.5 and a great fraction are expected to exhibit fidelities $F > 0.8$ without any post-growth tuning.

We envision that a number of key enabling quantum photonic elements can be practically implemented by using this novel material system, in particular a quantum repeater as the backbone for long-range quantum communication.

- [1] A. K. Ekert, Phys. Rev. Lett. 67, 661 (1991)
- [2] C.H. Bennett et al., Phys. Rev. Lett. 70, 1895 (1993)
- [3] H. J. Kimble, Nature 453, 1023–1030 (2008)
- [4] Y. Shih & C.O. Alley, Phys. Rev. Lett. 61, 2921 (1988)
- [5] G. Juska et al., Nat. Photonics 7, 527 (2013)
- [6] M. Müller et al., Nat. Photonics 8, 224–228 (2014)
- [7] T. Kuroda et al., Phys. Rev. B 88, 031306 (2013)
- [8] M. A. Versteegh et al., Nat. Commun. 5, 6298 (2014)
- [9] R. Keil and M. Zopf et al., Nat. Commun. 8, 15501 (2017)
- [10] J. Zhang et al., Nat. Commun. 6, 10067 (2015)
- [11] A. J. Hudson et al., Phys. Rev. Lett. 99, 266802 (2007)

Funding: ERC Starting Grant No. 715770 (QD-NOMS), BMBF Q.Com-H (16KIS0106), European Union Seventh Framework Program 209 (FP7/2007–2013) under Grant Agreement No. 601126 210 (HANAS)

Single-electron lanthanide- lanthanide bonds inside the fullerene cage: en route to unusual electronic and magnetic properties

F. Liu, D. S. Krylov, N. A. Samoylova, L. Spree, M. Rosenkranz, S. M. Avdoshenko, A. U. B. Wolter, T. Greber¹, A. A. Popov

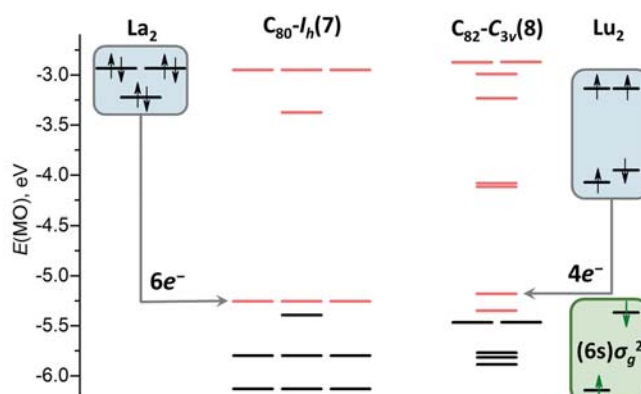
Abstract: High chemical and thermal stability of fullerenes protects endohedral entities from the environment and stabilizes unusual species, which cannot exist otherwise. In particular, when lanthanide dimers are enclosed inside the carbon cage, the covalent lanthanide-lanthanide bond can be formed. The metal-metal bonding orbital occupied with one or two electrons is then the frontier orbital of the fullerene molecule, and its population can be manipulated by redox reactions. Especially interesting are dimetallofullerenes featuring single-electron metal-metal bond, because the presence of an unpaired valence spin results in giant exchange interactions and strong coupling of the 4f-derived spins. For the lanthanides with large magnetic anisotropy (Dy, Tb), such dimetallofullerenes exhibit single molecule magnetism with high blocking temperature of magnetization.

Magnetic and optical properties of lanthanides earned them a plethora of practical applications and reinforce continuous exploration of the new possibilities the partially-filled 4f-shell can provide for academic and applied research in chemistry, physics, and material science. The search for unusual oxidation states of lanthanides is one of the directions, in which the research is going, and the compounds with a formal 2+ oxidation state have been obtained for a majority of the lanthanide row. However, the synthesis of molecular compound with covalent lanthanide-lanthanide bonds is still challenging for traditional organometallic chemistry. This obstacle can be circumvented by confining lanthanide ions within a limited space, such as the inner space of a fullerene molecule.

In endohedral metallofullerenes (EMFs), metal atoms transfer their valence electrons to the carbon cage. The EMFs can be then described as non-dissociative “salts,” with endohedral metal atoms as cations and fullerene cages as anions [1]. In dimetallofullerenes (di-EMFs, i.e. EMFs with two metal atoms), positively charged metal atoms repel each other. However, certain typically trivalent metal atoms in di-EMFs form a metal-metal bonding orbital, whose energy is close to the energy of the frontier fullerene molecular orbitals (MOs). Whether the M–M bonding MO in a given di-EMF involves the HOMO or the LUMO depends on the relative energies of the cage frontier MO and the energy of the metal-metal bonding orbital [2].

Fig. 1 compares MO energies of two representative fullerene cages often found in di-EMFs, $C_{80}-I_h$ and $C_{82}-C_{3v}$, to the orbital energies of two lanthanide dimers, La_2 and Lu_2 [3, 4].

Fig. 1: Molecular orbital energy levels of empty fullerenes $C_{80}-I_h$ and $C_{82}-C_{3v}$ compared to those of the metal dimers La_2 and Lu_2 . Occupied MO levels of fullerenes are shown as black lines, unoccupied levels – as pink lines. Gray arrows indicate donation of 6 or 4 electrons from metal dimer to fullerene in corresponding dimetallofullerenes.



$C_{80}-I_h$ has a small gap between the HOMO and the 3-fold degenerate LUMO, and the open-shell electronic structure of the molecule is very unstable. However, if the LUMO is filled with six electrons, the structure is stabilized. $C_{80}-I_h$ is thus an archetypical cage for EMFs with 6-fold electron transfer from endohedral species to the fullerene. A good example of such species is La_2 dimer. It has 6 valence electrons with relatively high energies (higher than the energy of the fullerene LUMO), so that when the La_2 dimer is encapsulated inside $C_{80}-I_h$, a complete transfer of all six valence electrons to the fullerene occurs. The formal charge distribution in the resulting di-EMF molecule is then $(La^{3+})_2@C_{80}^{6-}$, the HOMO is localized on the fullerene, whereas the LUMO resembles the $(6s)\sigma_g^2$ orbital of the pristine La_2 dimer.

The lanthanide contraction results in a substantially different electronic structure of Lu_2 when compared to that of La_2 . The valence MOs of the Lu_2 span a broader energy range, and its $(6s)\sigma_g^2$ level is lower than the LUMO of $C_{80}-I_h$. As a result, the hypothetical $Lu_2@C_{80}-I_h$ has an open-shell electronic structure with 5 electrons transferred from Lu_2 to the $C_{80}-I_h$ cage. One electron still occupies the Lu–Lu bonding MO, forming thus a single-electron metal-metal bond. The fullerene $C_{82}-C_{3v}$ appears to be a more suitable host for Lu_2 because it has two low-energy unoccupied MOs and hence acts as an acceptor of four electrons. In $Lu_2@C_{82}-C_{3v}$, four electrons of Lu_2 are donated to the fullerene cage, whereas the $(6s)\sigma_g^2$ orbital of Lu_2 remains occupied by two electrons. The formal charge distribution in the di-EMF is then $(Lu^{2+})_2@C_{82}^{4-}$, and the molecule features two-electron Lu–Lu bond [2].

Thus, early lanthanides prefer to form di-EMF without M–M bonds, whereas lanthanides close to the end of the 4f-row are predisposed to form di-EMFs with M–M bond. In both types of di-EMFs, the metal-metal bonding MO is the frontier orbital, and hence its population can be changed in the course of suitably chosen redox reaction. For instance, oxidation of $M_2@C_{82}$ molecules ($M = Sc, Y, Er, Lu$) corresponds to the removal of the electron from the metal-metal bond. Therefore, their oxidation potentials are metal-dependent and vary in a rather broad potential range of 0.4 V (Fig. 2) [3]. Enhanced contribution of metal s-atomic orbital to the *spd*-hybrid M–M HOMO of $M_2@C_{82}$ yields a large isotropic hyperfine coupling constant for metals with non-zero nuclear spin in

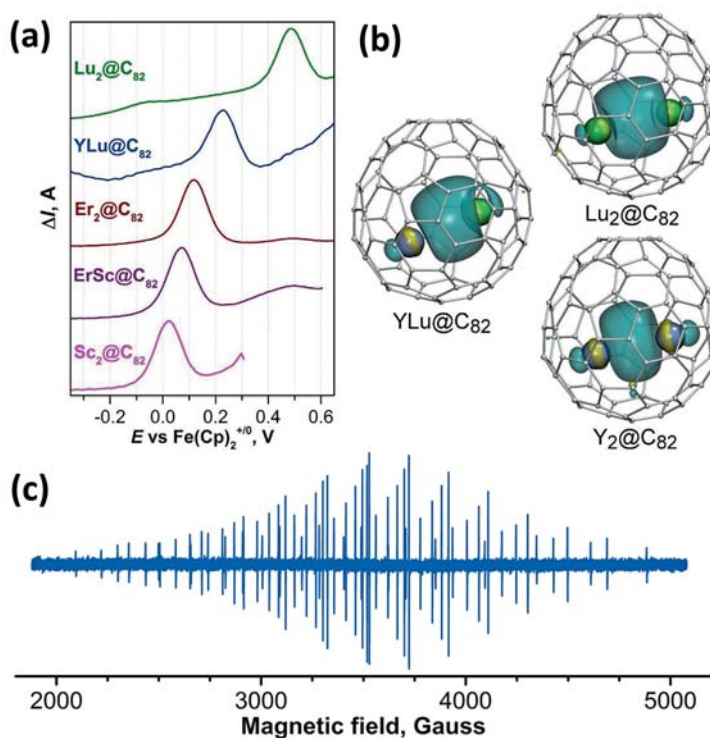


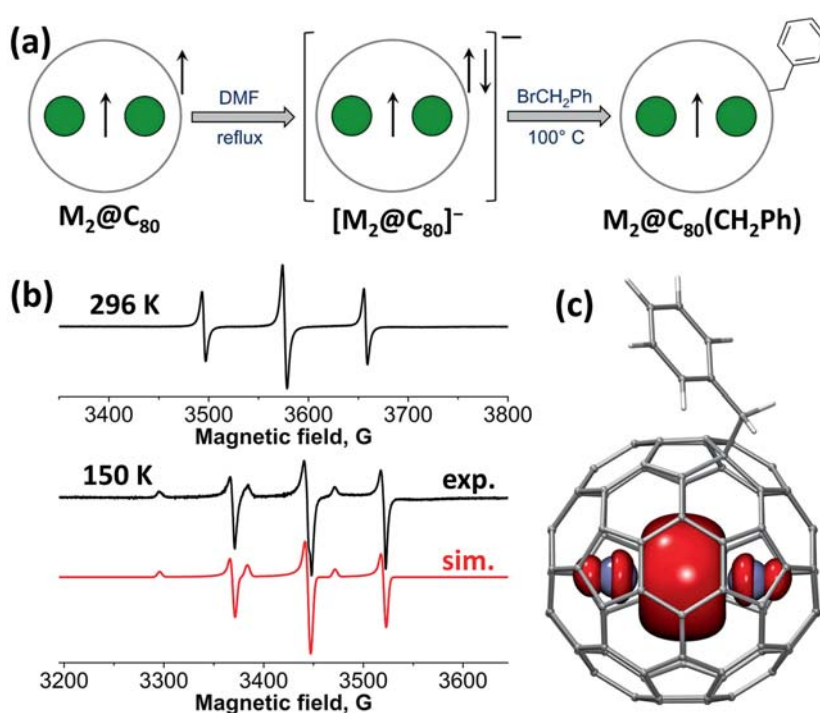
Fig. 2: (a) Square wave voltammetry of several $M_2@C_{82}-C_{3v}$ fullerenes at their first oxidation step ($M_2 = Lu_2, YLu, Er_2, ErSc, Sc_2$); (b) HOMO orbitals for $Lu_2@C_{82}$, $Y_2@C_{82}$, and $YLu@C_{82}$; (c) EPR spectrum of $Sc_2@C_{82}^+$ cation in o-dichlorobenzene solution at room temperature, $a(^{45}Sc) = 199.2$ G, $g = 1.994$.

cation radicals $[M_2@C_{82}]^{*+}$. A striking example is the cation radical $[Sc_2@C_{82}]^{*+}$, which exhibits well-resolved EPR spectrum with the hyperfine structure spanning 2800 Gauss. Instead of 15 lines expected for two equivalent Sc with nuclear spin of 7/2, experimental spectrum comprises 64 lines caused by a hyperfine splitting with the large ^{45}Sc hyperfine constant of 199.2 G (Fig. 2c). Formation of the single-electron Er–Er bond in $[Er_2@C_{82}-C_{3v}]^{*+}$ was also supported by SQUID magnetometry. The oxidation of $Er_2@C_{82}$ strongly modified the spin state of the endohedral Er_2 unit, presumably creating a three-center $[Er^{3+}-e-Er^{3+}]$ system with stronger exchange interactions than in the pristine $Er_2@C_{82}$ [3].

Peculiar electronic structure is found in di-EMFs with Yttrium and lanthanides in the middle part of the lanthanide row (Gd–Ho). In the arc-discharge synthesis these metals do form $M_2@C_{80}-I_h$ molecules, but their ground electronic state is a triplet with the formal charge distribution $(M_2)^{5+}@C_{80}^{5-}$, similar to aforementioned $Lu_2@C_{80}$. The M–M bonding MO of such di-EMFs is occupied by a single electron, and another unpaired spin is delocalized over the fullerene cage. Electronic structure of $M_2@C_{80}-I_h$ can be stabilized by adding an electron, which yields to closed-shell electronic structure of the fullerene cage, $(M_2)^{5+}@C_{80}^{6-}$. The non-charged form of these di-EMFs are then obtained by substitution reaction with benzyl bromide, giving air-stable $M_2@C_{80}(CH_2Ph)$ derivatives still featuring the single-electron M–M bond (Fig. 3a) [5]. For $M = Y$, localization of the spin density on the Y–Y bonding MO is confirmed by EPR spectroscopy, which revealed large isotropic ^{89}Y hyperfine coupling constants near of 80 G and significant hyperfine- and g-tensor anisotropy in the frozen solution (Fig. 3b,c). The first reduction potentials of $M_2@C_{80}(CH_2Ph)$ derivatives are metal-dependent and span the range from -0.52 V in $Y_2@C_{80}(CH_2Ph)$ to -0.86 V in $Gd_2@C_{80}(CH_2Ph)$, showing that the surplus electron populates the single-occupied M–M bonding MO, thus forming a “standard” two-electron bond in anions [4].

$Dy_2@C_{80}(CH_2Ph)$ is found to be a single molecule magnet with broad hysteresis and unusually high blocking temperature of magnetization of 22 K (Fig. 4) [5]. Measurements of the relaxation times of magnetization showed that at low temperature the main relaxation mechanism is the temperature-independent quantum tunneling, whereas at

Fig. 3: (a) A chemical route to stabilize electronic structure of $M_2@C_{80}$ fullerenes via reduction and subsequent nucleophilic substitution yielding air-stable $M_2@C_{80}(CH_2Ph)$ monoadduct (arrows denote unpaired spins). (b) EPR spectra of the toluene solution of $Y_2@C_{80}(CH_2Ph)$ at room temperature and at 150 K (below the freezing point of the solvent); the isotropic RT spectrum has g-factor of 1.9733 and the $a_{iso}(^{89}Y)$ value of 223.8 MHz; the axial spectral pattern in frozen solution is reproduced by $g_{\perp} = 1.9620$, $g_{\parallel} = 1.9982$, $a_{\perp}(^{89}Y) = 208.0$ MHz, $a_{\parallel}(^{89}Y) = 245.9$ MHz; (c) DFT-computed spin density distribution in $Y_2@C_{80}(CH_2Ph)$.



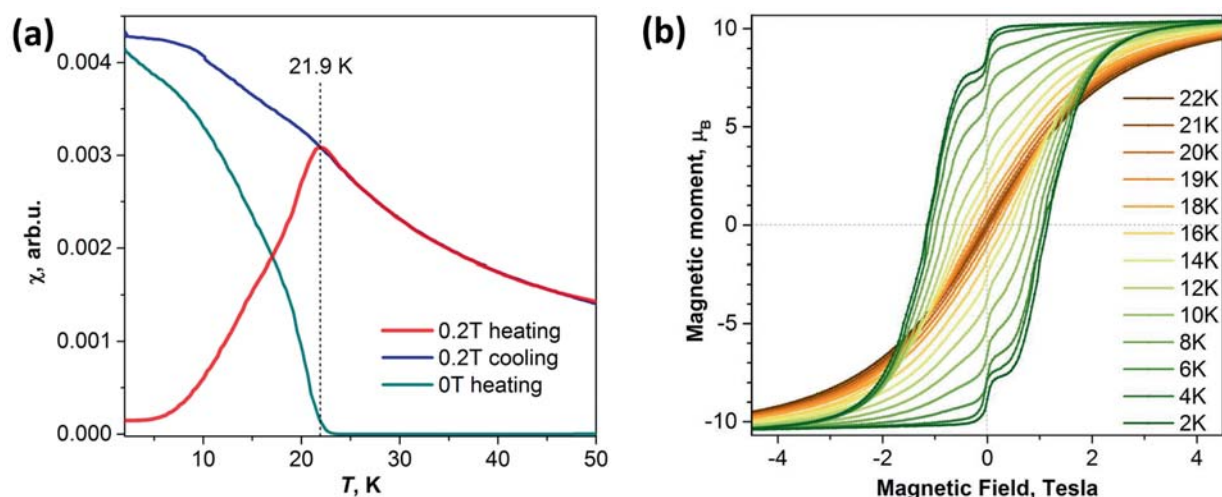


Fig. 4: (a) Determination of blocking temperature of magnetization T_B of $\text{Dy}_2@\text{C}_{80}(\text{CH}_2\text{Ph})$: the sample is first cooled in zero-field to 1.8 K, then magnetic susceptibility χ is measured in the field of 0.2 T with increasing temperature (red curve), then the measurement is performed at cooling down to 1.8 K (blue curve); the vertical bar denotes T_B . (b) Hysteresis of magnetization in $\text{Dy}_2@\text{C}_{80}(\text{CH}_2\text{Ph})$ measured at various temperatures.

higher temperature the relaxation is dominated by the Orbach mechanism with the barrier of 613 K (Fig. 5a). Unprecedented magnetic properties of $\text{Dy}_2@\text{C}_{80}(\text{CH}_2\text{Ph})$ are due to the giant exchange interaction between lanthanide ions mediated by the unpaired electron delocalized between them. The three-center spin system of $\text{Dy}_2@\text{C}_{80}(\text{CH}_2\text{Ph})$ is described as $[\text{Dy}^{3+}-e-\text{Dy}^{3+}]$. In the ground state, all three moments are parallel and couple ferromagnetically to form a single spin unit of $21 \mu_B$ with a Dy-electron exchange constant of 32 cm^{-1} (46 K). The barrier of the magnetization reversal is assigned to the exchange excited state, in which the spin of one Dy center is flipped (Fig. 5b) [5]. Semi-occupied M–M bonding MO is thus essential to achieve unprecedented magnetic properties in lanthanide di-EMFs. It may be also beneficial for the spin-polarized electronic transport through single fullerene molecules, which can lead to single-molecule electronic and spintronic devices.

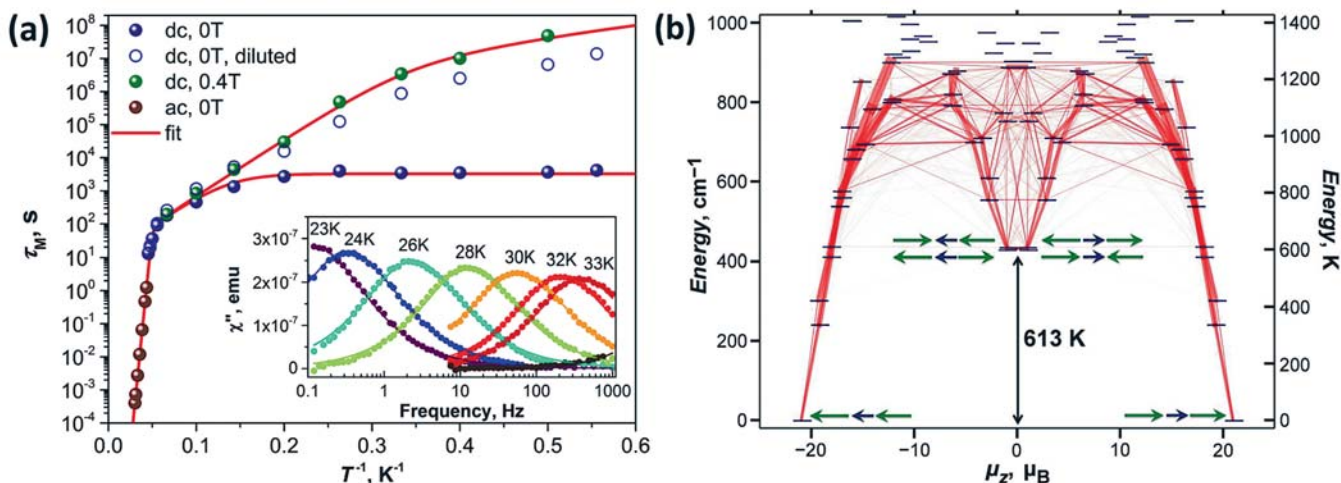


Fig. 5: (a) Magnetization relaxation times of $\text{Dy}_2@\text{C}_{80}(\text{CH}_2\text{Ph})$ obtained from dc- and ac-measurements in zero field and in the constant field of 0.4 T. The inset shows χ'' values measured at different temperatures and frequencies. (b) Low-energy part of the spectrum of the effective spin Hamiltonian of the $[\text{Dy}^{3+}-e-\text{Dy}^{3+}]$ system with transition probabilities visualized as lines of different thickness (thicker lines correspond to higher probabilities). A schematic description of the spin alignment in the ground state and exchange-excited states is also shown (Dy spins – green arrows, single electron spin – dark blue arrow). With the exchange coupling constant $J_{\text{Dy},e} = 32 \text{ cm}^{-1}$, the energy of the first exchange excited state matches the Orbach barrier of 613 K.

- [1] A. A. Popov (Ed). *Endohedral Fullerenes: Electron Transfer and Spin*, Springer International Publishing, Germany, 2017.
- [2] A. A. Popov et al., *Chem. Commun.* 48 (2012) 8031.
- [3] N. A. Samoylova et al., *Nanoscale* 9 (2017) 7977.
- [4] A. A. Popov, *Curr. Opin. Electrochem.* 8 (2018) DOI: 10.1016/j.coelec.2017.12.003
- [5] F. Liu et al., *Nat. Commun.* 8 (2017) 16098

Funding: European Research Council (ERC): grant agreement No 648295 "GraM3"

Cooperation: ¹Univ. Zürich

Theoretical prediction of a giant anisotropic magnetoresistance in carbon nanoscrolls

C. H. Chang and C. Ortix

Abstract: Advanced nanotechnology is continually gifting us with low-dimension nanoarchitectures that have rich forms of geometry to host novel magnetic states. Snake orbits, for instance, are trajectories of charge carriers curving back and forth, which form at an interface where either the magnetic field direction or the charge carrier type is inverted. In graphene p-n junctions, their presence is manifested in the appearance of magnetoconductance oscillations at small magnetic field. Here we show that signatures of snake orbits can also be found in curved nanomaterials by studying the classical magnetotransport properties of carbon tubular nanostructures subject to relatively weak transversal magnetic fields where snake trajectories appear in close proximity to the zero radial field projections. In carbon nanoscrolls the formation of snake orbits leads to a strongly directional dependent positive magnetoresistance with an anisotropy up to 80 %.

Carbon Nanomaterials

Carbon nanomaterials, such as carbon nanotubes (CNT) [1] and graphene [2], continue to trigger a lot of attention due to their very unique structural and physical properties [3]. In recent years, another carbon nanomaterial, called carbon nanoscroll (CNS), has emerged [4]. It is a spirally wrapped graphite layer that, unlike a multiwalled carbon nanotube (MWCNT), is open at two edges and does not form a closed structure. CNSs are scrolled from an undefined number of graphene layers. In addition, the chemical process can potentially induce unexpected defects in the material, thereby lowering its quality. Controlled fabrication of high-quality CNSs has been instead achieved [5] using isopropyl alcohol solutions to roll up high-quality monolayer graphene predefined on Si/SiO₂ substrates.

The peculiar geometric structure of CNSs yields unusual electronic, and transport properties in uniform electric and magnetic fields. The natural presence of edge nanoscrolls in graphene, for instance, has been predicted to be at the basis of the poor quantization of the Hall conductance in suspended samples [6]. This is due to the fact that inside the scrolls, the electrons respond primarily to the normal component of the externally applied magnetic field [7], which oscillates in sign and largely averages out.

In this work, we theoretically predict a strongly directional dependent magnetoresistance (MR) in CNSs subject to relatively weak transversal magnetic fields. The reason for the occurrence of this phenomenon is that the oscillation of the effective magnetic field felt by the electrons in a CNS leads to the formation of classical snake orbits, whose number changes with the direction of the externally applied magnetic field. As a result, we find a giant anisotropic magnetoresistance (AMR) with a magnitude of up to 80%, a value comparable to the AMR observed in the quantum anomalous Hall phase of ferromagnetic topological insulator thin films [8], and an order of magnitude larger than the bulk AMR of conventional ferromagnetic alloys [9]. This suggests a novel route towards miniaturized nanoscale devices exploiting the AMR effect for magnetic recording, for instance.

Magnetic states and Magnetotransport of Carbon Nanotubes

To prove the assertions above, we first elucidate the effect of snake orbit formation by analyzing the magnetotransport properties of single-walled CNTs subject to transversal magnetic fields in the classical diffusive transport regime. Figure 1 shows the ensuing behavior of the MR $\Delta\rho_{||}/\rho_b = \rho_{yy}(B)/\rho_{yy}(0) - 1$. When the applied magnetic field is weak, the Lorentz force bends the trajectory of a carrier into the helix orbit (see left-up

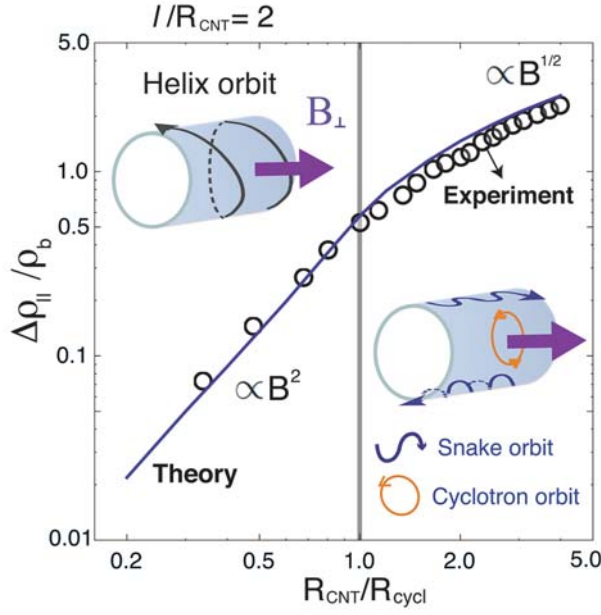


Fig. 1: Classical magnetoresistance of a CNT. Log-log plot of the MR as a function of the magnetic field strength B measured by the ratio between the CNT radius R_{CNT} and the characteristic cyclotron radius R_{cycl} . ρ_b is the longitudinal resistivity in the absence of externally applied magnetic fields. The circles are rescaled experimental results adapted from Ref..

panel in Fig. 1), which leads to the MR increasing with the square of the strength of applied field. When the magnetic field is large enough, the carrier at the surface perpendicular to the field moves in a cyclotron orbit, and the carrier at the surface parallel to the field moves in a snake orbit for it inverts chirality around the surface. The surfaces with cyclotron orbits are insulating, and the two surfaces with snake orbits are respected to two conduction channels (see right-down panel in Fig. 1). Since the width of conduction channels decreases with the field strength by a ratio $B^{-0.5}$, snake orbits finally results in a MR increasing with the square root of the field. The details of theoretical approach using Kubo formula are provided in Ref. 10.

To verify the validity of our approach, we have compared our theoretical results with the MR measurements performed by Kasumov and collaborators [11] on a 6 nm outer radius isolated multi-winding CNT, which show an inflexion point in the MR at an external moderate magnetic field ≈ 1.6 T. From the condition that the inflexion point occurs when the CNT radius exactly matches the effective cyclotron radius, we obtain $m v_F = 1.54 \times 10^{-27} \text{ m} \cdot \text{kg/s}$, which is compatible with a Fermi velocity [12,13] of the order of 10^5 m/s and a cyclotron mass approximately two order of magnitudes smaller than the mass of free carriers. By further taking into account a sizable magnetic-field independent resistivity, which we attribute to inter-wall and contact resistivities suppressing the MR by approximately one order of magnitude, we find a perfect agreement in the behavior of the MR as a function of the magnetic-field strength [see Fig. 1]. Moreover, the value of the mean free path $l = 2R_{\text{CNT}} \approx 12 \text{ nm}$ is consistent with the experimental values reported in high-biased SWCNT [14].

Magnetic states and Magnetotransport of Carbon Nanoscrolls

Having established that our analysis in the classical diffusive transport regime correctly accounts for the behavior of the MR in CNTs up to moderate magnetic field strengths, we now move to analyze the magnetotransport properties of CNSs taking into account their peculiar geometric structure. In the remainder we will restrict ourselves to a one-winding CNS. Figure 2b shows the magnetic field dependence of the conductivity along the CNS azimuthal direction $\sigma_t = \sigma_{ss}$ measured in units of the conventional

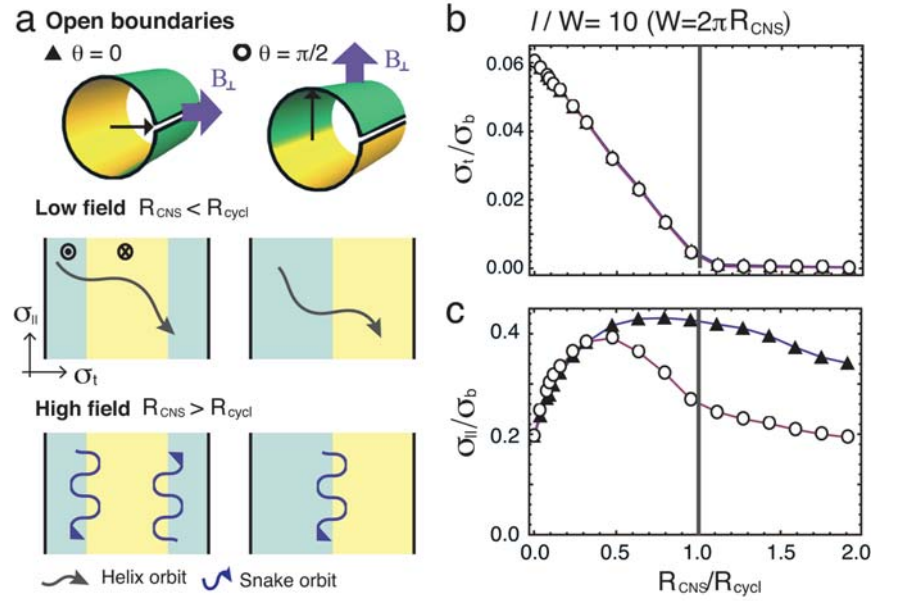


Fig. 2: Electron orbits and magnetoconductivity of a one-winding CNS for different magnetic field directions. **a** The green and yellow regions indicate the portion of the CNS where the effective magnetic field felt by the electrons is positive and negative, respectively. The top panels schematically show the native three-dimensional description whereas the middle and bottom panels sketch the effective two-dimensional description with the characteristic electron trajectories in the weak and moderate field strength regime for different orientations. **b**, **c** σ_t ($\sigma_{||}$) denotes the conductivity across (along) the tube axis, with σ_b the conductivity of a bulk 2D channel in the absence of magnetic fields. The triangles (circles) are the theoretical results for a one-winding CNS with mean free path $l/W = 10$ subject to a field in the $\theta = 0$ ($\theta = \pi/2$) direction.

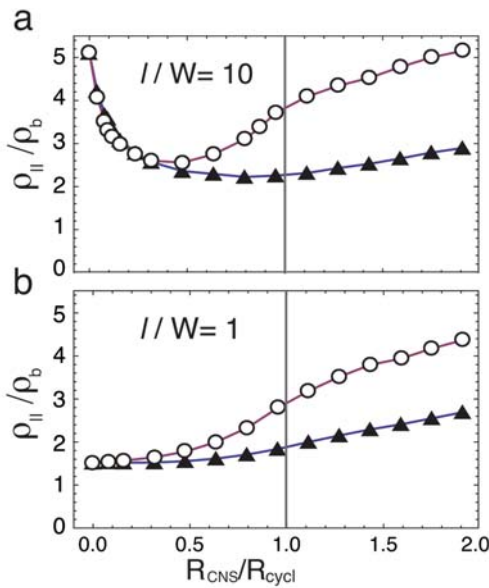


Fig. 3: Classical magnetoresistance of a one-winding CNS. MR as a function of the magnetic field strength B measured by the ratio between the CNS radius R_{CNS} and the characteristic cyclotron radius R_{cycl} . ρ_b is the longitudinal resistivity of a bulk 2D channel in the absence of magnetic fields. The triangles are the result for a magnetic field direction $\theta = 0$ while the circles are for $\theta = \pi/2$. The mean free path has been set to $l = 10W$ and $l = W$ in **a** and **b** respectively.

conductivity of a “bulk” (arclength $W = 2\pi R_{\text{CNS}} \rightarrow \infty$) 2D channel in zero magnetic field. Here, we have set the mean free path l to be one order of magnitude larger than the CNS width to assure the transport is well inside the quasi-ballistic regime. For zero magnetic field, diffusive boundary scattering strongly suppresses the conductivity along the CNS width. A finite magnetic field leads to a further decrease of the conductivity, independent on the direction of the transversal magnetic field. The behavior of the conductivity component along the CNS axis $\sigma_{||} = \sigma_{yy}$ is instead entirely different (see Fig. 2c). In the weak-field regime $R_{\text{CNS}} \ll R_{\text{cycl}}$ we find an enhancement of the conductivity due to magnetic reduction of backscattering [15]. This enhancement of the conductivity is followed by an ultimate suppression due to the formation of snake orbits, which, as discussed above, yield a positive MR. Moreover, we find the conductivity $\sigma_{||}$ to strongly depend on the magnetic field direction. This is because for a magnetic field oriented along the edge axis ($\theta = 0$) there are two regions where its normal component switches sign (c.f. Fig. 2a), contrary to the case of a magnetic field oriented perpendicularly to the edge axis $\theta = \pi/2$ in which case the magnetic field switch is encountered only along one line of the scroll. The ensuing proliferation of snake orbits for $\theta = 0$ then leads to a much slower suppression of the conductivity since their contribution proportional to $B^{-0.5}$ instead of the usual B^{-2} contribution of cyclotron orbits.

The knowledge of the magnetoconductivity tensor components allows us to obtain the behavior of the magnetoresistance $\rho_{||}$. For $l/W \leq 10$, the zero-field resistivity is well described by the well-known formula [15] $\rho_{||} = \rho_b (1 + 4l/(3\pi W))$ accounting for boundary scattering effects on the resistivity. In the weak-field regime a negative MR due to magnetic suppression of backscattering is explicitly manifest only when the mean free path largely exceeds the width of the CNS (c.f. Fig. 3), which is in perfect analogy with the situation encountered in a 2D channel subject to an homogeneous perpendicular magnetic field [16]. In the intermediate field regime, the MR behavior strongly

resembles the MR in the absence of boundary scattering (c.f. Fig. 1) but acquires a strong directional dependence independent of the ratio l/W . As long as the boundary scattering is completely diffusive, the directional dependence comes entirely from the aforementioned proliferation of snake orbits, and therefore the AMR in both cases in Fig. 3 reaches a giant value $\approx 80\%$.

- [1] M. S. Dresselhaus et al., *Carbon Nanotubes: Synthesis, Structure, Properties, and Applications*, Springer-Verlag Berlin Heidelberg, 2001
- [2] A. K. Geim et al., *Nat. Mater.* 6 (2007) 183
- [3] D. Jariwala et al., *Chem. Soc. Rev.* 42 (2013) 2824
- [4] L. M. Viculis et al., 299 (2003) 1361
- [5] X. Xie et al., *Nano Lett.* 9 (2009) 2565
- [6] A. Cresti et al., *Phys. Rev. Lett.* 108 (2012) 166602
- [7] G. Ferrari et al., *Phys. Rev. B* 78 (2008) 115326
- [8] A. Kandala et al., *Nat. Commun.* 6 (2015) 7434
- [9] T. McGuire et al., *IEEE Trans. Magn.* 11 (1975) 1018
- [10] C. H. Chang et al., *Nano Lett.* 17 (2017) 3076
- [11] A. Kasumov et al., *Europhys. Lett.* 34 (1996) 429
- [12] S. G. Lemay et al., *Nature* 412 (2001) 617
- [13] W. Liang et al., *Nature* 411 (2001) 665
- [14] J.-Y. Park et al., *Nano Lett.* 4 (2004) 517
- [15] C. W. J. Beenakker et al., *Solid State Phys.* 44 (1991) 1
- [16] E. Ditlefsen et al., *J. Philos. Mag.* 14 (1966) 759

Funding: ¹Future and Emerging Technologies (FET) programme within the Seventh Frame- work Programme for Research of the European Commission under FET-Open grant number: 618083 (CNTQC).

²DFG Research Fellowship: OR 404/1-1

³Netherlands Organization for Scientific Research (NWO) VIDI Grant: 680-47-543

Chemical Gating of a Weak Topological Insulator: $\text{Bi}_{14}\text{Rh}_3\text{I}_9$

M. P. Ghimire and M. Richter

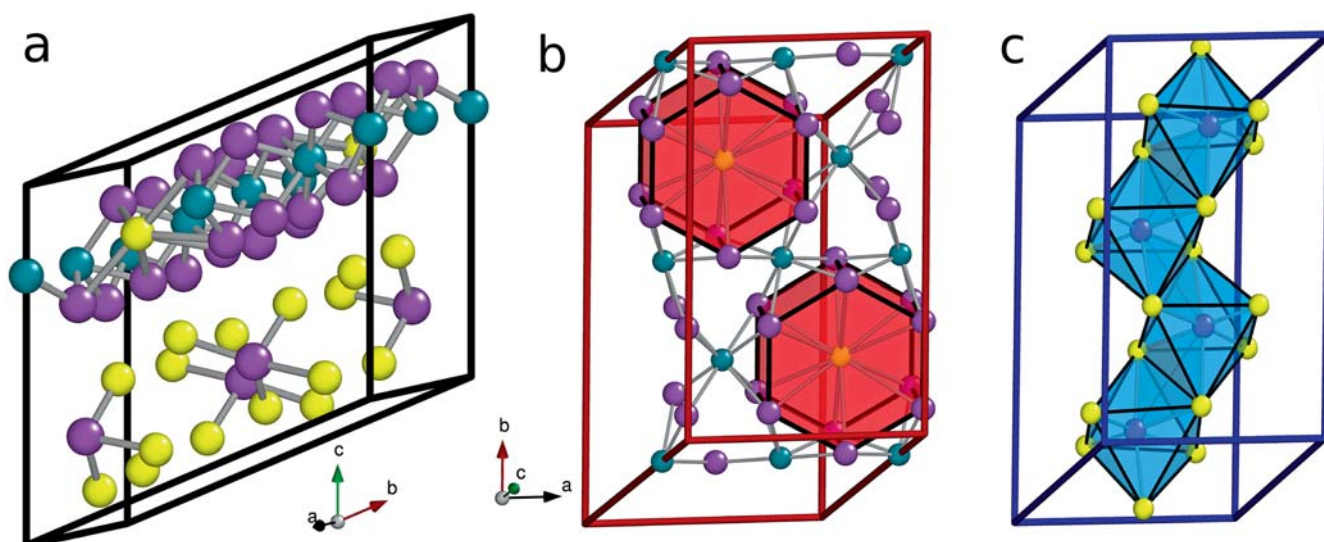
Abstract: The compound $\text{Bi}_{14}\text{Rh}_3\text{I}_9$ has been suggested as a weak three-dimensional topological insulator on the basis of angle-resolved photoemission and scanning-tunneling experiments in combination with density functional (DF) calculations [1,2]. These methods unanimously support the topological character of the headline compound, but a compelling confirmation could only be obtained by dedicated transport experiments. The latter, however, are biased by an intrinsic n-doping of the material's surface: Electronic reconstruction of the polar surface shifts the topological gap below the Fermi energy [3], which would also prevent any future device application. Here, we report the results of DF calculations for chemically gated and for counter-doped surfaces of $\text{Bi}_{14}\text{Rh}_3\text{I}_9$. We demonstrate that both methods can be used to compensate the surface polarity without closing the electronic gap [4].

Introduction

Topological insulators (TIs) have recently attracted attention due to their massless Dirac-cone-like surface states protected by time-reversal symmetry (TRS). In a nutshell, TIs are characterized by these gapless surface states and a bulk energy gap. Three-dimensional (3D) TIs are called strong or weak based on four Z_2 invariants ($\nu_0; \nu_1, \nu_2, \nu_3$). If $\nu_0 = 1$, the material is a strong TI; if $\nu_0 = 0$ and any of the indices (ν_1, ν_2, ν_3) is equal to one, it is a weak TI. In the former case, including the wellknown compounds Bi_2Se_3 and Bi_2Te_3 , the TRS-protected surface states are present on all facets, while in the latter case, such surface states are present only on certain facets. Their peculiar properties bear the potential for novel types of information processing [5].

Weak 3D TIs suggested hitherto are usually hosted by layered crystal structures. The strength of the related interlayer coupling influences their bulk band structure: (i) In Bi_2TeI with strong interlayer coupling, this coupling is essential for the formation of the weak 3D TI state [6]; (ii) a weak interlayer coupling, however, results in a quasi two-dimensional (2D) band structure. This situation is found, among others, in $\text{Bi}_{14}\text{Rh}_3\text{I}_9$ [1,2]. Weak 3D TIs of the second kind may allow to produce 2D TI structures that are expected to show the quantum spin-Hall (QSH) effect. This can be achieved by cleaving off thin layers from the bulk 3D TI as an alternative way to the fabrication of quantum wells [7]. Indeed, a single, charge-compensated layer of $\text{Bi}_{14}\text{Rh}_3\text{I}_9$ was predicted to be a 2D TI in a recent calculation [8].

Fig. 1: (from Ref. [4]): Bulk structure of $\text{Bi}_{14}\text{Rh}_3\text{I}_9$. (a) Elementary cell with $[(\text{Bi}_4\text{Rh})_3\text{I}]^{2+}$ in the upper part and $[\text{Bi}_2\text{I}_8]^{2-}$ in the lower part. The color code is violet for Bismuth, green for Rhodium, and yellow for Iodine. (b) Rotated view of the $[(\text{Bi}_4\text{Rh})_3\text{I}]^{2+}$ layer, also denoted as 2D TI layer; (c) the same for the $[\text{Bi}_2\text{I}_8]^{2-}$ layer, also denoted as spacer layer.



The recently synthesized title compound was characterized as a layered ionic structure with alternating cationic $[(\text{Bi}_4\text{Rh})_3\text{I}]^{2+}$ and anionic $[\text{Bi}_2\text{I}_8]^{2-}$ layers, as shown in Fig. 1. DF calculations for this material found $(\nu_0; \nu_1, \nu_2, \nu_3) = (0; 0, 0, 1)$. Further, the electronic band structure grossly agreed with angle-resolved photoemission spectra (ARPES) obtained on single crystals. On this basis, $\text{Bi}_{14}\text{Rh}_3\text{I}_9$ was claimed to be a weak TI [1]. Subsequently, this hypothesis was strengthened by scanning tunneling microscopy (STM) experiments [2]. By STM topography, the investigated [001] surface was found to exhibit areas with both types of layers. Clear signatures of one-dimensional (1D) states were observed in the band gap only at step edges of cationic surface layers. However, the related surface-layer gap was found 0.25 eV below the Fermi level (E_F) [2]. The $[(\text{Bi}_4\text{Rh})_3\text{I}]^{2+}$ layer carrying the edge states was observed to be structurally intact. The $[\text{Bi}_2\text{I}_8]^{2-}$ layer, however, contained holes that were attributed to the evaporation of iodine atoms during cleavage. Such a chemical reconstruction is one possibility [9] to compensate the obvious surface polarity of the system. DF calculations confirmed the observed down-shift of the topologically nontrivial band gap at the cationic [001] surface [3]. This is a clear sign of an electronic reconstruction as a second possibility [9] to compensate surface polarity.

A confirmation of the weak 3D TI state of $\text{Bi}_{14}\text{Rh}_3\text{I}_9$ would require to observe the QSH effect on the mentioned 1D edge states [10]. However, related transport experiments only make sense if the observed intrinsic doping is compensated by reasonable means, and thus, the topological gap with the edge states is shifted to E_F . There are several possible ways to compensate the surface polarity:

- (i) physical gating by preparation of a dielectric gate structure and applying the electric field effect;
- (ii) chemical gating by deposition of an oxidizing agent; or
- (iii) counterdoping of the surface layer.

Here, we report results of investigations into the two latter possibilities by means of DF calculations. In particular, we study the effects of Iodine deposition as a sparse overlayer and of counter-doping by exchanging surface layer Bi atoms by Sn. The results are expected to provide suggestions for the preparation of forthcoming transport experiments, which are required to confirm the topological state of $\text{Bi}_{14}\text{Rh}_3\text{I}_9$ or similar systems.

Method

All DF calculations were done with the full-potential local-orbital (FPLO) code developed at IFW Dresden [11]. The self-consistent calculations were carried out in the four-component Dirac mode. This effort is necessary because the involved elements have a sizable spin-orbit coupling, which is responsible for opening the band gap. In order to simulate the [001] surface of a bulk sample, we considered a series of slabs with thickness varying from 1.25 to 3.75 nm, i.e., from one to three structural layers. The considered layer stacks have the same lateral cell dimensions as the experimental bulk structure [1], and equivalent atomic positions.

In Ref. [4], we considered chemical modifications on both cationic and anionic surfaces. First, the experimentally observed desorption of Iodine from the anionic (spacer) layer was modeled, where about two Iodine atoms per surface elementary cell are removed during cleavage [2,3]. Second, adsorption of a sparse Iodine layer on top of the cationic (2D TI) surface was investigated for the sake of tuning E_F . Third, we investigated the effect of surface doping by replacing part of the Bi atoms in the outermost atomic layer of the 2D TI surface by Sn. Details of the second type of modification are presented in the following section, while the summary mentions results of the third type as well.

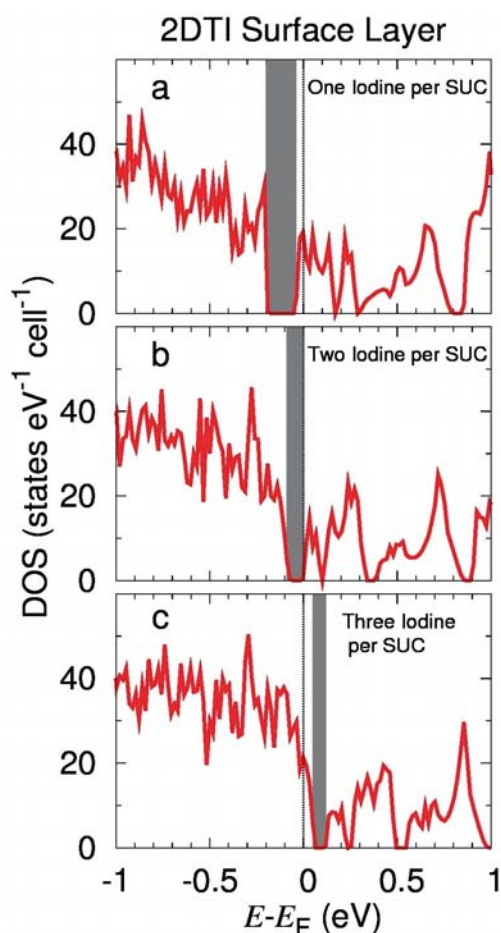


Fig. 2: (from Ref. [4]): Layer-resolved density of states (DOS) of the 2D TI surface layer (Bi_4Rh) $_3\text{I}_{1+n}$ for deposition of $n = 1$ (a), $n = 2$ (b), and $n = 3$ (c) iodine atoms per surface unit cell (SUC) on top of the 2D TI surface. The spacer surface is chemically reconstructed by removing two iodine atoms per SUC as observed in experiment [2].

Chemical gating

With the aim to compensate the surface charge and to move the surface gap with the topological edge states toward E_F , we generate a sparse layer of 1 – 3 Iodine atoms per surface unit cell (SUC) on top of the 2D TI surface. This concentration, about 0.08 – 0.25 monolayers, is similar to the concentration of Copper atoms that were recently used in chemical gating of the strong 3D TI Bi_2Se_3 [12]. The calculated adsorption energy gain amounts to 1.7 eV for the first Iodine atom per SUC, 1.6 eV for the second, and 1.4 eV for the third one, if deposition of atomized Iodine is assumed. These numbers have to be reduced by 1.0 eV for the case of molecular Iodine deposition.

The related density of states (DOS) contributions of the 2D TI surface are shown in Fig. 2 for the simplest case of one structural layer. For the lowest concentration of one Iodine atom per SUC, E_F is shifted downward in comparison to the pristine case (not shown), indicating a reduction of electron-type bulk carriers, but stays within the conduction band (Fig. 2a). Next, for two Iodine atoms per SUC, E_F moves to the bottom of the conduction band. The calculated surface band gap of 0.07 eV (Fig. 2b) is smaller than the bulk gap, but transport experiments would be feasible. Further, if three Iodine atoms per SUC are deposited, E_F shifts into the valence band and a crossover from electron type to hole type behavior occurs (Fig. 2c). These findings confirm the naive expectation that the formal surface charge of +2 can be compensated by two Iodine atoms. In the following, we will restrict our investigation to this adsorbant concentration.

Fig. 3 shows the surface-layer projected DOS for slabs of one, two, and three structural layers. We first consider the 2D TI surface DOS, Fig. 3(a,c,e). In all cases, the valence band and the lower part of the conduction band (up to about 0.35 eV) is dominated by contributions of similar weight from Bi-6p and from 5p states located at the adsorbed Iodine atoms. Above the narrow gap at 0.35 eV, the DOS is dominated by Bi-6p states. With increasing thickness of the slab, the 2D TI gap is found to increase from about 0.07 eV to about 0.12 eV. The smaller gap size in the case of a slab with only one structural layer is due to the presence of a narrow band with a width of 0.10 eV just above E_F .

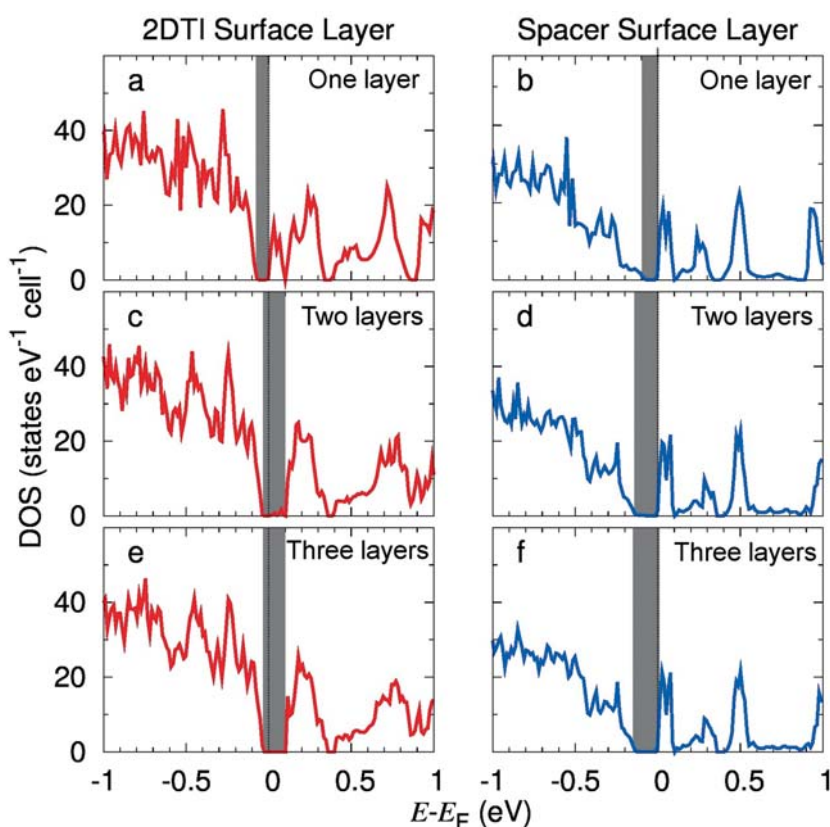


Fig. 3: (from Ref. [4]): Layer-resolved density of states (DOS) of 2D TI surface layers (Bi_4Rh) $_3\text{I}_3$ (a,c,e) and spacer surface layers Bi_2I_6 (b,d,f) for one (a,b), two (c,d), and three (e,f) structural layers with two iodine atoms per surface unit cell (SUC) deposited on top of the 2D TI surface. The spacer surface is chemically reconstructed by removing two iodine atoms per SUC as observed in experiment [2].

By comparison with the data of the thicker slabs it becomes obvious that this band originates from hybridization with spacer surface states being present at the same energy for all considered slab thicknesses, Fig. 3(b,d,f). The integrated weight of that band, projected to the 2D TI surface, amounts to 0.82 (0.05, 0.0034) electrons for slabs with one (two, three) structural layers. With increasing slab thickness, the interaction between the two surfaces and the related in-gap states at the 2D TI surface becomes weak and finally negligible for slab thickness larger than 2.5 nm. This means that ultra-thin films, in particular those with only one structural layer, may not be advantageous for the demonstration of the QSH effect in $\text{Bi}_{14}\text{Rh}_3\text{I}_9$ due to possible narrowing of the gap by interaction with the opposite surface. Rather, films with a thickness larger than 2.5 nm may serve the goal if their surface is doped with Iodine or other oxidizing agents in an appropriate concentration. We suggest that the concentration could be naturally stabilized by a self-limited adsorption process, as overdoping might be thermodynamically unstable. This idea is supported by the calculated adsorption energy gain, which is considerably reduced with growing concentration of adsorbed Iodine. A fine-tuning of the concentration should be possible by the substrate temperature.

Summary

We have demonstrated that chemical gating can compensate the intrinsic n-doping at the surface of $\text{Bi}_{14}\text{Rh}_3\text{I}_9$, a suggested weak 3D topological insulator. By deposition of Iodine adatoms in an appropriate concentration or by partial exchange of surface Bismuth atoms by Tin, the topological gap is shifted to the Fermi level. While the former method might be easier implemented for a proof-of-principle experiment, the latter might be more robust for potential applications. Importantly, the gap is not closed upon chemical gating. As the applied local density approximation usually underestimates the gap size, this statement should be robust. Thus, the gated material will be suitable for transport experiments with the particular aim to confirm its topological character. We further find that the gap size grows with the thickness of the material. Therefore, no improvement of transport-related properties is expected upon extreme reduction of the sample thickness to one structural layer (1.25 nm).

- [1] B. Rasche *et al.*, Nature Materials 12 (2013) 422.
- [2] C. Pauly *et al.*, Nature Physics 11 (2015) 338.
- [3] C. Pauly *et al.*, ACS Nano 10 (2016) 3995.
- [4] M. P. Ghimire and M. Richter, Nano Letters 17 (2017) 6303.
- [5] J. Alicea, Rep. Prog. Phys. 75 (2012) 076501.
- [6] P. Tang *et al.*, Phys. Rev. B 89 (2014) 041409.
- [7] H. Weng *et al.*, Phys. Rev. X 4 (2014) 011002.
- [8] B. Rasche *et al.*, Sci. Rep. 6 (2016) 20645.
- [9] C. Noguera *et al.*, Surf. Sci. 507 (2002) 245.
- [10] C.-C. Liu *et al.*, Phys. Rev. Lett. 116 (2016) 066801.
- [11] <http://www.fplo.de/>
- [12] L. A. Wray *et al.*, J. Phys.: Conf. Ser. 449 (2013) 012037.

Funding: Georg Forster Research Fellowship of the Alexander von Humboldt Foundation

Cooperation: TU Dresden, Germany; RWTH Aachen, Germany.

Research Area 4

Surface Acoustic Waves: concepts, materials and applications

S. Biryukov, E. Brachman, A. Darinskii¹, T. Gemming, V. Hoffman, E. Lattner, S. Menzel, S. Oswald, E. Park, G. Rane, H. Schmidt, M. Seifert, A. Sotnikov, M. Weihnacht², R. Weser, A. Winkler

Abstract: Besides fundamental investigations on the dynamic behavior of polar dielectrics our main research was devoted to the application-oriented fields of micro-acoustics. Highlighted topics comprise the utilization of surface acoustic waves (SAW) in the two growing branches of next generation SAW devices, namely acoustofluidic devices and wireless, self-sufficient sensors for harsh environments. For the first branch, the implementation of SAW actuators in advanced fluidic setups was investigated, e.g. for the controlled generation of aerosols by compact and mass-producible devices and regarding the exploitation of SAW electric fields to enhance streaming in microfluidic channels of lab-on-a-chip systems. For the second branch, we investigated two of the most important aspects for high temperature sensors, i.e. the establishment of novel electrode metallization systems with increased temperature capability as well as the precise microacoustic characterization of promising piezoelectric crystal materials.

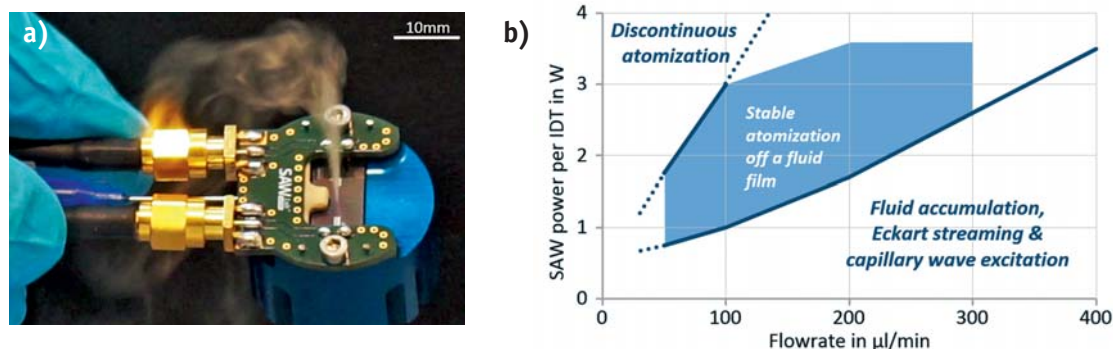
Compact SAW aerosol generator

Surface acoustic wave (SAW) aerosol generators hold substantial promise for therapeutic and industrial applications, including medical inhalators, particle and film synthesis, olfactory displays and mass spectrometry. In previous studies, the aerosol generation from different fluids including such with high viscosity [1] and issues of power efficiency in SAW devices were investigated [2]. Furthermore, a new application in the field of aerosol based film deposition [3] was demonstrated in the IFW Dresden.

Based on extensive fundamental and applied material research efforts in combination with technology development, a compact SAW aerosol generator, mass-producible by highly accurate standard techniques and on-chip integrated fluid supply, was developed [4]. This setup was employed to investigate relevant influences on the acoustofluidic interaction, including the local acoustic wave field, the electric load power, the fluid flow rate and the fluid supply position.

In SAW atomization, aerosol droplets originate from a fluid film stabilized by the acoustofluidic interaction on the chip surface. The driving force is a balance between acoustic radiation pressure and capillary stress, leading to film shaping based on the standing acoustic wave field, i.e. the lateral distribution of the SAW amplitude. Therefore, the acoustic wave field and the geometrical boundary conditions of the fluid supply are crucial for the device operation, defining the fluid film extension, the transient device behavior and the aerosol generation. Based on our studies, criteria for the design of ideal SAW atomization chips were formulated. With accordingly improved experimental conditions, a stable atomization was achieved in a broad range of power and flowrate combinations, different atomization regimes were identified, and the possibility of droplet size distribution tailoring was demonstrated (Fig. 1).

Fig. 1: a) Compact SAW aerosol generator during Ethanol atomization (140 $\mu\text{l}/\text{min}$), **b)** Atomization regimes observed for a 90 μm SAW chip and water with improved fluid supply position



Depending on the intended task, the future use of SAW aerosol generators based on disposable chips or chips with long lifetime is possible. Additionally, the setup is compatible to the future integration together with other microfluidic components, miniaturized fluid reservoirs / pumps and intelligent electronics for more complex signaling and analysis.

SAW electric field effect on acoustic streaming

When studying the fundamentals of acoustic streaming, one commonly takes into account only the force related to the high-frequency acoustic field in the liquid as a second-order effect. However, in SAW-driven microfluidic devices, the initial wave propagates along the surface of a strong piezoelectric substrate, typically LiNbO_3 . Hence, the SAW induces in the liquid not only an acoustic field, but also an electric field. The latter polarizes the liquid and, correspondingly, exerts on it an instantaneous force with quadratic dependence on the electric field. As a result, a time-independent non-conservative force appears which is able to set in motion the liquid in a closed channel.

Our investigations reveal that the ‘electric’ contribution due to the electric field accompanying the SAW can be comparable to, or even more significant than, the ‘mechanical’ contribution due to the acoustic field which is generated in the liquid by the SAW [5]. An example is depicted in Fig. 2.

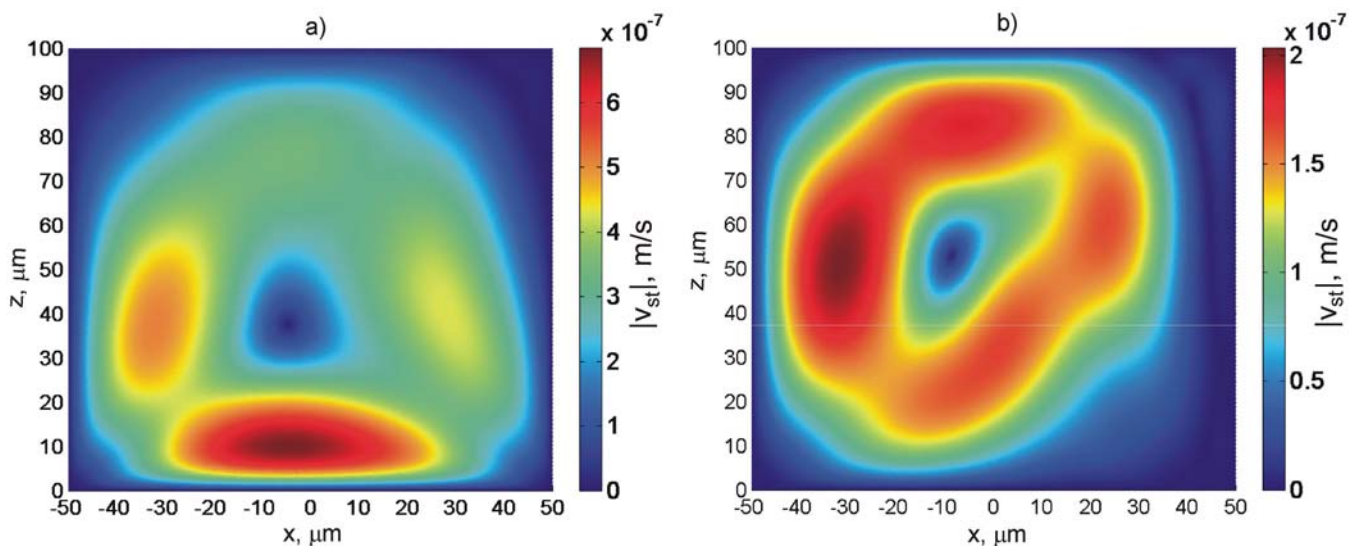


Fig. 2: Absolute values of the streaming velocity v_{st} in pure water; **(a)** the effect of combined ‘electric’ force and ‘mechanical’ force; **(b)** only the mechanical force is taken into account. The acoustic streaming is activated by the leaky SAW propagating on 64°Y -rotated LiNbO_3 . The channel x-z cross section is $100 \times 100 \mu\text{m}^2$, the leaky SAW wavelength is $100 \mu\text{m}$.

The electric force can be significant only at distances from the channel bottom not exceeding half wavelength, in contrast to the mechanical force acting over the whole channel. Therefore, the electric field effect weakens with increasing the channel height since the relative volume of the channel space where the electric force drives the acoustic streaming reduces. The frequency dependence of the relative contribution of these two forces is controlled by the frequency dependence of the dielectric loss in the liquid. The relative contribution of the electric field decreases with increasing the liquid viscosity.

High temperature SAW device electrode metallization

Another current research topic is the development of wireless temperature sensor devices for high temperature range above 400°C based on the SAW operation principle. To realize such devices, high demands are put on the high temperature stability of the piezoelectric substrate, the metallization for the interdigital transducers as well as of the

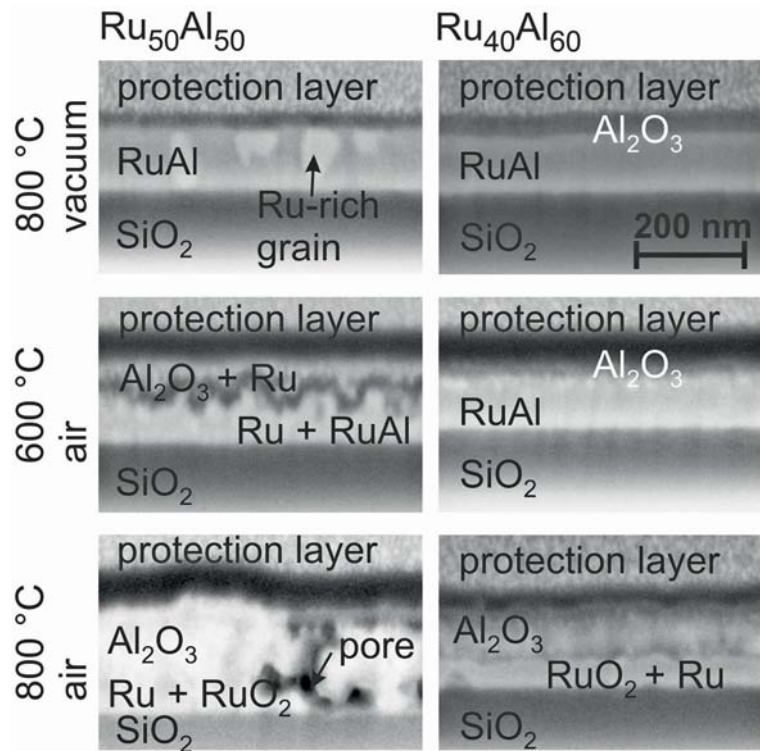


Fig. 3: Cross section images of RuAl thin films with various compositions after annealing for 10 h at 800°C under high vacuum and at 600 and 800°C in air.

antenna. In 2017, a preparation routine for the deposition of Pt antennae on Al_2O_3 high temperature ceramics was developed using a combination of electron beam evaporation of a 100 nm Pt seed layer and subsequent electrochemical deposition of a thicker Pt layer, respectively, to reach a total Pt film thickness of about 1 μm [6]. A second key aspect concerned the optimization of the cleaning procedure for both, the ceramic and the piezoelectric substrates prior to the film deposition since any contamination on the substrate surface might deteriorate the adhesion of the grown film. For $\text{Ca}_3\text{TaGa}_3\text{Si}_2\text{O}_{14}$ (CTGS), a two-step cleaning procedure combining a SC-1 cleaning at a reduced temperature of 30°C and a subsequent UV-ozone cleaning prior to deposition of the metallization resulted in lowest residual contamination [7].

In one of our most promising metallizations, RuAl, a high-temperature treatment at above 600°C leads to an oxidation of Al to Al_2O_3 at the sample surface even under high vacuum conditions and to a chemical reaction with the CTGS substrate. The latter is successfully suppressed by introducing a 10 nm SiO_2 barrier layer at the interface [8]. The lack of Al due to aluminum oxidation at the surface was tried to be countered by increasing the nominal Al content in the films. The study of a wide range of film composition (series of $\text{Ru}_{100-x}\text{Al}_x$, $x = 50, 55, 60, 67$) showed that after heat treatment the films are more homogeneous (Fig. 3) but the RuAl phase formation is reduced [9]. However, extended layers of this material are stable up to 900°C under high vacuum and up to 600°C in air, respectively.

High precision microacoustic material data set for CTGS single crystal

Since the beginning of using piezoelectric single crystals for highly-precise microacoustic components rigorous knowledge of material constant (MC) sets was an indispensable requirement. The sets have to be both accurate and complete. Accuracy is important for acceptable agreement between device simulation and experimental reality, completeness preferentially plays a role for finding out figure-of-merit issues for optimum practical use of crystals. The present material under study is CTGS. It belongs to the point group 32, i.e., it has 10 electromechanical MC's, in addition to the mass density. The aim of our work was to develop calculation ways of accuracies and to use this knowledge for getting optimum combinations of SAW experiments for the best MC extraction.

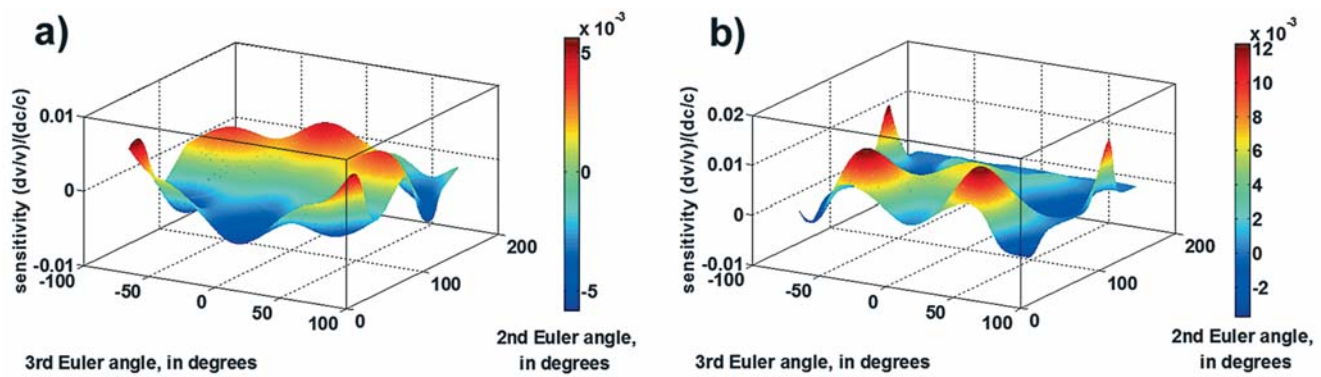


Fig. 4: Sensitivity of SAW velocity in CTGS w.r.t. the considered material constant as a function of 2nd and 3rd Euler angle (1st Euler angle: 0°); **a)** elastic constant c_{14} , **b)** piezoelectric constant e_{11} .

On the base of the least squares method which is arranged to our problem of fitting theoretical to experimental values of crystal orientation dependent SAW phase velocity the surroundings of the minimum sum (MSS) of velocity deviation squares has been analyzed, similarly to [10]. This was done by forming a 'sensitivity matrix' (or Jacobian matrix: derivatives of each considered velocity w.r.t. each searched MC) based on a MC set found in first approximation. Figures 4a and 4b depict examples of such matrices demonstrating quite different sensitivity dependencies on orientation which is an important condition for successful MC extraction. The subsequent evaluation of the quadratic dependence of MSS on all MC's enables to obtain the full set of MC accuracies.

We have demonstrated that angular dependent measurements of SAW velocities combining samples with different surface orientations, e.g. on Y-cut, 45°rotated Y-cut, 135°rotated Y-cut, and X-cut result in a distinctly more accurate set of MC's with uncertainties up to 2 orders smaller compared to experiments on samples with only one surface orientation (Y-cut) [11].

- [1] A. Winkler et al., J. Sol-Gel Sci. and Techn. 78 (2016) 26.
- [2] A. Winkler et al. Sens Act A: Physical 247 (2016) 259-268.
- [3] A. Winkler et al., Open Journal of Acoustics 6 (2016) 23-33.
- [4] A. Winkler et al., Biomedical Microdevices 19:9 (2017).
- [5] A.N. Darinskii et al., J. Appl. Phys. 123, 014902 (2018).
- [6] M. Seifert et al., Materials 10 (2017) 54.
- [7] E. Brachmann et al., Materials 12 (2017) 1373.
- [8] M. Seifert et al., J. Alloys Compd. 668 (2016) 228
- [9] M. Seifert et al., Materials 10 (2017) 277.
- [10] G. Kovacs et al., Proc. IEEE 1988 Ultrasonics Symp. (1988) 269.
- [11] M. Weihnacht et al., Proc. 2017 IEEE Ultrasonics Symp. (2017).

Funding: BMBF InnoProfile-Transfer (03IPT610Y HoBelAB); Deutsche Forschungsgemeinschaft (SCHM 2365/14-1, SO 1085/2-1); DAAD PPP Australia, IFW Excellence Program; Creavac, SAW Components Dresden, Vectron International

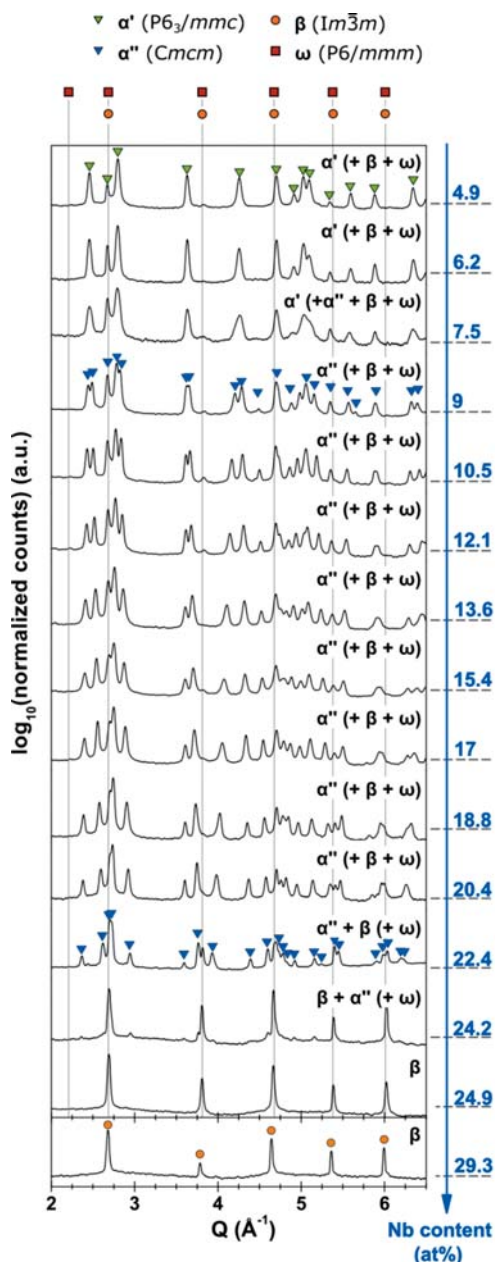
Cooperation: TU Dresden; TU Clausthal, Goslar; Fraunhofer IWS Dresden; Ioffe Physical Technical Institute RAS, St. Petersburg, Russia; ¹Institute of Crystallography RAS, Moscow, Russia; Monash University Melbourne, Australia; Singapore University of Technology and Design SUTD, Singapore

Industry: BelektroniG; Creavac; Lumicks, Netherlands; ²InnoXacs; SAW Components Dresden; Vectron International

Materials for Biomedical Applications

A. Gebert, M. Calin, M. Bönisch, S. Pilz, R. Schmidt, I. Lindemann, D. Geißler, M. Uhlemann, A. Voß, S. Oswald, V. Hoffmann, T. Gemming, J. Freudenberger

Abstract: Metastable Ti alloys are new materials of load-bearing implants for hard tissue support. Suitable mechanical biofunctionality demands much lower stiffness than present clinical implants combined with high strength, fatigue and wear resistance, as well as excellent biocompatibility. Alloys based on the metastable Ti-Nb system are particularly promising: Selecting composition and thermomechanical processing paths for controlled adjustment of microstructural parameters leads to phase configurations which yield outstanding mechanical properties. Activation of athermal and isothermal phase transformations through recently uncovered precipitation pathways opens new microstructural design approaches. Furthermore, α'' martensite exhibits some of the largest thermal expansion rates ever reported for solid crystalline metals (giant thermal expansion). For cast β -type Ti-40Nb alloys recrystallization and cold rolling routes were developed resulting in significant tensile strength increase while maintaining the Young's modulus low (~ 60 GPa). Alternatively, powder metallurgical processing can generate nanostructured states with remarkable strength. For improved surface bioactivity of β -type Ti-Nb alloys anodization treatments were successfully developed to grow oxide layers with characteristic morphologies at the nano- and microscale. From those alloys osteosynthesis plates were produced according to industrial standards.



Phase formation and unusual thermal behaviour in the metastable Ti-Nb system

In collaboration with a research team from University of Ioannina (Greece) a fundamental experimental and theoretical study concerning the formation of phases in the metastable Ti-Nb system, their crystallographic structure and electronic properties was conducted, aiming to enlighten the electronic origins of the β -phase stability. Both quantum-mechanical calculations and X-ray diffraction found several structural phases depending on the Nb concentration [1]. Fig. 1 shows X-ray diffraction patterns of cast and homogenized Ti-xNb ($x \leq 29.3$ at.%; 45.8 wt.%) alloy samples. The main structural constituent in these alloys is either α' , α'' or β . In all martensitic alloys minor amounts of ω and/or retained β are present. In Nb-lean alloys containing less than 9 at.% Nb mainly hexagonal martensite α' was found. Alloys with Nb contents from 9 at.% to 20.4 at.% consist primarily of the orthorhombic martensite α'' . Besides α'' , alloys containing 22.4 at.% Nb and more contained increasing amounts of retained β that did not transform into martensite by quenching. For Nb contents higher than 24.9 at.% (38 wt.%) no secondary phases were detected besides the β -phase.

Since the discovery of shape memory (SM) effects in Ti-Nb this system serves as a prototype to study SM in Ni-free Ti alloys. The transformation pathways triggered by heating of α'' martensite depend on the Nb content [2]. Calorimetry (DSC) analysis at a constant heating rate was conducted for homogenized Ti-xNb alloys.

Reversion of α'' martensite followed by substantial ω_{iso} precipitation occurs for $x \geq 28.5$. In contrast, for $x \leq 21$ α'' decomposes directly into $\alpha + \beta$ phase mixture. Formation of ω_{iso} starts during the martensitic reversion of α'' for $x = 28.5$, whereas more than 100°C above the austenite finish temperature A_f for $x = 36$. During further heating ω_{iso} transforms back to β . For $x = 28.5$ this reaction overlaps and is followed by α precipitation.

Fig. 1: X-ray diffraction patterns of cast and homogenized Ti-Nb alloys (at. %) [1].

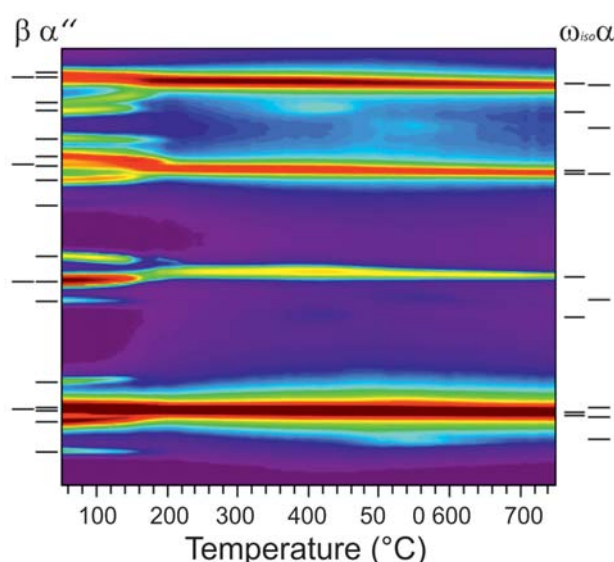


Fig. 2: Evolution of in situ synchrotron X-ray diffraction patterns of homogenized Ti-36Nb (wt.%): **left side** – initial phases; **right side** – phases formed during heating [2].

Variable-temperature synchrotron X-ray diffraction (SXRD) was employed to track these transformations in situ for the same alloys and new phases were detected including α , β , ω_{iso} , a Nb-depleted α'' (α''_{lean}) and a thermally formed α''_{iso} [2]. Fig. 2 shows exemplarily the pattern evolution during heating of Ti-36Nb up to 760°C confirming the formation of ω_{iso} and α . Using the diffractograms the lattice parameters for all phases were determined including the three types of α'' (martensite, α''_{lean} , α''_{iso}). The lattice parameters of α'' martensite are strongly affected by the Nb content. Nb-lean α'' is structurally closer to hcp α' whereas Nb-rich α'' is more similar to bcc β . The highlight of this study was the demonstration that α'' martensite displays both one of the largest positive and one of the largest negative linear thermal expansion coefficients α_L ever reported for solid crystalline metallic systems [2]. A remarkable anisotropy of the thermal expansion of α'' martensite for Ti-36Nb was observed: While the $a_{\alpha''}$ and $c_{\alpha''}$ spacings expand at a rate of $163.9 \times 10^{-6} \text{ } ^\circ\text{C}^{-1}$ and $24.4 \times 10^{-6} \text{ } ^\circ\text{C}^{-1}$, respectively, the $b_{\alpha''}$ spacing contracts by $-95.1 \times 10^{-6} \text{ } ^\circ\text{C}^{-1}$ between 50°C and 210°C. Fig. 3 illustrates this schematically. Typical values for α_L for engineering metals and alloys are positive and range between $0 - 40 \times 10^{-6} \text{ } ^\circ\text{C}^{-1}$. Expansion rates comparable to or larger than those for Ti-36Nb are only found for members of other material classes. In case of α'' martensite in Ti-Nb, the expansion and contraction along the unit cell edges partially compensate each other leading to a volumetric expansion rate α_V between $24.7 \times 10^{-6} \text{ } ^\circ\text{C}^{-1}$ and $91.0 \times 10^{-6} \text{ } ^\circ\text{C}^{-1}$.

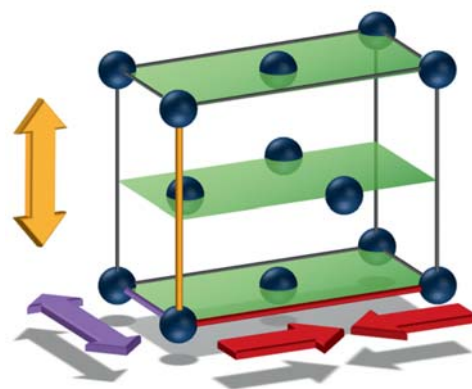
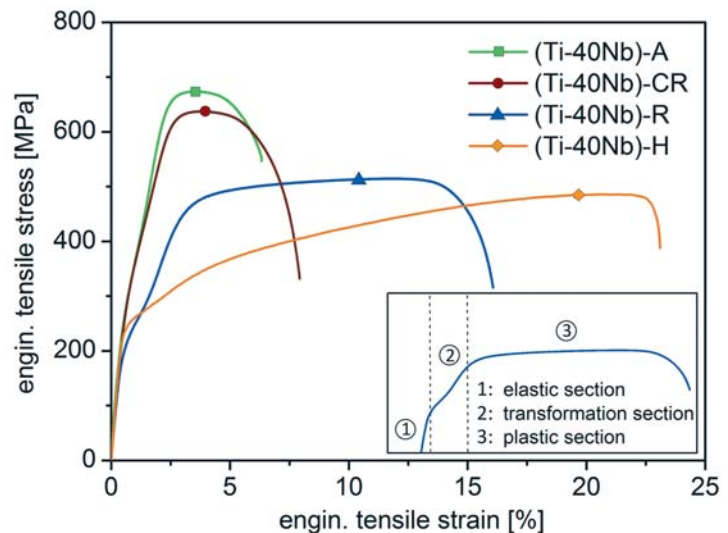


Fig. 3: Schematic illustration of the anisotropy of the thermal expansion of α'' martensite for Ti-36Nb (wt.%): $a_{\alpha''}$ and $c_{\alpha''}$ spacings expand at a rate of $163.9 \times 10^{-6} \text{ } ^\circ\text{C}^{-1}$ and $24.4 \times 10^{-6} \text{ } ^\circ\text{C}^{-1}$, b spacing contracts by $-95.1 \times 10^{-6} \text{ } ^\circ\text{C}^{-1}$ between 50 °C and 210 °C.

Thermomechanical processing of β -type Ti-Nb alloys

For β -type Ti-40Nb (wt.%) alloys thermomechanical processing routines were developed to evaluate the effectiveness of different hardening strategies for the improvement of their mechanical biofunctionality. The aim was to significantly increase the yield and tensile strength in comparison to the cast and homogenized state (H) while maintaining a very low Young's modulus of ≤ 60 GPa. Fig. 4 shows tensile test curves of Ti-40Nb samples after different processing treatments including warm and cold rolling as well as annealing steps. To exploit grain boundary hardening, a grain refinement of the β -phase was anticipated by a recrystallization treatment (R) and a significant drop of the grain size from 230 to 26 μm was achieved. The ultimate tensile strength was increased by 3% to 495 MPa, while the Young's modulus remained unchanged. Cold-rolling (CR) with 36% thickness reduction was applied after recrystallization and led to a pronounced work hardening which caused an increase of the ultimate tensile strength by about 32% to 650 MPa. The precipitation of small amounts of α -phase obtained by aging at 450°C (A) resulted in an increase of the ultimate tensile strength to 674 MPa. However, the Young's modulus also increased to 68 GPa. Therefore, the CR route was identified as the most promising one [3]. Those hardening strategies were found to be also transferrable to

Fig. 4: Tensile test curves of Ti-40Nb (wt.%) after different thermomechanical treatments: (H) homogenized, (R) recrystallized, (CR) cold rolled, (A) aged [3].



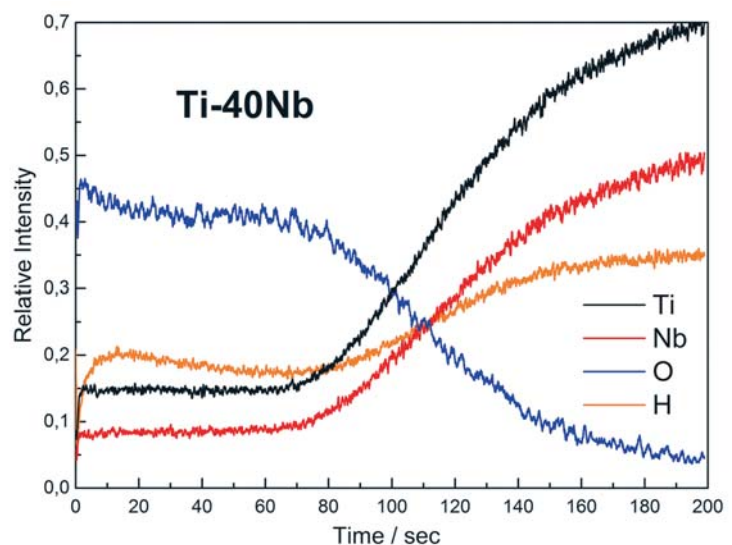
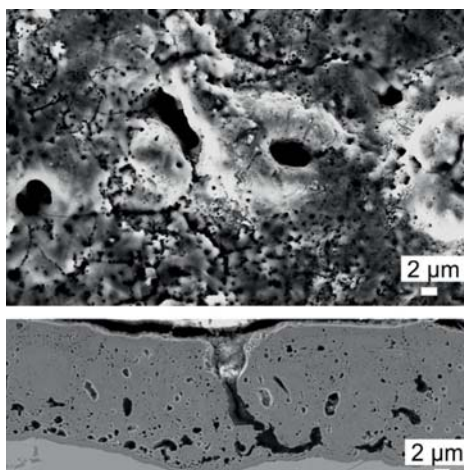
In-containing β -type Ti-Nb alloys with further reduced Young's modulus and indium effects on the deformation mechanisms, in particular on stress-induced martensite formation were discussed [4]. Alternatively, powder metallurgical processing of β -phase Ti-Nb alloys was successfully applied [5]. Hot compaction of gas-atomized and additionally intensively milled Ti-45Nb powder yielded fully dense samples with nanograin microstructure. Those exhibit a very high compressive yield strength of 940MPa and a low Young's modulus of 70 GPa. An efficient new approach to produce ultrafine-grained β -type Ti-Nb powder by reactive milling of the elements in hydrogen atmosphere was developed [6].

Surface engineering of Ti alloy surfaces for hard tissue implant application

For β -type Ti-40Nb alloys different anodization techniques were applied to grow oxide layers with characteristic morphologies at the nano- and microscale [7].

Anodization in fluoride-containing solutions generates self-organized oxide nanotube layers whereby the nanotubes have higher aspect ratios than those grown on cp2-Ti. The electrolyte composition has a significant influence on the resulting oxide morphology. The transfer of such anodization to Ti-Nb-Zr-Si metallic glass surfaces was demonstrated yielding double-wall oxide nanotubes with incorporation of all alloying constituents [8]. Those tubular structures are targeted as containers for drug-delivery systems. *Plasma electrolytic oxidation of Ti-40Nb in strongly alkaline solution* yields a two-layer oxide structure with a thin compact inner layer and a much thicker outer layer with micropores and microchannels, as shown in Fig. 5. The latter is due to spark discharging

Fig. 5: Surface state of Ti-40Nb (wt.%) after plasma electrolytic oxidation (PEO): SEM top surface and cross section and GDOES depth profile [7].



and arcing during the severe anodization process. In comparison to oxide growth on cp-Ti, on the β -phase alloy thickness growth is much more enhanced and slightly larger dimensions of micropores are detected. The oxides are crystalline mainly with rutile structure. In result of GD-OES depth profile analysis of treated alloy surfaces as shown in Fig. 5, these were identified as mixed oxides $(\text{Ti}_x\text{Nb}_{1-x})\text{O}_2$. *Inductively coupled RF oxygen plasma anodization* was done in cooperation with a team at JLU Gießen. It causes the formation of microstructured oxides on the Ti-40Nb surface. With increasing processing temperature a transition from random structured to patterned oxides was observed which is opposite to the trend for cp2-Ti. For all three techniques the oxide layer growth on the Ti-40Nb alloy follows the principal mechanisms that are established for Ti. Nb species are always involved in the oxidation processes which causes enhanced layer thickness growth, morphology changes and mixed oxides. All obtained oxide types are promising as coatings of bone implants for improved bioactivity.

In a pilot study, from thermomechanically processed β -type Ti-40Nb sheets osteosynthesis plates were manufactured by an industrial standard procedure developed for clinical Ti which comprises laser cutting, deburring and vibration grinding and surface anodization oxidation. A typical plate is shown in Fig. 6. In collaboration with a team from TU Dresden the fatigue behaviour of those plates and tensile test samples was analysed and superimposed influences of the surface state, the sample geometry and the microstructure were discussed [9].



Fig. 6: Osteosynthesis plate made of thermomechanically processed Ti-40Nb (wt. %) with industrial surface finish [9].

- [1] J.J. Gutierrez Moreno et al., J. Alloys Compd. 696 (2017) 481
- [2] M. Bönisch et al., Nature Communications 8 (2017) 1429
- [3] A. Helth, S. Pilz et al., J. Mechan. Beh. Biomed. Mater. 65 (2017) 137
- [4] S. Pilz et al., J. Mechan. Beh. Biomed. Mater. 79 (2018) 283
- [5] R. Schmidt et al., Powder Technol. 322 (2017) 393
- [6] I. Lindemann et al., J. Alloys Compd. 729 (2017) 1244
- [7] A. Gebert et al., Surf. Coat. Technol. 302 (2016) 88
- [8] H. Sopha et al., Mater. Sci. Eng. C 70 (2017) 258
- [9] A. Reck et al., Int. J. Fatigue 103 (2017) 147

Funding: DFG SFB/Transregio 79, DFG LI 2536/1, DFG SPP 1594 GE1106/11, EU ITN BioTiNet grant agreement 264635, EU ETN SELECTA grant agreement 642642

Cooperation: TU Dresden (G), TU Bergakademie Freiberg (G), Leibniz IPF Dresden (G), Justus-Liebig-Universität Giessen (G), University of Illinois at Urbana-Champaign (USA), University of Ioannina (Greece), Montanuniversität Leoben (Austria), University of Vienna (Austria), University of Pardubice (Czech Republic)

Ultra-high-strength tool steels prepared by selective laser melting and casting – a comparative study

J. Sander, J. Hufenbach, L. Giebeler, H. Wendrock, T. Gemming, U. Kühn

Abstract: Selective laser melting is an additive manufacturing process, which enables industrial scale production of complex shaped metal parts. Moreover, high cooling rates are realized in the SLM process leading to highly refined microstructure. This report shows the influence of the SLM process on a FeCrMoVC alloy regarding microstructure, behavior under compressive load, and wear resistance. A comparison is drawn with the cast state of the FeCrMoVC alloy and with commercial 1.2379 cold work tool steel (X153CrMoV12). The results demonstrate that the SLM process is beneficial to the investigated properties. SLM samples achieved a hardness of 65 HRC and a compression strength of 5300 MPa. Furthermore, the wear resistance of SLM processed samples is 65% higher in comparison to cast FeCrMoVC and 25% higher compared to that of commercial 1.2379. The increased wear resistance of SLM samples is caused by the successful prevention of carbide breakouts under wear load and the increased hardness.

General aspects

Tool steels are known for their marked wear resistance as well as hardness, strength, and adequate toughness. By an appropriate alloy design and manufacturing process, the microstructure and related properties of the tool steels can be tailored adjusted within a large spread. Thereby, as-cast steels may show an enhanced wear resistance and strength compared to heat-treated steels resulting in a longer tool life [1]. Though, the impact toughness of high-alloyed cast tool steels is in general lower compared to conventionally produced steels, due to the coarse carbide network along the primary grain boundaries [2]. However, by an appropriate grain refinement an increase in toughness and strength can be obtained.

Selective laser melting presents an additive manufacturing technology enabling a significant refinement of the grains and microstructural constituents due to very high solidification rates within the process. As shown in previous work, this leads to an increase of compression strength and hardness [3].

Various authors report a significantly different mechanical and wear behavior of SLM fabricated samples compared to their cast equivalents. For aluminum alloys [4,5], titanium alloys [6,7], CoCr alloys [8,9], and tool steels [10] an increase of the wear resistance of SLM produced parts could be observed. Although, there is no general increase of wear resistance with increasing material strength properties or hardness [11]. Further studies are necessary to fully understand the influence of the SLM process on the mechanical and wear properties.

Microstructure and mechanical behaviour of $\text{Fe}_{85}\text{Cr}_4\text{Mo}_8\text{V}_1\text{C}_1$

In Fig. 1 SEM images of the deep etched microstructure of the investigated FeCrMoVC modifications and the reference material is presented. The arrangement of the carbides is exposed.

The cast sample of the FeCrMoVC alloy consists of martensite (71 wt.%), retained austenite (24%), as well as Mo-rich M_2C ($\text{M}=\text{Mo}, \text{V}, \text{Cr}$) carbides (3 wt.%), and V-rich MC ($\text{M}=\text{V}, \text{Mo}$) carbides (2 wt.%) [13]. These complex carbides form a fine network-like structure as displayed in Fig. 1a. In Fig. 1b a SEM image of the reference steel (1.2379) is shown, which is composed of martensite (64 wt.%), retained austenite (3 wt.%), and dense isolated clusters of Cr_7C_3 carbides (33 wt.%). The FeCrMoVC SLM sample consists of martensite (73 wt.%), retained austenite (15 wt.%), carbides of the M_2C type

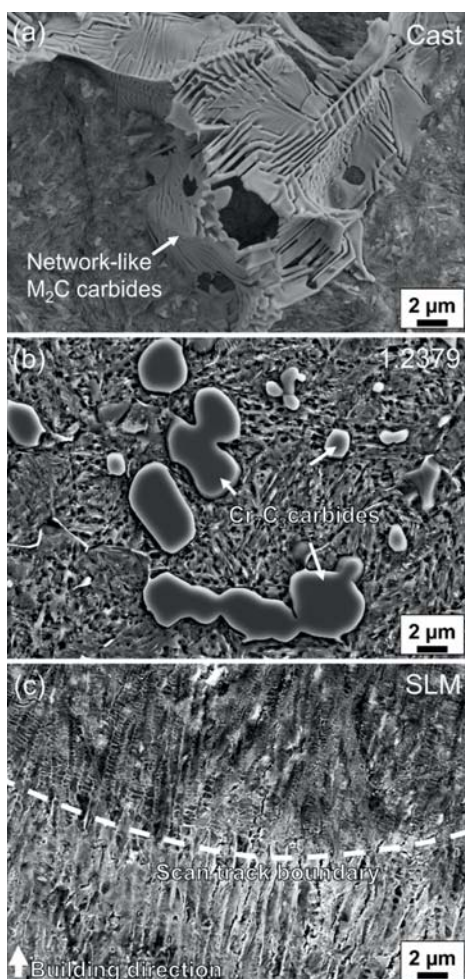


Fig. 1: SEM images of deep etched samples. **a)** cast state of the FeCrMoVC alloy, **b)** 1.2379 used as reference material, **c)** SLM sample of the FeCrMoVC alloy, here only the carbide network is visible.

(M=Mo, V, Cr) (6 wt.%), and MC (M=V, Mo) (6 wt.%). The carbide network has a long drawn cell structure (Fig. 1c) and is orientated in building direction. In comparison to the cast sample, the carbides are refined and homogeneously distributed. The refinement is caused by the high cooling rates in the SLM process, which are around one thousand times higher than in the presented casting process [3,13].

A summary of the mechanical properties of the tested alloys can be found in Tab. 1. The cast FeCrMoVC has a hardness of about 60 HRC, resulting of the high martensite content as well as the M_2C and MC carbides. Moreover, the compression strength is around 3500 MPa combined with a fracture strain of 17%. In comparison, the 1.2379 shows a hardness of 61 HRC due to the higher martensite content and the much higher carbide content. Nevertheless, the difference of the average hardness is only 1 HRC despite the 33 wt.% Cr_7C_3 carbides in the 1.2379 compared to 5 wt.% carbides in the cast sample. This is explained by the lower microhardness of the M_7C_3 carbides compared to M_2C and MC carbides [14]. The compression strength of the 1.2379 is 3200 MPa, whereby the fracture strain amounts 24%. The higher average compression strength of the cast FeCrMoVC sample mainly results from the network-like structure of the carbides and the deformation induced transformation of retained austenite into martensite [12]. However, the network-like structure of the M_2C carbides in the cast sample provides fracture sites [2], which lead to a reduced fracture strain compared to the 1.2379 steel.

The SLM sample has a significantly increased hardness of 65 HRC compared to the cast sample, an increased compression strength of 5326 MPa, and a fracture strain of 15.6%. This can be explained by the refined microstructure of the SLM sample and the homogeneously dispersion of alloying elements and carbides leading to a Hall-Petch strengthening [3]. Furthermore, the carbide and martensite content is increased, which provides high hardness but causes embrittlement and, consequently, lowers the fracture strain.

The different wear behavior of the tool steel samples are reflected by the wear rate (Tab. 1). The SLM samples show a significantly higher wear resistance compared to the cast FeCrMoVC samples and the 1.2379 reference steel. Fig. 2 presents height mappings and SEM images of the wear surfaces. It is observable that with decreasing wear rate also the roughness of the wear surface decreases. This is because of the decreasing depth

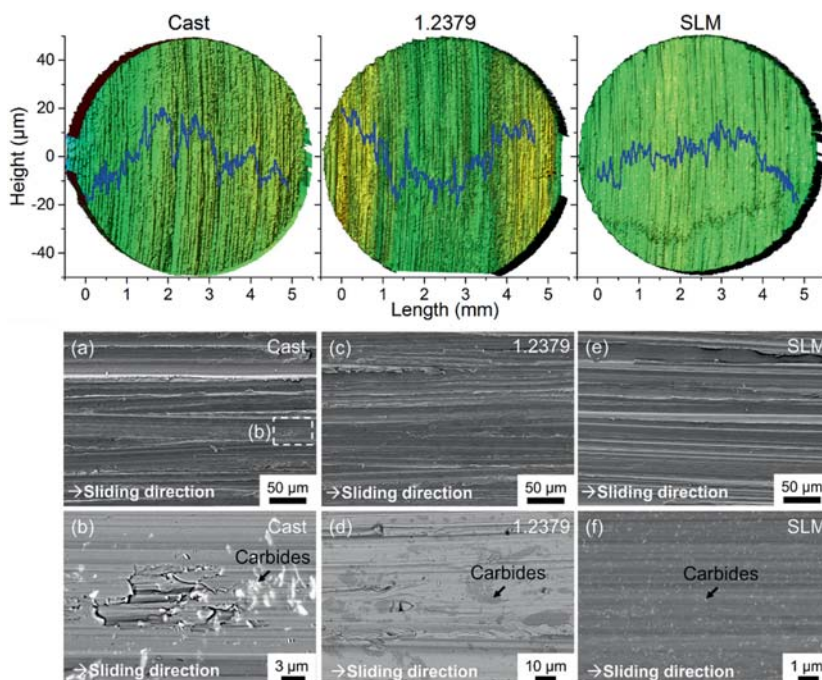


Fig. 2: Height mappings and SEM images of the wear surfaces of cast FeCrMoVC (a, b), 1.2379 reference (c, d), and SLM processed FeCrMoVC (e, f) samples.

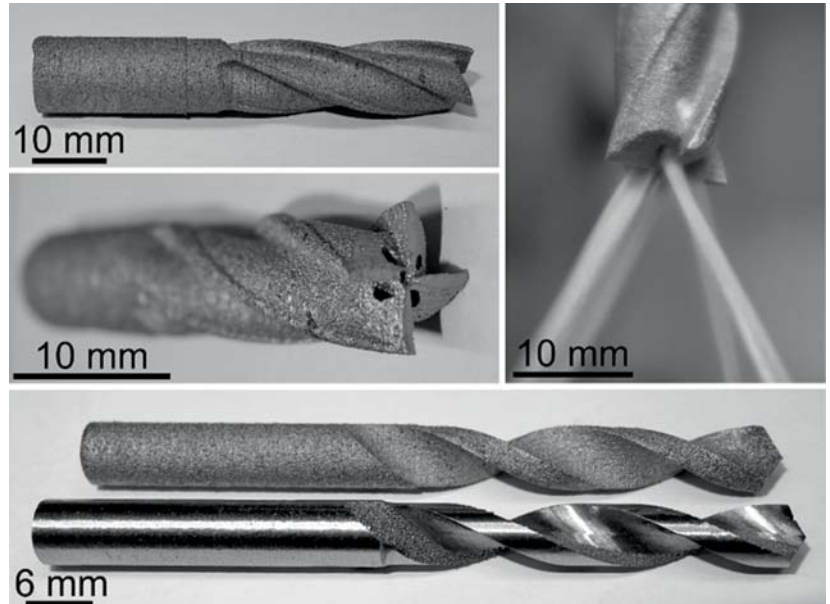
	Hardness (HRC)	Wear rate (mm ³ /Nm)	Compression strength (MPa)	Fracture strain (%)
1.2379	61	0.06039	3190	24
Cast FeCrMoVC	59	0.08379	3536	17
SLM FeCrMoVC	65	0.04506	5326	16

Tab. 1: Mechanical properties of SLM processed FeCrMoVC, cast FeCrMoVC, and 1.2379 reference sample.

of the scratches. The depth of the scratches is strongly influenced by the morphology and properties of the phase constituents of the tested materials. With increasing hardness of phases, a decreasing penetration depth of the abrasive SiC-particles of the grinding wheel was observed, leading to less material removal. Microcutting and microploughing are the underlying wear mechanisms and, amongst other things, depend on the hardness of the material [15]. However, bearing in mind the similar hardness of the cast samples and the 1.2379 further influences than the hardness need to be considered.

The SEM images of the wear surfaces reveal additional wear mechanisms. The type, shape, size, and volume fraction of the carbides play an important role in wear behavior. The M_2C and MC carbide types are reported to have high hardness and fracture toughness [14], leading to high wear resistance against softer abrasives, but they also tend to break out in larger areas [16]. Those breakouts can be observed in the cast sample in Fig. 3b. The Cr_7C_3 type carbides in the 1.2379 are softer than the M_2C and MC carbide types [14]. Consequently, they are cut by harder abrasives instead of breaking out [16] visible in Fig. 1d. This behavior and the higher carbide content is cause for the higher wear resistance of the 1.2379 compared to the cast FeCrMoVC sample.

Fig. 3: Application-oriented parts were manufactured.
Top: milling cutter with integrated cooling channels.
Bottom: drill with integrated cooling channels, after SLM process and after grinding, sharpening, and testing.



The carbides in the SLM sample are of the same type as in the castings, but occur in higher volume fractions (M_2C and MC type). Nevertheless, no breakout areas have been found on the wear surface. Fig. 1c and Fig. 2f show the structure of the carbides in the SLM sample. They are highly refined and arranged in a continuous network structure compared to the carbides in the as cast sample (Fig. 1a, Fig. 2a). Consequently, they have a bigger surface and stronger bonding to the matrix, which prevents breakouts. The combination of a high matrix hardness, high carbide content, and homogeneously dispersed carbide phases, leads to a tailored microstructure and, therefore, to superior wear resistance of SLM processed FeCrMoVC alloy.

Conclusions

The investigated mechanical properties of SLM processed FeCrMoVC alloy benefit from the refinement of the microstructure resulting from the high cooling rates in the SLM process. In fact, the compression strength, hardness, and wear resistance are significantly increased compared to the cast state and 1.2379 reference steel. The reason is given by the enhanced hardness and the prevention of carbide breakouts, which appeared in the cast state.

Application-orientated parts have been built to show the potential of this technology (Fig. 3). A milling cutter with integrated cooling channels, as well as, a drill with integrated cooling channels was produced. The drill has been grinded and sharpened and was successfully tested. In conclusion, the SLM process is advantageous for the processing of high-strength FeCrMoVC tool steel.

- [1] J. Hufenbach et al., *Mater. Sci. Eng. A* 586 (2013) 267
- [2] K. C. Hwang et al., *Mater. Sci. Eng. A* 254 (1998) 296
- [3] J. Sander et al., *Materials & Design* 89 (2016) 335
- [4] K. G. Prashanth et al., *J. Mater. Res.* 31(01) (2016) 55
- [5] N. Kang et al., *Materials & Design* 99 (2016) 120
- [6] H. Attar et al., *Mat. Lett.* 142 (2015) 38
- [7] D. Gu et al., *Comp. Sci. Techn.* 71(13) (2011) 1612
- [8] F. S. Schwindling et al., *Tribol. Lett.* 60(2) (2015)
- [9] T. V. Tarasova et al., *J. Frict. Wear* 35(5) (2014) 365
- [10] S. Kumar et al., *Adv. Eng. Mater.* 10(8) (2008) 750
- [11] A. Tsouknidas et al., *Advances in Tribology* 2011 (2) (2011) 1
- [12] U. Kühn et al., *Appl. Phys. Lett.* 90(26) (2007) 261901
- [13] J. Hufenbach et al., *Acta Mater.* 60(11) (2012) 4468
- [14] D. Casellas et al., *Acta Mater.* 55(13) (2007) 4277
- [15] H. Czichos et al., *Tribologie-Handbuch*, Vieweg+Teubner Verlag (2010) 143
- [16] F. Bergman et al., *Tribology Inter.* 30(3) (1997) 183

Funding: Wehrwissenschaftliches Institut für Werk- und Betriebsstoffe (WIWeB), Erding

Cooperation: Wehrwissenschaftliches Institut für Werk- und Betriebsstoffe (WIWeB), Erding; Dep. Mechanical Engineering of the Research Technology of IFW re captions

Publications and invited talks 2017

Journal Papers

- 1) M.A. Abdulmalic, S. Weheabby, F.E. Meva, A. Aliabadi, V. Kataev, B. Buechner, F. Schleife, B. Kersting, T. Rueffer, *Probing the magnetic superexchange couplings between terminal Cu^{II} ions in heterotrinnuclear bis(oxamidato) type complexes*, Beilstein Journal of Nanotechnology 8 (2017), S. 789-800.
- 2) J. Aberl, P. Klenovsky, J.S. Wildmann, J. Martin-Sanchez, T. Fromherz, E. Zalo, J. Humlicek, A. Rastelli, R. Trotta, *Inversion of the exciton built-in dipole moment in In(Ga)As quantum dots via nonlinear piezoelectric effect*, Physical Review B 96 (2017) Nr. 4, S. 45414/1-6.
- 3) R. Adam, M. Lepple, N.A. Mayer, D.M. Cupid, Y. Qian, P. Niehoff, F.M. Schappacher, D. Wadewitz, G. Balachandran, A. Bahaskar, N. Bramnik, V. Klemm, E. Ahrens, L. Giebeler, F. Fauth, C.A. Popescu, H.J. Seifert, M. Winter, H. Ehrenberg, D. Rafaja, *Coexistence of conversion and intercalation mechanisms in lithium ion batteries: Consequences for microstructure and interaction between the active material and electrolyte*, International Journal of Materials Research 108 (2017) Nr. 11, S. 971-983.
- 4) C.E. Agrapidis, S.-L. Drechsler, J. van den Brink, S. Nishimoto, *Crossover from an incommensurate singlet spiral state with a vanishingly small spin gap to a valence-bond solid state in dimerized frustrated ferromagnetic spin chains*, Physical Review B 95 (2017) Nr. 22, S. 220404/1-5.
- 5) S. Agrestini, C.-Y. Kuo, D. Mikhailova, K. Chen, P. Ohresser, T.W. Pi, H. Guo, A.C. Komarek, A. Tanaka, Z. Hu, L.H. Tjeng, *Intricacies of the Co³⁺ spin state in Sr₂Co_{0.5}Ir_{0.5}O₄: An x-ray absorption and magnetic circular dichroism study*, Physical Review B 95 (2017), S. 245131/1-7.
- 6) M. Ahmad, E. Mueller, C. Habenicht, R. Schuster, M. Knupfer, B. Buechner, *Semiconductor-to-metal transition in the bulk of WSe₂ upon potassium intercalation*, Journal of Physics: Condensed Matter 29 (2017) Nr. 16, S. 165502/1-5.
- 7) D.Y. Ahn, D.Y. Lee, C.Y. Shin, H.T. Bui, N.K. Shrestha, L. Giebeler, Y.Y. Noh, S.-H. Han, *Novel Solid-State Solar Cell Based on Hole-Conducting MOFSensitizer Demonstrating Power Conversion Efficiency of 2.1%*, ACS Applied Materials and Interfaces 9 (2017) Nr. 15, S. 12930-12935.
- 8) K. Al Khalyfeh, J.F. Nawroth, M. Uhlemann, U. Stoeck, L. Giebeler, R. Jordan, A. Hildebrandt, *Anionic polymerization of multi-vinylferrocenes*, Journal of Organometallic Chemistry 853 (2017), S. 149-158.
- 9) R. Al-Shewiki, C. Mende, R. Buschbeck, P.F. Siles, O.G. Schmidt, T. Rueffer, H. Lang, *Synthesis, spectroscopic characterization and thermogravimetric analysis of two series of substituted (metallo)tetraphenylporphyrins*, Beilstein Journal of Nanotechnology 8 (2017), S. 1191-1204.
- 10) A. Aliabadi, B. Buechner, V. Kataev, T. Rueffer, *The interplay between spin densities and magnetic superexchange interactions: case studies of monoand trinuclear bis(oxamato)-type complexes*, Beilstein Journal of Nanotechnology 8 (2017), S. 2245-2256.
- 11) M.T. Allen, O. Shtanko, I.C. Fulga, J.I.-J. Wang, D. Nurgaliev, K. Watanabe, T. Taniguchi, A.R. Akhmerov, P. Jarillo-Herrero, L.S. Levitov, A. Yacoby, *Observation of Electron Coherence and Fabry-Perot Standing Waves at a Graphene Edge*, Nano Letters 17 (2017) Nr. 12, S. 7380-7386.
- 12) K. Assim, S. Schulze, M. Puegner, M. Uhlemann, T. Gemming, L. Giebeler, M. Hietschold, T. Lampke, H. Lang, *Co(II) ethylene glycol carboxylates for Co₃O₄ nanoparticle and nanocomposite formation*, Journal of Materials Science 52 (2017) Nr. 11, S. 6697-6711.
- 13) H. Attar, S. Ehtemam-Haghighi, D. Kent, I.V. Okulov, H. Wendrock, M. Boenisch, A.S. Volegov, M. Calin, J. Eckert, M.S. Dargusch, *Nanoindentation and wear properties of Ti and Ti-TiB composite materials produced by selective laser melting*, Materials Science and Engineering A 688 (2017), S. 20-26.
- 14) S.M. Avdoshenko, A. Das, R. Satija, G.A. Papoian, D.E. Makarov, *Theoretical and computational validation of the Kuhn barrier friction mechanism in unfolded proteins*, Scientific Reports 7 (2017), S. 269/1-14.
- 15) Avigo, S. Thirupathaiah, E.D.L. Rienks, L. Rettig, A. Charnukha, M. Ligges, R. Cortes, J. Nayak, H.S. Jeevan, T. Wolf, Y. Huang, S. Wurmehl, M.I. Sturza, P. Gegenwart, M.S. Golden, L.X. Yang, K. Rosnagel, M. Bauer, B. Buechner, M. Vojta, M. Wolf, C. Felser, J. Fink, U. Bovensiepen, *Electronic structure and ultrafast dynamics of FeAs-based superconductors by angle- and time-resolved photoemission spectroscopy*, Physica Status Solidi B 254 (2017) Nr. 1, S. 1600382/1-15.
- 16) D. Baczysmaliski, F. Karnbach, G. Mutschke, X. Yang, K. Eckert, M. Uhlemann, C. Cierpka, *Growth and detachment of single hydrogen bubbles in a magnetohydrodynamic shear flow*, Physical Review Fluids 2 (2017) Nr. 9, S. 93701/1-19.
- 17) S.-H. Baek, S.-H. Do, K.-Y. Choi, Y.S. Kwon, A.U.B. Wolter, S. Nishimoto, J. van den Brink, B. Buechner, *Evidence for a Field-Induced Quantum Spin Liquid in alpha-RuCl₃*, Physical Review Letters 119 (2017) Nr. 3, S. 37201/1-5.

- 18) A. Bajpai, Z. Aslam, S. Hampel, R. Klingeler, N. Grobert, *A carbon-nanotube based nano-furnace for in-situ restructuring of a magnetoelectric oxide*, Carbon 114 (2017), S. 291-300.
- 19) J. Balach, T. Jaumann, L. Giebeler, *Nanosized Li₂S-based cathodes derived from MoS₂ for high-energy density Li-S cells and Si-Li₂S full cells in carbonate-based electrolyte*, Energy Storage Materials 8 (2017), S. 209-216.
- 20) S. Bance, F. Bittner, T.G. Woodcock, L. Schultz, T. Schrefl, *Role of twin and anti-phase defects in MnAl permanent magnets*, Acta Materialia 131 (2017), S. 48-56.
- 21) V.K. Bandari, L. Varadharajan, L. Xu, A.R. Jalil, M. Devarajulu, P.F. Siles, F. Zhu, O.G. Schmidt, *Charge transport in organic nano-crystal diodes based on rolled-up robust nanomembrane contacts*, Beilstein Journal of Nanotechnology 8 (2017), S. 1277-1282.
- 22) E.D. Barriga-Castro, J. Garcia, R. Mendoza-Resendez, V.M. Prida, C. Luna, *Pseudo-monocrystalline properties of cylindrical nanowires confined by electrodeposition in nanoporous alumina templates*, RSC Advances 7 (2017) Nr. 23, S. 13817-13826.
- 23) S. Bera, B. Sarac, S. Balakin, P. Ramasamy, M. Stoica, M. Calin, J. Eckert, *Micro-patterning by thermoplastic forming of Ni-free Ti-based bulk metallic glasses*, Materials and Design 120 (2017), S. 204-211.
- 24) X. Bian, G. Wang, Q. Wang, B. Sun, I. Hussain, Q. Zhai, N. Mattern, J. Bednarcik, Eckert J., *Cryogenic-temperature-induced structural transformation of a metallic glass*, Materials Research Letters 5 (2017) Nr. 4, S. 284-291.
- 25) X.L. Bian, G. Wang, J. Yi, Y.D. Jia, J. Bednarcik, Q.J. Zhai, I. Kaban, B. Sarac, M. Muehlbacher, F. Spieckermann, J. Keckes, J. Eckert, *Atomic origin for rejuvenation of a Zr-based metallic glass at cryogenic temperature*, Journal of Alloys and Compounds 718 (2017), S. 254-259.
- 26) F. Bittner, J. Freudenberger, L. Schultz, T.G. Woodcock, *The impact of dislocations on coercivity in L1₀-MnAl*, Journal of Alloys and Compounds 704 (2017), S. 528-536.
- 27) F. Bittner, L. Schultz, T.G. Woodcock, *The role of the interface distribution in the decomposition of metastable L1₀-Mn₅₄Al₄₆*, Journal of Alloys and Compounds 727 (2017), S. 1095-1099.
- 28) F. Bittner, T.G. Woodcock, L. Schultz, C. Schwoebel, O. Gutfleisch, G.A. Zickler, J. Fidler, K. Uestuener, M. Katter, *Normal and abnormal grain growth in fine-grained Nd-Fe-B sintered magnets prepared from He jet milled powders*, Journal of Magnetism and Magnetic Materials 426 (2017), S. 698-707.
- 29) A. Boehnke, U. Martens, C. Sterwerf, A. Niesen, T. Huebner, M. von der Ehe, M. Meinert, T. Kusschel, A. Thomas, C. Heiliger, M. Muenzenberg, *Large magneto-Seebeck effect in magnetic tunnel junctions with half-metallic Heusler electrodes*, Nature communications 8 (2017) Nr. 1, S. 1626/1-7.
- 30) M. Boenisch, A. Panigrahi, M. Calin, T. Waitz, M. Zehetbauer, W. Skrotzki, J. Eckert, *Thermal stability and latent heat of Nb-rich martensitic Ti-Nb alloys*, Journal of Alloys and Compounds 697 (2017), S. 300-309.
- 31) M. Boenisch, A. Panigrahi, M. Stoica, M. Calin, E. Ahrens, M. Zehetbauer, W. Skrotzki, J. Eckert, *Giant thermal expansion and a-precipitation pathways in Ti-alloys*, Nature Communications 8 (2017), S. 1429/1-9.
- 32) M. Boerner, L. Bloemer, M. Kischel, P. Richter, G. Salvan, D.R.T. Zahn, P. F. Siles, M.E.N. Fuentes, C.C.B. Bufon, D. Grimm, O.G. Schmidt, D. Breite, B. Abel, B. Kersting, *Deposition of exchange-coupled dinickel complexes on gold substrates utilizing ambidentate mercapto-carboxylato ligands*, Beilstein Journal of Nanotechnology 8 (2017), S. 1375-1387.
- 33) F. Boerrnert, H. Mueller, T. Riedel, T. Linck, A.I. Kirkland, M. Haider, B. Buechner, H. Lichte, *Corrigendum to: „A flexible multi-stimuli in-situ (S)TEM: Concept and optical performance“ [Ultramicroscopy 151 (2015) 31-36]*, Ultramicroscopy 182 (2017), S. 308.
- 34) N.A. Bogdanov, V. Bisogni, R. Kraus, C. Monney, K. Zhou, T. Schmitt, J. Geck, A.O. Mitrushchenkov, H. Stoll, J. van den Brink, L. Hozoi, *Orbital breathing effects in the computation of x-ray d-ion spectra in solids by ab initio wave-function-based methods*, Journal of Physics: Condensed Matter 29 (2017), S. 35502/1-7.
- 35) S. Borisenko, D. Evtushinsky, Z. Liu, I. Morozov, R. Kappenberger, S. Wurmehl, B. Buechner, A. Yaresko, T. Kim, M. Hoesch, T. Wolf, N. Zhigadlo, *The role of spin-orbit coupling in the electronic structure of iron-based superconductors*, Physica Status Solidi B 254 (2017) Nr. 1, S. 1600550/1-8.
- 36) E. Brachmann, M. Seifert, S. Oswald, S.B. Menzel, T. Gemming, *Evaluation of Surface Cleaning Procedures for CTGS Substrates for SAW Technology with XPS*, Materials 12 (2017), S. 1373.
- 37) D. Brick, V. Engemaier, Y. Guo, M. Grossmann, G. Li, D. Grimm, O.G. Schmidt, M. Schubert, V.E. Gusev, M. Hettich, T. Dekorsy, *Interface Adhesion and Structural Characterization of Rolled-up GaAs/In_{0.2}Ga_{0.8}As Multilayer Tubes by Coherent Phonon Spectroscopy*, Scientific Reports 7 (2017), S. 5385/1-8.
- 38) H. Bryja, R. Huehne, K. Iida, S. Molatta, A. Sala, M. Putti, L. Schultz, K. Nielsch, J. Haenisch, *Deposition and properties of Fe(Se,Te) thin films on vicinal CaF₂ substrates*, Superconductor Science and Technology 30 (2017) Nr. 11, S. 115008/1-8.

- 39) S. Buchenau, P. Sergelius, C. Wiegand, S. Baessler, R. Zierold, H.S. Shin, M. Ruebhausen, J. Gooth, K. Nielsch, *Symmetry breaking of the surface mediated quantum Hall Effect in Bi₂Se₃ nanoplates using Fe₃O₄ substrates*, 2D Materials 4 (2017) Nr. 1, S. 15044/1-7.
- 40) D. Buerger, S. Baunack, J. Thomas, S. Oswald, H. Wendrock, L. Rebohle, T. Schumann, W. Skorupa, D. Blaschke, T. Gemming, O.G. Schmidt, H. Schmidt, *Evidence for self-organized formation of logarithmic spirals during explosive crystallization of amorphous Ge:Mn layers*, Journal of Applied Physics 121 (2017) Nr. 18, S. 184901/1-15.
- 41) D.E. Bugaris, C.D. Malliakas, F. Han, N.P. Calta, M. Sturza, M.J. Krogstad, R. Osborn, S. Rosenkranz, J.P.C. Ruff, G. Trimarchi, S.L. Bud ko, M. Balasubramanian, D.Y. Chung, M.G. Kanatzidis, *Charge Density Wave in the New Polymorphs of RE₂Ru₃Ge₅ (RE = Pr, Sm, Dy)*, Journal of the American Chemical Society 139 (2017) Nr. 11, S. 4130-4143.
- 42) H.T. Bui, N.K. Shrestha, S. Khadtare, C.D. Bathula, L. Giebeler, Y.-Y. Noh, S.-H. Han, *Anodically Grown Binder-Free Nickel Hexacyanoferrate Film: Toward Efficient Water Reduction and Hexacyanoferrate Film Based Full Device for Overall Water Splitting*, ACS Applied Materials and Interfaces 9 (2017) Nr. 21, S. 18015-18021.
- 43) A.T. Burkov, S.V. Novikov, V.V. Khovaylo, J. Schumann, *Energy filtering enhancement of thermoelectric performance nanocrystalline Cr_{1-x}Si_x composites*, Journal of Alloys and Compounds 691 (2017), S. 89-94.
- 44) A.T. Burkov, S.V. Novikov, V.K. Zaitsev, H. Reith, *Transport properties of cobalt monosilicide and its alloys at low temperatures*, Semiconductors 51 (2017) Nr. 6, S. 689-691.
- 45) M. Burrello, I.C. Fulga, L. Lepori, A. Trombettoni, *Exact diagonalization of cubic lattice models in commensurate Abelian magnetic fluxes and translational invariant non-Abelian potentials*, Journal of Physics a-Mathematical and Theoretical 50 (2017) Nr. 45, S. 455301/1-26.
- 46) F. Caglieris, A. Leveratto, I. Pallecchi, F. Bernardini, M. Fujioka, Y. Takano, L. Repetto, A. Jost, U. Zeitler, M. Putti, *Quantum oscillations in the SmFeAsO parent compound and superconducting SmFeAs(O,F)*, Physical Review B 96 (2017) Nr. 10, S. 104508/1-5.
- 47) B. Cai, A. Dianat, R. Huebner, W. Liu, D. Wen, A. Benad, L. Sonntag, T. Gemming, G. Cuniberti, A. Eychmueller, *Multimetallic Hierarchical Aerogels: Shape Engineering of the Building Blocks for Efficient Electrocatalysis*, Advanced Materials 29 (2017) Nr. 11, S. 1605254/1-8.
- 48) S. Calder, J.G. Vale, N. Bogdanov, C. Donnerer, D. Pincini, M. Moretti Sala, X. Liu, M.H. Upton, D. Casa, Y.G. Shi, Y. Tsujimoto, K. Yamaura, J.P. Hill, J.P. Hill, J. van den Brink, D.F. McMorrow, A.D. Christianson, *Strongly gapped spin-wave excitation in the insulating phase of NaOsO₃*, Physical Review B 95 (2017) Nr. 2, S. 20413(R)/1-5.
- 49) K. Chandra Babu Naidua, S. Roopaskirana, M. Wuppuluri, *Investigations on transport, impedance and electromagnetic interference shielding properties of microwave processed NiMg ferrites*, Materials Research Bulletin 89 (2017), S. 125-138.
- 50) C.-H. Chang, K.-P. Dou, G.-Y. Guo, C.-C. Kaun, *Quantum-well-induced engineering of magnetocrystalline anisotropy in ferromagnetic films*, Npg Asia Materials 9 (2017), S. 424/1-6.
- 51) C.-H. Chang, A. Huang, S. Das, H.-T. Jeng, S. Kumar, R. Ganesh, *Carrier-driven coupling in ferromagnetic oxide heterostructures*, Physical Review B 96 (2017) Nr. 18, S. 184408/1-8.
- 52) C.-H. Chang, C. Ortix, *Theoretical Prediction of a Giant Anisotropic Magnetoresistance in Carbon Nanoscrolls*, Nano Letters 17 (2017) Nr. 5, S. 3076-3080.
- 53) C.-H. Chang, C. Ortix, *Ballistic anisotropic magnetoresistance in core-shell nanowires and rolled-up nanotubes*, International Journal of Modern Physics B 31 (2017) Nr. 1, S. 1630016/1-23.
- 54) J. Chao, J. Deng, W. Zhou, J. Liu, R. Hu, L. Yang, M. Zhu, O.G. Schmidt, *Hierarchical nanoflowers assembled from MoS₂/polyaniline sandwiched nanosheets for high-performance supercapacitors*, Electrochimica Acta 243 (2017), S. 98-104.
- 55) P. Chekhonin, M. Mietschke, D. Pohl, F. Schmidt, S. Faehler, W. Skrotzki, K. Nielsch, R. Huehne, *Effect of substrate miscut on the microstructure in epitaxial Pb(Mg_{1/3}Nb_{2/3}) O₃-PbTiO₃ thin films*, Materials Characterization 129 (2017), S. 234-241.
- 56) E.A. Chekhovich, A. Ulhaq, E. Zallo, F. Ding, O.G. Schmidt, M.S. Skolnick, *Measurement of the spin temperature of optically cooled nuclei and GaAs hyperfine constants in GaAs/AlGaAs quantum dots*, Nature Materials 16 (2017), S. 982-987.
- 57) C.-H. Chen, D.S. Krylov, S.M. Avdoshenko, F. Liu, L. Spree, R. Yadav, A. Alvertis, L. Hozoi, K. Nenkov, A. Kostanyan, T. Greber, A.U.B. Wolter, A.A. Popov, *Selective arc-discharge synthesis of Dy₂S-clusterfullerenes and their isomer-dependent single molecule magnetism*, Chemical Science 8 (2017) Nr. 9, S. 6451-6465.
- 58) Y. Chen, Y. Zhang, D. Karnaushenko, L. Chen, J. Hao, F. Ding, O.G. Schmidt, *Addressable and Color-Tunable Piezophotonic Light-Emitting Stripes*, Advanced Materials 29 (2017) Nr. 19, S. 1605165/1-8.
- 59) Y. Chen, Y. Zhang, R. Keil, M. Zopf, F. Schmidt, O.G. Ding, *Temperature-Dependent Coercive Field Measured by a Quantum Dot Strain Gauge*, Nano Letters 17 (2017) Nr. 12, S. 7864-7868.

- 60) Y. Chen, Y. Zhang, F. Yuan, F. Ding, O.G. Schmidt, *A Flexible PMN-PT Ribbon-Based Piezoelectric-Pyroelectric Hybrid Generator for Human-Activity Energy Harvesting and Monitoring*, Advanced Electronic Materials 3 (2017) Nr. 3, S. 1600540/1-7.
- 61) Y. Chen, Y. Zhang, L. Zhang, F. Ding, O.G. Schmidt, *Scalable single crystalline PMN-PT nanobelts sculpted from bulk for energy harvesting*, Nano Energy 31 (2017), S. 239-246.
- 62) M. Chernysheva, A. Bednyakova, M. Al Aarimi, R.C.T. Howe, G. Hu, T. Hasan, A. Gambetta, G. Galzerano, M. Ruemmeli, A. Rozhin, *Double-Wall Carbon Nanotube Hybrid Mode-Locker in Tm-doped Fibre Laser: A Novel Mechanism for Robust Bound-State Solitons Generation*, Scientific Reports 7 (2017), S. 44314/1-11.
- 63) Y.-Y. Chin, H.-J. Lin, Z. Hu, C.-Y. Kuo, D. Mikhailova, J.-M. Lee, S.-C. Haw, S.-A. Chen, W. Schnelle, H. Ishii, N. Hiraoka, Y.-F. Liao, K.-D. Tsuei, A. Tanaka, L.H. Tjeng, C.-T. Chen, J.-M. Chen, *Relation between the Co-O bond lengths and the spin state of Co in layered Cobaltates: a high-pressure study*, Scientific Reports 7 (2017), S. 3656/1-9.
- 64) Chirkova, F. Bittner, K. Nenkov, N.V. Baranov, L. Schultz, K. Nielsch, T.G. Woodcock, *The effect of the microstructure on the antiferromagnetic to ferromagnetic transition in FeRh alloys*, Acta Materialia 131 (2017), S. 31-38.
- 65) S. Choi, S. Johnston, W.-J. Jang, K. Koepernik, K. Nakatsukasa, J.M. Ok, H.-J. Lee, H.W. Choi, A.T. Lee, A. Akbari, Y.K. Semertzidis, Y. Bang, J.S. Kim, J. Lee, *Correlation of Fe-Based Superconductivity and Electron-Phonon Coupling in an FeAs=Oxide Heterostructure*, Physical Review Letters 119 (2017) Nr. 10, S. 107003/1-6.
- 66) V.B. Chzhan, E.A. Tereshina, A.B. Mikhailova, G.A. Politova, I.S. Tereshina, V.I. Kozlov, J. Cwik, K. Nenkov, O.A. Alekseeva, A.V. Filimonov, *Effect of Tb and Al substitution within the rare earth and cobalt sublattices on magnetothermal properties of Dy_{0.5}Ho_{0.5}Co₂*, Journal of Magnetism and Magnetic Materials 432 (2017), S. 461-465.
- 67) P. Cimalla, J. Walther, C. Mueller, S. Almedawar, B. Rellinghaus, D. Wittig, M. Ader, M.O. Karl, R.H.W. Funk, M. Brand, E. Koch, *Improved Imaging of Magnetically Labeled Cells Using Rotational Magnetomotive Optical Coherence Tomography*, Applied Sciences 7 (2017) Nr. 5, S. 444/1-10.
- 68) G. Cirillo, M. Curcio, U.G. Spizzirri, O. Vittorio, P. Tucci, N. Picci, F. Iemma, S. Hampel, F.P. Nicoletta, *Carbon nanotubes hybrid hydrogels for electrically tunable release of Curcumin*, European Polymer Journal 90 (2017), S. 1-12.
- 69) D.J. Collins, B.L. Khoo, Z. Ma, A. Winkler, R. Weser, H. Schmidt, J. Han, Y. Ai, *Selective particle and cell capture in a continuous flow using micro-vortex acoustic streaming*, Lab on a Chip 17 (2017) Nr. 10, S. 1769-1777.
- 70) D.J. Collins, B.L. Khoo, Z. Ma, A. Winkler, R. Weser, H. Schmidt, J. Han, A. Ye, *Correction: Selective particle and cell capture in a continuous flow using micro-vortex acoustic streaming*, Lab on a Chip 17 (2017) Nr. 10, S. 1843.
- 71) L.T. Corredor, G. Aslan-Cansever, M. Sturza, K. Manna, A. Maljuk, S. Gass, T. Dey, A.U.B. Wolter, O. Kataeva, A. Zimmermann, M. Geyer, C.G.F. Blum, S. Wurmehl, B. Buechner, *Iridium double perovskite Sr₂YrO₆: A combined structural and specific heat study*, Physical Review B 95 (2017) Nr. 6, S. 64418/1-8.
- 72) J. Cwik, Y. Koshkid'ko, N.A. de Oliveira, K. Nenkov, A. Hackemer, E. Dilmieva, N. Kolchugina, S. Nikitin, K. Rogacki, *Magnetocaloric effect in Laves-phase rare-earth compounds with the second-order magnetic phase transition: Estimation of the high-field properties*, Acta Materialia 133 (2017), S. 230-239.
- 73) A.N. Darinskii, M. Weihnacht, H. Schmidt, *Acoustomicrofluidic application of quasi-shear surface waves*, Ultrasonics 78 (2017), S. 10-17.
- 74) A.N. Darinskii, M. Weihnacht, H. Schmidt, *Finite element analysis of the Rayleigh wave scattering in isotropic bi-material wedge structures*, Ultrasonics 73 (2017), S. 67-76.
- 75) N. di Leo, M. Battaglini, M. Giannaccini, L. Dente, S. Hampel, O. Vittorio, G. Cirillo, V. Raffa, *A catechin nanoformulation inhibits WM266 melanoma cell proliferation, migration and associated neo-angiogenesis.*, European Journal of Pharmaceutics and Biopharmaceutics (2017), S. 114/1-10.
- 76) A.M. Diederichs, F. Thiel, T. Fischer, U. Lienert, W. Pantleon, *Monitoring microstructural evolution in-situ during cyclic deformation by high resolution reciprocal space mapping*, Journal of Physics: Conference Series 843 (2017) Nr. 1, S. 12031/1-9.
- 77) A.M. Diederichs, F. Thiel, U. Lienert, W. Pantleon, *In-situ investigations of structural changes during cyclic loading by high resolution reciprocal space mapping*, Procedia Structural Integrity 7 (2017), S. 268-274.
- 78) C. Draeger, F. Sigel, S. Indris, D. Mikhailova, L. Pfaffmann, M. Knapp, H. Ehrenberg, *Delithiation/relithiation process of LiCoMnO₄ spinel as 5 V electrode material*, Journal of Power Sources 371 (2017), S. 55-64.
- 79) S.-L. Drechsler, S. Johnston, V. Grinenko, J.M. Tomczak, H. Rosner, *Constraints on the total coupling strength to bosons in the iron based superconductors*, Physica Status Solidi B 254 (2017) Nr. 10, S. 1700006/1-22.
- 80) L. Dreval, M. Zschornak, W. Muenchgesang, O. Fabrichnaya, D. Rafaja, M.L. Martine, L. Giebel, M. Motylenko, *Thermodynamic assessment and first principle calculations of the Na-Sb-Sn system*, Journal of Alloys and Compounds 695 (2017), S. 1725-1742.

- 81) J. Dufouleur, L. Veyrat, B. Dassonneville, E. Xypakis, J.H. Bardarson, C. Nowka, S. Hampel, J. Schumann, B. Eichler, O.G. Schmidt, B. Buechner, R. Giraud, *Weakly-coupled quasi-1D helical modes in disordered 3D topological insulator quantum wires*, Scientific Reports 7 (2017), S. 45276/1-9.
- 82) D.V. Efremov, S.-L. Drechsler, H. Rosner, V. Grinenko, O.V. Dolgov, *A multiband Eliashberg-approach to iron-based superconductors*, Physica Status Solidi B 254 (2017) Nr. 7, S. 1600828/1-16.
- 83) B.J. Eleazer, M.D. Smith, A.A. Popov, D.V. Peryshkov, *Rapid reversible borane to boryl hydride exchange by metal shuttling on the carborane cluster surface*, Chemical Science 8 (2017) Nr. 8, S. 5399-5407.
- 84) K. Erdmann, J. Ringel, S. Hampel, M.P. Wirth, S. Fuessel, *Carbon nanomaterials sensitize prostate cancer cells to docetaxel and mitomycin C via induction of apoptosis and inhibition of proliferation*, Beilstein Journal of Nanotechnology 8 (2017), S. 1307-1317.
- 85) T. Espenhahn, D. Berger, S. Hameister, R. Huehne, L. Schultz, K. Nielsch, *Design and Validation of Switchable Tracks for Superconducting Levitation Systems*, IEEE Transactions on Applied Superconductivity 27 (2017) Nr. 4, S. 3600605/1-5.
- 86) D.V. Evtushinsky, A.N. Yaresko, V.B. Zabolotnyy, J. Maletz, T.K. Kim, A.A. Kordyuk, M.S. Viazovska, M. Roslova, I. Morozov, R. Beck, S. Aswartham, L. Harnagea, S. Wurmehl, H. Berger, V.A. Rogalev, V.N. Strocov, T. Wolf, N.D. Zhigadlo, B. Buechner, S.V. Borisenko, *High-energy electronic interaction in the 3d band of high-temperature iron-based superconductors*, Physical Review B 96 (2017) Nr. 6, S. 60501(R)/1-5.
- 87) G. Fabbri, D. Meyers, L. Xu, V.M. Katukuri, L. Hozoi, X. Liu, Z.-Y. Chen, J. Okamoto, T. Schmitt, A. Uldry, B. Delley, G.D. Gu, D. Prabhakaran, A.T. Boothroyd, J. van den Brink, D.J. Huang, M.P.M. Dean, *Doping Dependence of Collective Spin and Orbital Excitations in the Spin-1 Quantum Antiferromagnet La₂-xSr_xNiO₄ Observed by X Rays*, Physical Review Letters 118 (2017) Nr. 15, S. 156402/1-8.
- 88) J. Fink, E.D.L. Rienks, S. Thirupathaiah, J. Nayak, A. van Roekeghem, S. Biermann, T. Wolf, P. Adelmann, H.S. Jeevan, P. Gegenwart, S. Wurmehl, C. Felser, B. Buechner, *Experimental evidence for importance of Hund's exchange interaction for incoherence of charge carriers in iron-based superconductors*, Physical Review B 95 (2017), S. 144513/1-6.
- 89) V.M. Fomin, R.O. Rezaev, E.A. Levchenko, D. Grimm, O.G. Schmidt, *Superconducting properties of nanostructured microhelices*, Journal of Physics: Condensed Matter 29 (2017) Nr. 39, S. 395301/1-9.
- 90) D.G. Franco, Y. Prots, C. Geibel, S. Seiro, *Fluctuation-induced first-order transition in Eu-based trillium lattices*, Physical Review B 96 (2017) Nr. 1, S. 14401/1-5.
- 91) J. Freudenberger, D. Rafaja, D. Geissler, L. Giebeler, C. Ullrich, A. Kauffmann, M. Heilmaier, K. Nielsch, *Face Centred Cubic Multi-Component Equiatomic Solid Solutions in the Au-Cu-Ni-Pd-Pt System*, Metals 7 (2017) Nr. 4, S. 135/1-18.
- 92) F. Fritz, R. Westerstroem, A. Kostanyan, C. Schlesier, J. Dreiser, B. Watts, L. Houben, M. Luysberg, S.M. Avdoshenko, A.A. Popov, C.M. Schneider, C. Meyer, *Nanoscale x-ray investigation of magnetic metallofullerene peapods*, Nanotechnology 28 (2017) Nr. 43, S. 435703.
- 93) Y. Fu, V. Romy, Y. Liu, B. Ibarlucea, L. Barabana, V. Khavrusa, S. Oswald, A. Bachmatiuk, I. Ibrahim, M. Ruemmel, T. Gemming, V. Bezugly, G. Cuniberti, *Chemiresistive biosensors based on carbon nanotubes for label-free detection of DNA sequences derived from avian influenza virus H5N1*, Sensors and Actuators B: Chemical 249 (2017), S. 691-699.
- 94) I.C. Fulga, A. Stern, *Triple point fermions in a minimal symmorphic model*, Physical Review B 95 (2017) Nr. 24, S. 241116/1-5.
- 95) K.P. Furlan, T. Krekeler, M. Ritter, R. Blick, G.A. Schneider, K. Nielsch, R. Zierold, R. Janssen, *Low-Temperature Mullite Formation in Ternary Oxide Coatings Deposited by ALD for High-Temperature Applications*, Advanced Materials 4 (2017) Nr. 23, S. 1700912/1-8.
- 96) Y. Gaididei, A. Goussev, V.P. Kravchuk, J.M. Pylypovskyi, J.M. Robbins, D.D. Sheka, V. Slastikov, S. Vasylyevych, *Magnetization in narrow ribbons: curvature effects*, Journal of Physics A 50 (2017) Nr. 38, S. 385401/1-17.
- 97) C. Gammer, B. Escher, C. Ebner, A.M. Minor, H.P. Karthaler, J. Eckert, S. Pauly, C. Rentenberger, *Influence of the Ag concentration on the medium-range order in a CuZrAlAg bulk metallic glass*, Scientific Reports 7 (2017), S. 44903/1-7.
- 98) J. Garcia, D.A. Lara Ramos, M. Mohn, H. Schloerb, N. Perez Rodriguez, L. Akinsinde, K. Nielsch, G. Schierning, H. Reith, *Fabrication and Modeling of Integrated Micro-Thermoelectric Cooler by Template-Assisted Electrochemical Deposition*, ECS Journal of Solid State Science and Technology 6 (2017) Nr. 3, S. N3022-N3028.
- 99) P. Gargarella, S. Pauly, C. Shyinti Kiminami, J. Eckert, *Effect of Co additions on the phase formation, thermal stability, and mechanical properties of rapidly solidified Ti-Cu-based alloys*, Journal of Materials Research 32 (2017) Nr. 13, S. 2578-2584.
- 100) D. Geissler, J. Grosse, S. Donath, D. Ehinger, M. Stoica, J. Eckert, U. Kuehn, *Granulation of Bulk Metallic Glass Forming Alloys as a Feedstock for Thermoplastic Forming and their Compaction into Bulk Samples*, Materials Science Forum 879 (2017), S. 589-594.
- 101) M. Gellesch, F. Hammerath, V. Suess, M. Haft, S. Hampel, S. Wurmehl, B. Buechner, *Compositional analysis of multi-element magnetic nanoparticles with a combined NMR and TEM approach*, Journal of Nanoparticle Research 19 (2017) Nr. 9, S. 307/1-7.

- 102) A. Generalov, M.M. Otrokov, A. Chikina, K. Kliemt, K. Kummer, M. Hoepfner, M. Guettler, S. Seiro, A. Fedorov, S. Schulz, S. Danzenbaeher, E.V. Chulkov, C. Geibel, C. Laubschat, P. Dudin, M. Hoesch, T. Kim, M. Radovic, M. Shi, N.C. Plumb, C. Krellner, D.V. Vylikh, *Spin Orientation of Two-Dimensional Electrons Driven by Temperature-Tunable Competition of Spin-Orbit and Exchange-Magnetic Interactions*, Nano Letters 17 (2017) Nr. 2, S. 811-820.
- 103) M.P. Ghimire, M. Richter, *Chemical Gating of a Weak Topological Insulator: $Bi_{14}Rh_3I_9$* , Nano Letters 17 (2017) Nr. 10, S. 6303-6308.
- 104) A. Godfrin, A. Kario, R. Gyuraki, E. Demencik, R. Nast, J. Scheiter, A. Mankevich, A. Molodyk, W. Goldacker, F. Grilli, *Influence of the Striation Process and the Thickness of the Cu-Stabilization on the AC Magnetization Loss of Striated REBCO Tape*, IEEE Transactions on Applied Superconductivity 27 (2017) Nr. 6, S. 5900809/1-9.
- 105) T. Goehlert, P.F. Siles, T. Paessler, R. Sommer, S. Baunack, S. Oswald, O.G. Schmidt, *Ultra-thin all-solid-state micro-supercapacitors with exceptional performance and device flexibility*, Nano Energy 33 (2017), S. 387-392.
- 106) M. Goettlicher, M. Rohnke, Y. Moryson, J. Thomas, J. Sann, A. Lode, M. Schumacher, R. Schmidt, S. Pilz, A. Gebert, T. Gemming, J. Janek, *Functionalization of Ti-40Nb implant material with strontium by reactive sputtering*, Biomaterials Research online only (2017), S. 2118/1-11.
- 107) H. Gong, X. Cao, F. Li, Y. Gong, L. Gu, R.G. Mendes, M.H. Rummeli, P. Strasser, R. Yang, *PdAuCu Nanobranched as Self-Repairing Electrocatalyst for Oxygen Reduction Reaction*, ChemSusChem 10 (2017) Nr. 7, S. 1469-1474.
- 108) H.Y. Gong, X.C. Cao, R.G. Mendes, M.H. Rummeli, J.Y. Zhang, R.Z. Yang, *Self-Supported NiS Nanoparticle-Coupled Ni₂P Nanoflake Array Architecture: An Advanced Catalyst for Electrochemical Hydrogen Evolution*, ChemElectroChem 4 (2017) Nr. 6, S. 1554-1559.
- 109) J. Gooth, A.C. Niemann, T. Meng, A.G. Crushin, K. Lansteiner, B. Gotsmann, F. Menges, M. Schmidt, C. Shekhar, V. Suess, R. Huehne, B. Rellinghaus, C. Felser, B. Yan, K. Nielsch, *Experimental signatures of the mixed axial-gravitational anomaly in the Weyl semimetal NbP*, Nature 547 (2017) Nr. 7663, S. 324-327.
- 110) H.-J. Grafe, S. Nishimoto, M. Iakovleva, E. Vavilova, L. Spillecke, A. Alfonsov, M.-I. Sturza, S. Wurmehl, H. Nojiri, H. Rosner, J. Richter, U.K. Roessler, S.-L. Drechsler, V. Kataev, B. Buechner, *Signatures of a magnetic field-induced unconventional nematic liquid in the frustrated and anisotropic spin-chain cuprate $LiCuSbO_4$* , Scientific Reports 7 (2017), S. 6720/1-16.
- 111) D. Grell, J. Gibmeier, S. Dietrich, F. Silze, L. Boehme, V. Schulze, U. Kuehn, E. Kerscher, *Influence of shot peening on the mechanical properties of bulk amorphous Vitreloy 105*, Surface Engineering 33 (2017) Nr. 9, S. 721-730.
- 112) D. Grell, Y. Wilkin, P.F. Gostin, A. Gebert, E. Kerscher, *Corrosion Fatigue Studies on a Bulk Glassy Zr-Based Alloy under Three-Point Bending*, Frontiers in Materials 3 (2017), S. 60/1-10.
- 113) V. Grinenko, K. Iida, F. Kurth, D.V. Efremov, S.-L. Drechsler, I. Cherniavskii, I. Morozov, J. Haenisch, T. Foerster, C. Tarantini, J. Jaroszynski, B. Maiorov, M. Jaime, A. Yamamoto, I. Nakamura, R. Fujimoto, T. Hatano, H. Ikuta, R. Huehne, *Selective mass enhancement close to the quantum critical point in $BaFe_2(As_{1-x}P_x)_2$* , Scientific Reports 7 (2017), S. 4859/1-7.
- 114) V. Grinenko, P. Materne, R. Sarkar, H. Luetkens, K. Kihou, C.H. Lee, S. Akhmadaliev, D.V. Efremov, S.-L. Drechsler, H.-H. Klauss, *Superconductivity with broken time-reversal symmetry in ion-irradiated $Ba_{0.27}K_{0.73}Fe_2As_2$ single crystals*, Physical Review B 95 (2017) Nr. 21, S. 214511/1-5.
- 115) F. Grote, C. Gruber, F. Boerrnert, U. Kaiser, S. Eigler, *Thermal Disproportionation of Oxo-Functionalized Graphene*, Angewandte Chemie 56 (2017) Nr. 31, S. 9222-9225.
- 116) A. Gubal, A. Ganeev, V. Hoffmann, M. Voronov, V. Brackmann, S. Oswald, *Combined hollow cathode vs. Grimm cell: semiconductive and nonconductive samples*, Journal of Analytical Atomic Spectrometry 32 (2017) Nr. 2, S. 354-366.
- 117) H.J. Guo, M.T. Fernandez-Diaz, A.C. Komarek, S. Huh, P. Adler, M. Valldor, *Long-Range Antiferromagnetic Order on Spin Ladders $SrFe_2S_2O$ and $SrFe_2Se_2O$ As Probed by Neutron Diffraction and Mossbauer Spectroscopy*, European Journal of Inorganic Chemistry (2017) Nr. 32, S. 3829-3833.
- 118) J.J. Gutierrez Moreno, M. Boenisch, N.T. Panagiotopoulos, M. Calin, D.G. Papageorgiou, A. Gebert, J. Eckert, G.A. Evangelakis, C.E. Lekka, *Ab-initio and experimental study of phase stability of Ti-Nb alloys*, Journal of Alloys and Compounds 696 (2017), S. 481-489.
- 119) W. Haessler, P. Kovac, J. Scheiter, A. Rosova, W. Pachla, *MgB₂ Multicore Wire Prepared by IMD Technology - Investigation of the MgB₂ Layer Formation During Annealing*, IEEE Transactions on Applied Superconductivity 27 (2017) Nr. 4, S. 6200504/1-4.
- 120) S. Haindl, M. Kieszun, E. Kampert, *Iron pnictide thin films: Synthesis and Physics*, Physica Status Solidi B 254 (2017) Nr. 1, S. 201600341/1-12.
- 121) J.E. Hamann-Borrero, S. Macke, B. Gray, M. Kareev, E. Schierle, S. Partzsch, M. Zwiebler, U. Treske, A. Koitzsch, B. Buechner, J.W. Freeland, J. Chakhalian, J. Geck, *Site-selective spectroscopy with depth resolution using resonant x-ray reflectometry*, Scientific Reports 7 (2017), S. 13792/1-11.

- 122) F. Hammerath, R. Sarkar, S. Kamusella, C. Baines, H.-H. Klauss, T. Dey, A. Maljuk, S. Gass, A.U.B. Wolter, H.-J. Grafe, S. Wurmehl, B. Buechner, *Diluted paramagnetic impurities in nonmagnetic $Ba_2\text{YrO}_6$* , Physical Review B 96 (2017) Nr. 16, S. 165108/1-8.
- 123) Q. Hao, H. Huang, X. Fan, Y. Yin, J. Wang, W. Li, T. Qiu, L. Ma, P.K. Chu, O.G. Schmidt, *Controlled Patterning of Plasmonic Dimers by Using an Ultrathin Nanoporous Alumina Membrane as a Shadow Mask*, ACS Applied Materials and Interfaces 9 (2017) Nr. 41, S. 36199-36205.
- 124) E. Haubold, K. Koepernik, D. Efremov, S. Khim, A. Fedorov, Y. Kushnirenko, J. van den Brink, S. Wurmehl, B. Buechner, T.K. Kim, M. Hoesch, K. Sumida, K. Taguchi, T. Yoshikawa, A. Kimura, T. Okuda, S.V. Borisenko, *Experimental realization of type-II Weyl state in noncentrosymmetric TaIrTe_4* , Physical Review B 95 (2017) Nr. 24, S. 241108/1-7.
- 125) Z. He, L. Zhang, W. Shan, Y. Zhang, R. Zhou, Y. Jiang, J. Tan, *Mechanical and corrosion properties of Ti-35Nb-7Zr-xHA composites fabricated by spark plasma sintering*, Transactions of Nonferrous Metals Society of China 27 (2017) Nr. 4, S. 848-856.
- 126) O. Heczko, O. Perevertov, D. Kral, M. Veis, I.V. Soldatov, R. Schaefer, *Using Kerr Microscopy for Direct Observation of Magnetic Domains in Ni-Mn-Ga Magnetic Shape Memory Alloy*, IEEE Transactions on Magnetics 53 (2017) Nr. 11, S. 2502605/1-5.
- 127) L. Helmich, M. Bartke, N. Teichert, B. Schleicher, S. Faehler, A. Huetten, *Gadolinium thin films as benchmark for magneto-caloric thin films*, AIP Advances 7 (2017) Nr. 5, S. 56429/1-5.
- 128) A. Helth, S. Pilz, T. Kirsten, L. Giebler, J. Freudenberger, M. Calin, J. Eckert, A. Gebert, *Effect of thermomechanical processing on the mechanical biofunctionality of a low modulus Ti-40Nb alloy*, Journal of the Mechanical Behavior of Biomedical Materials 65 (2017), S. 137-150.
- 129) C. Hengst, S.B. Menzel, G.K. Rane, V. Smirnov, K. Wilken, B. Leszczynska, D. Fischer, N. Prager, *Mechanical Properties of ZTO, ITO, and a-Si:H Multilayer Films for Flexible Thin Film Solar Cells*, Materials 10 (2017) Nr. 3, S. 245.
- 130) C. Hess, H. Grafe, A. Kondrat, G. Lang, F. Hammerath, L. Wang, R. Klingeler, G. Behr, B. Buechner, *Nematicity in $\text{LaFeAsO}_{1-x}\text{F}_x$* , Physica Status Solidi B 254 (2017) Nr. 1, S. 1600214/1-8.
- 131) V. Hlukhyi, A.V. Hoffmann, V. Grinenko, J. Scheiter, F. Hummel, D. Johrendt, T.F. Faessler, *Structural instability and superconductivity in the solid solution $\text{SrNi}_2(\text{P}_{1-x}\text{Ge}_x)_2$* , Physica Status Solidi B 254 (2017) Nr. 1, S. 1600351/1-13.
- 132) B. Hoefer, J. Zhang, J. Wildmann, E. Zallo, R. Trotta, F. Ding, A. Rastelli, O.G. Schmidt, *Independent tuning of excitonic emission energy and decay time in single semiconductor quantum dots*, Applied Physics Letters 110 (2017) Nr. 15, S. 151102/1-4.
- 133) F. Holzmueller, N. Graessler, M. Sedighi, E. Mueller, M. Knupfer, O. Zeika, K. Vandewal, C. Koerner, K. Leo, *H-aggregated small molecular nanowires as near infrared absorbers for organic solar cells*, Organic Electronics 45 (2017), S. 198-202.
- 134) M. Hossain, C. Telke, M. Sparing, A. Abdkader, A. Nocke, R. Unger, G. Fuchs, A. Berger, C. Cherif, M. Beitelschmidt, L. Schultz, *Mathematical modeling, simulation and validation of the dynamic yarn path in a superconducting magnet bearing (SMB) ring spinning system*, Textile Research Journal 87 (2017) Nr. 8, S. 1011-1022.
- 135) A. Huang, C.-H. Chang, H.-T. Jeng, *Magnetic Phase Transition of $\text{La}_{1-x}\text{Sr}_x\text{MnO}_3$ Induced by Charge Transfer and Interdiffusion*, IEEE Magnetics Letters 8 (2017), S. 1402905.
- 136) H. Huang, R. Trotta, Y. Huo, T. Lettner, J.S. Wildmann, J. Martin-Sanchez, D. Huber, M. Reindl, J. Zhang, E. Zallo, O.G. Schmidt, A. Rastelli, *Electrically-Pumped Wavelength-Tunable GaAs Quantum Dots Interfaced with Rubidium Atoms*, ACS Photonics 4 (2017) Nr. 4, S. 868-872.
- 137) L. Huang, Q. Zhang, Y. Wang, R. He, J. Shuai, J. Zhang, C. Wang, Z. Ren, *The effect of Sn doping on thermoelectric performance of n-type half-Heusler NbCoSb* , Physical Chemistry Chemical physics 19 (2017) Nr. 37, S. 25683-25690.
- 138) S. Huang, L. Zhang, X. Lu, L. Liu, L. Liu, X. Sun, Y. Yin, S. Oswald, Z. Zou, F. Ding, O.G. Schmidt, *Tunable Pseudocapacitance in 3D TiO_2 -delta Nanomembranes Enabling Superior Lithium Storage Performance*, ACS Nano 11 (2017) Nr. 1, S. 821-830.
- 139) D. Huber, M. Reindl, Y. Huo, H. Huang, J.S. Wildmann, O.G. Schmidt, A. Rastelli, R. Trotta, *Highly indistinguishable and strongly entangled photons from symmetric GaAs quantum dots*, Nature Communications 8 (2017), S. 15506/1-7.
- 140) J. Hufenbach, H. Wendrock, F. Kochta, U. Kuehn, A. Gebert, *Novel biodegradable Fe-Mn-C-S alloy with superior mechanical and corrosion properties*, Materials Letters 186 (2017), S. 330-333.
- 141) Y.H. Huo, V. Krapek, O.G. Schmidt, A. Rastelli, *Spontaneous brightening of dark excitons in GaAs/AlGaAs quantum dots near a cleaved facet*, Physical Review B 95 (2017) Nr. 16, S. 165304/1-8.
- 142) M. Iakovleva, S. Zimmermann, J. Zeisner, A. Alfonsov, H.-J. Grafe, M. Valldor, E. Vavilova, B. Buechner, V. Kataev, *Magnetic resonance spectroscopy on the spin-frustrated magnets $\text{YBaCo}_3\text{MO}_7$ ($M=\text{Al}, \text{Fe}$)*, Physical Review B 96 (2017) Nr. 6, S. 64417/1-11.
- 143) T. Jaumann, J. Balach, U. Langklotz, V. Sauchuk, M. Fritsch, A. Michaelis, V. Telteviskij, D. Mikhailova, S. Oswald, M. Klose, G. Stephani, R. Hauser, J. Eckert, L. Giebler, *Lifetime vs. rate capability: Understanding the role of FEC and VC in high-energy Li-ion batteries with nano-silicon anodes*, Energy Storage Materials 6 (2017), S. 26-35.

- 144) T. Jaumann, M. Gerwig, J. Balach, S. Oswald, E. Brendler, R. Hauser, B. Kieback, J. Eckert, L. Giebeler, E. Kroke, *Dichlorosilane-derived nano-silicon inside hollow carbon spheres as a high-performance anode for Li-ion batteries*, Journal of Materials Chemistry A 5 (2017), S. 9262-9271.
- 145) D. Jehnichen, D. Pospiech, P. Friedel, A. Horechyy, A. Korwitz, A. Janke, F. Naether, C.M. Papadakis, J. Perlich, V. Neu, *Effects of nanoparticles on phase morphology in thin films of phase-separated diblock copolymers*, Powder Diffraction 32 (2017), S. 141-150.
- 146) Y.D. Jia, P. Ma, K.G. Prashanth, G. Wang, J. Yi, S. Scudino, F.Y. Cao, J.F. Sun, J. Eckert, *Microstructure and thermal expansion behavior of Al-50Si synthesized by selective laser melting*, Journal of Alloys and Compounds 699 (2017), S. 548-553.
- 147) L. Jiao, C.-H. Huang, S. Roessler, C. Koz, U.K. Roessler, U. Schwarz, S. Wirth, *Superconducting gap structure of FeSe*, Scientific Reports 7 (2017), S. 44024/1-8.
- 148) L. Jiao, S. Roessler, C. Koz, U. Schwarz, D. Kasinathan, U.K. Roessler, S. Wirth, *Impurity-induced bound states inside the superconducting gap of FeSe*, Physical Review B 96 (2017) Nr. 9, S. 94504/1-7.
- 149) K.D. Joens, K. Stensson, M. Reindl, M. Swillo, Y. Huo, V. Zwiller, A. Rastelli, R. Trotta, G. Bjoerk, *Two-photon interference from two blinking quantum emitters*, Physical Review B 96 (2017) Nr. 7, S. 75430/1-10.
- 150) P. Jovari, I. Kaban, B. Escher, K.K. Song, J. Eckert, B. Beuneu, M.A. Webb, N. Chen, *Structure of glassy Cu_{47.5}Zr_{47.5}Ag₅ investigated with neutron diffraction with isotopic substitution, X-ray diffraction, EXAFS and reverse Monte Carlo simulation*, Journal of Non-Crystalline Solids 459 (2017), S. 99-102.
- 151) M. Ju, X.Y. Liang, J.X. Liu, L. Zhou, Z. Liu, R.G. Mendes, M.H. Ruemmel, L. Fu, *Universal Substrate Trapping Strategy To Grow Strictly Monolayer Transition Metal Dichalcogenides Crystals*, Chemistry of Materials 29 (2017) Nr. 14, S. 6095-6103.
- 152) M. Junige, M. Loeffler, M. Geidel, M. Albert, J.W. Bartha, E. Zschech, B. Rellinghaus, W.F. van Dorp, *Area-selective atomic layer deposition of Ru on electron-beam-written Pt(C) patterns versus SiO₂ substratum*, Nanotechnology 28 (2017) Nr. 39, S. 395301/1-10.
- 153) C.B.N. Kadiyala, M. Wuppuluri, *Effect of microwave heat treatment on pure phase formation of hydrothermal synthesized nano NiMg ferrites*, Phase Transitions 90 (2017) Nr. 9, S. 847-862.
- 154) A.A. Kalenyuk, A. Pagliero, E.A. Borodianskyi, S. Aswartham, S. Wurmehl, B. Buechner, D.A. Chareev, A.A. Kordyuk, V.M. Krasnov, *Unusual two-dimensional behavior of iron-based superconductors with low anisotropy*, Physical Review B 96 (2017) Nr. 13, S. 134512/1-11.
- 155) A.A. Kamashev, P.V. Leksin, J. Schumann, V. Kataev, J. Thomas, T. Gemming, B. Buechner, I.A. Garifullin, *Proximity effect between a superconductor and a partially spin-polarized ferromagnet: Case study of the Pb/Cu/Co₂Cr_{1-x}Fe_xAl trilayer*, Physical Review B 96 (2017) Nr. 2, S. 24512/1-7.
- 156) S. Kamusella, K.T. Lai, L. Harnagea, R. Beck, U. Pachmayr, G.S. Thakur, H.-H. Klauss, *⁵⁷Fe Moessbauer spectroscopy on iron based pnictides and chalcogenides in applied magnetic fields*, Physica Status Solidi B 254 (2017) Nr. 1, S. 1600160/1-9.
- 157) L.H. Karlsson, J. Birch, A. Mockute, A.S. Ingason, H.Q. Ta, M.H. Ruemmel, J. Rosen, P.O.A. Persson, *Graphene on graphene formation from PMMA residues during annealing*, Vacuum 137 (2017), S. 191-194.
- 158) K. Karmakar, M. Skoulatos, G. Prando, B. Roessli, U. Stuhr, F. Hammerath, C. Rueegg, S. Singh, *Effects of Quantum Spin-1/2 Impurities on the Magnetic Properties of Zigzag Spin Chains*, Physical Review Letters 118 (2017) Nr. 10, S. 107201/1-5.
- 159) S. Kauffmann-Weiss, W. Haessler, E. Guenther, J. Scheiter, S. Dennele, P. Glosse, T. Berthold, M. Oomen, T. Arndt, T. Stoecker, D. Hanft, R. Moos, M. Weiss, F. Weis, B. Holzapfel, *Superconducting Properties of Thick Films on Hastelloy Prepared by the Aerosol Deposition Method With Ex Situ MgB₂ Powder*, IEEE Transactions on Applied Superconductivity 27 (2017) Nr. 4, S. 6200904.
- 160) S. Kauffmann-Weiss, S. Hahn, C. Weigelt, L. Schultz, M.F.-X. Wagner, S. Faehler, *Growth, microstructure and thermal transformation behaviour of epitaxial Ni-Ti films*, Acta Materialia 132 (2017), S. 255-263.
- 161) S. Kaufmann, S. Hampel, C. Rieger, D. Kunhardt, D. Schendel, S. Fuessel, B. Schwenzer, K. Erdmann, *Systematic evaluation of oligodeoxynucleotide binding and hybridization to modified multi-walled carbon nanotubes*, Journal of Nanobiotechnology 15 (2017).
- 162) R. Keil, M. Zopf, Y. Chen, B. Hoefer, J. Zhang, F. Ding, O.G. Schmidt, *Solid-state ensemble of highly entangled photon sources at rubidium atomic transitions*, Nature Communications 8 (2017), S. 15501/1-8.
- 163) S. Khim, S. Aswartham, V. Grinenko, D. Efremov, C.G.F. Blum, F. Steckel, D. Gruner, A.U.B. Wolter, S.-L. Drechsler, C. Hess, S. Wurmehl, B. Buechner, *A calorimetric investigation of RbFe₂As₂ single crystals*, Physica Status Solidi B 254 (2017) Nr. 1, S. 1600214/1-8.
- 164) F. Kiebert, S. Wege, J. Massing, J. Koenig, C. Cierpka, R. Weser, H. Schmidt, *3D measurement and simulation of surface acoustic wave driven fluid motion: a comparison*, Lab on a Chip 17 (2017) Nr. 12, S. 2104-2114.

- 165) B.S. Kim, B.I. Lee, N. Lee, G. Choi, T. Gemming, H.H. Cho, *Nano-inspired smart interfaces: fluidic interactivity and its impact on heat transfer*, Scientific Reports 7 (2017), S. 45323/1-10.
- 166) S.-Y. Kim, G.-H. Park, H.-A. Kim, A.-Y. Lee, H.-R. Oh, C.-W. Lee, M.-H. Lee, *Micro-deposition of Cu-based metallic glass wire by direct laser melting process*, Materials Letters 202 (2017), S. 1-4.
- 167) A. Klingner, I.S.M. Khalil, V. Magdanz, V.M. Fomin, O.G. Schmidt, S. Misra, *Modeling of Unidirectional-Overloaded Transition in Catalytic Tubular Microjets*, The Journal of Physical Chemistry C 121 (2017) Nr. 27, S. 14854-14863.
- 168) M. Klose, R. Reinhold, F. Logsch, F. Wolke, J. Linnemann, U. Stoeck, S. Oswald, M. Uhlemann, J. Balach, J. Markowski, P. Ay, L. Giebeler, *Softwood Lignin as a Sustainable Feedstock for Porous Carbons as Active Material for Supercapacitors Using an Ionic Liquid Electrolyte*, ACS Sustainable Chemistry and Engineering 5 (2017), S. 4094-4102.
- 169) J. Koerner, C.F. Reiche, R. Ghunaim, R. Fuge, S. Hampel, B. Buechner, T. Muehl, *Magnetic properties of individual Co₂FeGa Heusler nanoparticles studied at room temperature by a highly sensitive co-resonant cantilever sensor*, Scientific Reports 7 (2017), S. 8881/1-12.
- 170) J. Koeszegi, O. Kugeler, D. Abou-Ras, J. Knobloch, R. Schaefer, *A magneto-optical study on magnetic flux expulsion and pinning in high-purity niobium*, Journal of Applied Physics 122 (2017) Nr. 17, S. 173901/1-9.
- 171) A. Koitzsch, C. Habenicht, E. Mueller, M. Knapfer, B. Buechner, S. Kretschmer, M. Richter, J. van den Brink, F. Boerrnert, D. Nowak, A. Isaeva, Doert, T., *Nearest-neighbor Kitaev exchange blocked by charge order in electron-doped alpha-RuCl₃*, Physical Review Materials 1 (2017) Nr. 5, S. 52001.
- 172) K. Kosiba, S. Pauly, *Inductive flash-annealing of bulk metallic glasses*, Scientific Reports 7 (2017), S. 2151/1-11.
- 173) K. Kosiba, S. Scudino, R. Kobold, U. Kuehn, A.L. Greer, J. Eckert, S. Pauly, *Transient nucleation and microstructural design in flash-annealed bulk metallic glasses*, Acta Materialia 127 (2017), S. 416-425.
- 174) A. Kostanyan, R. Westerstroem, Y. Zhang, D. Kunhardt, R. Stania, B. Buechner, A.A. Popov, T. Greber, *Switching Molecular Conformation with the Torque on a Single Magnetic Moment*, Physical Review Letters 119 (2017) Nr. 23, S. 237202/1-5.
- 175) T. Kosub, M. Kopte, R. Huehne, P. Appel, B. Shields, P. Maletinsky, R. Huebner, M.O. Liedke, J. Fassbender, O.G. Schmidt, D. Makarov, *Purely antiferromagnetic magnetoelectric random access memory*, Nature Communications 8 (2017), S. 13985/1-7.
- 176) M. Krautz, D. Werner, M. Schrödner, A. Funk, A. Jantz, J. Popp, J. Eckert, A. Waske, *Hysteretic behavior of soft magnetic elastomer composites*, Journal of Magnetism and Magnetic Materials 426 (2017), S. 60-63.
- 177) J. Krehl, A. Lubk, *Rytov approximation in electron scattering*, Physical Review B 95 (2017) Nr. 24, S. 245106/1-7.
- 178) A. Krest, A. Sandleben, M. Valldor, M. Werker, U. Ruschewitz, A. Klein, *Heteroleptic Complexes of the Tridentate Pyridine-2,6-di-tetrazolate Ligand*, Chemistryselect 2 (2017) Nr. 21, S. 5849-5859.
- 179) M.J. Kriegel, O. Fabrichnaya, M. Conrad, V. Klemm, J. Freudenberger, A. Leineweber, *High temperature phase equilibria in the Ti-poor part of the Al-Mo-Ti system*, Journal of Alloys and Compounds 706 (2017), S. 616-628.
- 180) M.J. Kriegel, A. Walnsch, O. Fabrichnaya, D. Pavlyuchkov, V. Klemm, J. Freudenberger, D. Rafaja, A. Leineweber, *High-temperature phase equilibria with the bcc-type b (AlMo) phase in the binary AlMo system*, Intermetallics 83 (2017), S. 29-37.
- 181) B. Kruppke, C. Heinemann, A. Keroue, J. Thomas, S. Roessler, H.-P. Wiesmann, T. Gemming, H. Worch, T. Hanke, *Calcite and Hydroxyapatite Gelatin Composites as Bone Substitution Material Made by the Double Migration Technique*, Crystal Growth and Design 17 (2017) Nr. 2, S. 738-745.
- 182) Y. Krupskaya, M. Schaeppers, A.U.B. Wolter, H.-J. Grafe, E. Vavilova, A. Moeller, B. Buechner, V. Kataev, *Magnetic Resonance Study of the Spin-1/2 Quantum Magnet BaAg₂Cu[VO₄]₂*, Zeitschrift für Physikalische Chemie 231 (2017) Nr. 4, S. 759-775.
- 183) D.S. Krylov, F. Liu, S.M. Avdoshenko, L. Spree, B. Weise, A. Waske, A.U.B. Wolter, B. Buechner, A.A. Popov, *Record-high thermal barrier of the relaxation of magnetization in the nitride clusterfullerene Dy₂ScN@C₈₀-I_h*, Chemical Communications 53 (2017) Nr. 56, S. 7901-7904.
- 184) P. Kumar, M. Pfeffer, N. Peranio, O. Eibl, S. Baessler, H. Reith, K. Nielsch, *Ternary, single-crystalline Bi₂ (Te, Se)₃ nanowires grown by electrodeposition*, Acta Materialia 125 (2017), S. 238-245.
- 185) S.S. Kumar, M. Medina-Sanchez, O.G. Schmidt, *Autonomously propelled microscavengers for precious metal recovery*, Chemical Communications 53 (2017) Nr. 58, S. 8140-8143.
- 186) L.A. Kunz-Schughart, A. Dubrovskaya, C. Peitzsch, A. Ewe, A. Aigner, S. Schellenburg, M.H. Muders, S. Hampel, G. Cirillo, F. Iemma, R. Tietze, C. Alexiou, H. Stephan, K. Zarschler, O. Vittorio, M. Kavallaris, W.J. Parak, L. Maedler, S. Pokhrel, *Nanoparticles for radiooncology: Mission, vision, challenges*, Biomaterials 120 (2017), S. 155-184.
- 187) Y.S. Kushnirenko, A.A. Kordyuk, A.V. Fedorov, E. Haubold, T. Wolf, B. Buechner, S.V. Borisenko, *Anomalous temperature evolution of the electronic structure of FeSe*, Physical Review B 96 (2017) Nr. 10, S. 100504/1-5.

- 188) K.T. Lai, P. Adler, Y. Prots, Z. Hu, C.-Y. Kuo, T.-W. Pi, M. Valldor, *Successive Phase Transitions in Fe²⁺ Ladder Compounds Sr₂Fe₃Ch₂O₃ (Ch = S, Se)*, Inorganic Chemistry 56 (2017) Nr. 20, S. 12606-12614.
- 189) K.T. Lai, I. Antonyshyn, Y. Prots, M. Valldor, *Anti-Perovskite Li-Battery Cathode Materials*, Journal of the American Chemical Society 139 (2017) Nr. 28, S. 9645-9649.
- 190) M. Lao, J. Hecher, P. Pahlke, M. Sieger, R. Huehne, M. Eisterer, *Magnetic granularity in pulsed laser deposited YBCO films on technical templates at 5K*, Superconductor Science and Technology 30 (2017) Nr. 10, S. 104003/1-8.
- 191) M. Lao, J. Hecher, M. Sieger, P. Pahlke, M. Bauer, R. Huehne, M. Eisterer, *Planar current anisotropy and field dependence of J_c in coated conductors assessed by scanning Hall probe microscopy*, Superconductor Science and Technology 30 (2017) Nr. 2, S. 24004/1-9.
- 192) E. Lattner, M. Seifert, T. Gemming, S. Heicke, S.B. Menzel, *Coevaporation and structuring of titanium-aluminum alloy thin films*, Journal of Vacuum Science and Technology A: Vacuum, Surfaces, and Films 35 (2017) Nr. 6, S. 61603/1-7.
- 193) A. Lau, K. Koepernik, J. van den Brink, C. Ortix, *Generic Coexistence of Fermi Arcs and Dirac Cones on the Surface of Time-Reversal Invariant Weyl Semimetals*, Physical Review Letters 119 (2017) Nr. 7, S. 76801/1-6.
- 194) A. Lau, C. Ortix, *Synthesizing Weyl semimetals in weak topological insulator and topological crystalline insulator multilayers*, Physical Review B 96 (2017) Nr. 8, S. 81411/1-5.
- 195) S. Lebernegg, O. Janson, I. Rousochatzakis, S. Nishimoto, H. Rosner, A.A. Tsirlin, *Frustrated spin chain physics near the Majumdar-Ghosh point in szenicsite Cu₃(MoO₄)(OH)₄*, Physical Review B 95 (2017) Nr. 3, S. 35145/1-10.
- 196) J.K. Lee, M.-W. Oh, B. Ryu, J.E. Lee, B.-S. Kim, B.-K. Min, S.-J. Joo, H.-W. Lee, S.-D. Park, *Enhanced thermoelectric properties of AgSbTe₂ obtained by controlling heterophases with Ce doping*, Scientific Reports 7 (2017), S. 4496/1-8.
- 197) N. Lee, B.S. Kim, T. Kim, J.-Y. Bae, H.H. Cho, *Thermal design of helium cooled divertor for reliable operation*, Applied Thermal Engineering 110 (2017), S. 1578-1588.
- 198) N.R. Lee-Hone, R. Thanhoffer, V. Neu, R. Schaefer, M. Arora, R. Huebner, D. Suess, D.M. Broun, E. Girt, *Roughness-induced domain structure in perpendicular Co/Ni multilayers*, Journal of Magnetism and Magnetic Materials 441 (2017), S. 283-289.
- 199) K. Leistner, M. Yang, C. Damm, S. Oswald, A. Petr, V. Kataev, K. Nielsch, K.L. Kavanagh, *Aligned cuboid iron nanoparticles by epitaxial electrodeposition*, Nanoscale 9 (2017), S. 5315-5322.
- 200) C.E. Lekka, J.J. Gutierrez-Moreno, M. Calin, *Electronic origin and structural instabilities of Ti-based alloys suitable for orthopaedic implants*, Journal of Physics and Chemistry of Solids 102 (2017), S. 49-61.
- 201) K. Lepicka, P. Pieta, A. Shkurenko, P. Borowicz, M. Majewska, M. Rosenkranz, S. Avdoshenko, A.A. Popov, W. Kutner, *Spectroelectrochemical Approaches to Mechanistic Aspects of Charge Transport in meso-Nickel(II) Schiff Base Electrochromic Polymer*, The Journal of Physical Chemistry C 121 (2017) Nr. 31, S. 16710-16720.
- 202) G. Li, M. Yarali, A. Cocemasov, S. Baunack, D.L. Nika, V.M. Fomin, S. Singh, T. Gemming, F. Zhu, A. Mavrokefalos, O.G. Schmidt, *In-Plane Thermal Conductivity of Radial and Planar Si/SiO_x Hybrid Nanomembrane Superlattices*, ACS Nano 11 (2017) Nr. 8, S. 8215-8222.
- 203) H. Li, F. Cao, S. Guo, Y. Jia, D. Zhang, Z. Liu, P. Wang, S. Scudino, J. Sun, *Effects of Mg and Cu on microstructures and properties of spray-deposited Al-Zn-Mg-Cu alloys*, Journal of Alloys and Compounds 719 (2017), S. 89-96.
- 204) H. Li, F. Cao, S. Guo, Z. Ning, Z. Liu, Y. Jia, S. Scudino, T. Gemming, J. Sun, *Microstructures and properties evolution of spray-deposited Al-Zn-Mg-Cu-Zr alloys with scandium addition*, Journal of Alloys and Compounds 691 (2017), S. 482-488.
- 205) S. Li, E. Khatami, S. Johnston, *Competing phases and orbital-selective behaviors in the two-orbital Hubbard-Holstein model*, Physical Review B 95 (2017), S. 121112/1-5.
- 206) Z. Li, Y. Dong, S. Pauly, C. Chang, R. Wei, F. Li, X.-M. Wang, *Enhanced soft magnetic properties of Fe-based amorphous powder cores by longitude magnetic field annealing*, Journal of Alloys and Compounds 706 (2017), S. 1-6.
- 207) M. Liebscher, R. Fuge, C. Schroefl, A. Lange, A. Caspari, C. Bellmann, V. Mechtcherine, J. Plank, A. Leonhardt, *Temperature- and pH-Dependent Dispersion of Highly Purified Multiwalled Carbon Nanotubes Using Polycarboxylate-Based Surfactants in Aqueous Suspension*, The Journal of Physical Chemistry C 121 (2017) Nr. 31, S. 16903-16910.
- 208) M. Liebscher, A. Lange, C. Schroefl, R. Fuge, V. Mechtcherine, J. Plank, A. Leonhardt, *Impact of the molecular architecture of polycarboxylate superplasticizers on the dispersion of multi-walled carbon nanotubes in aqueous phase*, Journal of Materials Science 52 (2017) Nr. 4, S. 2296-2307.
- 209) R. Limbach, K. Kosiba, S. Pauly, U. Kuehn, L. Wondraczek, *Serrated flow of CuZr-based bulk metallic glasses probed by nano-indentation: Role of the activation barrier, size and distribution of shear transformation zones*, Journal of Non-Crystalline Solids 459 (2017), S. 130-141.

- 210) G. Lin, D. Makarov, O.G. Schmidt, *Magnetic sensing platform technologies for biomedical applications*, Lab on a Chip 17 (2017), S. 1884-1912.
- 211) Lindemann, M. Herrich, B. Gebel, R. Schmidt, U. Stoeck, M. Uhlemann, A. Gebert, *Synthesis of spherical nanocrystalline titanium hydride powder via calciothermic low temperature reduction*, Scripta Materialia 130 (2017), S. 256-259.
- 212) Lindemann, R. Schmidt, S. Pilz, B. Gebel, A. Teresiak, A. Gebert, *Ultrafine-grained Ti-40Nb prepared by reactive milling of the elements in hydrogen*, Journal of Alloys and Compounds 729 (2017), S. 1244-1249.
- 213) J. Linnemann, L. Taudien, M. Klose, L. Giebler, *Electrodeposited films to MOF-derived electrochemical energy storage electrodes: a concept of simplified additive-free electrode processing for self-standing, ready-to-use materials*, Journal of Materials Chemistry A 5 (2017) Nr. 35, S. 18420-18428.
- 214) A. Liu, H. Liu, M. Liang, L. Liu, Z. Lv, H. Zhou, H. Guo, *Controlled synthesis of hollow octahedral ZnCo_2O_4 nanocages assembled from ultrathin 2D nanosheets for enhanced lithium storage*, Nanoscale 9 (2017) Nr. 44, S. 17174-17180.
- 215) F. Liu, F. Jin, S. Wang, A.A. Popov, S. Yang, *Pyramidal TiTb_2C cluster encapsulated within the popular I-h(7)-C-80 fullerene cage*, Inorganica Chimica Acta 468 (2017), S. 203-208.
- 216) F. Liu, D.S. Krylov, L. Spree, S.M. Avdoshenko, N.A. Samoylova, M. rosenkranz, A. Kostanyan, T. Greber, A.U.B. Wolter, B. Buechner, A.A. Popov, *Single molecule magnet with an unpaired electron trapped between two lanthanide ions inside a fullerene*, Nature Communications 8 (2017), S. 16098/1-9.
- 217) F.P. Liu, C.L. Wang, C.-L. Gao, Q. Deng, X. Zhu, A. Kostanyan, R. Westerstroem, F. Jin, S.-Y. Xie, A.A. Popov, T. Greber, S. Yang, *Mononuclear Clusterfullerene Single-Molecule Magnet Containing Strained Fused-Pentagons Stabilized by a Nearly Linear Metal Cyanide Cluster*, Angewandte Chemie 56 (2017) Nr. 7, S. 1830-1834.
- 218) J. Liu, J. Ma, K. Zhang, P. Ravat, S. Avdoshenko, F. Hennersdorf, H. Komber, W. Pisula, J.J. Weigand, A.A. Popov, R. Berger, K. Muellen, X. Feng, *π -Extended and Curved Antiaromatic Polycyclic Hydrocarbons*, Journal of the American Chemical Society 139 (2017) Nr. 22, S. 7513-7521.
- 219) L. Liu, Q. Weng, X. Lu, X. Sun, L. Zhang, O.G. Schmidt, *Advances on Microsized On-Chip Lithium-Ion Batteries*, Small 13 (2017) Nr. 45, S. 1701847/1-12.
- 220) W.F. Lu, C.J. Li, B. Sarac, D. Sopu, J.H. Yi, J. Tan, M. Stoica, J. Eckert, *Structural, elastic and electronic properties of CoZr in B2 and B33 structures under high pressure*, Journal of Alloys and Compounds 705 (2017), S. 445-455.
- 221) X. Lu, G.-P. Hao, X. Sun, S. Kaskel, O.G. Schmidt, *Highly dispersed metal and oxide nanoparticles on ultra-polar carbon as efficient cathode materials for Li-O₂ batteries*, Journal of Materials Chemistry A 5 (2017) Nr. 13, S. 6284-6291.
- 222) A. Madani, H.R. Azarinia, *Design and fabrication of all-polymeric photonic waveguides in optical integrated circuits*, Optik 138 (2017), S. 33-39.
- 223) A. Madani, S.M. Harazim, V.A. Bolanos Quinones, M. Kleinert, A. Finn, E. Saei Ghareh Naz, L. Ma, O.G. Schmidt, *Optical microtube cavities monolithically integrated on photonic chips for optofluidic sensing*, Optics Letters 42 (2017) Nr. 3, S. 486-489.
- 224) M. Madian, R. Ummethala, A.O.A.E. Naga, N. Ismail, M.H. Ruemmeli, A. Eychmueller, L. Giebler, *Ternary $\text{CNTs@TiO}_2/\text{CoO}$ Nanotube Composites: Improved Anode Materials for High Performance Lithium Ion Batteries*, Materials 10 (2017) Nr. 6, S. 678/1-13.
- 225) V. Magdanz, M. Medina-Sanchez, L. Schwarz, H. Xu, J. Elgeti, O.G. Schmidt, *Spermatozoa as Functional Components of Robotic Microswimmers*, Advanced Materials 29 (2017) Nr. 24, S. 1606301/1-18.
- 226) A. Mansikkamaeki, A.A. Popov, Q. Deng, N. Iwahara, L.F. Chibotaru, *Interplay of spin-dependent delocalization and magnetic anisotropy in the ground and excited states of $[\text{Gd}_2@\text{C}_{78}]^-$ and $\text{Gd}_2@\text{C}_{80}]^-$* , The Journal of Chemical Physics 147 (2017) Nr. 12, S. 124305/1-14.
- 227) Y. Mao, L. Peng, S. Wang, L. Xi, *Microstructural characterization of graphite/ CuCrZr joints brazed with CuTiH_2Ni -based fillers*, Journal of Alloys and Compounds 716 (2017), S. 81-87.
- 228) U. Martens, J. Walowski, T. Schumann, M. Mansurova, A. Boehnke, T. Huebner, G. Reiss, A. Thomas, M. Muenzenberg, *Pumping laser excited spins through MgO barriers*, Journal of Physics D 50 (2017) Nr. 14.
- 229) N. Martin, M. Deutsch, G. Chaboussant, F. Damay, P. Bonville, L.N. Fomicheva, A.V. Tsvyashchenko, U.K. Roessler, I. Mirebeau, *Long-period helical structures and twist-grain boundary phases induced by chemical substitution in the $\text{Mn}_{1-x}(\text{Co,Rh})_x\text{Ge}$ chiral magnet*, Physical Review B 96 (2017) Nr. 2, S. 20413/1-5.
- 230) M. Matczak, R. Schaefer, M. Urbaniak, P. Kuswik, B. Szymanski, M. Schmidt, J. Aleksiejew, F. Stobiecki, *Influence of domain structure induced coupling on magnetization reversal of Co/Pt/Co film with perpendicular anisotropy*, Journal of Magnetism and Magnetic Materials 422 (2017), S. 465-469.

- 231) D.M Matson, X. Xiao, J.E. Rodriguez, J. Lee, R.W. Hyers, O. Shuleshova, I. Kaban, S. Schneider, C. Karrasch, S. Burggraff, R. Wunderlich, H.-J. Fecht, *Use of Thermophysical Properties to Select and Control Convection During Rapid Solidification of Steel Alloys Using Electromagnetic Levitation on the Space Station*, JOM 69 (2017) Nr. 8, S. 1311-1318.
- 232) M. Medina-Sanchez, O.G. Schmidt, *Medical microbots need better imaging and control*, Nature 545 (2017) Nr. 7655, S. 406-408.
- 233) R.G. Mendes, A. Mandarino, B. Koch, A.K. Meyer, A. Bachmatiuk, C. Hirsch, T. Gemming, O.G. Schmidt, Z. Liu, M.H. Ruemmeli, *Size and time dependent internalization of label-free nano-graphene oxide in human macrophages*, Nano Research 10 (2017) Nr. 6, S. 1980-1995.
- 234) S. Miao, S. He, M. Liang, G. Lin, B. Cai, O.G. Schmidt, *Microtubular Fuel Cell with Ultrahigh Power Output per Footprint*, Advanced Materials 29 (2017) Nr. 34, S. 1607046/1-7.
- 235) A.-K. Michel, A.C. Niemann, T. Boehnert, S. Martens, J.P. Montero Moreno, D. Goerlitz, R. Zierold, H. Reith, V. Vega, V.M. Prida, A. Thomas, J. Gooth, K. Nielsch, *Temperature gradient-induced magnetization reversal of single ferromagnetic nanowires*, Journal of Physics D 50 (2017) Nr. 49, S. 494007/1-6.
- 236) D. Mikhailova, Z. Hu, C.-Y. Kuo, S. Oswald, K.M. Mogare, S. Agrestini, J.-F. Lee, C.-W. Pao, S.-A. Chen, J.-M. Lee, S.-C. Haw, J.-M. Chen, Y.-F. Liao, H. Ishii, K.-D. Tsuei, A. Senyshyn, H. Ehrenberg, *Charge Transfer and Structural Anomaly in Stoichiometric Layered Perovskite $Sr_2CoO_{0.5}Ir_{0.5}O_4$* , European Journal of Inorganic Chemistry (2017) Nr. 3, S. 587-595.
- 237) D. Mikhailova, N.N. Kuratieva, Y. Utsumi, A.A. Tsirlin, A.M. Abakumov, M. Schmidt, S. Oswald, H. Fuess, H. Ehrenberg, *Composition-dependent charge transfer and phase separation in the $V_{1-x}Re_xO_2$ solid solution*, Dalton Transactions 46 (2017) Nr. 5, S. 1606-1617.
- 238) T. Mix, F. Bittner, K.-H. Mueller, L. Schultz, T.G. Woodcock, *Alloying with a few atomic percent of Ga makes MnAl thermodynamically stable*, Acta Materialia 128 (2017), S. 160-165.
- 239) T. Miyazaki, S. Fukui, J. Ogawa, T. Sato, T. Oka, J. Scheiter, W. Haessler, E. Kulawansha, Z. Yuanding, K. Yokoyama, *Pulse-Field Magnetization for Disc-Shaped MgB_2 Bulk Magnets*, IEEE Transactions on Applied Superconductivity 27 (2017) Nr. 4, S. 6800504/1-4.
- 240) S. Mohapatra, J. van den Brink, A. Singh, *Magnetic excitations in a three-orbital model for the strongly spin-orbit coupled iridates: Effect of mixing between the $J = 1/2$ and $3/2$ sectors*, Physical Review B 95 (2017) Nr. 9, S. 94435/1-11.
- 241) E.V. Monaico, I.M. Tiginyanu, V.V. Ursaki, K. Nielsch, D. Balan, M. Prodana, M. Enachescu, *Gold Electroplating as a Tool for Assessing the Conductivity of InP Nanostructures Fabricated by Anodic Etching of Crystalline Substrates*, Journal of The Electrochemical Society 164 (2017) Nr. 4, S. 179-183.
- 242) Z. Moravkova, E. Dmitrieva, *Structural changes in polyaniline near the middle oxidation peak studied by in situ Raman spectroelectrochemistry*, Journal of Raman Spectroscopy 48 (2017) Nr. 9, S. 1229-1234.
- 243) O. Moscoso-Londono, P. Tancredi, D. Muraca, P. Mendoza Zelis, D. Coral, M.B. Fernandez van Raap, U. Wolff, V. Neu, C. Damm, C.L.P. de Oliveira, K.R. Pirota, M. Knobel, L.M. Socolovsky, *Different approaches to analyze the dipolar interaction effects on diluted and concentrated granular superparamagnetic systems*, Journal of Magnetism and Magnetic Materials 428 (2017), S. 105-118.
- 244) K.A. Motovilov, M. Savinov, E.S. Zhukova, A.A. Pronin, Z.V. Gagkaeva, V. Grinenko, K.V. Sidoruk, T.A. Voeikova, P.Y. Barzilovich, A.K. Grebenko, S.V. Lisovskii, V.I. Torgashev, P. Bednyakov, J. Pokorny, M. Dressel, B.P. Gorshunov, *Observation of dielectric universalities in albumin, cytochrome C and Shewanella oneidensis MR-1 extracellular matrix*, Scientific Reports 7 (2017), S. 15731/1-11.
- 245) C. Mueller, I.T. Neckel, V. Engemaier, D. Pohl, W.H. Schreiner, D.H. Mosca, *$Ni_{74}Mn_{20}Ga_6$ alloys grown by molecular beam epitaxy on $GaAs/AlAs/In_{0.2}Ga_{0.8}As$ (001)*, Thin Solid Films 638 (2017), S. 298-304.
- 246) E. Mueller, B. Buechner, M. Knupfer, H. Berger, *Unscreened plasmon dispersion of 2H transition metal dichalcogenides*, Physical review B 95 (2017) Nr. 7, S. 75150/1-5.
- 247) M. Mueller, H. Vural, C. Schneider, A. Rastelli, O.G. Schmidt, S. Hoefling, P. Michler, *Quantum-Dot Single-Photon Sources for Entanglement Enhanced Interferometry*, Physical Review Letters 118 (2017) Nr. 25, S. 257402/1-6.
- 248) P. Mueller, Y. Koval, I. Lazareva, C. Steiner, S. Wurmehl, B. Buechner, T. Stuerzer, D. Johrendt, *C-axis transport of pnictide superconductors*, Physica Status Solidi B 254 (2017) Nr. 1, S. 1600157/1-7.
- 249) G. Mutschke, D. Baczynski, C. Cierpka, F. Karnbach, M. Uhlemann, X. Yang, K. Eckert, J. Froehlich, *Numerical simulation of mass transfer and convection near a hydrogen bubble during water electrolysis in a magnetic field*, Magnetohydrodynamics 53 (2017) Nr. 1, S. 193-199.
- 250) K.C.B. Naidu, S.R. Kiran, M. Wuppuluri, *Microwave Processed NiMgZn Ferrites for Electromagnetic Intereference Shielding Applications*, IEEE Transactions on Magnetics 53 (2017) Nr. 2.

- 251) K.C.B. Naidu, M. Wuppururi, *Microwave processed bulk and nano NiMg ferrites: A comparative study on X-band electromagnetic interference shielding properties*, Materials Chemistry and Physics 187 (2017), S. 164-176.
- 252) Y.G. Naidyuk, O.E. Kvitsnitskaya, N.V. Gamayunova, D.L. Bashlakov, L.V. Tyutrina, G. Fuchs, R. Huehne, D.A. Chareev, A.N. Vasiliev, *Superconducting gaps in FeSe studied by soft point-contact Andreev reflection spectroscopy*, Physical Review B 96 (2017) Nr. 9, S. 94517/1-7.
- 253) A.K. Nayak, V. Kumar, T. Ma, P. Werner, E. Pippel, R. Sahoo, F. Damay, U.K. Roessler, C. Felser, S.S.P. Parkin, *Magnetic antiskyrmions above room temperature in tetragonal Heusler materials*, Nature 548 (2017) Nr. 7669, S. 561.
- 254) J. Nayak, K. Filsinger, G.H. Fecher, S. Chadov, J. Minar, E.D.L. Rienks, B. Buechner, S.P. Parkin, J. Fink, C. Felser, *Observation of a remarkable reduction of correlation effects in BaCr2As2 by ARPES*, PNAS 114 (2017) 47, S. 12425-12429.
- 255) J. Nayak, S.-C. Wu, N. Kumar, C. Shekhar, S. Singh, J. Fink, E.E.D. Rienks, G.H. Fecher, S.S.P. Parkin, B. Yan, C. Felser, *Multiple Dirac cones at the surface of the topological metal LaBi*, Nature Communications 8 (2017), S. 13942/1-5.
- 256) M. Nicoara, C. Locovei, C. Opris, D. Ursu, R. Vasii, M. Stoica, *Optimizing the parameters for in situ fabrication of hybrid Al-Al2O3 composites*, Journal of Thermal Analysis and Calorimetry 127 (2017) Nr. 1, S. 115-122.
- 257) A.C. Niemann, J. Gooth, S.-C. Wu, S. Baessler, P. Sergelius, R. Huehne, B. Rellinghaus, C. Shekhar, V. Suess, M. Schmidt, C. Felser, B. Yan, K. Nielsch, *Chiral magnetoresistance in the Weyl semimetal NbP*, Scientific Reports 7 (2017), S. 43394/1-6.
- 258) R. Niemann, A. Backen, S. Kauffmann-Weiss, C. Behler, U.K. Roessler, H. Seiner, O. Heczko, K. Nielsch, L. Schultz, S. Faehler, *Nucleation and growth of hierarchical martensite in epitaxial shape memory films*, Acta Materialia 132 (2017), S. 327-334.
- 259) R. Niemann, S. Faehler, *Geometry of adaptive martensite in Ni-Mn-based Heusler alloys*, Journal of Alloys and Compounds 703 (2017), S. 280-288.
- 260) J. Noessler, R. Seerig, S. Yasin, M. Uhlarz, S. Zherlitsyn, G. Behr, S.-L. Drechsler, G. Fuchs, H. Rosner, J. Wosnitza, *Field-induced gapless electron pocket in the superconducting vortex phase of YNi2B2C as probed by magnetoacoustic quantum oscillations*, Physical Review B 95 (2017), S. 14523/1-6.
- 261) C. Nowka, M. Gellesch, J.E. Hamann Borrero, S. Partzsch, C. Wuttke, F. Steckel, C. Hess, U.B. Wolter, L.T. Corredor Bohorquez, B. Buechner, S. Hampel, *Chemical vapor transport and characterization of MnBi2Se4*, Journal of Crystal Growth 459 (2017), S. 81-86.
- 262) I.V. Okulov, M. Boenisch, A.S. Volegov, H. Shakur Shahabi, H. Wendrock, T. Gemming, J. Eckert, *Micro-to-nano-scale deformation mechanism of a Ti-based dendriticultrafine eutectic alloy exhibiting large tensile ductility*, Materials Science and Engineering A 682 (2017), S. 673-678.
- 263) I.V. Okulov, A.S. Volegov, H. Attar, M. Boenisch, S. Ehtemam-Haghighi, M. Calin, J. Eckert, *Composition optimization of low modulus and high-strength TiNb-based alloys for biomedical applications*, Journal of the Mechanical Behavior of Biomedical Materials 65 (2017), S. 866-871.
- 264) K. Olszowska, J. Pang, P.S. Wrobel, L. Zhao, H.Q. Ta, Z. Liu, B. Trzebicka, A. Bachmatiuk, M.H. Ruemmeli, *Three-dimensional nanostructured graphene: Synthesis and energy, environmental and biomedical applications*, Synthetic Metals 234 (2017), S. 53-85.
- 265) R.B., Shimoyama, J. Onyancha, S.J. Singh, Hayashi, K., H. Ogino, V.V. Srinivasu, *Anomalous non-resonant microwave absorption in SmFeAs(O,F) polycrystalline sample*, Physica C 533 (2017), S. 49-52.
- 266) S. Oswald, M. Hoffmann, M. Zier, *Peak position differences observed during XPS sputter depth profiling of the SEI on lithiated and delithiated carbon-based anode material for Li-ion batteries*, Applied Surface Science 401 (2017), S. 408-413.
- 267) J.A. Otalora, M. Yan, H. Schultheiss, R. Hertel, A. Kákay, *Asymmetric spin-wave dispersion in ferromagnetic nanotubes induced by surface curvature*, Physical Review B 95 (2017) Nr. 18, S. 184415/1-10.
- 268) A. Ottmann, M. Scholz, M. Haft, E. Thauer, P. Schneider, M. Gellesch, C. Nowka, S. Wurmehl, S. Hampel, R. Klingeler, *Electrochemical Magnetization Switching and Energy Storage in Manganese Oxide filled Carbon Nanotubes*, Scientific Reports 7 (2017), S. 13625/1-8.
- 269) E.M. Paerschke, K. Wohlfeld, K. Foyevtsova, J. van den Brink, *Correlation induced electron-hole asymmetry in quasi- two-dimensional iridates*, Nature Communications 8 (2017), S. 686/1-6.
- 270) V. Panchal, H. Corte-Leon, B. Gribkov, L.A. Rodriguez, E. Snoeck, A. Manzin, E. Simonetto, S. Vock, V. Neu, O. Kazakova, *Controllable multi-stable probes with low/high magnetic moment*, Scientific Reports 7 (2017) Nr. 1, S. 7224/1-13.
- 271) J. Pang, R.G. Mendes, P.S. Wrobel, M.D. Wlodarski, M.D. Wlodarski, H.Q. Ta, L. Zhao, L. Giebeler, B. Trzebicka, T. Gemming, L. Fu, Z. Liu, J. Eckert, A. Bachmatiuk, M.H. Ruemmeli, *Self-Terminating Confinement Approach for Large-Area Uniform Monolayer Graphene Directly over Si/SiOx by Chemical Vapor Deposition*, ACS Nano 11 (2017) Nr. 2, S. 1946-1956.
- 272) S. Pauly, C. Schrickner, S. Scudino, L. Deng, U. Kuehn, *Processing a glass-forming Zr-based alloy by selective laser melting*, Materials and Design 135 (2017), S. 133-141.

- 273) A.S. Pawlik, T. Kaempfe, A. Haussmann, T. Woike, U. Treske, M. Knupfer, B. Buechner, E. Soergel, R. Streubel, A. Koitzsch, L.M. Eng, *Polarization driven conductance variations at charged ferroelectric domain walls*, *Nanoscale* 9 (2017) Nr. 30, S. 10933-10939.
- 274) D. Pelc, H.-J. Grafe, G.D. Gu, M. Pozek, *Cu nuclear magnetic resonance study of charge and spin stripe order in $\text{La}_{1.875}\text{Ba}_{0.125}\text{CuO}_4$* , *Physical Review B* 95 (2017) Nr. 5, S. 54508/1-8.
- 275) O. Perevertov, Heczko, R. Schaefer, *Direct observation of magnetic domains by Kerr microscopy in a Ni-Mn-Ga magnetic shape-memory alloy*, *Physical Review B* 95 (2017), S. 144431/1-5.
- 276) N. Perez, C. Moya, P. Tartaj, A. Labarta, X. Batlle, *Aggregation state and magnetic properties of magnetite nanoparticles controlled by an optimized silica coating*, *Journal of Applied Physics* 121 (2017) Nr. 4, S. 44304/1-9.
- 277) D. Pohl, S. Schneider, P. Zeiger, J. Ruzs, P. Tiemeijer, S. Lazar, K. Nielsch, B. Rellinghaus, *Atom size electron vortex beams with selectable orbital angular momentum*, *Scientific Reports* 7 (2017), S. 934/1-8.
- 278) P. Potapov, *On the loss of information in PCA of spectrum-images*, *Ultramicroscopy* 182 (2017), S. 191-194.
- 279) P. Pramanik, S. Thota, S. Singh, D.C. Joshi, B. Weise, A. Waske, M.S. Seehra, *Effects of Cu doping on the electronic structure and magnetic properties of MnCo_2O_4 nanostructures*, *Journal of Physics: Condensed Matter* 29 (2017) Nr. 42, S. 425803/1-13.
- 280) K.G. Prashanth, S. Scudino, R.P. Chatterjee, O.O. Salman, J. Eckert, *Additive Manufacturing: Reproducibility of Metallic Parts*, *Technologies* 5 (2017) Nr. 8, S. 5010008/1-7.
- 281) K.G. Prashanth, S. Scudino, J. Eckert, *Defining the tensile properties of Al-12Si parts produced by selective laser melting*, *Acta Materialia* 126 (2017), S. 25-35.
- 282) K.G. Prashanth, S. Scudino, T. Maity, J. Das, J. Eckert, *Is the energy density a reliable parameter for materials synthesis by selective laser melting?*, *Materials Research Letters* 5 (2017) Nr. 6, S. 386-390.
- 283) K.G. Prashantha, R. Damodaramc, T. Maityd, P. Wang, J. Eckert, *Friction welding of selective laser melted Ti6Al4V parts*, *Materials Science and Engineering A* 704 (2017), S. 66-71.
- 284) S. Prathap, M. Wuppuluri, *Multiferroic properties of microwave sintered $\text{PbFe}_{12-x}\text{O}_{19-\text{delta}}$* , *Journal of Magnetism and Magnetic Materials* 430 (2017), S. 114-122.
- 285) Z. Pribulova, Z. Medvecká, J. Kacmarcik, V. Komanicky, T. Klein, P. Rodiere, F. Levy-Bertrand, B. Michon, C. Marcenat, P. Husanikova, V. Cambel, J. Soltys, G. Karapetrov, S. Borisenko, D. Evtushinsky, H. Berger, P. Samuely, *Magnetic and thermodynamic properties of Cu_xTiSe_2 single crystals*, *Physical Review B* 95 (2017) Nr. 17, S. 174512/1-8.
- 286) K. Prokes, E. Ressouche, A. Mohan, A.U.B. Wolter, B. Buechner, C. Hess, *Magnetic structure of $\text{La}_8\text{Cu}_7\text{O}_{19}$* , *Physical Review B* 95 (2017) Nr. 2, S. 24405.
- 287) R. Puttock, H. Corte-Leon, V. Neu, D. Cox, A. Manzin, V. Antonov, P. Vavassori, O. Kazakova, *V-shaped domain wall probes for calibrated magnetic force microscopy*, *IEEE Transactions on Magnetics* 53 (2017) Nr. 11, S. 6500805/1-5.
- 288) Y. Qin, X. Han, K. Song, L. Wang, Y. Cheng, Z. Zhang, Q. Xue, N. Sun, J. Wang, B. Sun, B. Sarac, F. Spieckermann, G. Wang, I. Kaban, J. Eckert, *Stability of shear banding process in bulk metallic glasses and composites*, *Journal of Materials Research* 32 (2017) Nr. 13, S. 2560-2569.
- 289) Y.-S. Qin, X.-L. Han, K.-K. Song, Y.-H. Tian, C.-X. Peng, L. Wang, B.-A. Sun, G. Wang, I. Kaban, J. Eckert, *Local melting to design strong and plastically deformable bulk metallic glass composites*, *Scientific Reports* 7 (2017), S. 42518/1-10.
- 290) A. Queralto, M. de la Mata, J. Arbiol, R. Huehne, X. Obradors, T. Puig, *Unveiling the nucleation and coarsening mechanisms of solution-derived self-assembled epitaxial CeGdO nanostructures*, *Crystal Growth and Design* 17 (2017) Nr. 2, S. 504-516.
- 291) M. Rafique, A. Herklotz, K. Doerr, S. Manzoor, *Giant room temperature magnetoelectric response in strain controlled nanocomposites*, *Applied Physics Letters* 110 (2017) Nr. 20, S. 202902/1-5.
- 292) D.P. Rai, Sandeep, A. Shankar, A.P. Sakhya, T.P. Sinha, P. Grima-Gallardo, H. Cabrera, R. Khenata, M.P. Ghimire, R.K. Thapa, *Electronic, optical and thermoelectric properties of bulk and surface (001) CuInTe_2 : A first principles study*, *Journal of Alloys and Compounds* 699 (2017), S. 1003-1011.
- 293) P. Ramasamy, R.N. Shahid, S. Scudino, J. Eckert, M. Stoica, *Influencing the crystallization of $\text{Fe}_{80}\text{Nb}_{10}\text{B}_{10}$ metallic glass by ball milling*, *Journal of Alloys and Compounds* 725 (2017), S. 227-236.
- 294) P. Ramasamy, M. Stoica, S. Bera, M. Calin, J. Eckert, *Effect of replacing Nb with (Mo and Zr) on glass forming ability, magnetic and mechanical properties of FeCoBSiNb bulk metallic glass*, *Journal of Alloys and Compounds* 707 (2017), S. 78-81.
- 295) M. Rams, M. Boehme, V. Kataev, Y. Krupskaya, B. Buechner, W. Plass, T. Neumann, Z. Tomkowicz, C. Naether, *Static and dynamic magnetic properties of the ferromagnetic coordination polymer $[\text{Co}(\text{NCS})_2(\text{py})_2]_n$* , *Physical Chemistry Chemical Physics* 19 (2017) Nr. 36, S. 24534-24544.

- 296) R. Ray, A.K. Himanshu, P. Sen, U. Kumar, M. Richter, T.P. Sinha, *Effects of octahedral tilting on the electronic structure and optical properties of d^0 double perovskites $A_2\text{ScSbO}_6$ ($A = \text{Sr}, \text{Ca}$)*, Journal of Alloys and Compounds 705 (2017), S. 497-506.
- 297) R. Ray, S. Kumar, *Switchable Multiple Spin States in the Kondo description of Doped Molecular Magnets*, Scientific Reports 7 (2017), S. 42255/1-10.
- 298) A. Reck, S. Pilz, M. Calin, A. Gebert, M. Zimmermann, *Fatigue properties of a new generation β -type Ti-Nb alloy for osteosynthesis with an industrial standard surface condition*, International Journal of Fatigue 103 (2017), S. 147-156.
- 299) G.J. Redhammer, A. Senyshyn, S. Lebernegg, G. Tippelt, E. Dachs, G. Roth, *A neutron diffraction study of crystal and low-temperature magnetic structures within the $(\text{Na}, \text{Li})\text{FeGe}_2\text{O}_6$ pyroxene-type solid solution series*, Physics and Chemistry of Minerals 44 (2017) Nr. 9, S. 669-684.
- 300) L. Reichel, A. Edstroem, D. Pohl, J. Rusz, O. Eriksson, L. Schultz, S. Faehler, *On the origin of perpendicular magnetic anisotropy in strained Fe-Co(-X) films*, Journal of Physics D 50 (2017) Nr. 4, S. 45003/1-8.
- 301) M. Reindl, K.D. Joens, D. Huber, C. Schimpf, Y. Huo, V. Zwiller, A. Rastelli, R. Trotta, *Phonon-Assisted Two-Photon Interference from Remote Quantum Emitters*, Nano Letters 17 (2017) Nr. 7, S. 4090-4095.
- 302) S. Reja, P.S. Anisimov, M. Daghofer, *From frustrated to unfrustrated: Coupling two triangular-lattice itinerant quantum magnets*, Physical Review B 96 (2017) Nr. 8, S. 85144/1-11.
- 303) A.J.E. Rettie, M. Sturza, C.D. Malliakas, A.S. Botana, D.Y. Chung, M.G. Kanatzidis, *Copper Vacancies and Heavy Holes in the Two-Dimensional Semiconductor $\text{KCu}_3\text{-xSe}_2$* , Chemistry of Materials 29 (2017) Nr. 14, S. 6114-6121.
- 304) S. Rex, F.S. Nogueira, A. Sudbo, *Topological staggered field electric effect with bipartite magnets*, Physical Review B 95 (2017), S. 155430/1-10.
- 305) A.M. Rice, W.B. Fellows, E.A. Dolgoplova, A.B. Greytak, A.K. Vannucci, M.D. Smith, S.G. Karakalos, J.A. Krause, S.M. Avdoshenko, A.A. Popov, N.B. Shustova, *Hierarchical Corannulene-Based Materials: Energy Transfer and Solid-State Photophysics*, Angewandte Chemie 56 (2017) Nr. 16, S. 4525-4529.
- 306) M. Richter, K.S. Schellhammer, P. Machata, G. Cuniberti, A. Popov, F. Ortmann, R. Berger, K. Muellen, X. Feng, *Polycyclic heteroaromatic hydrocarbons containing a benzoisindole core*, Organic Chemistry Frontiers 4 (2017) Nr. 5, S. 847-852.
- 307) S. Richter, S. Aswartham, A. Pukenas, V. Grinenko, S. Wurmehl, K. Nielsch, W. Skrotzki, B. Buechner, R. Huehne, *Superconductivity in Ni doped Ba-Fe-As thin films prepared from single crystal targets using PLD*, IEEE Transactions on Applied Superconductivity 27 (2017) Nr. 4, S. 7300304/1-4.
- 308) S. Richter, F. Kurth, K. Iida, K. Pervakov, A. Pukenas, C. Tarantini, J. Jaroszynski, J. Haenisch, V. Grinenko, W. Skrotzki, K. Nielsch, R. Huehne, *Superconducting properties of $\text{Ba}(\text{Fe}_{1-x}\text{Ni}_x)_2\text{As}_2$ thin films in high magnetic fields*, Applied Physics Letters 110 (2017) Nr. 2, S. 22601/1-5.
- 309) H. Rijckaert, G. Pollefeyt, M. Sieger, J. Haenisch, J. Bennewitz, K. De Keukeleere, J. De Roo, R. Huehne, M. Baecker, P. Paturi, H. Huhtinen, M. Hemgesberg, I. Van Driessche, *Optimizing Nanocomposites through Nanocrystal Surface Chemistry: Superconducting $\text{YBa}_2\text{Cu}_3\text{O}_7$ Thin Films via Low-Fluorine Metal Organic Deposition and Preformed Metal Oxide Nanocrystals*, Chemistry of Materials 29 (2017) Nr. 14, S. 6104-6113.
- 310) F. Roeder, K. Vogel, D. Wolf, O. Hellwig, S.H. Wee, S. Wicht, B. Rellinghaus, *Model-based magnetization retrieval from holographic phase images*, Ultramicroscopy 175 (2017), S. 177-187.
- 311) M. Rohnke, S. Pfitzenreuter, B. Mogwitz, A. Henss, J. Thomas, D. Bieberstein, T. Gemming, S.K. Otto, S. Ray, M. Schumacher, M. Gelinsky, V. Alt, *Strontium release from Sr^{2+} -loaded bone cements and dispersion in healthy and osteoporotic rat bone*, Journal of Controlled Release 262 (2017), S. 159-169.
- 312) A. Rosova, M. Kulich, P. Kovac, B. Brunner, J. Scheiter, W. Haessler, *The effect of boron powder on the microstructure of MgB_2 filaments prepared by the modified internal magnesium diffusion technique*, Superconductor Science and Technology 30 (2017) Nr. 5, S. 55001/1-12.
- 313) S.A. Rounaghi, D.E.P. Vanpoucke, H. Eshghi, S. Scudino, E. Esmaeili, S. Oswald, J. Eckert, *Mechanochemical synthesis of nanostructured metal nitrides, carbonitrides and carbon nitride: a combined theoretical and experimental study*, Physical Chemistry Chemical Physics 19 (2017), S. 12414-12424.
- 314) S.A. Rounaghi, D.E.P. Vanpoucke, H. Eshgi, S. Scudino, E. Esmaeili, S. Oswald, S. Eckert, *A combined experimental and theoretical investigation of the Al-Melamine reactive milling system: A mechanistic study towards AlN-based ceramics*, Journal of Alloys and Compounds 729 (2017), S. 240-248.
- 315) F. Rueckerl, T. Klaproth, R. Schuster, B. Buechner, M. Knupfer, *Surface functionalization of WSe_2 by F_{16}CoPc* , Physica Status Solidi B 254 (2017) Nr. 6, S. 1600656/1-5.

- 316) F. Rueckerl, D. Waas, B. Buechner, M. Knupfer, *Particular electronic properties of $F_{16}\text{CoPc}$: A decent electron acceptor material*, Journal of Electron Spectroscopy and Related Phenomena 215 (2017), S. 1-7.
- 317) F. Rueckertl, D. Waas, B. Buechner, M. Knupfer, D.R.T. Zahn, F. Haidu, T. Hahn, J. Kortus, *Charge transfer from and to manganese phthalocyanine: bulk materials and interfaces*, Beilstein Journal of Nanotechnology 8 (2017), S. 1601-1615.
- 318) K. Ruehlig, A. Abylaikhan, A. Aliabadi, V. Kataev, S. Liebing, S. Schwalbe, K. Trepte, C. Ludt, J. Kortus, B. Buechner, T. Rueffer, H. Lang, *Ni^{II} formate complexes with bi- and tridentate nitrogen-donor ligands: synthesis, characterization, and magnetic and thermal properties*, Dalton Transactions 46 (2017) Nr. 12, S. 3963-3979.
- 319) K.C. Rule, B. Willenberg, M. Schaepers, A.U.B. Wolter, B. Buechner, S.-L. Drechsler, G. Ehlers, D.A. Tennant, R.A. Mole, J.S. Gardner, S. Suellow, S. Nishimoto, *Dynamics of linarite: Observations of magnetic excitations*, Physical Review B 95 (2017), S. 24430/1-6.
- 320) J. Ruzs, A. Lubk, J. Spiegelberg, D. Tyutyunnikov, *Fully nonlocal inelastic scattering computations for spectroscopical transmission electron microscopy methods*, Physical Review B 96 (2017) Nr. 24, S. 245121/1-10.
- 321) E. Saei Ghareh Naz, M.R. Jorgensen, O.G. Schmidt, *Density of optical states in rolled-up photonic crystals and quasi crystals*, Computer Physics Communications 214 (2017), S. 117-127.
- 322) K.L. Salcedo Rodriguez, M. Hoffmann, F. Golmar, G. Pasquevich, P. Werner, W. Hergert, C.E. Rodriguez Torres, *Producing ZnFe_2O_4 thin films from ZnO/FeO multilayers*, Applied Surface Science 393 (2017), S. 256-261.
- 323) M.S. Salem, K. Nielsch, *Crossover between axial and radial magnetic anisotropy in self-organized permalloy nanowires*, Materials Science and Engineering B 223 (2017), S. 120-124.
- 324) R. Salikhov, L. Reichel, B. Zingsem, R. Abrudan, A. Edstroem, D. Thonig, J. Ruzs, O. Eriksson, L. Schultz, S. Faehler, M. Farle, U. Wiedwald, *Enhanced spin-orbit coupling in tetragonally strained Fe-Co-B films*, Journal of Physics: Condensed Matter 29 (2017) Nr. 27, S. 275802/1-9.
- 325) N.A. Samoylova, S.M. Avdoshenko, D.S. Krylov, H.R. Thompson, A.C. Kirkhorn, M. Rosenkranz, S. Schiemenz, F. Ziegls, A.U.B. Wolter, S. Yang, S. Stevenson, A.A. Popov, *Confining the spin between two metal atoms within the carbon cage: redox-active metal-metal bonds in dimetallofullerenes and their stable cation radicals*, Nanoscale 9 (2017) Nr. 23, S. 7977-7990.
- 326) Sandeep, D.P. Rai, A. Shankar, M.P. Ghimire, R. Khenata, S.B. Omran, S.V. Syrotyuk, R.K. Thapa, *Investigation of the structural, electronic and optical properties of the cubic RbMF_3 perovskites ($M = \text{Be}, \text{Mg}, \text{Ca}, \text{Sr}$ and Ba) using modified Becke-Johnson exchange potential*, Materials Chemistry and Physics 192 (2017), S. 282-290.
- 327) J. Sander, *Additive Herstellung von Bauteilen aus Hochleistungswerkzeugstahl*, Dresdner Transferbrief 25 (2017) Nr. 2, S. 18.
- 328) J. Sander, J. Hufenbach, M. Bleckmann, L. Giebeler, H. Wendrock, S. Oswald, T. Gemming, J. Eckert, U. Kuehn, *Selective laser melting of ultra-high-strength TRIP steel: processing, microstructure, and properties*, Journal of Materials Science 52 (2017) Nr. 9, S. 4944-4956.
- 329) J. Sander, J. Hufenbach, L. Giebeler, M. Bleckmann, J. Eckert, U. Kuehn, *Microstructure, mechanical behavior, and wear properties of FeCrMoVC steel prepared by selective laser melting and casting*, Scripta Materialia 126 (2017), S. 41-44.
- 330) B. Sarac, S. Bera, S. Balakin, M. Stoica, M. Calin, J. Eckert, *Hierarchical surface patterning of Ni- and Be-free Ti- and Zr-based bulk metallic glasses by thermoplastic net-shaping*, Materials Science and Engineering C 73 (2017), S. 398-405.
- 331) B. Sarac, S. Bera, F. Spieckermann, S. Balakin, M. Stoica, M. Calin, J. Eckert, *Micropatterning kinetics of different glass-forming systems investigated by thermoplastic net-shaping*, Scripta Materialia 137 (2017), S. 127-131.
- 332) T. Schachinger, S. Loeffler, A. Steiger-Thirsfeld, M. Stoeger-Pollach, S. Schneider, D. Pohl, B. Rellinghaus, P. Schattschneider, *EMCD with an electron vortex filter: Limitations and possibilities*, Ultramicroscopy 179 (2017), S. 15-23.
- 333) J. Schaumann, M. Loor, D. Unal, A. Mudring, S. Heimann, U. Hagemann, S. Schulz, F. Maculewicz, G. Schierring, *Improving the zT value of thermoelectrics by nanostructuring: Tuning the nanoparticle morphology of Sb_2Te_3 by ionic liquids*, Dalton Transactions 46 (2017) Nr. 3, S. 656-668.
- 334) S. Schimmel, Z. Sun, D. Baumann, D. Krylov, N. Samoylova, A. Popov, B. Buechner, C. Hess, *Adsorption characteristics of $\text{Er}_3\text{N}@C(80)$ on $\text{W}(110)$ and $\text{Au}(111)$ studied via scanning tunneling microscopy and spectroscopy*, Beilstein Journal of Nanotechnology 8 (2017), S. 1127-1134.
- 335) R. Schlegel, P.K. Nag, D. Baumann, R. Beck, S. Wurmehl, B. Buechner, C. Hess, *Defect states in LiFeAs as seen by low-temperature scanning tunneling microscopy and spectroscopy*, Physica Status Solidi B 254 (2017) Nr. 1, S. 1600159/1-11.
- 336) B. Schleicher, D. Klar, K. Ollefs, A. Diestel, Walecki D., E. Weschke, L. Schultz, K. Nielsch, S. Faehler, H. Wende, M.E. Gruner, *Electronic structure and magnetism of epitaxial $\text{Ni-Mn-Ga}(-\text{Co})$ thin films with partial disorder: a view across the phase transition*, Journal of Physics D 50 (2017) Nr. 46, S. 465005/1-13.

- 337) B. Schleicher, R. Niemann, S. Schwabe, R. Huehne, L. Schultz, K. Nielsch, S. Faehler, *Reversible tuning of magnetocaloric Ni-Mn-Ga-Co films on ferroelectric PMN-PT substrates*, Scientific Reports 7 (2017), S. 14462/1-7.
- 338) C. Schliebe, T. Graske, T., Lang, H. Gemming, *Metal nanoparticle-loaded porous carbon hollow spheres by twin polymerization*, Journal of Materials Science 52 (2017) Nr. 21, S. 12653-12662.
- 339) O.G. Schmidt, *Adapt to stay ahead*, Nature 549 (2017) Nr. 7670, S. 22.
- 340) R. Schmidt, S. Pilz, I. Lindemann, C. Damm, J. Hufenbach, A. Helth, D. Geissler, A. Henss, M. Rohnke, M. Calin, M. Zimmermann, J. Eckert, M.H. Lee, A. Gebert, *Powder metallurgical processing of low modulus beta-type Ti-45Nb to bulk and macro-porous compacts*, Powder Technology 322 (2017), S. 393-401.
- 341) S. Schmidt, S. Doering, N. Hasan, F. Schmidl, V. Tynpel, F. Kurth, K. Iida, H. Ikuta, T. Wolf, P. Seidel, *Josephson effects at iron pnictide superconductors: Approaching phasesensitive experiments*, Physica Status Solidi B 254 (2017) Nr. 1, S. 1600165/1-15.
- 342) S.F.M. Schmidt, C. Koo, V. Mereacre, J. Park, D.W. Heermann, V. Kataev, C.E. Anson, D. Prodius, G. Novitchi, R. Klingeler, A.K. Powell, *A Three-Pronged Attack To Investigate the Electronic Structure of a Family of Ferromagnetic Fe₄Ln₂ Cyclic Coordination Clusters: A Combined Magnetic Susceptibility, High-Field/High-Frequency Electron Paramagnetic Resonance, and ⁵⁷Fe Moessbauer Study*, Inorganic Chemistry 56 (2017) Nr. 9, S. 4796-4806.
- 343) L. Schnaubelt, H. Petzold, J.M. Speck, E. Dmitrieva, M. Rosenkranz, M. Korb, *Redox properties and electron transfer in a triarylamine-substituted HS-Co²⁺/LS-Co³⁺ redox couple*, Dalton Transactions 46 (2017) Nr. 8, S. 2690-2698.
- 344) C. Schneidermann, N. Jaeckel, S. Oswald, L. Giebel, V. Presser, L. Borchardt, *Solvent-Free Mechanochemical Synthesis of Nitrogen-Doped Nanoporous Carbon for Electrochemical Energy Storage*, ChemSusChem 10 (2017) Nr. 11, S. 2416-2424.
- 345) M. Schumacher, L. Reither, J. Thomas, M. Kampschulte, U. Gbureck, A. Lode, M. Gelinsky, *Calcium phosphate bone cement/mesoporous bioactive glass composites for controlled growth factor delivery*, Biomaterials Science 5 (2017) Nr. 3, S. 578-588.
- 346) R. Schuster, C. Habenicht, M. Ahmad, M. Knupfer, B. Buechner, *Direct observation of the lowest indirect exciton state in the bulk of hexagonal boron nitride*, Physical Review B 97 (2017) Nr. 4, S. 41201/1-5.
- 347) H. Schwab, M. Boenisch, L. Giebel, T. Gustmann, J. Eckert, U. Kuehn, *Processing of Ti-5553 with improved mechanical properties via an in-situ heat treatment combining selective laser melting and substrate plate heating*, Materials and Design 130 (2017), S. 83-89.
- 348) L. Schwarz, M. Medina Sanchez, O.G. Schmidt, *Hybrid BioMicromotors*, Applied Physics Reviews 4 (2017) Nr. 3, S. 31301/1-23.
- 349) S.A. Scott, C. Deneke, D.M. Paskiewicz, H.J. Ryu, A. Malachias, S. Baunack, O.G. Schmidt, D.E. Savage, M.A. Eriksson, M.G. Lagally, *Silicon Nanomembranes with Hybrid Crystal Orientations and Strain States*, ACS Applied Materials and Interfaces 9 (2017) Nr. 48, S. 42372-42382.
- 350) S. Scudino, R.N. Shahid, B. Escher, M. Stoica, B.S. Li, J.J. Kruzic, *Mapping the cyclic plastic zone to elucidate the mechanisms of crack tip deformation in bulk metallic glasses*, Applied Physics Letters 110 (2017) Nr. 8, S. 81903/1-4.
- 351) S. Scudino, K.B. Surreddi, *Shear band morphology and fracture behavior of cold-rolled Zr_{52.5}Ti₅Cu₁₈Ni_{14.5}Al₁₀ bulk metallic glass under tensile loading*, Journal of Alloys and Compounds 708 (2017), S. 722-727.
- 352) A. Sedky, E. Nazarova, K. Nenkov, K. Buchkov, *A Comparative Study Between Electro and Magneto Excess Conductivities in FeTeSe Superconductors*, Journal of Superconductivity and Novel Magnetism 30 (2017) Nr. 1, S. 1-12.
- 353) M. Seifert, E. Brachmann, G.K. Rane, S.B. Menzel, T. Gemming, *Capability Study of Ti, Cr, W, Ta and Pt as Seed Layers for Electrodeposited Platinum Films on gamma-Al₂O₃ for High Temperature and Harsh Environment Applications*, Materials 10 (2017) Nr. 1, S. 10010054/1-20.
- 354) M. Seifert, G.K. Rane, S. Oswald, S.B. Menzel, T. Gemming, *The Influence of the Composition of Ru_{100-x}Al_x (x = 50, 55, 60, 67) Thin Films on Their Thermal Stability*, Materials 10 (2017) Nr. 3, S. 277.
- 355) M. Seifert, L. Schultz, R. Schaefer, S. Hankemeier, R. Froemter, H.P. Oepen, V. Neu, *Micromagnetic investigation of domain and domain wall evolution through the spin-reorientation transition of an epitaxial NdCo₅ film*, New Journal of Physics 19 (2017), S. 33002/1-15.
- 356) B.V. Senkovskiy, A.V. Fedorov, D. Haberer, M. Farjam, K.A. Simonov, A.B. Preobrajenski, N. Martensson, N. Atodiressei, V. Caciuc, S. Bluegel, A. Rosch, N.I. Verbitskiy, M. Hell, D.V. Evtushinsky, R. German, T. Marangoni, P.H.M. van Loosdrecht, F.R. Fischer, A. Grueneis, *Semiconductor-to-Metal Transition and Quasiparticle Renormalization in Doped Graphene Nanoribbons*, Advanced Electronic Materials 3 (2017), S. 1600490/1-8.
- 357) B.V. Senkovskiy, D. Haberer, D.Y. Usachov, A.V. Fedorov, N. Ehlen, M. Hell, L. Petaccia, G. Di Santo, R.A. Durr, F.R. Fischer, A. Grueneis, *Spectroscopic characterization of N=9 armchair graphene nanoribbons*, Physica Status Solidi RRL 11 (2017) Nr. 8, S. 1700157/1-5.

- 358) B.V. Senkovskiy, M. Pfeiffer, S.K. Alavi, A. Bliesener, J. Zhu, S. Michel, A.V. Fedorov, R. German, D. Hertel, D. Haberer, L. Petaccia, F.R. Fischer, K. Meerholz, P.H.M. van Loosdrecht, K. Lindfors, A. Grueneis, *Making Graphene Nanoribbons Photoluminescent*, Nano Letters 17 (2017) Nr. 7, S. 4029-4037.
- 359) H. Sepehri-Amin, J. Thielsch, J. Fischbacher, T. Ohkubo, T. Schrefl, O. Gutfleisch, K. Hono, *Correlation of microchemistry of cell boundary phase and interface structure to the coercivity of $\text{Sm}(\text{Co}_{0.784}\text{Fe}_{0.100}\text{Cu}_{0.088}\text{Zr}_{0.028})_{7.19}$ sintered magnets*, Acta Materialia 126 (2017), S. 1-10.
- 360) P. Sergelius, J.H. Lee, O. Fruchart, M.S. Salem, S. Allende, R.A. Escobar, J. Gooth, R. Zierold, J.-C. Toussaint, S. Schneider, D. Pohl, B. Rellinghaus, S. Martin, J. Garcia, H. Reith, A. Spende, M.-E. Toimil-Molares, D. Altbir, R. Cowburn, D. Goerlitz, K. Nielsch, *Intra-wire coupling in segmented Ni/Cu nanowires deposited by electrodeposition*, Nanotechnology 28 (2017), S. 65709/1-11.
- 361) R.N. Shahid, S. Scudino, *Microstructural strengthening by phase transformation in Al-Fe₃Al composites*, Journal of Alloys and Compounds 705 (2017), S. 590-597.
- 362) D.I. Shim, G. Choi, N. Lee, T. Kim, B.S. Kim, H.H. Cho, *Enhancement of Pool Boiling Heat Transfer Using Aligned Silicon Nanowire Arrays*, ACS Applied Materials and Interfaces 9 (2017) Nr. 20, S. 17595-17602.
- 363) M. Sieger, P. Pahlke, M. Lao, M. Eisterer, A. Meledin, G. Van Tendeloo, J. Haenisch, B. Holzapfel, A. Usoskin, A. Kursumovic, J.L. MacManus-Driscoll, B.H. Stafford, M. Bauer, K. Nielsch, L. Schultz, R. Huehne, *Tailoring microstructure and superconducting properties in thick BaHfO₃ and Ba₂Y(Nb/Ta)O₆ doped YBCO films on technical templates*, IEEE Transactions on Applied Superconductivity 27 (2017) Nr. 4, S. 6601407/1-7.
- 364) M. Sieger, P. Pahlke, R. Ottolinger, B.H. Stafford, M. Lao, A. Meledin, M. Bauer, M. Eisterer, G. Van Tendeloo, L. Schultz, K. Nielsch, R. Huehne, *Influence of substrate tilt angle on the incorporation of BaHfO₃ in thick YBa₂Cu₃O_{7-delta} films*, IEEE Transactions on Applied Superconductivity 27 (2017) Nr. 4, S. 7500505/1-4.
- 365) G. Simutis, S. Gvasaliya, N.S. Beesetty, T. Yoshida, J. Robert, S. Petit, A.I. Kolesnikov, M.B. Stone, F. Bourdarot, H.C. Walker, D.T. Adroja, O. Sobolev, C. Hess, T. Masuda, A. Revcolevschi, B. Buechner, A. Zheludev, *Spin pseudogap in the $S = 1/2$ chain material Sr₂CuO₃ with impurities*, Physical Review B 95 (2017) Nr. 5, S. 54409/1-6.
- 366) S. Singh, P. Pramanik, S. Sangaraju, A. Mallick, L. Giebeler, S. Thota, *Size-dependent structural, magnetic, and optical properties of MnCo₂O₄ nanocrystallites*, Journal of Applied Physics 121 (2017) Nr. 19, S. 194303/1-12.
- 367) E. Smirnova, A. Sotnikov, S. Ktitorov, H. Schmidt, *Low temperature acoustic characterization of PMN single crystal*, Journal of Applied Physics 122 (2017) Nr. 8, S. 84103/1-6.
- 368) L. Smykalla, C. Mende, M. Fronk, P.F. Siles, M. Hietschold, G. Salvan, D.R.T. Zahn, O.G. Schmidt, T. Rueffer, H. Lang, *(Metallo)porphyrins for potential materials science applications*, Beilstein Journal of Technology 8 (2017), S. 1786-1800.
- 369) I.V. Soldatov, R. Schaefer, *Advances in quantitative Kerr microscopy*, Physical Review B 95 (2017) Nr. 1, S. 14426/1-6.
- 370) I.V. Soldatov, R. Schaefer, *Selective sensitivity in Kerr microscopy*, Review of Scientific Instruments 88 (2017) Nr. 7, S. 73701/1-9.
- 371) I.V. Soldatov, R. Schaefer, *Advanced MOKE magnetometry in wide-field Kerr-microscopy*, Journal of Applied Physics 122 (2017), S. 153906/1-7.
- 372) H. Sopha, D. Pohl, C. Damm, L. Hromadko, B. Rellinghaus, A. Gebert, J.M. Macak, *Self-organized double-wall oxide nanotube layers on glass-forming Ti-Zr-Si(-Nb) alloys*, Materials Science and Engineering C 70 (2017) Nr. 2, S. 258-263.
- 373) D. Söpu, A. Stukowski, M. Stoica, S. Scudino, *Atomic-Level Processes of Shear Band Nucleation in Metallic Glasses*, Physical Review Letters 119 (2017) Nr. 19, S. 195503/1-5.
- 374) M. Sparing, E. Reich, J. Haenisch, T. Gottschall, R. Huehne, S. Faehler, B. Rellinghaus, L. Schultz, B. Holzapfel, *Controlling particle properties in YBa₂Cu₃O_{7-delta} nanocomposites by combining PLD with an inert gas condensation system*, Superconductor Science and Technology 30 (2017) Nr. 10, S. 104007/1-10.
- 375) B.H. Stafford, M. Sieger, R. Ottolinger, A. Meledin, N.M. Strickland, S.C. Wimbush, G.V. Tendeloo, R. Huehne, L. Schultz, *Tilted BaHfO₃ nanorod artificial pinning centres in REBCO films on inclined substrate deposited-MgO coated conductor templates*, Superconductor Science and Technology 30 (2017) Nr. 5, S. 55002/1-7.
- 376) J. Stoetzel, T. Schneider, M.M. Mueller, H.-J. Kleebe, H. Wiggers, G. Schierning, R. Schmechel, *Microstructure and thermoelectric properties of Si-WSi₂ nanocomposites*, Acta Materialia 125 (2017), S. 321-326.
- 377) A.P. Storey, S.J. Ray, V. Hoffmann, M. Voronov, C. Engelhard, W. Buscher, G.M. Hieftje, *Wavelength Scanning with a Tilting Interference Filter for Glow-Discharge Elemental Imaging*, Applied Spectroscopy 71 (2017) Nr. 6, S. 1280-1288.
- 378) X. Sun, X. Lu, S. Huang, L. Xi, L. Liu, B. Liu, Q. Weng, L. Zhang, O.G. Schmidt, *Reinforcing Germanium Electrode with Polymer Matrix Decoration for Long Cycle Life Rechargeable Lithium Ion Batteries*, ACS Applied Materials and Interfaces 9 (2017) Nr. 44, S. 38556-38566.

- 379) X. Sun, L. Qiao, L. Qiao, H. Pang, D. Li, *Synthesis of nanosheet-constructed SnO₂ spheres with efficient photocatalytic activity and high lithium storage capacity*, *Ionics* 23 (2017) Nr. 11, S. 3177-3185.
- 380) A. Surrey, K. Nielsch, B. Rellinghaus, *Comments on „Evidence of the hydrogen release mechanism in bulk MgH₂“, Scientific Reports* 7 (2017), S. 44216/1-4.
- 381) A. Surrey, L. Schultz, B. Rellinghaus, *Multislice simulations for in-situ HRTEM studies of nanostructured magnesium hydride at ambient hydrogen pressure*, *Ultramicroscopy* 175 (2017), S. 111-115.
- 382) T. Takenaka, Y. Mizukami, J.A. Wilcox, M. Konczykowski, S. Seiro, C. Geibel, Y. Tokiwa, Y. Kasahara, C. Putzke, Y. Matsuda, A. Carrington, T. Shibauchi, *Full-Gap Superconductivity Robust against Disorder in Heavy-Fermion CeCu₂Si₂*, *Physical Review Letters* 119 (2017) Nr. 7, S. 77001/1-5.
- 383) P. Tancredi, P.C. Rivas Rojas, O. Moscoso-Londono, U. Wolff, V. Neu, C. Damm, B. Rellinghaus, M. Knobel, L.M. Socolovsky, *Synthesis process, size and composition effects of spherical Fe₃O₄ and FeO@Fe₃O₄ core/shell nanoparticles*, *New Journal of Chemistry : NJC* 41 (2017), S. 15033-15041.
- 384) J. Thielsch, F. Bittner, T.G. Woodcock, *Magnetization reversal processes in hot-extruded tau-MnAl-C*, *Journal of Magnetism and Magnetic Materials* 426 (2017), S. 25-31.
- 385) S. Thota, M. Reehuis, A. Maljuk, A. Hoser, J.U. Hoffmann, B. Weise, A. Waske, M. Krautz, D.C. Joshi, S. Nayak, S. Ghosh, P. Suresh, K. Dasari, S. Wurmehl, O. Prokhnenko, B. Buechner, *Neutron diffraction study of the inverse spinels Co₂TiO₄ and Co₂SnO₄*, *Physical Review B* 96 (2017) Nr. 14, S. 144104/1-13.
- 386) J. Torrens-Serra, P. Bruna, M. Stoica, J. Eckert, *Glass-forming ability and microstructural evolution of [(Fe_{0.6}Co_{0.4})_{0.75}Si_{0.05}B_{0.20}]_{96-x}Nb₄M_x metallic glasses studied by Moessbauer spectroscopy*, *Journal of Alloys and Compounds* 704 (2017), S. 748-759.
- 387) J. Torrens-Serra, F. Solivellas, M.L. Corro, M. Stoica, S. Kustov, *Erratum: Effect of temperature and magnetic field on magnetomechanical damping of Fe-based bulk metallic glasses (J. Phys. D: Appl. Phys. 49 505003)*, *Journal of Physics D* 50 (2017) Nr. 3, S. 39601/1.
- 388) P. Turalaska, M. Homa, G. Bruzda, N. Sobczak, I. Kaban, N. Mattern, J. Eckert, *Wetting behavior and reactivity between liquid Gd and ZrO₂ Substrate*, *Journal of Mining and Metallurgy B: Metallurgy* 53 (2017) Nr. 3, S. 285-293.
- 389) Y.V. Tymoshenko, Y.A. Onyikienko, T. Mueller, R. Thomale, S. Rachel, A.S. Cameron, P.Y. Portnichenko, D.V. Efremov, V. Tsurkan, D.L. Abernathy, J. Ollivier, A. Schneidewind, A. Piovano, V. Felea, A. Loidl, D.S. Inosov, *Pseudo-Goldstone Magnons in the Frustrated S=3/2 Heisenberg Helimagnet ZnCr₂Se₄ with a Pyrochlore Magnetic Sublattice*, *Physical Review X* 7 (2017) Nr. 4, S. 41049/1-14.
- 390) Y. Utz, F. Hammerath, R. Kraus, T. Ritschel, J. Geck, L. Hozoi, J. van den Brink, A. Mohan, C. Hess, K. Karmakar, S. Singh, D. Bounoua, R. Saint-Martin, L. Pinsard-Gaudart, A. Revcolevschi, B. Buechner, H.-J. Grafe, *Effect of different in-chain impurities on the magnetic properties of the spin chain compound SrCuO₂ probed by NMR*, *Physical Review B* 96 (2017) Nr. 11, S. 115135/1-12.
- 391) M. Valldor, R. Yadav, L. Hozoi, J. van den Brink, A. Maljuk, J. Werner, F. Scaravaggi, A.U.B. Wolter, B. Buechner, *Swedenborgite CaBa(Mn₂Fe₂)O₇ with Spin Ordering on a Geometrically Frustrated, Polar, Non-centrosymmetric S=5/2 Lattice*, *Zeitschrift fuer Anorganische Und Allgemeine Chemie* 643 (2017) Nr. 21, S. 1543-1550.
- 392) G. van Miert, C. Ortix, C.M. Smith, *Topological origin of edge states in two-dimensional inversion-symmetric insulators and semimetals*, *2D Materials* 4 (2017) Nr. 1, S. 15023/1-9.
- 393) S.V. Vegesna, D. Buerger, R. Patra, B. Abendroth, I. Skorupa, O.G. Schmidt, H. Schmidt, *Thouless length and valley degeneracy factor of ZnMnO thin films with anisotropic, highly conductive surface layers*, *Journal of Applied Physics* 121 (2017) Nr. 22, S. 225105/1-8.
- 394) O. Vittorio, M. Curcio, M. Cojoc, G.F. Goya, S. Hampel, F. Iemma, A. Dubrovskaya, G. Cirillo, *Polyphenols delivery by polymeric materials: challenges in cancer treatment*, *Drug Delivery* 24 (2017) Nr. 1, S. 162-180.
- 395) S. Vock, C. Hengst, Z. Sasvari, R. Schaefer, L. Schultz, V. Neu, *The role of the inhomogeneous demagnetizing field on the reversal mechanism in nanowire arrays*, *Journal of Physics D-Applied Physics* 50 (2017) Nr. 47, S. 475002/1-10.
- 396) B. Voelker, N. Jaeger, M. Calin, M. Zehetbauer, J. Eckert, A. Hohenwarter, *Influence of testing orientation on mechanical properties of Ti₄₅Nb deformed by high pressure torsion*, *Materials and Design* 114 (2017), S. 40-46.
- 397) U. Vogel, S. Oswald, J. Eckert, *Interface and stability analysis of Tantalum- and Titanium nitride thin films onto Lithiumniobate*, *Applied Surface Science* 425 (2017), S. 254-260.
- 398) A.S. Volegov, K.-H. Mueller, F. Bittner, T. Mix, D.S. Neznakhin, E.A. Volegova, K. Nenkov, L. Schultz, T.G. Woodcock, *Magnetic viscosity of L1₀ structured Mn-Ga and Mn-Al alloys*, *Journal of Magnetism and Magnetic Materials* 441 (2017), S. 750-756.

- 399) M. Voronov, V. Hoffmann, W. Buscher, C. Engelhard, *Computational model of inductively coupled plasma sources in comparison to experimental data for different torch designs and plasma conditions. Part II: theoretical model*, Journal of Analytical Atomic Spectrometry 32 (2017) Nr. 1, S. 181-192.
- 400) M. Voronov, V. Hoffmann, C. Engelhard, W. Buscher, *Computational model of inductively coupled plasma sources in comparison to experimental data for different torch designs and plasma conditions. Part I: experimental study*, Journal of Analytical Atomic Spectrometry 32 (2017) Nr. 1, S. 167-180.
- 401) D. Waas, F. Rueckerl, M. Knupfer, B. Buechner, *Energy-level alignment at interfaces between manganese phthalocyanine and C₆₀*, Beilstein Journal of Nanotechnology 8 (2017), S. 927-932.
- 402) J. Wang, G.-Z. Liu, D.V. Efremov, J. van den Brink, *Order parameter fluctuation and ordering competition in Ba_{1-x}K_xFe₂As₂*, Physical Review B 95 (2017) Nr. 2, S. 24511/.
- 403) J. Wang, C. Ortix, J. van den Brink, D.V. Efremov, *Fate of interaction-driven topological insulators under disorder*, Physical Review B 96 (2017) Nr. 20, S. 201104/1-6.
- 404) P. Wang, H.C. Li, K.G. Prashanth, J. Eckert, S. Scudino, *Selective laser melting of Al-Zn-Mg-Cu: Heat treatment, microstructure and mechanical properties*, Journal of Alloys and Compounds 707 (2017), S. 287-290.
- 405) Z. Wang, K. Georgarakis, W.W., Prashanth, K.G. Zhang, J. Eckert, S. Scudino, *Reciprocating sliding wear behavior of high-strength nanocrystalline Al₈₄Ni₇Gd₆Co₃ alloys*, Wear 382-383 (2017), S. 78-84.
- 406) Z. Wang, S. Scudino, K.G. Prashanth, J. Eckert, *Corrosion properties of high-strength nanocrystalline Al₈₄Ni₇Gd₆Co₃ alloy produced by hot pressing of metallic glass*, Journal of Alloys and Compounds 707 (2017), S. 63-67.
- 407) F. Wasser, S. Wurmehl, S. Aswartham, Y. Sidis, J.T. Park, A. Schneidewind, B. Buechner, M. Braden, *Spin reorientation transition in Na-doped BaFe₂As₂ studied by single-crystal neutron diffraction*, Physica Status Solidi B 254 (2017) Nr. 1, S. 1600181/1-9.
- 408) H. Weber, M. Schumacher, P. Jovari, Y. Tsuchiya, W. Skrotzki, R. Mazzarello, I. Kaban, *Experimental and ab initio molecular dynamics study of the structure and physical properties of liquid GeTe*, Physical Review B 96 (2017) Nr. 5, S. 54204/1-11.
- 409) A. Werner, P. Bludovsky, C. Selzer, U. Koch, L. Giebeler, S. Oswald, S. Kaskel, *Hierarchical Ti-Beta Obtained by Simultaneous Desilication and Titanation as an Efficient Catalyst for Cyclooctene Epoxidation*, ChemCatChem 9 (2017) Nr. 20, S. 3860-3869.
- 410) H. Wilsenach, K. Zuber, D. Degering, R. Heller, V. Neu, *High precision half-life measurement of ¹⁴⁷Sm alpha decay from thin-film sources*, Physical Review C 95 (2017) Nr. 3, S. 34618.
- 411) A. Winkler, S. Harazim, D.J. Collins, R. Bruenig, H. Schmidt, S.B. Menzel, *Compact SAW aerosol generator*, Biomed Microdevices 19 (2017), S. 9/1-10.
- 412) S.M. Winter, A.A. Tsirlin, M. Daghofer, J. van den Brink, Y. Singh, P. Gegenwart, R. Valenti, *Models and materials for generalized Kitaev magnetism*, Journal of Physics: Condensed Matter 29 (2017) Nr. 49, S. 493002/1-27.
- 413) A.U.B. Wolter, L.T. Corredor, L. Janssen, K. Nenkov, S. Schoenecker, S.-H. Do, K.-Y. Choi, R. Albrecht, J. Hunger, T. Doert, M. Vojta, B. Buechner, *Field-induced quantum criticality in the Kitaev system α -RuCl₃*, Physical Review B 96 (2017) Nr. 4, S. 41405/1-5.
- 414) X. Wu, P. Jiang, G. Razinskas, Y. Huo, H. Zhang, M. Kamp, A. Rastelli, O.G. Schmidt, B. Hecht, K. Lindfors, M. Lippitz, *On-Chip Single-Plasmon Nanocircuit Driven by a Self-Assembled Quantum Dot*, Nano Letters 17 (2017) Nr. 7, S. 4291-4296.
- 415) M. Wuppuluri, S.R. Kiran, M.P. Reddy, N.R. Reddy, K.V.S. Kumar, *DC conductivity and Seebeck coefficient of nonstoichiometric MgCuZn ferrites*, Materials Science-Poland 35 (2017) Nr. 1, S. 40-44.
- 416) K. Xu, Y. Fu, Y. Zhou, F. Hennersdorf, P. Machata, I. Vincon, J.I. Weigand, A.A. Popov, R. Berger, X. Feng, *Cationic Nitrogen-Doped Helical Nanographenes*, Angewandte Chemie 56 (2017) Nr. 50, S. 15876-15881.
- 417) L. Xu, Z. Zangeneh, R. Yadav, S. Avdoshenko, J. van den Brink, A. Jesche, L. Hozoi, *Spin-reversal energy barriers of 305 K for Fe²⁺ d⁶ ions with linear ligand coordination*, Nanoscale 9 (2017) Nr. 30, S. 10596-10600.
- 418) H. Yang, Y. Sun, Y. Zhang, W.-J. Shi, S.S.P. Parkin, B. Yan, *Topological Weyl semimetals in the chiral antiferromagnetic materials Mn₃Ge and Mn₃Sn*, New Journal of Physics 19 (2017), S. 15008/1-8.
- 419) H. Yasuoka, T. Kubo, Y. Kishimoto, D. Kasinathan, M. Schmidt, B. Yan, Y. Zhang, H. Tou, C. Felser, A.P. Mackenzie, M. Baenitz, *Emergent Weyl Fermion Excitations in TaP Explored by ¹⁸¹Ta Quadrupole Resonance*, Physical Review Letters 118 (2017) Nr. 23, S. 236403/1-6.
- 420) Y. Yerin, A. Omelyanchouk, S.L. Drechsler, D.V. Efremov, J. van den Brink, *Anomalous diamagnetic response in multiband superconductors with broken time-reversal symmetry*, Physical Review B 96 (2017) Nr. 14, S. 144513/1-7.
- 421) Y. Yin, Y. Chen, E. Saei Ghareh Naz, X. Lu, S. Li, V. Engemaier, L. Ma, O.G. Schmidt, *Silver Nanocap Enabled Conversion and Tuning of Hybrid Photon-Plasmon Modes in Microtubular Cavities*, ACS Photonics 4 (2017) Nr. 4, S. 736-740.

- 422) Y. Yin, S. Li, V. Engemaier, E.S. Ghareh Naz, S. Giudicatti, L. Ma, O.G. Schmidt, *Topology induced anomalous plasmon modes in metallic Moebius nanorings*, Laser and Photonics Reviews 11 (2017) Nr. 2, S. 1600219.
- 423) Z.-J. Ying, M. Cuoco, C. Ortix, P. Gentile, *Tuning pairing amplitude and spin-triplet texture by curving superconducting nanostructures*, Physical Review B 96 (2017) Nr. 10, S. 100506/1-6.
- 424) F. Yuan, K. Iida, V. Grinenko, P. Chekhonin, A. Pukenas, W. Skrotzki, M. Sakoda, Naito, M., A. Sala, M. Putti, A. Yamashita, Y. Takano, Z. Shi, K. Nielsch, R. Huehne, *The influence of the in-plane lattice constant on the superconducting transition temperature of FeSe_{0.7}Te_{0.3} thin films*, AIP Advances 7 (2017) Nr. 6, S. 65015/1-14.
- 425) R. Zaripov, E. Vavilova, I. Khairuzhdinov, K. Salikhov, V. Voronkova, M.A. Abdulmalic, F.E. Meva, S. Weheabby, T. Rueffer, B. Buechner, V. Kataev, *Tuning the spin coherence time of Cu(II)-(bis)oxamato and Cu(II)-(bis)oxamidato complexes by advanced ESR pulse protocols*, Beilstein Journal of Nanotechnology 8 (2017), S. 943-955.
- 426) M.G. Zavareh, Y. Skourski, K.P. Skokov, D.Y. Karpenkov, L. Zvyagina, A. Waske, D. Haskel, M. Zhernenkov, J. Wosnitza, O. Gutfleisch, *Direct Measurement of the Magnetocaloric Effect in La(Fe,Si,Co)(13) Compounds in Pulsed Magnetic Fields*, Physical Review Applied 8 (2017) Nr. 1, S. 14037/1-9.
- 427) J. Zeisig, N. Schaedlich, L. Giebeler, J. Sander, J. Eckert, U. Kuehn, J. Hufenbach, *Microstructure and abrasive wear behavior of a novel FeCrMoVC laser cladding alloy for high-performance tool steels*, Wear 382-383 (2017), S. 107-112.
- 428) J. Zeisner, M. Brockmann, S. Zimmermann, A. Weisse, M. Thede, E. Ressouche, K.Y. Povarov, A. Zheludev, A. Kluemper, B. Buechner, V. Kataev, F. Goehmann, *Anisotropic magnetic interactions and spin dynamics in the spin-chain compound Cu(py)₂Br₂: An experimental and theoretical study*, Physical Review B 96 (2017) Nr. 2, S. 24429/1-24.
- 429) J. Zelezny, Y. Zhang, C. Felser, B. Yan, *Spin-Polarized Current in Noncollinear Antiferromagnets*, Physical Review Letters 119 (2017) Nr. 18, S. 187204/1-7.
- 430) M. Zeng, Y. Chen, J. Li, H. Xue, R.G. Mendes, J. Liu, T. Zhang, M.H. Ruemmeli, L. Fu, *2D WC single crystal embedded in graphene for enhancing hydrogen evolution reaction*, Nano Energy 33 (2017), S. 356-362.
- 431) J. Zhang, E. Zallo, B. Hoefer, Y. Chen, R. Keil, M. Zopf, S. Boettner, F. Ding, O.G. Schmidt, *Electric-Field-Induced Energy Tuning of On-Demand Entangled-Photon Emission from Self-Assembled Quantum Dots*, Nano Letters 17 (2017) Nr. 1, S. 501-507.
- 432) L. Zhang, Z.Y. He, J. Tan, M. Calin, K.G. Prashanth, B. Sarac, B. Voelker, Y.H. Jiang, R. Zhou, J. Eckert, *Designing a multifunctional Ti-2Cu-4Ca porous biomaterial with favorable mechanical properties and high bioactivity*, Journal of Alloys and Compounds 727 (2017), S. 338-345.
- 433) L. Zhang, Z.Y. He, J. Tan, Y.Q. Zhang, M. Stoica, M. Calin, K.G. Prashant, M.J. Cordill, Y.H. Jiang, R. Zhou, J. Eckert, *Designing a novel functional-structural NiTi/hydroxyapatite composite with enhanced mechanical properties and high bioactivity*, Intermetallics 84 (2017), S. 35-41.
- 434) L. Zhang, Z.Y. He, J. Tan, Y.Q. Zhang, M. Stoica, K.G. Prashant, M.J. Cordill, Y.H. Jiang, R. Zhou, J. Eckert, *Rapid fabrication of function-structure-integrated NiTi alloys: Towards a combination of excellent superelasticity and favorable bioactivity*, Intermetallics 82 (2017), S. 1-13.
- 435) L. Zhang, J. Tan, Z.D. Meng, Z.Y. He, Y.Q. Zhang, Y.H. Jiang, R. Zhou, *Low elastic modulus Ti-Ag/Ti radial gradient porous composite with high strength and large plasticity prepared by spark plasma sintering*, Materials Science and Engineering A 688 (2017), S. 330-337.
- 436) L. Zhang, H. Zhang, W. Li, T. Gemming, P. Wang, Boenisch M., D. Söpu, J. Eckert, S. Pauly, *Beta-type Ti-based bulk metallic glass composites with tailored structural metastability*, Journal of Alloys and Compounds 708 (2017), S. 972-981.
- 437) Q. Zhang, Y. Xiao, T. Zhang, Z. Weng, M. Zeng, S. Yue, R.G. Mendes, L. Wang, S. Chen, M.H. Ruemmeli, L. Peng, L. Fu, *Iodine-Mediated Chemical Vapor Deposition Growth of Metastable Transition Metal Dichalcogenides*, Chemistry of Materials 29 (2017) Nr. 11, S. 4641-4644.
- 438) Y. Zhang, Y. Sun, H. Yang, J. Zelezny, S.P.P. Parkin, C. Felser, B. Yan, *Strong anisotropic anomalous Hall effect and spin Hall effect in the chiral antiferromagnetic compounds Mn₃X (X = Ge, Sn, Ga, Ir, Rh, and Pt)*, Physical Review B 95 (2017) Nr. 7, S. 75128/1-9.
- 439) L. Zhao, H.Q. Ta, A. Dianat, A. Soni, A. Fediai, W. Yin, T. Gemming, B. Trzebicka, G. Cuniberti, Z. Liu, A. Bachmatiuk, M.H. Ruemmeli, *In Situ Electron Driven Carbon Nanopillar-Fullerene Transformation through Cr Atom Mediation*, Nano Letters 17 (2017) Nr. 8, S. 4725-4732.
- 440) Q. Zhou, J. Pu, X. Sun, C. Zhu, J. Li, J. Wang, S. Chang, H. Zhang, *In situ surface engineering of nickel inverse opal for enhanced overall electrocatalytic water splitting*, Journal of Materials Chemistry A 5 (2017) Nr. 28, S. 14873-14880.

- 441) D. Zilic, K. Molcanov, M. Juric, J. Habjanic, B. Rakvin, Y. Krupskaya, V. Kataev, S. Wurmehl, B. Buechner, *3D oxalate-based coordination polymers: Relationship between structure, magnetism and color, studied by high-field ESR spectroscopy*, Polyhedron 126 (2017), S. 120-126.
- 442) N. Zingsem, F. Ahrend, S. Vock, D. Gottlob, I. Krug, H. Doganay, D. Holzinger, V. Neu, A. Ehresmann, *Magnetic charge distribution and stray field landscape of asymmetric neel walls in a magnetically patterned exchange bias layer system*, Journal of Physics D 50 (2017) Nr. 49, S. 495006/1-9.
- 443) X. Zotos, *A TBA approach to thermal transport in the XXZ Heisenberg model*, Journal of Statistical Mechanics: Theory and Experiment (2017), S. 103101/1-9.
- 444) C. Zwahr, D. Guenther, T. Brinkmann, N. Gulow, S. Oswald, M. Gross Holthaus, A.F. Lasagni, *Laser Surface Patterning of Titanium for Improving the Biological Performance of Dental Implants*, Advanced Healthcare Materials 6 (2017) Nr. 3, S. 1600858/1-9.

Contributions to conferences proceedings and monographs

- 1) A. Bengtson, V. Hoffmann, M. Kasik, K. Marshall, *Analytical Glow Discharges: Fundamentals, Applications and New Developments*, in: Encyclopedia of Analytical Chemistry, S. 1-76 (2017).
- 2) S.V. Biryukov, M. Weihnacht, A. Sotnikov, H. Schmidt, *SAW based rotation force of a cylindrical solid*, IEEE International Ultrasonics Symposium (IUS), Washington, DC/ USA, 6.-9.9.17, S. 1-4 (2017).
- 3) F. Ding, O.G. Schmidt, *Polarization Entangled Photons from Semiconductor Quantum Dots*, in: Quantum Dots for Quantum Information Technologies (Nano-Optics and Nanophotonics; Bd.3); print 978-3-319-56377-0; online 978-3-319-56378-7, S. 235-266 (2017).
- 4) T. Doehring, A.-C. Probst, F. Emmerich, M. Stollenwerk, V. Stehlikova, P. Friedrich, C. Damm, *Development of iridium coated x-ray mirrors for astronomical applications*, SPIE Optical Engineering and Applications, 2017, San Diego, California/ USA, 29.8.17, in: Proceedings Volume 10399, Optics for EUV, X-Ray, and Gamma-Ray Astronomy VIII; 103991C, 2017, S. 103991C/1-9 (2017).
- 5) V. Hoffmann, *Latest developments in analytical glow discharge contribution to conference proceedings*, Japanese Discussing Group for Plasma Spectrochemistry, Tokyo/ Japan, 14.4.17, S. 30-33 (2017).
- 6) A.F. Khusnuriyalova, A. Petr, A.T. Gubaidullin, A.V. Sukhov, V.I. Morozov, B. Buechner, V. Kataev, O.G. Sinyashin, D.G. Yakhvarov, *Electrochemical generation and observation by magnetic resonance of superparamagnetic cobalt nanoparticles*, Electrochimica Acta (2017).
- 7) S. Makharza, G. Cirillo, O. Vittorio, S. Hampel, *Physiological and Clinical Considerations of Drug Delivery Systems Containing Carbon Nanotubes and Graphene*, in: Drug Delivery Approaches and Nanosystems, Volume 2: Drug Targeting Aspects of Nanotechnology. Hard ISBN: 9781771885843; E-Book ISBN: 9781315225364 (2017).
- 8) M. Medina-Sanchez, V. Magdanz, L. Schwarz, H. Xu, O.G. Schmidt, *Spermibots: Concept and Applications*, 6th International Conference, Living Machines 2017, Stanford, CA/ USA, 26.-28.7.17, Proceedings: Biomimetic and Biohybrid Systems, in: Living Machines: Conference on Biomimetic and Biohybrid Systems. Lecture Notes in Computer Science (LNCS); volume 10384, S. 579-588 (2017).
- 9) A. Sotnikov, H. Schmidt, M.H. Haghighi, M. Gorev, Y. Suhak, H. Fritze, S. Sakharov, *Material Parameters of Ca₃TaGa₃Si₂O₁₄ (CTGS) Piezoelectric Single Crystal at Extreme Temperatures*, Joint Conference of the European Frequency and Time Forum and IEEE International Frequency Control Symposium (EFTF/IFCS), Besancon/ France, 9.-13.7.17, S. 193-197 (2017).
- 10) M. Weihnacht, A. Sotnikov, Y. Suhak, H. Fritze, H. Schmidt, *Accuracy analysis and deduced strategy of measurements applied to Ca₃TaGa₃Si₂O₁₄ (CTGS) material characterization*, IEEE International Ultrasonics Symposium (IUS), Washington, DC/ USA 6.-9.9.17, S. 1-4 (2017).

Editorship

- 1) A.A. Popov, A.A. Popov (ed.) *Endohedral Fullerenes: Electron Transfer and Spin*, Springer International Publishing, 2017.

Invited talks

- 1) S.H. Baek, *Orbital-related electronic instabilities in Fe-based superconductors*, Seminar, Pohang/ South Korea, 16.10.17 (2017).
- 2) S. Borisenko, *Superconducting gap in BSCCO*, Superstripes 2017 - Quantum Physics in Complex Matter: Superconductivity, Magnetism and Ferroelectricity, Ischia/ Italy, 5.-9.6.17 (2017).
- 3) S. Borisenko, *Materials Architecture: Design of Functional Systems in Reciprocal Space*, Solid State Physics Seminar, University of Regensburg, Regensburg/ Germany, 27.7.17 (2017).
- 4) S. Borisenko, *Experimental realization of type-II Weyl state in non-centrosymmetric TaIrTe₄*, SMEC'17, Caribbean Islands/ Caribbean , 1.-9.4.17 (2017).
- 5) B. Buechner, *Anisotropic Magnetism and Spin Gap in alpha Ru Cl₃*, Moscow International Symposium on Magnetism, Moscow/ Russia, 1.-5.7.17 (2017).
- 6) B. Buechner, *Magnetic field induced spin gap in the Kitaev system RuCl₃*, 15th Theoretical and Experimental Magnetism Meeting (TEMM), Abingdon/ England, 4.-6.7.17 (2017).
- 7) B. Buechner, *Orbitals and short range order in Fe-based superconductors*, Workshop „Common Threads in the Electronic Phase Diagram of Unconventional Superconductors“, Lorentz Center, Leiden/ Netherlands, 27.2.-3.3.17 (2017).
- 8) B. Buechner, *Orbitals and Polarons in Fe-based superconductors*, MSU-IFW-ILTPE Joint Workshop, Moskau/ Russia, 13.-16.6.17 (2017).
- 9) B. Buechner, *Orbitals and Polarons in Fe-based superconductors*, Superstripes 2017, Ischia/ Italy, 6.-10.6.17 (2017).
- 10) B. Buechner, *Anisotropic Magnetism and Spin Gap in a Ru Cl₃*, DPG Tagung 2017, Dresden/ Germany, 20.-24.3.17 (2017).
- 11) B. Buechner, *TBD - Fe-based Superconductors*, APS March Meeting, New Orleans/ USA, 17.-13.3.17 (2017).
- 12) M. Calin, S. Abdi, P.F. Gostin, J. Sort, M.D. Baro, J. Eckert, A. Gebert, *Novel biocompatible Ni- and Cu-free Ti-based metallic glasses: thermal stability, corrosion resistance and apatite-forming ability*, ISMANAM 2017, San Sebastian/ Spain, 18.-23.6.17 (2017).
- 13) M. Calin, S. Bera, P. Ramasamy, M. Stoica, J. Eckert, *Improving the glass formation and mechanical behavior of Ni-free TiZr-based bulk metallic glasses by Ga additions*, TMS 2017, San Diego/ USA, 26.2-2.3.17 (2017).
- 14) M. Calin, S. Bera, B. Sarac, R. Parthiban, M. Stoica, J. Eckert, *Role of minor addition of 'soft' metallic elements in formation and properties of Ti-based bulk metallic glasses*, EUROMAT 2017, Thessaloniki /Greece, 17.-22.9.17 (2017).
- 15) M. Calin, M. Boenisch, A. Panigrahi, J. Hohler, M. Zehetbauer, J. Eckert, *Nanostructured biocompatible Ti-Nb alloys processed by severe plastic deformation*, NANOMAT 2017, Brotas/ Brasil, 19.-22.3.17 (2017).
- 16) M. Calin, M. Boenisch, S. Pilz, S. Bera, A. Gebert, J. Eckert, *Properties optimization of Ti-based biomaterials by structural design*, BRAMAT 2017, Brasov/ Romania, 9.-11.3.17 (2017).
- 17) M. Calin, B. Sarac, S. Bera, R. Parthiban, A. Gebert, J. Eckert, *Properties optimization of Ti-based biomaterials by structural design*, SELECTA International Summer School, Ioannina/Greece, 3.-8.9.17 (2017).
- 18) M. Calin, B. Sarac, S. Bera, R. Parthiban, M. Stoica, J. Eckert, *Surface patterning of Ni-free Ti- and Zr-based bulk metallic glasses via thermoplastic forming*, The 16th International Conference on Rapidly Quenched and Metastable Materials (RQ16), Leoben/ Austria, 27.8.-1.9.17 (2017).
- 19) C.-H. Chang, *Giant anisotropic magnetoresistance due to snake orbits in carbon nanoscrolls*, Quantum Transport Workshop, Taipei/ Taiwan 17.8.17 (2017).
- 20) F. Ding, *Semiconductor quantum photonic chips*, The 4th International Conference on Quantum Foundation and Technology, Shanghai/ China, 16.11.16 (2017).
- 21) F. Ding, *Towards an ideal semiconductor source of polarization entangled photons*, DPG-Frühjahrstagung, Dresden/ Germany, 22.3.17 (2017).
- 22) F. Ding, *An invitation from a semiconductor physicist: Bridging semiconductors and quantum optics*, Institute for Quantum Optics, Leibniz University Hannover, Hannover/ Germany, 10.5.17 (2017).
- 23) F. Ding, *Towards an ideal entangled photon sources*, The 1st International Semiconductor Conference for Global Challenges, Nanjing/ China, 16.-19.7.17 (2017).
- 24) F. Ding, *Why I am optimistic about semiconductor entangled photon sources?*, OSA Incubator Integrated Semiconductor Quantum Photonic Devices, Washington DC/ USA, 18.-20.6.17 (2017).
- 25) F. Ding, *Why I am optimistic about semiconductor entangled photon sources?*, Walter-Schottky Insitute, TU Munich, Munich/ Germany, 8.5.17 (2017).
- 26) F. Ding, *Towards quantum interference with semiconductor entangled photon sources*, Physics of Quantum Electronics, Snowbird/ USA, 8.-13.1.17 (2017).

- 27) F. Ding, *Semiconductor entangled photon sources*, Faculty of Physics, University of Bremen, Bremen/ Germany, 20.4.17 (2017).
- 28) F. Ding, *An optimistic view on semiconductor entangled photon sources*, Festkörpertag Südniedersachsen, Braunschweig/ Germany, 5.7.17 (2017).
- 29) F. Ding, *Progress in semiconductor entangled photon sources*, Fudan University, Shanghai/ China, 17.7.17 (2017).
- 30) S.-L. Drechsler, *Constraints on the total coupling strength to low-energy bosons in iron based superconductors*, International Conference „Superstripes 2017“, Ischia/ Italy, 5.6.17 (2017).
- 31) S.-L. Drechsler, *Constraints on the coupling to low-energy bosons in Fe based superconductors*, 14.06.2017, Lomonosov Moscow State University, Department of Chemistry, Moscow/ Russia, 14.6.17 (2017).
- 32) S.-L. Drechsler, H. Rosner, V. Grinenko, S. Aswartham, I. Morozov, L. Ming, A. Boltalin, K. Kihou, C. Lee, T. Kim, D. Evtushinsky, J. Tomczak, S. Johnston, S. Borisenko, *Mass enhancements and band shifts in strongly hole overdoped Fe-based pnictide superconductors: KFe₂As₂ and CsFe₂As₂*, Superstripes 2017, Ischia/ Italy, 4.-10.6.17 (2017).
- 33) J. Dufouleur, R. Giraud, *Quantum Transport in low-D Systems*, Eingeladener Vortrag - Workshop IFW-SPINTEC, Dresden/ Germany, 16.-17.11.17 (2017).
- 34) J. Dufouleur, L. Veyrat, B. Dassonneville, E. Xypakis, J. Bardarson, B. Buechner, R. Giraud, *Transport properties of disordered 3DTIs nanostructures*, Synthesis, Theoretical Examination and Experimental Investigation of Emergent Materials, Moscow/ Russia, 13.-16.6.17 (2017).
- 35) J. Dufouleur, L. Veyrat, B. Dassonneville, E. Xypakis, J. Bardarson, B. Buechner, R. Giraud, *Transport properties of disordered 3DTIs nanostructures*, Boundary Effects and Correlations in One-Dimensional Systems, Regensburg/ Germany, 1.-2.6.17 (2017).
- 36) S. Faehler, M.E. Gruner, H. Seiner, R. Niemann, P. Entel, K. Nielsch, *Towards a scale bridging understanding of transformation hysteresis in Heusler alloys*, International Workshop on Hysteresis in magnetocaloric, electrocaloric and elastocaloric refrigeration, Dresden/ Germany, 7.-10.2.17 (2017).
- 37) J. Fink, *Non-Fermi-liquid behavior, Lifshitz transitions, and Hund's metal behavior of iron-based superconductors from ARPES*, SFB Kolloquium, Universität Halle, Halle/ Germany, 6.4.17 (2017).
- 38) J. Fink, *Electronic structure studies of topological insulators and related compounds by ARPES*, 31st International Winterschool on Electronic Properties of Kirchberg/ Austria, 4.-10.3.17 (2017).
- 39) J. Fink, *Hund's metal behavior and Lifshitz transitions in iron-based superconductors and related compounds*, International Conference „Electron correlation in superconductors and Nanostructure (ECSN-2017)“, Odessa/ Ukraine, 17.-20.8.17 (2017).
- 40) J. Fink, *Angle-resolved photoemission spectroscopy-a many-body spectroscopy*, Intensive week, Universität Köln, Köln/ Germany, 28.-30.3.17 (2017).
- 41) J. Fink, *Non-Fermi-liquid behavior, Lifshitz transitions, and Hund's metal behavior in iron-based superconductors from ARPES*, Institut Strukturforschung TU Dresden, Dresden/ Germany, 17.1.17 (2017).
- 42) J. Fink, *ARPES studies of charge carrier scattering rates in iron-based superconductors and related compounds*, Electronic Properties of Strongly Correlated Materials, Vancouver/ Canada, 4.-6.12.17 (2017).
- 43) J. Fink, *Non-Fermi-liquid behavior, Lifshitz transitions, and Hund's metal behavior of iron-based superconductors and related compounds from ARPES*, International Conference „Superstripes 2017“: Quantum physics in Complex Matter: Superconductivity, Magnetism and Ferroelectricity, Ischia/ Italy, 5.-10.6.17 (2017).
- 44) V.M. Fomin, *Topology-driven effects in advanced nanoarchitectures*, 4th World Congress and Expo on Nanotechnology and Materials Science, Barcelona/ Spain, 5.-7.4.17 (2017).
- 45) V.M. Fomin, *Topology-driven effects in advanced nanoarchitectures*, 2017 EMN Vienna Meeting, Vienna/ Austria, 18.-22.6.17 (2017).
- 46) V.M. Fomin, *Quantum Physics. Nanophotonics, Lecture Series*, Quantum Physics. Nanophotonics, Lecture Series, Pusan National University, Busan/ South Korea, 21.12.16-17.1.17 (2017).
- 47) V.M. Fomin, *Theory of phonons in advanced micro- and nanoarchitectures for thermoelectric applications*, 4th Central and Eastern European Conference on Thermal Analysis and Calorimetry, Chisinau/ Republic of Moldova, 28.-31.8.17 (2017).
- 48) V.M. Fomin, *Topology-driven effects in advanced nanoarchitectures*, Seminar, Northwestern University, Evanston/ USA, 15.12.17 (2017).
- 49) V.M. Fomin, *Geometry- and topology-induced effects in advanced nanoarchitectures*, Humboldt Kolleg on Multidisciplinarity in Modern Science for the Benefit of Society Chisinau/ Republic of Moldova, 21.-22.9.17 (2017).
- 50) V.M. Fomin, *Key concepts of the self-propulsion of catalytic tubular micromotors*, Micromotors Summer School, Dresden/ Germany, 15.-18.8.17 (2017).
- 51) V.M. Fomin, *Topology- and geometry-driven effects in advanced nanoarchitectures*, Seminar, Pusan National University, Busan/ Republic of Korea, 13.11.17 (2017).

- 52) V.M. Fomin, *Topology-driven effects in advanced nanoarchitectures*, The 4th International Conference & Exhibition for Nanotechnology NANOPIA 2017, Changwon/ Republic of Korea, 8.-10.11.17 (2017).
- 53) V.M. Fomin, *Vortex matter in rolled-up superconductor micro- and nanoarchitectures*, Seminar, Argonne National Laboratory, Argonne/ USA, 14.12.17 (2017).
- 54) V.M. Fomin, *Theory of phonons in advanced nanostructured microarchitectures*, Seminar, University of California Riverside, California/ USA, 11.12.17 (2017).
- 55) I.C. Fulga, *Integer spin fermions - a minimal model*, Topology meets materials workshop, Dresden/ Germany, June 2017 (2017).
- 56) I.C. Fulga, *Integer spin fermions - a minimal model*, FKT Seminar, University of Regensburg, Regensburg/ Germany, July 2017 (2017).
- 57) I.C. Fulga, *Scattering matrix invariants of Floquet topological phases*, TU Delft, Delft/ The Netherlands, September 2017 (2017).
- 58) I.O. Fulga, *Integer spin fermions - a minimal model*, Lorentz Institute, Leiden University, Leiden/ The Netherlands, September 2017 (2017).
- 59) A. Gebert, *Development of low modulus beta Ti-Nb alloys for bone implant applications*, Dresden Concept Scientific Area Network „Innovations in Medical Technology“, Dresden/ Germany, 23.10.17 (2017).
- 60) A. Gebert, *Corrosion behaviour of bulk glass-forming alloys*, Kolloquium des Instituts für Materialphysik, WWU Muenster, Muenster/ Germany, 17.10.17 (2017).
- 61) A. Gebert, R. Schmidt, S. Pilz, J. Eckert, M. Rohnke, M. Zimmermann, M. Calin, *Metastable Ti-based alloys for biomedical use*, International Conference on rapidly Quenched & Metastable Materials (RQ16), Leoben/ Austria, 27.8.-1.9.17 (2017).
- 62) D. Geissler, H. Wendrock, P.F. Gostin, D. Grell, E. Kerscher, A. Gebert, *In-situ investigation of cracking and stress corrosion cracking in Zr-based bulk metallic glass*, International Conference on rapidly Quenched & Metastable Materials (RQ16), Leoben/ Austria, 27.8.-1.9.17 (2017).
- 63) D. Geissler, H. Wendrock, P.F. Gostin, D. Grell, E. Kerscher, A. Gebert, *Cracking and stress corrosion cracking of Zr-based glasses*, Kolloquium des Instituts für Materialphysik (IMP) der WWU Muenster, Muenster/ Germany, 17.-18.10.17 (2017).
- 64) H.-J. Grafe, *Spin chains probed by Nuclear Magnetic Resonance: I. SrCuO₂ and Sr₂CuO₃ II. LiCuSbO₄*, Seminar talk, University of Zagreb, Zagreb/ Croatia, 18.5.17 (2017).
- 65) J.E. Hamann Borrero, *Valence state reflectometry of complex oxide heterointerfaces*, Workshop on Surface and Interface Diffraction in Condensed Matter Physics and Chemistry, DESY, Hamburg/ Germany, 8.-10.3.17 (2017).
- 66) J.E. Hamann-Borrero, *Valence state reflectometry of complex oxide heterointerfaces*, Energy Materials Nanotechnology Meeting, La Habana/ Cuba, 4.-8.5.17 (2017).
- 67) J. Han, N. Mattern, *Phase equilibria and structure investigation of metallic alloy systems by X-ray diffraction*, Modeling of multiscale metastable materials, Institute of Materials, Shanghai University, Shanghai/ China, 2.8.17 (2017).
- 68) J. Han, P. Thirathipiwat, J. Bednarcik, N. Mattern, J. Freudenberger, T. Gemming, *Lattice strain and solid solution strengthening in single phase high-entropy alloys*, International Workshop on metastable new materials for young scientists, Kunming University of Science and Technology, Kunming, Yunnan Province/ China, 3.8.17 (2017).
- 69) C. Hess, *Resonance-like enhancement of quasiparticle interference in LiFeAs*, International Conference - Electron Correlation in Superconductors and Nanostructures (ECSN-2017), Odessa/ Ukraine, 17.-20.8.17 (2017).
- 70) C. Hess, *Electron-boson interaction revealed by resonantly enhanced Friedel oscillations*, Seminar, Universitaet Stuttgart, Stuttgart/ Germany, 6.12.17 (2017).
- 71) C. Hess, *Temperature dependent quasiparticle interference of LiFeAs*, Superstripes 2017 - Quantum Physics in Complex Matter: Superconductivity, Magnetism and Ferroelectricity, Ischia/ Italy, 4.-10.6.17 (2017).
- 72) C. Hess, *Boson-assisted Friedel oscillation resonance in LiFeAs: evidence for $q \sim 0$ modes*, SFB-Kolloquium, Universität zu Koeln, Koeln/ Germany, 18.10.17 (2017).
- 73) C. Hess, *Heat transport of low-dimensional quantum magnets: signatures of fractional excitations*, Theory Seminar, LMU Muenchen, Muenchen/ Germany, 20.10.17 (2017).
- 74) V. Hoffmann, *New developments in glow discharge optical and mass spectrometry*, ZFM Festkoerpertag 2017, Leibniz Universität Hannover, Hannover/ Germany, 3.2.17 (2017).
- 75) V. Hoffmann, *Latest developments in analytical glow discharge*, Japanese Discussing Group for Plasma Spectrochemistry, Tokyo/ Japan, 14.4.17 (2017).
- 76) V. Kataev, *Signatures of fractionalized spin excitations in the proximate quantum spin liquid α -RuCl₃ from sub-THz spectroscopy in strong magnetic fields*, International Conference „Modern Development of Magnetic Resonance 2017“, Kazan/ Russia, 25.9.-29.9.17 (2017).

- 77) V. Kataev, *Insights into the spin-orbital entanglement in complex iridium oxides from high-field ESR spectroscopy*, International Conference „Superstripes 2017“: Quantum physics in Complex Matter: Superconductivity, Magnetism and Ferroelectricity, Ischia/ Italy, 4.-10.6.17 (2017).
- 78) V. Kataev, *Spin-orbit coupling effects in complex iridium oxides as seen by high-field ESR spectroscopy*, Quantum Matter and Materials Colloquium, University of Cologne, Köln/ Germany, 29.3.17 (2017).
- 79) V. Kataev, *Signatures of the field-induced spin-nematic state in the frustrated anisotropic spin-chain compound LiCuSbO₄*, Moscow International Symposium on Magnetism MISM 2017, Moscow/ Russia, 1.-5.7.17 (2017).
- 80) J. Krzuc, B. Li, S.H. Xie, H. Shakur Shahabi, S. Scudino, J. Eckert, *Improving the fracture toughness of bulk metallic glasses by thermomechanical treatments*, TMS 2017, The 146th Annual meeting and exhibition, San Diego/ USA, 26.2.-2.3.17 (2017).
- 81) A. Lau, *A study of topological states of matter: from butterflies to Weyl fermions*, Quantum Tinkerer Seminar, TU Delft, Delft/ Netherlands, 6.3.17 (2017).
- 82) A. Lau, *A study of topological states of matter: from butterflies to Weyl fermions*, Quantum Many-Body Theory Seminar, MPI for Solid State Research, Stuttgart, Germany/ 30.3.17 (2017).
- 83) A. Lubk, *Quantitative Coherent Imaging*, Summer School on Quantitative Electron Microscopy 2017/ York/ UK, 22.5.-2.6.17 (2017).
- 84) A. Lubk, *Advanced Holographic Tomography for 3D Magnetic Imaging in Magnetic Textures*, Interregio Seminar, Universität Augsburg, 21.-22.11.17 (2017).
- 85) A. Lubk, *Advanced Holographic Tomographie for Nanoscale Materials*, SFB Seminar, Universität Konstanz/ Germany, 10.-12.5.17 (2017).
- 86) A. Lubk, F. Roeder, *Quantum state reconstruction using a Transmission Electron Microscope*, *Frontiers of Electron Microscopy in Materials Science*, International Conference (FEMMS) 2017, Johannesburg/ South Afrika, 10.-15.9.17 (2017).
- 87) A. Lubk, D. Wolf, J. Krehl, S. Sturm, F. Seifert, F. Kern, *Advanced Holographic Tomographie for Nanoscale Materials*, Third Salve Symposium at Ulm University, Ulm/ Germany, 11-14.12.17 (2017).
- 88) L. Ma, *Berry phase in optical ring microcavities*, International Workshop on Fundamentals and Applications of Optical Microcavity, Fudan University, Shanghai/ China, 15.10.17 (2017).
- 89) L. Ma, *Micro-ring cavities as novel platform for fundamental and applied research*, Seminar, Hunan University, Changsha/ China, 23.3.17 (2017).
- 90) L. Ma, *Rolled-up microtube cavities and their various applications*, 653. WE-Heraeus-Seminar: Optical Microcavities and Their Applications, Physikzentrum Bad Honnef/ Germany, 9.11.17 (2017).
- 91) L. Ma, *Photon-plasmon modes and directional emission in asymmetric optoplasmonic microcavities*, Workshop on Asymmetric Microcavity and Wave Chaos, Beijing/ China, 19.-22.3.17 (2017).
- 92) M. Medina Sanchez, *Spermibots for assisted fertilization and drug delivery*, Workshop „Brainstorm on Assisted Reproduction Techniques (ART)“, Colombian Fertility and Sterility Center Bogota/ Colombia, 1.-2.6.17 (2017).
- 93) M. Medina Sanchez, *Sperm-hybrid microbots for fertilization and drug delivery*, Seminar - ECCI University, Bogota/ Colombia, 25.10.17 (2017).
- 94) M. Medina-Sanchez, *Miniaturized and ultrasensitive biosensors*, Symposium of Innovation and Technologic Development in Healthcare, ECCI University and Military Hospital, Bogota/ Colombia, 27.10.17 (2017).
- 95) M. Medina-Sanchez, *Microbots for biomedical applications*, Symposium of Innovation and Technologic Development in Healthcare, ECCI University and Military Hospital, Bogota/ Colombia, 26.10.17 (2017).
- 96) T. Muehl, *Magnetic sensors based on coupled nanowire-microcantilever resonators*, Seminar an der Universität Basel, Basel/ Switzerland, 27.1.17 (2017).
- 97) J.A. Otalora Arias, *Towards a 3D curvilinear magnonic transducer*, Spins, Waves and Interactions, Greifswald University, Greifswald/ Germany, 6.-8.9.17 (2017).
- 98) J.A. Otalora Arias, *Curvilinear Magnonics*, 62nd Annual Conference on Magnetism and Magnetic Materials (2017).
- 99) P. Pahlke, M. Sieger, R. Ottolinger, J. Haenisch, B. Holzapfel, A. Usoskin, M. Lao, M. Eisterer, A. Meledin, V. Van Tendeloo, A. Kursumovic, J.L. MacManus-Driscoll, B.H. Stafford, M. Bauer, K. Nielsch, L. Schultz, R. Huehne, *Influence of granularity and artificial pinning centers on superconducting properties of thick YBCO films grown on technical templates*, Nanoselect Annual Meeting, Sant Feliu de Guixols/ Spain, 10.-12.7.17 (2017).
- 100) S. Pauly, L. Deng, U. Kuehn, *Metallic glasses and selective laser melting*, Tamilnadu Science and Technology Centre Chennai - Meet the Scientist Programme - Special lecture on Metallic glasses, B.M. Birla Planetarium, Chennai, Tamil Nadu/ India, 21.11.17 (2017).

- 101) S. Pauly, T. Gustmann, L. Deng, U. Kuehn, *Selective laser melting and metastability*, International Workshop on Laser Additive Manufacturing and Surface Processing, Indian Institute of Technology Indore, Simrol campus, Indore, Madhya Pradesh/ India, 18.11.17 (2017).
- 102) D. Pohl, J. Ruzs, J. Spiegelberg, P. Zeiger, S. Schneider, X. Zhong, P. Tiemeijer, S. Lazar, K. Nielsch, B. Rellinghaus, *Towards atomic resolution magnetic measurements in the TEM*, Science Colloquium, FEI Company, Eindhoven/ Netherlands, 11.5.17 (2017).
- 103) D. Pohl, S. Schneider, P. Zeiger, J. Ruzs, P. Tiemeijer, S. Lazar, K. Nielsch, B. Rellinghaus, *Approaching atomic resolution magnetic characterization in a TEM*, 28. Edgar-Luescher-Seminar, Klosters/ Switzerland, 4.-11.2.17 (2017).
- 104) D. Pohl, S. Schneider, X. Zhong, J. Spiegelberg, P. Zeiger, J. Ruzs, P. Tiemeijer, S. Lazar, K. Nielsch, B. Rellinghaus, *Approaching atomic resolution magnetic characterization in a TEM*, 1st Dresden Symposium on Electron Microscopy, Dresden/ Germany, 15.3.17 (2017).
- 105) A. Popov, *Interior Design of endohedral metallofullerenes for single molecule magnetism*, First Sino Swiss Science and Technology (SSSTC) workshop on Castasegna/ Switzerland, 24.-27.6.17 (2017).
- 106) A. Popov, *Redox-active metal-metal bond in endohedral metallofullerenes*, 50th Heyrovsky Discussion: Molecular Electrochemistry in Organic and Organometallic Research, Castle Trest/ Czech Republic, 18.-22.6.17 (2017).
- 107) A. Popov, *New developments in single molecule magnetism of endohedral metallofullerenes*, 231st Electrochemical Society Meeting New Orleans/ USA, 28.5.-1.6.17 (2017).
- 108) A. Popov, *Interior design of metallofullerenes for single molecule magnetism*, 13th conference on Advanced Carbon Nanostructures, St. Petersburg/ Russia, 3.-9.7.17 (2017).
- 109) A.A. Popov, *Redox-active metal-metal bond in endohedral metallofullerenes*, 50th Heyrovsky Discussion: Molecular Electrochemistry in Organic and Organometallic Research, Castle Trest/ Czech Republic, 18.-22.6.17 (2017).
- 110) A.A. Popov, *Interior design of metallofullerenes for single molecule magnetism*, 13th conference on Advanced Carbon Nanostructures, St. Petersburg/ Russia, 3.-9.7.17 (2017).
- 111) A.A. Popov, *New developments in single molecule magnetism of endohedral metallofullerenes*, 231st Electrochemical Society Meeting, New Orleans/ USA, 28.5.-1.6.17 (2017).
- 112) A.A. Popov, *Interior Design of Endohedral Metallofullerenes for Single Molecule Magnetism*, 1st Sino Swiss Science and Technology (SSSTC) workshop on endohedral single molecule magnets, Castasegna/ Switzerland, 24.-27.6.17 (2017).
- 113) B. Rellinghaus, *The relevance of transmission electron microscopy to modern materials research*, FEI Sales & Service Meeting, Radebeul/ Germany, 18.5.17 (2017).
- 114) B. Rellinghaus, D. Pohl, S. Schneider, S. Wicht, F. Roeder, X. Zhong, K. Nielsch, *The added value of combined in-situ magnetic and structural characterization of nanomagnets with up to atomic resolution*, The Fourth Conference on the Frontiers of Aberration Corrected Electron Microscopy - PICO 2017, Kasteel Vaalsbroek/ Netherlands, 30.4.-3.5.17 (2017).
- 115) B. Rellinghaus, S. Schneider, A. Lubk, K. Nielsch, D. Pohl, *Magnetic characterization of nanoscopic materials in a TEM - Prospects and limitations*, 2nd Sino-German Symposium on Advanced Electron Microscopy and Spectroscopy of Materials, Xi'an Jiaotong University, Xi'an Jiaotong/ China, 13.-15.10.17 (2017).
- 116) B. Rellinghaus, S. Schneider, K. Nielsch, X. Zhong, J. Ruzs, P. Tiemeijer, D. Pohl, *Advanced spectroscopy methods: Magnetic dichroism in TEM*, Frontiers of Materials Science - FSM 2017, Greifswald/ Germany, 4.-6.9.17 (2017).
- 117) B. Rellinghaus, S. Schneider, K. Nielsch, X. Zhong, J. Ruzs, P. Tiemeijer, D. Pohl, *Advanced spectroscopy methods: Magnetic dichroism in a transmission electron microscope*, Frontiers in Materials Science - FSM 2017, Greifswald/ Germany, 4.-6.9.17 (2017).
- 118) M. Richter, *Quantitative Predictions by Electronic Structure Theory*, DFT 2017, Tällberg/ Sweden, 21.-25.8.17 (2017).
- 119) O. Salman, *Effect of scan strategy and annealing on microstructure and properties of 316L stainless steel synthesized by selective laser melting*, The 16th International Conference on Rapidly Quenched and Metastable Materials (RQ16) in Leoben/ Austria, 27.8.-1.9.17 (2017).
- 120) J. Sander, F. Kotcha, *Mikrostruktur und Eigenschaften von hochfesten Werkzeugstählen hergestellt mittels SLM*, Werkstoffwoche 2017, Dresden/ Germany, 27.-29.9.17 (2017).
- 121) R. Schaefer, *Advanced Magneto-Optical Domain Analysis in Soft Magnetic Materials*, 2017 TMS Annual Meeting and Exhibition, San Diego/ USA, 26.2.-2.3.17 (2017).
- 122) R. Schaefer, *Magneto-optical Kerr Microscopy: Status, Progress and Challenges*, Workshop „Frontiers in Metrology Techniques for Magnetic Nanodevices“, Oregon State University, Corvallis/ USA, 20.-21.7.17 (2017).

- 123) R. Schaefer, *Magnetic Materials*, Erasmus block lecture, University Polytechnica, Institute for Metallic Materials Science, Bucharest/ Romania, 13.-15.3.17 (2017).
- 124) R. Schaefer, I. Soldatov, *Micromagnetism, Magnetic Microstructure and their Magneto-Optical analysis*, Seminar at Department of Physics, Tsinghua University, Beijing/ China, 30.5.17 (2017).
- 125) R. Schaefer, I. Soldatov, *Micromagnetism, Magnetic Microstructure and their Magneto-Optical analysis*, Seminar at Key Lab for Magnetism and Magnetic Materials of Ministry of Education, Lanzhou University, Lanzhou/ China, 11.5.17 (2017).
- 126) Gabi Schierning, *Template Assisted Electrochemical Deposition and High Power Factor Materials for Integrated Thermoelectric Devices*, 232 ECS Meeting, National Harbor, Maryland/ USA, 1.-5.10.17 (2017).
- 127) Gabi Schierning, *Thermoelectric devices from nanocrystalline silicon: Materials processing and device concepts*, MCARE 2017 - Materials Challenges in Alternative and Renewable Energy, Jeju Island/ Korea, 20.-24.2.17 (2017).
- 128) O.G. Schmidt, *Microtubular NEMS for on- and off-chip biosensing and -medical applications*, NanoBioSensors Conference, Dresden/ Germany, 4.-5.9.17 (2017).
- 129) O.G. Schmidt, *Microtubular NEMS: From concepts to applications*, 19th Nano Congress for Next Generation, Brussels/ Belgium, 31.8.-1.9.17 (2017).
- 130) O.G. Schmidt, *3D microtubular NEMS: From nanophotonics to biomedical applications*, International Workshop on Advanced 3D Patterning, Dresden/ Germany, 5.-6.10.17 (2017).
- 131) O.G. Schmidt, *Semiconductor-based quantum light sources*, ESR Workshop on Nanoscale Quantum Optics, Budapest/ Hungary, 26.-27.10.17 (2017).
- 132) O.G. Schmidt, *Inorganic nanomembranes for quantum photonics and optoplasmonics*, SPIE Photonics West, San Francisco/ USA, 28.1.-2.2.17 (2017).
- 133) O.G. Schmidt, *Nanomembrane devices: From conception to implementation*, Colloquium, FU Berlin, Berlin/ Germany, 16.6.17 (2017).
- 134) O.G. Schmidt, *Nano- and quantum photonics with membranes and dots*, JST Agency and Leibniz Association Workshop Advanced Material Sciences Dresden/ Germany, 20.-22.9.17 (2017).
- 135) O.G. Schmidt, *Bubble-propelled and biohybrid micromotors*, The Hamlyn Symposium on Medical Robotics, London/ United Kingdom, 25.-28.6.17 (2017).
- 136) O.G. Schmidt, *3D Assembly of microtubular nanomembranes: From basics to devices*, XVI. DESY Research Course 2016: Nanoscience at modern x-ray sources, Hamburg/ Germany, 1.-3.3.17 (2017).
- 137) O.G. Schmidt, *Interfacing microtubular NEMS with single cells and biomolecules*, International Conference on Functional Nanomaterials and Nanodevices Budapest/ Hungary, 24.-27.9.17 (2017).
- 138) O.G. Schmidt, *Micromotors: From science fiction into the realm of possibilities*, Intelligent Systems Colloquium, Max Planck Institute for Intelligent Systems, Stuttgart/ Germany, 7.7.17 (2017).
- 139) O.G. Schmidt, *Micromotors: Opportunities and challenges*, International Conference on Micro/Nanomachines, Wuhan/ China, 25.-28.8.17 (2017).
- 140) O.G. Schmidt, *Microtubular NEMS for on- and off-chip applications*, International Conference on Materials for Advanced Metallization 2017 (MAM2017), Dresden/ Germany, 26.-29.3.17 (2017).
- 141) O.G. Schmidt, *Opportunities and challenges of micromotors*, Micromotors Summer School, Dresden/ Germany, 15.-18.8.17 (2017).
- 142) S. Schneider, D. Pohl, S. Loeffler, P. Schattschneider, M. Schmidt, D. Kasinathan, J. Ruzs, T. Gemming, A. Lubk, D. Wolf, U.K. Roessler, M.J. Stolt, S. Jin, L. Schultz, K. Nielsch, S.T.B. Goennenwein, B. Rellinghaus, *Quantitative magnetic characterization in the TEM*, Seminar Song Jin Group, Madison, WI/ USA, 3.8.17 (2017).
- 143) L. Schultz, *Interaction of Ferromagnetic and Superconducting Permanent Magnets: Quantum Levitation or: The Physics Behind the „Back to the Future II“ Hoverboard*, Physikalisches Kolloquium, Universität Augsburg, Augsburg/ Germany, 10.7.17 (2017).
- 144) L. Schultz, *Superconducting Magnetic Levitation - the Miraculous World of Superconductivity*, Humboldt-Kolleg „Limits of Knowledge“, Crakow/ Poland, 22.-25.6.17 (2017).
- 145) L. Schultz, *Vom Schweben auf Magnetfeldern - die wundersame Welt der Supraleitung*, Alexander von Humboldt Stiftung, Feodor-Lynen-Ausschuss – Langer Abend, Bad Godesberg/ Germany, 10.10.17 (2017).
- 146) L. Schultz, *Symposium on Heusler Compounds as Hardmagnetic Materials*, Dresden, MPI für Chemische Physik fester Stoffe, Dresden/ Germany, 24.3.17 (2017).
- 147) L. Schultz, D. Berger, *SupraTrans - ein schwebendes, umweltfreundliches, geraeuscharmes und sparsames Transportsystem fuer Personen und Gueter*, Verkehrsausschuss der IHK Dresden, Dresden/ Germany, 29.3.17 (2017).

- 148) L. Schultz, G. Fuchs, K. Nenkov, *Interaction of Ferromagnetic and Superconducting Permanent Magnets: Passively Stable Magnetic Levitation*, 1st Workshop of the ERA Net RUS Plus Project „Magnes“, Wroclaw/ Polen, 2.-3.2.17 (2017).
- 149) L. Schultz, G. Fuchs, K. Nenkov, *Possible Applications Related to the Results of the ERA.Net RUS Plus-Innovation Project MAGNES*, 2nd Workshop of the ERA.Net RUS Plus-Innovation Project MAGNES, Wroclaw/ Poland, 28.-29.12.17 (2017).
- 150) S. Scudino, *Strain analysis of plastically-deformed bulk metallic glasses: challenges and opportunities*, PETRA IV: Research with High Energy X-Rays at Ultra-Low Emittance Sources, DESY Hamburg/ Germany, 13.-15.2.17 (2017).
- 151) M. Sieger, P. Pahlke, J. Haenisch, M. Lao, M. Eisterer, A. Meledin, G. Van Tendeloo, K. Nielsch, L. Schultz, R. Huehne, *Fast PLD growth of nanostructured YBCO coated conductors with artificial pinning centers*, 30th International Symposium on Superconductivity 2017 (ISS2017), Tokio/ Japan, 13.-15.12.17 (2017).
- 152) M. Sieger, P. Pahlke, R. Ottolinger, J. Haenisch, B. Holzapfel, M. Lao, M. Eisterer, A. Meledin, G. Van Tendeloo, B.H. Stafford, M. Bauer, K. Nielsch, L. Schultz, R. Huehne, *Incorporation of artificial pinning centers in thick YBCO films grown on technical templates by pulsed laser deposition*, IUMRS-ICAM 2017, Kyoto/ Japan, 27.8.-1.9.17 (2017).
- 153) M. Stoica, P. Ramasamy, I. Kaban, S. Scudino, J. Eckert, *Crystallization behavior and soft magnetic properties of (Fe₃₆Co₃₆B_{19.2}Si_{4.8}Nb₄)_{99.5}Cu_{0.5} bulk metallic glass*, TMS 2017, The 146th Annual meeting and exhibition, San Diego/ USA, 26.2.-2.3.17 (2017).
- 154) M. Uhlemann, V. Haehnel, F.Z. Kahn, J. Koenig, G. Mutschke, H. Schloerb, I. Fritsch, *Combining magnetic forces for contactless manipulation of fluids and electrochemical detection in microfluidic systems*, 68th Annual Meeting of the International Society of Electrochemistry, Providence, Rhode Island/ USA, 27.8.-1.9.17 (2017).
- 155) J. van den Brink, *Iridates and RuCl₃: From Heisenberg antiferromagnets to potential Kitaev spin-liquids*, Recent Progress in Many Body Theories 19, POSTECH, Pohang/ Korea, 25.6.17 (2017).
- 156) J. van den Brink, *Iridates and RuCl₃: From Heisenberg antiferromagnets to potential Kitaev spin-liquids*, APS March Meeting Invited Talk, New Orleans/ USA, 13.3.17 (2017).
- 157) J. van den Brink, *Josephson Currents Induced by the Witten Effect*, Workshop Topology Meets Materials, Dresden/ Germany, 5.6.17 (2017).
- 158) J. van den Brink, *Josephson Currents Induced by the Witten Effect*, Physics Colloquium, University of Cologne/ Germany, 3.5.17 (2017).
- 159) J. van den Brink, *Iridates and RuCl₃: From Heisenberg antiferromagnets to potential Kitaev spin-liquids*, MSU-IFW-ILTPE workshop, Moscow/ Russia, 15.6.17 (2017).
- 160) J. van den Brink, *Resonant Inelastic X-ray Scattering on high T_c cuprates and magnetic iridates*, Spectroscopy Village Science Away Day, Abingdon/ United Kingdom, 31.3.17 (2017).
- 161) J. van den Brink, *Theory of Spectroscopy on Strongly Correlated Electron Systems*, 7th MaNEP Winterschool, Saas Fee/ Switzerland, 9.1.17 (2017).
- 162) J. van den Brink, *Tuneable anyon statistics of vortices at topological insulator interfaces*, CSF Conference - New Trends in Topological Insulators, Monte Verita/ Switzerland, 19.7.17 (2017).
- 163) J. van den Brink, *Josephson Currents Induced by the Witten Effect*, Nordita Workshop on Multicomponent and Strongly Correlated Superconductivity, Stockholm/ Sweden, 20.8.17 (2017).
- 164) A. Waske, *Magnetokalorische Materialien: Von den Grundlagen zur Anwendung*, Seminar des VDI-Arbeitskreis Werkstofftechnik, Bremen/ Germany, 21.6.17 (2017).
- 165) A. Waske, A. Funk, A. Rack, R. Schaefer, *In-situ imaging techniques for the study of hysteresis in magnetocaloric materials*, International workshop on Hysteresis in magnetocaloric, electrocaloric and elastocaloric refrigeration, Dresden/ Germany, 7.-10.2.17 (2017).
- 166) A. Waske, M. Krautz, A. Funk, B. Weise, J. Eckert, *Rapidly quenched and amorphous magnetocaloric alloys*, International Conference on rapidly Quenched & Metastable Materials (RQ16), Leoben/ Austria, 27.8.-1.9.17 (2017).
- 167) A. Winkler, *Applications for surface acoustic wave (SAW) devices and material-/technology related issues in their realization*, Micro/Nanofluidic BioMEMS Group, Massachusetts Institute of Technology (MIT), Boston/ USA, 30.11.17 (2017).
- 168) A. Winkler, *Acoustofluidics*, Einzelvorlesung im Rahmen der Vorlesungsreihe „Biotechnologische Verfahren“, Technische Universität Dresden, Dresden/ Germany, 1.6.17 (2017).
- 169) U. Wolff, B. Ambrozic, J. Zavasnik, K. Zuzek Rozman, K. Leistner, K. Nielsch, S. Sturm, *In-situ observation of the electrochemical deposition of Fe in a transmission electron microscope*, Institutsseminar „Nanostructured Materials“ Jozef Stefan Institute, Ljubljana/ Slovenia, 16.10.17 (2017).

Patents 2017

Issues of patents (issue decision date)

EP15732568.9 (11414 EP)	Batterieträger (02.08.2017) <i>Inventors:</i> Markus Herklotz, Jonas Weiß, Lars Giebeler, Michael Knapp
14/408,126 (11213 US)	Verfahren zur kontrollierten Bewegung von motilen Zellen in flüssigen oder gasförmigen Medien (26.09.2017) <i>Inventors:</i> Veronika Magdanz, Samuel Sanchez Ordonez, Oliver G. Schmidt
DE 10 2011 006 963.1 (11109 DE)	Mehrspur-Unidirektionalwandler (08.05.2017) <i>Inventors:</i> Sergey Biryukov, Günter Martin, Bert Wall
DE 10 2011 007 700.6 (11111 DE)	Verbundwerkstoff und Verfahren zu seiner Herstellung (19.10.2017) <i>Inventors:</i> Uwe Gaitzsch, Claudia Hürrich, Martin Pötschke, Jan Romberg, Stefan Roth, Ludwig Schultz, Sandra Kaufmann-Weiß
DE 10 2012 213 839.0 (11209 DE)	Verfahren zur kontrollierten Bewegung von Objekten in flüssigen Medien (24.02.2017) <i>Inventors:</i> Robert Streubel, Denys Makarov, Oliver G. Schmidt, Larysa Baraban, Gianaurelio Cuniberti

Priority patent applications (priority date)

11623 DE	Magnetokalorischer Wärmeübertrager mit anisotroper Wärmeleitfähigkeit und Verfahren zur Herstellung (03.02.2017) <i>Inventors:</i> Maria Krautz, Markus Klose, Anja Waske, Martin Uhlemann
11604 DE	Vorrichtung zur Steuerung und/oder Regelung der Strömung von Fluiden (12.05.2017) <i>Inventors:</i> Anja Waske, Maria Krautz, David Werner, Samuel Grasemann
11713 DE	Verfahren sowie Vorrichtung und Anordnung zur Filtration magnetischer Partikel (12.05.2017) <i>Inventors:</i> Anja Waske, Stefanie Hartmann
11714 DE	Kompakte Kondensatoren und Verfahren zu ihrer Herstellung (24.05.2017) <i>Inventor:</i> Oliver G. Schmidt
11525 DE	Aufgerollte magnetische Kondensatoren und Verfahren zu ihrer Herstellung (24.05.2017) <i>Inventors:</i> Oliver G. Schmidt, Stefan Harazim, Shoichiro Suzuki
11526 DE	Aufgerollte Energiespeicherbauelemente und Verfahren zu ihrer Herstellung (24.05.2017) <i>Inventor:</i> Oliver G. Schmidt
11712 DE	In situ-Verfahren und Vorrichtung zur Herstellung von Garnen aus Kohlenstoffnanotubes (12.06.2017) <i>Inventors:</i> Vyacheslav Khavrus, Albrecht Leonhardt, Ralf Voigtländer, Bernd Büchner
11630 DE	Brennstoffzelle (30.06.2017) <i>Inventors:</i> Jörg König, Sebastian Burgmann
11626 DE	Verfahren zur Herstellung omniphober Oberflächen (06.07.2017) <i>Inventors:</i> Julia Linnemann, Jakob Sablowski, Simon Unz, Michael Beckmann, Lars Giebler
11613 DE	Dreidimensionale Mikro-Bauelemente und Verfahren zu ihrer Herstellung (22.08.2017) <i>Inventors:</i> Daniil Karnaushenko, Dmitriy Karnaushenko, Oliver G. Schmidt
11717 DE	Vorrichtung und Verfahren zur Bestimmung von Eigenschaften leitfähiger oder dielektrischer Schichten (28.09.2017) <i>Inventors:</i> Hagen Schmidt, Günter Martin
11715 DE	Impulsauflösendes Photoelektronenspektrometer und Verfahren zur impulsauflösenden Photoelektronenspektroskopie (15.12.2017) <i>Inventor:</i> Sergey Borisenko

Graduation of young researchers 2017

Habilitation

Christian Hess	Spin-heat transport of low-dimensional quantum magnets, TU Dresden
Axel Lubk	Holography and Tomography with Electrons – From Quantum States to Three-Dimensional Fields and Back, TU Dresden

PhD Theses

Florian Bittner	Untersuchung der Wechselwirkung von Verarbeitung, Gefüge und Eigenschaften hartmagnetischer Mn-Al-Legierungen mit L10-Struktur, TU Dresden
Anja Bonatto Minella	One-dimensional carbon nanostructures grown from permalloy catalyst nanoparticles, TU Dresden
Tilo Espenhahn	Schaltbare Fahrwegkomponenten für supraleitende Magnetschwebbahnen, TU Dresden
Uwe Gräfe	Investigation of the Superconducting and Magnetic Phase Diagram of Off-Stoichiometric LiFeAs, TU Dresden
Marcel Haft	Synthese intermetallischer Nanostrukturen in Kohlenstoffnanoröhren, TU Dresden
Frank Kirtschig	Topological $k \cdot p$ Hamiltonians and their applications to uniaxially strained Mercury telluride, TU Dresden
Anett Förster	Epitaktische Ni-Mn-Ga-Co-Schichten für magnetokalorische Anwendungen, TU Dresden
Thomas Freudenberg	Integration prästabilisierter Nanopartikel in lösungsbasierten supraleitenden YBa ₂ Cu ₃ O _{7-δ} -Schichten, TU Dresden
Stephan Fuchs	Elektronenspinresonanz an Iridaten in Doppelperowskitstrukturen, TU Dresden
Katrin Junghans	Clusterfullerensynthese mit Methan, TU Dresden
Dmitriy Karnaushenko	Compact helical antenna for smart implant applications, TU Chemnitz
Konrad Kosiba	Flash-Annealing of Cu-Zr-Al-based Bulk Metallic Glasses, TU Dresden
Pranab Kumar Nag	Unusual electronic properties in LiFeAs probed by low temperature scanning tunneling microscopy and spectroscopy, TU Dresden
Xueyi Lu	Architectural nanomembranes as cathode materials for Li-O ₂ Batteries, TU Chemnitz
Abbas Madani	Titanium dioxide based microtubular cavities for on-chip integration, TU Chemnitz
Mahmoud Madian	Fabrication and characterization of highly-ordered TiO ₂ -CoO, CNTs@TiO ₂ -CoO and TiO ₂ -SnO ₂ nanotubes as novel anode materials in lithium ion batteries, TU Dresden
Miléna Martine	Na-Sb-Sn-based negative electrode materials for room-temperature sodium cells for stationary Applications, TU Dresden
Michael Mietschke	Zusammenhang von Gefüge und ferroelektrischen Eigenschaften texturierter PMT-PT-Dünnschichten, TU Dresden
Parthiban Ramasamy	Soft Ferromagnetic bulk metallic glasses with enhanced mechanical properties, TU Dresden
Jinbo Pang	Thermal deposition approaches for graphene growth over various substrates, TU Dresden
Florian Rückerl	Photoemission Spectroscopy at Organic Semiconductor Systems, TU Dresden
Nataliya Samoylova	Cluster-based redox activity in Endohedral Metallofullerenes: Electrochemical and EPR studies, TU Dresden
Benjamin Schleicher	Herstellung und multivariable Beeinflussung epitaktischer Ni-Mn-Ga-Co-Schichten auf piezoelektrischen Substraten, TU Dresden
Xiaolei Sun	Nanomembranes based on nickel oxide and germanium as anode materials for lithium-ion batteries, TU Chemnitz
Yannic Utz	The Effect of In-Chain Impurities on 1D Antiferromagnets - An NMR Study on Doped Cuprate Spin Chains, TU Dresden
Lixia Xi	High-temperature interactions of molten Ti-Al, Ni-Al and Ni-B alloys with TiB ceramic, TU Dresden

Diploma and Master Theses

Mirunalini Devarajulu	Local Photo-response Characteristics in Organic Nanosystems via Cs-AFM, TU Chemnitz
Kristina Ditte	Chemical derivatization of endohedral metallofullerene Y ₃ N@C ₈₀ and its influence on luminescent properties, TU Dresden
Esther Fischer	Electron Energy-Loss Spectroscopy of High-Temperature Superconductors Bi-2212 and Bi-2223, TU Dresden
Christian Frach	Verformungseigenschaften mechanisch vorbelasteter CuZr-Basis-Gläser, TU Dresden
Hannes Funke	Quantum Confinement in Bi ₂ Te ₃ Nanostructures, TU Dresden
Kevin Geishendorf	Annealing of YIG/Pt-Heterostructures for Spin Injection Experiments, TU Dresden
Lukas Graf	Transport properties of thin transition-metal dichalcogenide nanostructures
Yue Gu	Fabrication and Optimization of Organic Thin Film Transistors, TU Chemnitz
Georg Horn	Spinonischer Wärmetransport in Ladungsdotierten Heisenberg-Spinketten, TU Dresden
Esther Jarossey	Synthesis and Crystal Growth of Honeycomb Quantum Magnets, TU Dresden
Felix Kern	Development and Implementation of Liquid He Cryo Electron Microscopy and First Experiments, TU Dresden
Piotr Lepucki	Untersuchung von Kobalt-dotiertem LaOFeAs Poly- und Einkristallen mit NMR und NQR, TU Dresden
Sebastian Maletti	Temperatur- und zusammensetzungsabhängige Untersuchungen an Na-Ionen-Akkumulatoren und Na, Li-Hybridakkumulatoren mit Lithiumtrivanadat (LiV ₃ O ₈) als Kathodenmaterial, TU Dresden
Rick Ottolinger	Untersuchung der Dickenabhängigkeit charakteristischer Eigenschaften Ba ₂ Y(Nb,Ta) ₂ O ₆ dotierter YBa ₂ Cu ₃ O _{7-δ} -Schichten, TU Dresden
Viveksharma Prabhakara	Transport properties of Bi ₄ Br ₄ and Bi ₄ I ₄ topological insulators, TU Dresden
Norbert Puwenberg	Multi-Frequency Magnetic Force Microscopy of Curved Magnetic Thin Films, TU Dresden
Nicola Schädlich	Untersuchungen zum Einfluss der Erstarrungs- und Abkühlraten auf die Gefügebildung und die mechanischen Eigenschaften ausgewählter Stahlgusslegierungen, TU Dresden
Subao Shi	Fabrication of Single Crystal Organic Thin Film Transistor Arrays, TU Chemnitz
Pengfei Song	Strukturelle und ferroelektrische Eigenschaften von epitaktischen BaHf _x Ti _{1-x} O ₃ -Schichten, TU Dresden
Aoyu Tan	Spin Transport in Ultra-Thin Bi ₂ Te ₃ Nanostructures, TU Dresden
Lakshmi Varadharajan	Nanoscale Organic Photodetector based on Rolled-up Nanomembrane Contact, TU Chemnitz
Christoph Wuttke	Thermische und elektrische Transportuntersuchungen an Rhodium-dotiertem BaFe ₂ As ₂ , TU Dresden
Longqian Xu	Fabrication of Molecular Thin-Film Rectifier and Photodetector Based on Rolled-up Nanomembrane Electrodes, TU Chemnitz

Calls and Awards 2017

Professorships

Thirupathaiah Setti S.N. Bose National Centre for Basic Sciences, Under Department of Science and Technology, India

Awards

Oliver G. Schmidt Gottfried-Wilhelm-Leibniz-Preis 2018 of the German Research Foundation (DFG)
Jeroen van den Brink Zernike-Chair 2017, University of Groningen
Daniil Karnaushenko Wilhelm-Ostwald-Nachwuchspreis 2017 of the Wilhelm-Ostwald-Gesellschaft
Yan Chen Chinese Chinese Government Award for Outstanding Chinese Student Abroad
Julia Körner Messtechnik-Preis des Arbeitskreises der Hochschullehrer für Messtechnik e.V. (AHMT)

Best poster/best contribution awards

Sonja Maria Weiz Best Student Paper Award at the 18th International Conference on Biomedical Applications of Electrical Impedance Tomography (21.-24.6. at Dartmouth College, Hanover, NH)
Sonja M. Weiz Best Presentation Award of the NanoBioSensors conference (Sept. 4-5, 2017 in Dresden, Germany) f
Haifeng Xu Best Poster Award at the International Conference on Micro/nanomachines (Aug. 25-28, 2017 in Wuhan, China)

IFW Awards

Konrad Kosiba Tschirnhaus-Medal of the IFW for excellent PhD theses
Florian Rückerl Tschirnhaus-Medal of the IFW for excellent PhD theses
Florian Bittner Tschirnhaus-Medal of the IFW for excellent PhD theses

Scientific conferences and IFW colloquia 2017

March 13 – 14	Scientific Networking Workshop Thermoelectricity, IFW Dresden
March 15	1st Dresden Symposium on Electron Microscopy, jointly organized by cfaed, DCN, IFW and DFCNA
March 19 – 24	DPG-Frühjahrstagung der Sektion Kondensierte Materie (SKM) TU Dresden
April 3 – 5	XXVII International EPR seminar, IFW Dresden
April 24 – 28	Symposium on application of magneto-caloric materials on the Intermag Conference in Dublin (Ireland)
April 25 – 28	International Workshop TOP-SPIN 3: Spin and Topological Phenomena in Nanostructures, IFW Dresden
August 18 – 25	Summer School Spectroelectrochemistry, IFW Dresden
August, 28 – 30	3rd Condensed Matter Summer School 2017, Zbaszyn, Poland
Sep 6 – 8	Spins, waves and interactions 2017, Greifswald
Nov. 15 – 17	Cooperation Kick-Off Workshop mit SPINTEC Grenoble, IFW Dresden

IFW-Colloquium

- Mainzer, Prof. Dr. Klaus, TU München, Kosmos und Chaos - Ordnung und Unordnung um uns, 27.02.2017
- Schroers, Prof. Dr. Jan, Yale Univ., New Haven, USA, Materials Science and Development of Complex Materials, 03.05.2017
- Ludwig, Prof. Dr. Alfred, Ruhr-Univ. Bochum, Discovery and Optimization of Nanostructured Functional Materials for Future Energy Systems, 10.05.2017
- Christiansen, Prof. Dr. Silke, Helmholtz-Zentrum Berlin für Materialien und Energie 3D nanoarchitectures for energy- and bio-medical technologies - enhanced functionality through correlative microscopy and spectroscopy, 18.12.2017

Quantum Matter Colloquium

- Berndt, Prof. Richard, Univ. Kiel, A surface science approach to molecular and atomic contacts, 18.01.2017
- Janoschek, Dr. Marc, National Laboratory Los Alamos, USA, Neutron Spectroscopy on the Most Complex Element: Plutonium, 08.02.2017
- Eberhardt, Prof. Wolfgang, Technical Univ. Berlin, DESY-CFEL Science, Hamburg, New Dimensions in Angle Resolved Photoemission from Solids; a complementary approach to as-laser spectroscopy, 22.02.2017
- Krasnov, Prof. Vladimir, Stockholm University, Multiple quantum critical points in the doping phase diagram of cuprates, 12.04.2017
- Hill, Prof. Stephen, Florida State Univ. and NHMFL Tallahassee, USA, EPR Studies of Molecular Lanthanide Spin Qubits, 24.05.2017
- Rübhausen, Prof. Dr. Michael, Univ. Hamburg, Coupled Energy and Time Scales in Strongly Interacting Condensed Matter Systems, 31.05.2017
- Cao, Prof. Gang, Univ. of Colorado at Boulder, USA, The Challenge of Spin-Orbit-Tuned Ground States in Iridates, 11.07.2017
- Wrachtrup, Prof. Jörg, Univ. Stuttgart, Probing matter with quantum sensors, 23.08.2017
- Trauzettel, Prof. Dr. Björn, University of Würzburg, Correlation effects in topological insulators, 06.09.2017
- Heidrich-Meisner, Dr. Fabian, Ludwig-Maximilians-Univ. München, Advanced density matrix renormalization group methods for electron-phonon problems, 15.09.2017
- Ovchinnikov, Prof. Dr. Yury N., Landau Institute for Theoretical Physics, Russian Academy of Science, Some achievements in theory of Superconductivity in L.D. Landau Institute, 20.09.2017
- von Oppen, Prof. Dr. Felix, Dahlem Center for Complex Quantum Systems and Freie Univ. Berlin, Topological superconductivity and Majorana bound states in chains of magnetic adatoms on superconductors, 11.10.2017
- Chubukov, Prof. Dr. Andrey V., Univ. of Minnesota, Minneapolis, USA, Superconductivity from repulsion, 23.10.2017
- Renner, Prof. Christoph, Univ. of Geneva, Switzerland, Conventional aspects of 'unconventional' high temperature cuprate superconductors observed by scanning tunneling microscopy, 07.12.2017

Guests and Scholarships 2017

Guest scientists (stay of 4 weeks and more)

Name	Home Institute	Home country
Dr. Ahmad, Mushtaq	COMSATS Institute of Information Technology	Pakistan
Dr. Allison, Morgan Charles	University Sydney	Australia
Dr. Amigo, Maria Lourdes	Universidad Nacional de Cuyo	Italy
Dr. Amusan, Akinwumi Abimbola	Otto-von-Guericke Universität Magdeburg	Nigeria
Prof. Dr. Asthana, Rajiv	University of Wisconsin-Stout	USA
Dr. Aswartham, Saicharan	University of Kentucky	India
Dr. Balach, Juan	National Council of Scientific and Technical Res.	Argentina
Dr. Basbus, Juan Felipe	Centro Atomico Bariloche, Rio Negro	Argentina
Dr. Bashlakov, Dmytro	Verkin Insitute Kharkiv	Ukraine
Dr. Bastien, Gael	University Grenoble Alpes	France
Prof. Brenig, Wolfram	TU Braunschweig	Germany
Dr. Brünig, Raimund	BelektronikG	Germany
Dr. Cagliaris, Federico	CNR-SPIN-Institute, Università Genua	Italy
Prof. Dr. Cao, Gang	University of Colorado	China
Dr. Charnukha, Aliaksei	University of California	Belarus
Dr. Darinskiy, Alexander	Institut für Kristallographie Moskau	Russia
Prof. Dr. Dhagat-Jander, Pallavi	Oregon State University	India
Dr. Dioguardi, Adam Paul	Los Alamos National Laboratory	USA
Dr. Egunov, Aleksandr	Institute of Materials Science of Mulhouse	Russia
Dr. Ertugrul, Onur	Izmir Katip Celebi University	Russia
Dr. He, Ran	University of Houston, USA	China
Dr. Hu, Han	Nanyang Technological University Singapore	China
Dr. Huang, Shao-Zhuan	Wuhan University of Technology	China
Prof. Jander, Albrecht	Oregon State University, USA	USA / Germany
Dr. Karmakar, Koushik	Indian Institute of Science Education and Research	India
Dr. Kataeva, Olga	Arbuzov Institute, Kazan	Russia
Dr. Krupskaya, Yulia	Universität Genf	Russia
Dr. Kumar, Sanjeev	Iiser Mohali Faculty of Physics	India
Dr. Kuzian, Roman	Institute for Materials Science Kiev	Ukraine
Dr. Kvitnytska, Oksana	Verkin Insitute Kharkiv	Ukraine
Dr. Lee, Jae-Ki	Korea Electrotechnology Research Institute	South Korea
Dr. Lee, Minho	Korea Electrotechnology Research Institute	South Korea
Dr. Li, Yuan	Institute of Semiconductors Beijing	China
Dr. Liu, Fupin	University of Science and Technology Hefei	China
Dr. Machata, Peter	Slovak University of Technology Bratislava	Slovakia
Dr. Morozov, Igor	Lomonosov State University Moscow	Russia
Prof. Dr. Morr, Dirk	University of Illinois at Chicago	USA
Prof. Dr. Naidiuk, Iurii	Verkin Insitute Kharkiv	Ukraine
Dr. Novikov, Sergei	Ioffe Institut Sankt Petersburg	Russia
Dr. Nussinov, Zohar	Washington University	USA
Dr. Otalora Arias, Jorge Augusto	Center for Nanoscience & Nanotechnology	Colombia
Prof. Dr. Ovchinnikov, Yuri	Landau Institute for Theoretical Physics	Russia
Dr. Palani, Iyemperumal Anand	Indian Institute of Technology Indore	India
Prof. Patra, Ajit Kumar	Central University of Rajasthan	India
Dr. Ramachandran, Ganesh	Institute of Mathematical Sciences, Chennai	India
Prof. Dr. Rapta, Peter	Slovak University of Technology	Slovakia

Dr. Salazar, Enriquez	University Colombia	Colombia
Prof. Dr. Sobczak, Natalia	Foundry Research Institut Krakov	Poland
Dr. Stoeck, Ulrich	Zschimmer&Schwarz GmbH	Germany
Dr. Tian, Zhaoming	University Tokyo	China
Dr. Valligatla, Sreeramulu	CNR-IFN Trento	India
Dr. Vavilova, Evgeniia	Zavoisky Physical-Technical Institute Kazan	Russia
Dr. Volegov, Alexey	Ural Federal University	Russia
Dr. Wang, Jiawei	Hongkong University of Science and Technology	China
Dr. Wang, Liran	Universität Heidelberg	China
Dr. Weng, Qunhong	National Institute for Materials Science	China
Dr. Yerin, Yuriy	Institute for Physics of Microstructures N. Novgorod	Ukraine
Dr. You, Jhih-Shih	Harvard University	Taiwan
Dr. Zalibera, Michal	Universität Bratislava	Slovakia
Prof. Dr. Zhang, Lin	Leibniz Universität Hannover	China
Prof. Dr. Zotos, Xenophon	Universität von Kreta	Greek

Scholarships

Name	Home country	Donor
Dr. Ghimire, Madhav Prasad	Nepal	Alexander von Humboldt Foundation
Dr. Jayamani, Jayaraj	India	Alexander von Humboldt Foundation
Dr. Kim, Beom Seok	South Korea	Alexander von Humboldt Foundation
Dr. Kravchuk, Volodymyr	Ukraine	Alexander von Humboldt Foundation
Dr. Morrow, Ryan Christopher	USA	Alexander von Humboldt Foundation
Dr. Shrestha, Nabeen Kumar	Nepal	Alexander von Humboldt Foundation
Dr. Wenig, Qunhong	China	Alexander von Humboldt Foundation
Dr. Zhang, Yang	China	Alexander von Humboldt Foundation
Dedkova, Katerina	Czech Republic	DAAD
Dr. Hong, Xiaochen	China	DAAD
Dr. Kamashev, Andrey	Russia	DAAD
Meinero, Martina	Italy	DAAD
Charbonneau, Valerie	Canada	DAAD
Prabhune, Ameya	India	DAAD
Saha, Snehajyoti	India	DAAD
Ghunaim, Rasha	Palestinian territories	DAAD
Shahid, Rub Nawaz	Pakistan	DAAD
Dr. Ahmad, Mushtaq	Pakistan	DAAD Leibniz Program
Moo, Guo Sheng James	Singapore	BMBF - Green Talents
Linnemann, Julia	Germany	Deutsche Bundesstiftung Umwelt
Dr. Xi, Lixia	China	Graduiertenakademie TU Dresden
Bittner, Florian	Germany	Graduiertenakademie TU Dresden
Mix, Torsten	Germany	Graduiertenakademie TU Dresden
Pahlke, Patrick	Germany	Graduiertenakademie TU Dresden
Sieger, Max	Germany	Graduiertenakademie TU Dresden
Lupu, Oana-Gratiela	Romania	EU - ERASMUS MUNDUS
Manga, Mihaela-Monica	Romania	EU - ERASMUS MUNDUS
Batalha, Rodolfo Lisboa	Brazil	CAPES Foundation
Dr. Wang, Jing	China	China Scholarship Council
Deng, Liang	China	China Scholarship Council

Name	Home country	Donor
Ding, Ling	China	China Scholarship Council
Fan, Xingce	China	China Scholarship Council
Feng, Le	China	China Scholarship Council
He, Tianbing	China	China Scholarship Council
Li, Zichao	China	China Scholarship Council
Li, Yang	China	China Scholarship Council
Liu, Lixiang	China	China Scholarship Council
Lu, Xueyi	China	China Scholarship Council
Sui, Yan Fei	China	China Scholarship Council
Wang, Pei	China	China Scholarship Council
Wang, Ju	China	China Scholarship Council
Xu, Haifeng	China	China Scholarship Council
Xue, Peng	China	China Scholarship Council
Yin, Yin	China	China Scholarship Council
Dr. Wuppulluri, Madhuri	India	Eleonore Trefftz Guest Professorship
Dr. Tynell, Tommi Paavo	Finland	Finnish Cultural Foundation
Miyajima, Tomohiro	Japan	Kyushu University
Gao, Bo	China	Harbin Institute of Technology
Li, Haichao	China	Harbin Institute of Technology
Liu, Bo	China	Internationale Graduiertenschule
Park, Eunmi	South Korea	Internationale Graduiertenschule
Yousefli, Soroor	Iran, Islam. Rep.	Iran Powder Metallurgy Complex
Salman Omar, Oday	Iraq	Iraqi government
Lara Ramos, David Alberto	Mexico	Mexican government
Dr. Gan, Li-Hua	China	Natural Science Foundation of China
Takeda, Akira	Japan	Niigata University
Assoc. Prof. Dr. Wang, Shenghai	China	Shandong University Weihai
Fernandez Roldan, Jose Angel	Spain	Spanish government

Guest stays of IFW members at other institutes 2017

Gael Bastien	01.10.2017 – 23.10.2017, NMR Messungen, Laboratoire de Physique du solide, Orsay, France
Bernd Büchner	07.09.2017 – 22.09.2017, Lectures at KITP, St. Barbara, USA
Alexander Fedorov	01.06.2017 – 19.06.2017, Beamline Bessy, Berlin, Germany 07.07.2017 – 31.07.2017, Beamtime Bessy, Berlin, Germany
Monica Fernandez Barcia	11.11.2017 – 16.12.2017, ETHZ, Zürich, Schweiz, Switzerland, Training in ITN-SELECTA Project
Jeroen van den Brink	26.10.2017 – 15.12.2017, Zernike Institute for Advanced Materials, University of Groningen, The Netherlands, Zernike Chair
Ching-Hao Chang	13.02.2017 – 03.03.2017, Academia Sinica, National Tsing Hua University, and National Chiao Tung University, China, Research cooperation on spintronics, quantum transport, topological material, and magnetotransport 07.08.2017 – 24.08.2017, Academia Sinica, National Tsing Hua University, and National Chiao Tung University, China, Research cooperation on spintronics, quantum transport, topological material, and magnetotransport
Stefan-Ludwig Drechsler	18.06.2017 – 03.07.2017, Vereinigtes Institut für Kernforschung (VIK) Dubna, Russland, Working visit on super conductors and magnetism
Dmitri Efremov	16.07.2017 – 30.07.2017, The Abdus Salam International Centre for Theoretical Physics (ICTP), Trieste, Italy, Research cooperation on fluctuation effects in multiband superconductors
Jörg Fink	01.05.2017 – 31.05.2017, Gastaufenthalt an der Universität of British Columbia, Vancouver, Canada 03.04.2017 – 23.04.2017, Messungen bei Bessy, Berlin, Deutschland
Lars Giebeler	18.03.2017 – 06.04.2017, Centro Atómico Bariloche (CAB), San Carlos de Bariloche, Argentinien, Research cooperation 29.11.2017 – 15.12.2017, Centro Atómico Bariloche (CAB), San Carlos de Bariloche, Argentinien, Research cooperation
Romain Giraud	03.01.2017 – 20.01.2017, Collaboration SPINTEC, CNRS, Spintec, Grenoble, France 02.05.2017 – 24.05.2017, Collaboration SPINTEC, CNRS, Spintec, Grenoble, France 06.06.2017 – 23.06.2017, Collaboration SPINTEC, CNRS, Spintec, Grenoble, France 28.08.2017 – 14.09.2017, Collaboration SPINTEC, CNRS, Spintec, Grenoble, France 20.11.2017 – 08.12.2017, Collaboration SPINTEC, CNRS, Spintec, Grenoble, France
Junhee Han	29.07.2017 – 11.08.2017, Shanghai University, Shanghai, China, Research cooperation
Volker Hoffmann	09.04.2017 – 01.05.2017, Chuo University, Tokyo, Japan, Research cooperation
Vladislav Kataev	26.04.2017 – 11.05.2017, Measurements and research at Zavoisky Physical Technical Institute, Kazan, Russia 21.09.2017 – 08.10.2017, Measurements and invited talk at Zavoisky Physical Technical Institute, Kazan, Russia

Beom Seok Kim	20.01.2017 – 26.02.2017, Yonsei University, Seoul, Republic of Korea, Research cooperation
Denis Krylov	05.06.2017 – 18.07.2017, SQUID Messungen, Universität Zürich, Schwitterland
Andrey Malyuk	30.10.2017 – 24.11.2017, Crystal Growth Collaboration, Yamanashi University, Kofu, Japan
Rafael Gregorio Mendes	17.03.2017 – 16.05.2017, Soochow University, Suzhou, China, Measurements and research cooperation 22.10.2017 – 22.12.2017, Soochow University, Suzhou, China, Measurements and research cooperation
David Alberto Ramos Lara	25.02.2017 – 13.05.2017 Purdue Purdue University, Indiana, USA
Mark H. Rummeli	10.05.2017 – 15.07.2017, Soochow University, Suzhou, China, Measurements and research cooperation
Maik Scholz	02.02.2017 – 31.05.2017, Measurements and training, Universität Okayama, Japan
Mihai-Ionut Sturza	27.11.2017 – 22.12.2017, research stay, measurements and invited talk, National Institute of Materials Physics, Bukarest, Rumania
Stefan Schwabe	13.07.2017 – 23.07.2017, International School for Materials for Energy and Sustainability VI Pasadena, USA 09.10.2017 – 21.10.2017, European School on Magnetism Cargèse, Korsika, France
Ulrike Wolff	22.09.2017 – 05.11.2017, Jozef Stefan Institut Ljubljana, Slovenia, In-situ measurements TEM 01.04.2017 – 13.04.2017, Jozef Stefan Institut Ljubljana, Slowenien, In-situ measurements TEM
Lixia Xi	23.07.2017 – 12.08.2017, Foundry Research Institute, Krakow, Poland, Research cooperation
Xenophon Zotos	29.09.2017 – 01.12.2017, Lectures at Univ. Heraklion, Greece
Yang Zhang	12.01.2017 – 04.02.2017, IASTU Tsinghua University, Beijing, China, Research visit and talk on Spin Hall effect without spin orbit integration in non collinear magnets 19.05.2017 – 19.07.2017, Forschungszentrum Jülich, Research visit and collaboration on Photocurrent from circularly polarized light 01.10.2017 – 31.12.2017, RIKEN, Wako, Japan, Research visit - Circular photogalvanic effect and shift current In Weyl semimetals, and nonlinear inverse Nernst effect from Berry curvature dipole

Board of trustees

Jörg Geiger, Saxonian Ministry of Science and Art

- Head -

Dr. Peter Schroth, Federal Ministry of Education and Research

Prof. Dr. Gerhard Rödel, TU Dresden

Prof. Dr. Sibylle Günter, MPI for Plasma Physics

Scientific Advisory Board

Prof. Dr. Maria-Roser Valenti, Univ. Frankfurt, Germany

- Head -

Prof. Dr. Robert H. Blick, Univ. Hamburg, Germany

Prof. Dr. Sang-Wook Cheong, Rutgers, USA

Prof. Dr. Andrey Chubukov, Univ. of Minnesota, USA

Prof. Dr. Ralph Claessen, Univ. Würzburg, Germany

Prof. Dr. Matthias Göken, Univ. Erlangen-Nürnberg, Germany

Dr. Heinz Neubert, Siemens AG, Germany

Prof. Dr. Nini Pryds, TU Denmark Lyngby, Denmark

Dr. Jürgen Rapp, Robert Bosch GmbH, Germany

Prof. Dr. Roberta Sessoli, Univ. di Firenze, Italy

Scientific Advisory Board

Head: Prof. Dr. Maria-Roser Valenti
J.-W. Goethe-Univ. Frankfurt

Board of Trustees

Head: MDgt Jörg Geiger

Executive Board

Scientific Director

Prof. Dr. Burkard Hillebrands

Ass.: Dr. Carola Langer - 234

Secr.: Katja Steinbrink - 100

Administrative Director

Dr. Doreen Kirmse

Secr.: Anja Hänig - 200

Public Relation, Media

Safety Officer

Project Funding,
EU-Office

Internal Auditor

Knowledge and
Technology Transfer

Controlling

Institute for Solid State Research (IFF)

Prof. Dr.
Bernd Büchner - 808

Secr.: Kerstin Höllner - 300
Katja Schmiedel - 805

Surface dynamics

Transport and
scanning probe microscopy

Chemistry of nanomaterials

Magnetic properties

Electronic and
optical properties

Synchrotron methods

Crystal growth and synthesis
of inorganic materials

Institute for Metallic Materials (IMW)

Prof. Dr.
Kornelius Nielsch - 104

Secr.: Ines Firlle - 137
Linda Petersohn - 324

Nanoscale electrodeposition
and magnetoionic materials

Functional oxide layers
and superconductors

Magnetic materials

Functional magnetic films

Quantum materials
and devices

Thermoelectric materials
and devices

Metal physics

Magnetic microstructures

Metastable and
nanostructured materials

Institute for Complex Materials (IKM)

Dr.
Thomas Gemming (temp.) - 298

Secr.: Brit Präßler-Wüstling - 217

Solidification processes
and complex structures

Magnetic composites
and applications

Micro- and nanostructures

Chemistry of
functional materials

Electrochemical energy storage

Alloy design and processing

Metallic glasses and composites

Institute for Integrative Nanosciences (IIN)

Prof. Dr. Prof. h. c.
Oliver G. Schmidt - 800

Secr.: Kristina Krummer - 810
Annett Müller

Rolled-up photonics

Integrated nanophotonics

Micro- and nanobiomedical
engineering

Institute for Theoretical Solid State Physics (ITF)

Prof. Dr.
Jeroen van den Brink - 400

Secr.: Grit Rötzer - 380

Theoretical solid state physics

Numerical solid state physics

Quantum chemistry

Topological states of
interacting matter

Research Technology Division (BFT)

Prof. Dr.
Dirk Lindackers - 580

Secr.: Nicole Büttner - 505

Electrical Engineering
and Electronics

Mechanical Engineering

Information Technologies

Administrative Division (BVW)

Dipl.-Kffr. - 620
Friederike Jaeger

Secr.: n.n. - 621

Finance Department

Human Resources

Purchase and Disposal

Library

Facility Management

Labour Council

Equal Opportunity
Commissioner

Representative Body for
Disabled Employees

Confidential Representative
(Ombudsperson)

Data Security Officer

Scientific-Technical
Council (WTR)

Address	Phone	Internet
Helmholtzstrasse 20 D-01069 Dresden	Tel.: +49 351 46 59-0 Fax: +49 351 46 59-540	www.ifw-dresden.de info@ifw-dresden.de

Publisher:

Leibniz Institute for Solid State and Materials Research Dresden

Executive Board Prof. Dr. Burkard Hillebrands, Scientific Director
 Dr. Doreen Kirmse, Administrative Director

Address Helmholtzstrasse 20
 D-01069 Dresden

Phone +49 (0)351 4659 0

Fax +49 (0)351 4659 540

Internet <http://www.ifw-dresden.de>

e-mail info@ifw-dresden.de